Optimisation of Weld Inspection Processes using Advanced Simulation Tools

Matthew McInnes

Centre of Ultrasonic Engineering
Department of Electronic and Electrical Engineering
University of Strathclyde

A Thesis submitted for the degree of
Doctor of Engineering
2025

Declaration of Authorship

This Thesis is the result of the author's original research. It has been composed by the author and has not been previously submitted for examination which has led to the award of a degree.

Date:

Signed:

Acknowledgements

Along the journey to complete this EngD, I would like to acknowledge the support provided to me by:

Dr. Richard O'Leary, Prof. Anthony Gachagan and CUE

As my academic supervisors, I would like to thank them both for their guidance, encouragement, and patience. Their continued input and support have made my time as an EngD student incredibly enjoyable and extremely rewarding. I would also like to give thanks and praise to all that I had the pleasure of working alongside in CUE.

Alison Glover and QinetiQ

As my industrial supervisor at QinetiQ, I would like to thank Alison for her expertise, her guidance, and her relentless enthusiasm for learning. I would also like to thank my industrial sponsor, QinetiQ; especially the team at QinetiQ Rosyth for their continued interest and support.

RCNDE

I would extend thanks to the RCNDE who, without which, this opportunity would not have been possible. Through their EngD programme, I have had the chance to explore some fantastic opportunities and networked with some amazing; giving me a fantastic platform to further my career in NDE.

Family & Friends

Finally, I want to show my greatest of appreciation to my family and friends. To my parents, Jim and Carol, you instilled within me an eagerness to learn new things and develop my skills; you've only ever

wanted the best for me, and you've supported me in everything I've ever done. Thanks also to my brother, Martin, for being there to bounce ideas off, always checking in on how I was or what progress I had made and pushing me to take on new challenges. And to all my friends who were there to keep me motivated through the toughest moments and there to celebrate when I achieved my goals.

Abstract

The application of Non-Destructive Testing (NDT) techniques for the inspection of welded structures are widely used across many engineering industries. Inspection of weld joints is an essential component of structural assessment as it allows fatigue analysis to be carried out to quantify structural integrity and approximate remaining life span. A prominent methodology used for detecting and sizing defects within welded structures is ultrasonic inspection. An advanced ultrasonic technique, commonly implemented for weld inspection due to its robustness and adaptability is Phased Array Ultrasonic Testing (PAUT).

To complement the generation of inspection plans, the use of NDT modelling packages, such as CIVA, is increasing in popularity. They are particularly appealing when dealing with welded structures that have complications such as complex weld/structure geometries, limited surface accessibility or difficulties between the angle of propagation and flaw orientations. In such cases, identical test specimens of the in-situ structures can be made for lab-based analysis. However, these specimens can come at huge expense, have extensive manufacturing periods, require storage space, and cannot be altered once the structure has been made. For such structures, modelling packages can simulate inspection setups by recreating the weld geometries from CAD files, the user can select from a library of probes, position/orientate flaws in any given location, and run parametric studies of varying inspection setups and/or flaw settings.

To guarantee that inspection simulations are fully representative of a physical inspection, the simulation must also be calibrated in the same manner as used in a physical examination. This ensures that the approximated amplitude responses acquired for a given flaw are fully representative of what would be achieved in an in-situ examination. This thesis presents the development of a custom script and process that will allow inspection simulations to be calibrated in a similar manner to physical inspections. The efficacy of the approach for known flaws is demonstrated by its comparison to expected results and the results achieved by alternate approaches to recreate the same calibration method. Further enhancement to the procedure and custom script showed improved approximation capabilities when implemented for in-situ flaws.

Contents

List of Figures

List of Tables

Abbreviations

BWE	–	Back-Wall Echo
CAD	–	Computer-Aided Design
CRA	–	CIVA Reference Amplitude
CMS	–	Custom MATLAB Script
DAC	–	Distance Amplitude Correction
DGS	–	Distance Gain Size
FBH	–	Flat Bottomed Hole
FEA	–	Finite Element Analysis
FMC	–	Full Matrix Capture
GE	–	General Electric
GUI	–	Graphical User Interface
GTD	–	Geometrical Theory of Diffraction
HAZ	–	Heat Affected Zone
HIC	–	Hydrogen Induced Cracking
KA	–	Kirchhoff Approximation
LOF	–	Lack of Fusion
NDT / NDE	–	Non-Destructive Testing / Evaluation
PAC	–	Phased Array Controller
PAUT	–	Phased Array Ultrasonic Testing
P-C	–	Pitch-Catch
P-E	–	Pulse-Echo
PRF	–	Pulse Repetition Frequency
RCNDE	–	Research Centre in Non-Destructive Evaluation
SDH	–	Side Drilled Hole
SLS	–	Standard Linear Solid
SOV	–	Separation of Variables
TCG	–	Time Corrected Gain

TFM	–	Total Focussing Method
TOF	–	Time of Flight
VPA	–	Virtual Probe Aperture

Acronyms

CUE	–	Centre for Ultrasonic Engineering
MOD	–	Ministry of Defence
TOFD	–	Time of Flight Diffraction

1 Introduction

Non-Destructive Testing/Evaluation (NDT/NDE) is a safety critical process, used to quantify the integrity of weld-joints across a variety of structure types such as oil and gas pipelines, railway tracks, and maritime platforms. NDT techniques are utilised to find, characterize, and size defects, such that a specific governing standard's sentencing criteria can be applied. Across engineering industries, including defence, Ultrasonic Testing (UT) is a prominent NDT approach. Its distinct technique variations allow inspectors to maximise detection, characterize indications and size defects effectively. This has particular importance when inspecting complex geometry scenarios. To support the findings from physical inspections, NDT modelling/simulation packages are becoming increasingly popular due to their recent advances in defect approximation. This chapter outlines the motivation of the work within this thesis, highlights the objectives of the research and details the author's contributions.

1.1 Motivation

The motivation and the achieved outcomes of this research are driven by a collaboration of academic and industrial partners. The research of this Engineering Doctorate (EngD) was funded through the Research Centre in Non-Destructive Evaluation (RCNDE); whose goal is to match the needs of industry with the latest research in NDE. Bringing academia and industry together, the academic sponsor of this work was the Centre for Ultrasonic Engineering (CUE) from the University of Strathclyde and the industrial sponsor was QinetiQ.

QinetiQ are defence technology contractors that specialise providing engineering and scientific expertise for mission critical objectives, fast-track innovation, and test and evaluation services. The company are engaged in a variety of sectors including Cyber, Aviation/Aerospace and Law Enforcement. However, the outcomes of this thesis are primarily aimed at supporting the delivery of objectives to customers within the Maritime sector.

Leading up to the development of this EngD project, the NDE team had been following the changes in customer demand and objective complexity, relative to the expertise they could provide. Common deliverables included the generation and review of inspection procedures and setups to investigate specific weld geometries. The preferred method of approach is to have a replica of the desired geometry with artificial defects manufactured as a test specimen. Once built, an optimised inspection setup can be obtained/designed by trialling variations in inspection setup to be implemented and the results issued to the customer.

However, there are varying degrees of complexity within welded structures and geometries that have huge impacts on how an inspection plan is generated. Some factors are dependent on whether the geometry is being inspected at manufacture or while in-service with variations in access to the weld geometry for the inspector and variations in surface availability for probe positioning. Probe positioning can be further influenced by the location of the weld relative to structural features such as tapers/nozzles, curved surfaces, structural penetrations, and T-butt joints.

Consequently, as weld geometry complexity increases, the expense to manufacture, store, inspect, and analyse the replica test specimen will also rise. To highlight the potential difference in cost that can occur; manufacturing test specimens can range from a few thousand pounds to hundreds of thousands of pounds. Despite these valuations being dependent on a variety of factors such as dimensions, shape, included defects and chosen material, the difference in price is immense.

To overcome this issue, QinetiQ began investigating the use of NDT inspection simulation software to acquire an effective solution. Thus, QinetiQ acquired licenses for the semi-analytical NDT modelling package, CIVA [CEA-List, France]. With the ability to perform parametric studies on parameters such as weld geometry, flaw orientation and probe setup/positioning, numerous permutations of inspection setup can be generated without the same costs of manufacturing required for a test specimen.

QinetiQ operate under the guidance of the UK Defence Standards when performing NDT tasks. Where the British, European, and International Standards are applicable across a range of industries and not mandatory (unless required by law), the UK Defence Standards are a specialised and mandatory set of standards specific to military and defence applications within the UK. Within them, UT is one of the prominent inspection techniques due to its adaptability and defect sizing capabilities. Initial viewing of CIVA simulation results showed great potential in replicating the results of a physical inspection. However, more in-depth analysis of the data found that the calibrated simulations are not representative of physical inspection setups with respect to amplitude responses and simulation setup/approach. This led to the proposal of an EngD project to investigate and implement a process that would validate the use of CIVA and produce defect amplitude approximations that are representative of any physical inspection.

QinetiQ collaborate with other defence organisations to update and revise the UK Defence Standards. These Standards govern how UT inspections are carried out and how indications, flaws and defects are characterised and sentenced. At present, the use of NDT simulation software to approximate defect amplitude response within UT inspections is not included within the UK Defence Standards. A technology transfer has been acquired as QinetiQ have a foundation to further investigate and develop the presented research and procedures. Stemming from this project, QinetiQ can begin to present the argument of including this method and potentially others in future revisions of the UK Defence Standards.

1.2 Contribution to Knowledge & Technology Transfer

The completion of an EngD thesis requires demonstration of enhancement to scientific knowledge for the given field and the technology transfer of the scientific findings to the sponsoring industry partner.

1.2.1 Scientific Knowledge Contribution

Stemming from this thesis is a novel replication of the Time-Corrected Gain (TCG) calibration process used in experimental linear scanning Phased Array Ultrasonic Testing (PAUT) inspection setups for CIVA-simulated inspection setups. The contribution made was founded on the inappropriate difference in calibration approach between the physical and simulated setups. Consequently, the calibrated simulated setup would not fully reproduce the normalised image that a calibrated physical inspection would. A custom MATLAB script was created that extracted and interpolated the amplitude response data of a linear scanning PAUT calibration inspection simulation of Side-Drilled Holes (SDH) at varying depths. The script would then calibrate all data points within an inspection simulation, using the same PAUT setup, relative to the SDH response at the same depth.

Based on the success of this, another contribution was made in the implementation of a methodology that aligned the simulated correlation between two flaw types in CIVA that implemented two approximation algorithms respectively. The novelty of this contribution lies in the integration of experimental data into the calibration of the CIVA simulation results for a linear scanning PAUT setup to improve the amplitude approximations of known defects.

Further contributions were made in the amalgamation of the previous contributions into the investigation and development of a procedure used to approximate the amplitude response of unknown defects and prediction of their geometry definition. By implementing the amplitude response of a known flaw as a reference amplitude, the amplitude response from the defect can be accurately predicted. Similarly, the development of this procedure also provided improved reverse engineering capabilities to define the geometry of an unknown defect based on experimental scan data.

1.2.2 Technology Transfer

The scientific advancement of this thesis is the development and implementation of a methodology aimed at approximating the amplitude response, and potential geometry, of defects within any given test specimen. Across various industrial standards, including the UK Defence Standards (used by the industrial sponsor of this work), the use of modelling packages to simulate the outputs of inspection setups is very limited. Much of the reasoning behind this lies in the lack of confidence in the accuracy, consistency, and reliability of the simulated data.

The difficulties overcome within this thesis provide the industrial partner with a confidence in a procedural approach that attends to the need for simulated approaches to support and enhance the delivery and analysis of NDT inspections. The products of this thesis provide the industrial partner with a software tool that improves the quality of the deliverables for customers and enhances their stature to influence the direction of industrial standards.

1.3 Contributions & Publications

Through the presentation and publication of findings at relevant, international conferences, the author has ensured that the motivations and outcomes of this thesis piques interest with the wider industrial community throughout the EngD. Conference involvements include:

- Abstract Paper and Presentation – McInnes, M. & O'Leary, R. & Gachagan, A. & Glover, A., (2019) "CIVA calibration for linear scanning phased array ultrasonic testing", *Review of Progress in Quantitative Nondestructive Evaluation*, Portland, Oregon.

- Poster Presentation – McInnes, M. & O'Leary, R. & Gachagan, A. & Glover, A., (2019) "Time Corrected Gain Calibration for CIVA Simulated PAUT Inspection", International Ultrasonic Symposium, Glasgow, UK.

- Presentation – McInnes, M. & O'Leary, R. & Gachagan, A. & Glover, A., (2019) "Defect amplitude response approximation using TCG calibrated CIVA simulation of PAUT inspection", 58th Annual British Conference on Non-Destructive Testing, Telford, UK

- Virtual Conference Presentation – McInnes, M. & O'Leary, R. & Gachagan, A. & Glover, A., (2020) "Improved CIVA simulation of TCG calibration for PAUT inspection", BINDT NDT Webinar Week 2020, UK.

- Virtual Conference Presentation & Proceedings Paper – McInnes, M. & O'Leary, R. & Gachagan, A. & Glover, A., (2021) "Improving CIVA simulation of PAUT inspection using experimental TCG calibration data", BINDT NDT Webinar Week 2021, UK.

1.4 Thesis Structure

The breakdown of this thesis is presented across six chapters. This first section establishes the content and context of work addressed within the thesis, introducing the topic area, the underlying motivations, and the contributions to scientific knowledge and industrial application.

Section Two is a review of ultrasonic inspection techniques. It begins an overview of the well-established principles that relate to ultrasonic propagation, including Snell's Law and wave interference. This provides a basis into an evaluation of different ultrasonic testing probes and techniques for weld inspection.

Section Three gives an overview of weld inspection. Firstly, it describes different weld geometry types, why they are used, the welding approach used to manufacture, and common welding defects. This leads into the detection, sizing, characterisation and sentencing of the defects in relation to the UK Defence Standards and the established calibration processes for weld inspections using ultrasonic testing techniques.

Section Four instigates the use of modelling of ultrasonic testing inspection setups, providing an introduction to the NDT simulation platform CIVA and its methodology into replicating ultrasonic inspection setups. An overview into the design of a custom block manufactured with known reflectors and defects is demonstrated to validate simulation replicas against physical scans.

Section Five introduces the discovery and discussion of CIVA's calibration limitations, giving way to the development of a custom

calibration process. Implementation of the process and evaluation of its performance is analysed. a novel approach to correlate inspection and calibration simulations using experimental data from a custom carbon-steel test specimen. Implementing the process developed in Section Four, calibrated simulation scans of the block are compared with experimental scans to evaluate its performance. Further enhancements are discussed to improve the approaches' approximation capabilities before being trialled on a test specimen containing defects, before leading on to the use of the process in reverse engineering defect geometries from imaging data.

Section Six provides a discussion on the key findings and developments made within the thesis. This is supplemented by potential areas of future work.

2 Review of Ultrasonic Inspection Techniques

2.1 Fundamentals of Ultrasonic Propagation

2.1.1 Wave Propagation

Ultrasonic waves are mechanical vibrations above the threshold of human hearing (typically 20 kHz). They propagate *via* the vibrations of the particles within the medium of propagation and the interaction of these elastic oscillations with adjacent particles [1]. In most materials, the vibration of a particle can be modelled as the oscillatory motion of a mass suspended on a spring, as shown in Figure 1:

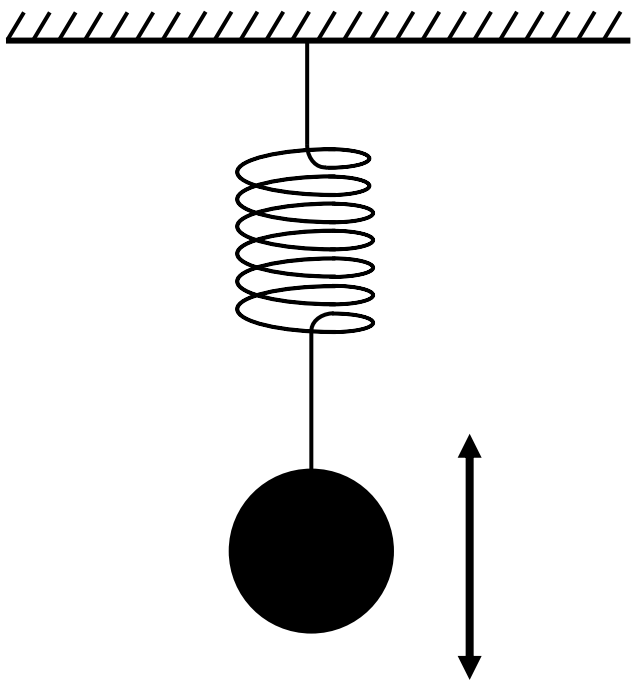

Figure 1: Schematic diagram of vibrational motion of a weight-loaded spring

When the system in Figure 1 is static, the gravitational force of the weight is in equilibrium with the tension force of the spring. Displacement in-line with the vertical axis from its resting position will cause the mass to oscillate about this position. If the position of the mass were tracked as a function of time, the resulting graph would follow a sinusoidal wave. The resulting vibrational motion would be generated

regardless of whether the initial mass position was adjusted to raise the mass and slacken the spring or the mass was pulled down in order to expand the spring.

In an ideal environment, where there is a complete conversion of potential energy to kinetic energy and *vice versa*, the sinusoidal displacement function of the mass oscillating about its equilibrium position would continue indefinitely. However, in a real-world scenario, the maximum displacement of the mass will decrease over time due to energy being lost as heat through friction. The elastic potential energy stored within a spring can be derived from Hooke's Law [2], where F is the spring force, k is the spring constant and x is the displacement the mass has been stretched or compressed:

$$F = k \cdot x \tag{2.1}$$

Hooke's Law gives the force required to extend or compress a spring by a distance of magnitude, x [3]. The energy required to accomplish this can be visualised as the area under the curve of spring force versus displacement. For a fixed magnitude spring constant, integration of this linear relationship generates the following equation, where E is the elastic potential energy, k is the spring constant and x is the displacement by which the spring has been stretched or compressed:

$$E_{EP} = \frac{1}{2} k \cdot x^2 \tag{2.2}$$

At the turning points of the vibrational motion, the mass can be considered stationary, with zero kinetic energy. The total potential energy at either turning point can be calculated using Equation 2.3, where m is the mass of the weight, g is the gravitational field strength and h is the vertical displacement of the mass [2]:

$$E_P = E_{EP} + E_G = \frac{1}{2}k \cdot x^2 + mgh \tag{2.3}$$

Due to the energy being lost through friction as heat, the total potential energy at either turning point will decrease through each oscillatory motion. With h being proportional to the square of x and all other variables remaining constant, the maximum mass displacement from the equilibrium position must decrease over time due to the conservation of energy. To counter the decrease in displacement of the vibrations over time, the oscillation amplitude can be maintained through a continuous sinusoidal excitation with a matching oscillation frequency [4].

Based on this simple concept, many metallic materials can be conceptualised as a framework of masses connected by springs, as shown in Figure 2, where the masses and springs represent the material particles and the elastic forces connecting them [1].

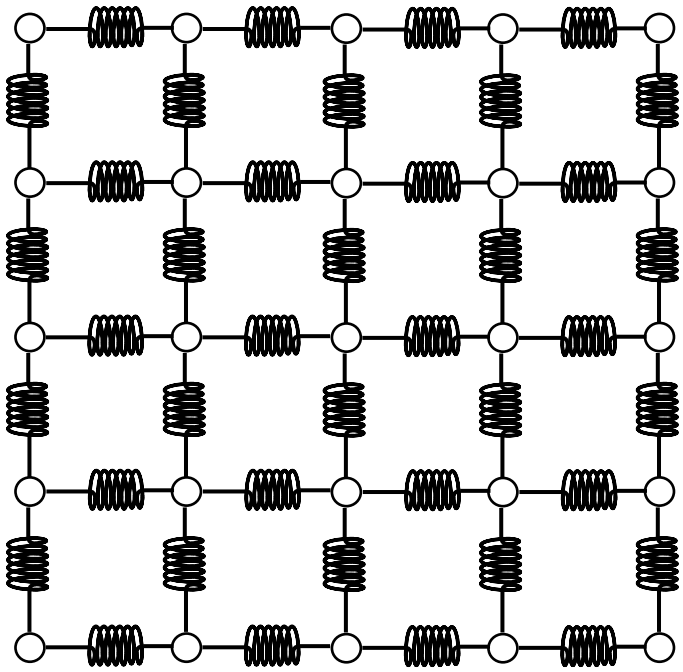

Figure 2: Schematic 2-dimensional representation of structure particle framework

The schematic in Figure 2 illustrates a two-dimensional cross-sectional model of a three-dimensional structure framework. Within this network, vibrating particles will interact with adjacent particles, creating a propagation of vibrational motion. Due to the elastic nature of the medium, the oscillation frequency of all excited particles will be constant. Consequently, the propagation of the vibrational motion will result in particles oscillating out of phase relative to previously excited particles. However, if the elastic forces connecting the particles were stiff, represented by the springs, then the entire network of particles would move together, in phase.

Alternative models to the mass and spring structure particle framework can be used to represent the material particle framework, such as the spring and dashpot model framework. Using the same gridded framework as shown in Figure 2, each spring connection will include one or multiple dashpots connected in series or parallel. A

dashpot can be interpreted as a device that dampens motion and dissipates the vibrational energy. In an ideal environment, excitation of the framework in Figure 2 would vibrate indefinitely. However, dampening the simulated vibrations within the model framework aims to replicate attenuation and acoustic impedance, discussed later in Sections 2.1.3 and 2.1.4.

A variety of spring and dashpot models can be used to represent the elastic forces connecting material particles, each with a differing vibrational behaviour. Figure 3 illustrates three example connections of the spring and dashpot models: (a) the Maxwell model, (b) the Kelvin Voigt model, and the Standard Linear Solid (SLS) model [5].

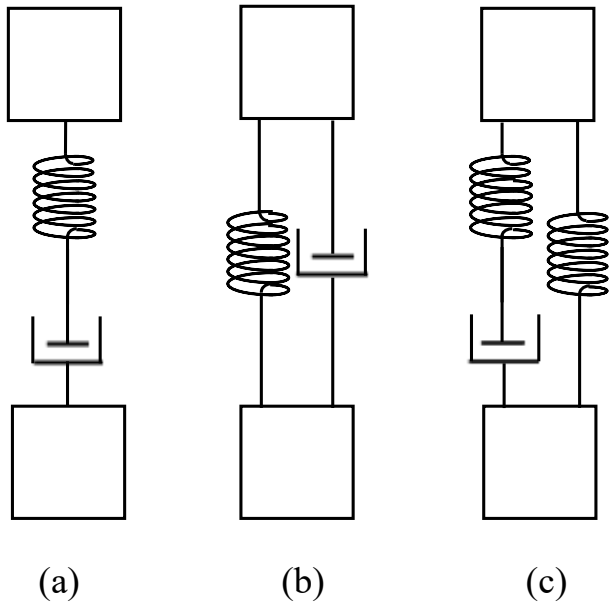

Figure 3: Schematic 2-dimensional representations of spring and dashpot structure particle connections: (a) Maxwell model, (b) Kelvin-Voigt model, and (c) SLS model

2.1.2 Propagation Modes

Variations in the collective excitation of particles can generate differing modes of wave propagation throughout a structure. Using the structure particle framework illustrated in Figure 2 for simplicity, there are two widely occurring propagation modes. One wave propagation method can be generated through simultaneous oscillation of all particles in the first column of the framework depicted in Figure 2. Repetitive oscillatory excitation aligned to the direction of propagation causes successive compression and rarefaction of the elastic joints between adjoining particles. This type of wave is termed a longitudinal or compression wave and can propagate within solid, liquid or gaseous media. For greater clarity, Figure 4 represents a snapshot of a longitudinal wave progressing through a structure, from left to right:

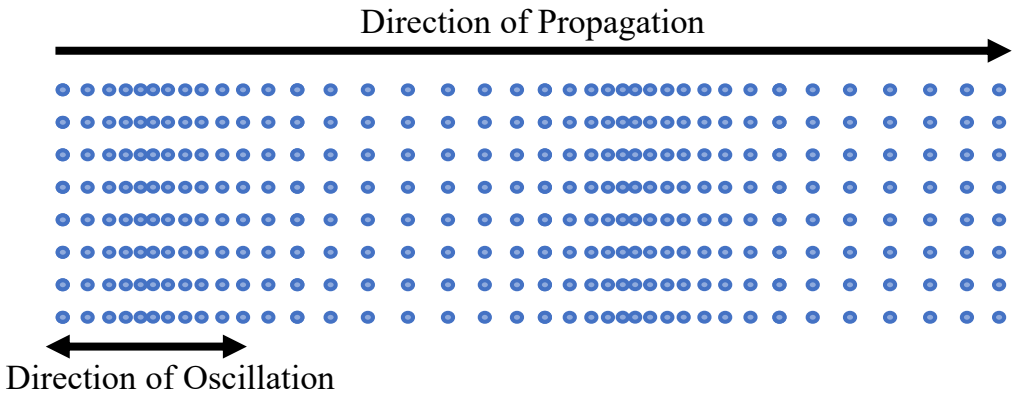

Figure 4: Schematic representation of longitudinal wave propagation

Figure 4 shows that longitudinal waves propagate parallel to the oscillation axis. The velocity of the propagation can be calculated from the material properties of the medium. Using Equation 2.4 [6], the longitudinal wave velocity, v_L, can be determined from E , the Young's Modulus (elasticity of a material [2]), ρ , the density of the material and υ, Poisson's ratio (ratio of transverse to longitudinal strain [7]).

$$v_L = \sqrt{\frac{E(1-\upsilon)}{\rho(1+\upsilon)(1-2\upsilon)}} \tag{2.4}$$

The second main bulk wave mode is known as transverse or shear wave mode as the particle vibration motion is perpendicular to the direction of propagation. The oscillatory motion of the particles and propagation of the wave, from left to right, can be visualised from the schematic shown in Figure 5.

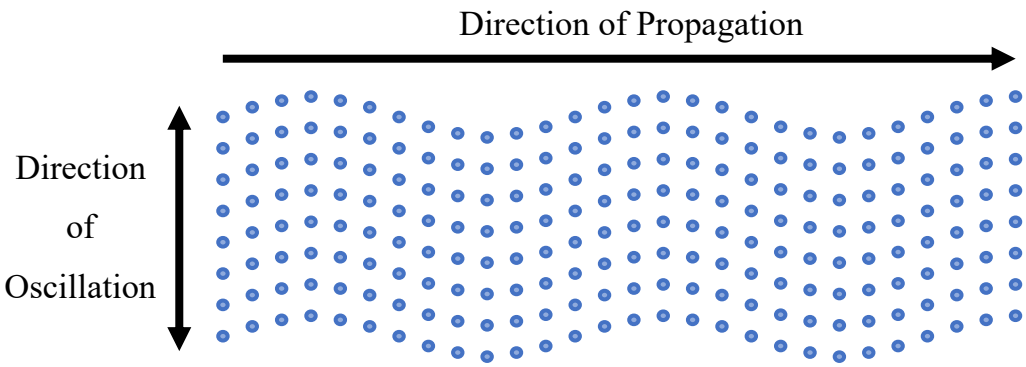

Figure 5: Schematic representation of transverse wave propagation

Unlike the compression and expansion forces endured by the bonds connecting particles during longitudinal wave propagation, the bonds within the transverse mode experience shear forces. In order to propagate transverse waves through a medium, the medium requires sufficient rigidity to resist shear forces [8]. Therefore, transverse waves cannot exist within fluid media, only within solids. Using Equation 2.5 [6], the transverse wave velocity, v_S, can be determined where G is the Shear Modulus (ratio of shear stress to shear strain [9]).

$$v_S = \sqrt{\frac{E}{2\rho(1+\upsilon)}} = \sqrt{\frac{G}{\rho}} \tag{2.5}$$

For either propagation mode, the wavelength depends on the oscillation frequency and the wave velocity of the medium. Frequency is measured in Hertz (Hz), which is defined as the number of complete oscillation/wave cycles per second.

The wavelength, λ, can be calculated from Equation 2.6, where V is the velocity of the wave mode in question (longitudinal or transverse) and f is the frequency of oscillation.

$$\lambda = \frac{V}{f} \tag{2.6}$$

Quantifying the wavelength, using Equation 2.6, is critically important when choosing an excitation frequency for an inspection. The wavelength of the propagating wave provides an indication of the size of defect that can be reliably detected for the designated frequency [1]. Therefore, due to the inversely proportional relationship of wavelength and frequency, smaller defects are more likely to be detected with higher frequencies.

The frequency range for industrial inspections is typically between 100 kHz and 50 MHz [10]. Ultrasound frequencies at the lower end of the spectrum (< 1MHz) are used for dry/air-coupled inspections [11] or composite material inspections [12]. Sound energy propagation capability decreases with reducing material density and air and

composite materials are significantly less dense than metallic materials like carbon steel. In addition, higher frequency waves attenuate more than lower frequency waves, as discussed later in Section 2.1.3. Therefore, waves with a lower frequency will have more suitable penetration capabilities for less dense materials.

By comparison, for inspections carried out using frequencies at the upper end of the frequency range (> 25 MHz), the wavelength continues to shorten, and the penetration capabilities become more limited. These frequencies are preferred for flaw detection/sizing and thickness measurements on small components such as those found on an integrated circuit board [13].

Most ultrasonic inspections are carried out using frequencies within the 1 MHz to 25 MHz range [14]. Inspections that are commonly carried out within industry include those on weld joints for manufacture and in-service defects [15], and pipelines suffering corrosion [16].

2.1.3 Attenuation

In an ideal environment, there would be no energy loss during the propagation of a wave from particle to particle across the structure framework illustrated in Figure 2. However, some of the kinetic energy is absorbed and converted into heat energy by the particles and the connecting bonds during the transfer of the vibrational motion. Consequently, the magnitude of the oscillations decreases with increasing distance from the initially excited particles. This phenomenon is known as attenuation.

The extent to which attenuation affects the propagation of ultrasound can be calculated from Equation 2.7 [17], where A_0 is the unattenuated amplitude of the propagating wave, z is the specified distance travelled by the wave, A is the reduced amplitude having travelled distance z, and α is the attenuation coefficient (which is proportional to the wave frequency [1]).

$$A = A_0 e^{-\alpha z} \tag{2.7}$$

Equation 2.7 shows that the amplitude of a propagating wave is inversely related to attenuation and propagation distance. Another factor that can have a negative impact on ultrasonic propagation is the grain structure within certain materials, such as austenitic stainless steel [18]. The grains within a material cause the ultrasonic wave to scatter. The magnitude of the scatter will depend on the size of the grains. Grain sizes that approach the wavelength of the propagating ultrasound will cause greater reductions in the penetration capabilities of the wave. In addition, the anisotropic and inhomogeneous nature of granularity has the undesirable effect of causing speckle patterns in ultrasonic imaging [19, 20]. This can lead to poorer signal to noise ratios and negatively impact defect detection capabilities [21].

These types of loss are the two main causes for reductions in wave propagation amplitude [22]. One way to counter the reduction is to decrease the frequency of the propagating wave as it is proportional to the attenuation coefficient, which is inversely proportional to wave amplitude, in accordance with Equation 2.7.

Furthermore, as previously mentioned in Section 2.1.2, frequency and wavelength have an inversely proportional relationship, thus a lower frequency will propagate with longer wavelengths that are affected less by larger grain structures.

2.1.4 Acoustic Impedance & Snell's Law

The resistance encountered by an ultrasonic wave as it passes through a medium is termed acoustic impedance. The magnitude of the acoustic impedance, Z, for a given material can be calculated using Equation 2.8 [23], where ρ is the density of the material and V is the acoustic velocity.

$$Z = \rho V \tag{2.8}$$

Evaluating the acoustic impedance of a material is critical when investigating the transfer of an ultrasonic wave between heterogeneous media at a boundary interface. Depending on the angle of incidence of the ultrasonic wave to a boundary interface, differences in acoustic impedance between the materials can greatly influence the ratio of transmitted to reflected wave energy.

At normal incidence, Equations 2.9 and 2.10 [24] can be used to calculate the pressure coefficients of transmission, T, and reflection, R, where Z_1 and Z_2 represent the acoustic impedances of the materials on each side of the interface.

$$T = \frac{2Z_2}{Z_1 + Z_2} \tag{2.9}$$

$$R = \frac{Z_2 - Z_1}{Z_1 + Z_2} \tag{2.10}$$

Through the conservation of energy, Equation 2.11 relates these two coefficients.

$$T = 1 + R \tag{2.11}$$

Multiplying the coefficients by 100 will provide a percentage of how much of the ultrasonic pressure has transmitted and how much has been reflected. In the case of wave propagating from a material of high acoustic impedance to a one of low impedance, a greater proportion of the wave pressure will be reflected. In this case, the reflection coefficient percentage will be negative; meaning that the reflected wave will have an inverse phase to the incident wave [25].

By contrast, when a wave propagates from a low acoustic impedance material to one of higher impedance, a greater proportion of the wave will be transmitted. This will result in a transmission coefficient percentage greater than 100%.

Despite this anomaly, the conservation of energy is still preserved as the coefficients relate to the sound pressure and not intensity. The magnitude of the wave intensity is related to the ratio between the sound pressure and the acoustic impedance. Therefore, despite the significant increase in sound pressure of the wave within the transmission material, the larger acoustic impedance will significantly reduce the intensity [1].

The intensity of a reflected waves can be calculated through the Equations 2.12 and 2.13 [26]:

$$R = \left(\frac{Z_2 - Z_1}{Z_1 + Z_2}\right)^2 \tag{2.12}$$

$$T = \frac{4Z_1Z_2}{(Z_1 + Z_2)^2} \tag{2.13}$$

To demonstrate how the ultrasonic intensity changes through the propagation between different materials, Figure 6 illustrates the transmission and reflection of waves at the three interface stages within an immersion inspection of a steel block.

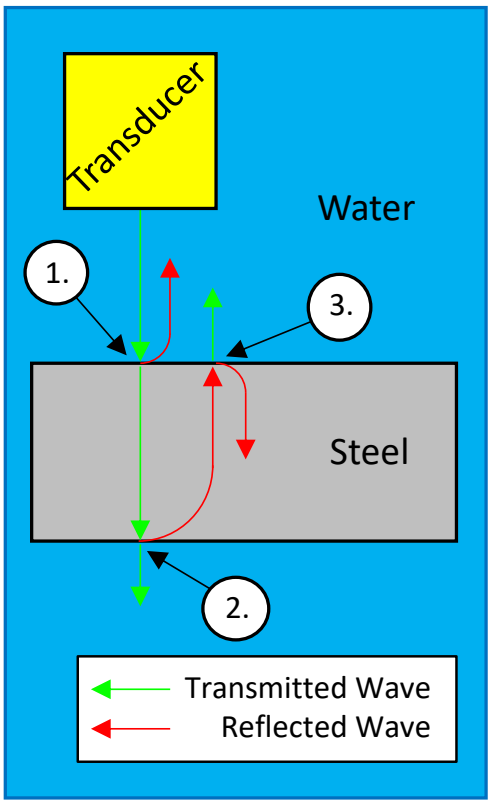

Figure 6: Schematic of ultrasonic transmission/reflection at material interfaces

Equations 2.12 and 2.13 can be applied at the three marked interfaces to calculate the transmitted and reflected intensities at each stage of the inspection. Numerical analysis can be applied to the example illustrated in Figure 6, assuming the acoustic impedances of the steel and the water to be 45 x 10^6 kg/m^{2}s and 1.5 x 10^6 kg/m^{2}s, and the densities to be 7850 kg/m^3 and 1000 kg/m^3 [1].

Assuming that no energy is lost through attenuation, the coefficients at each stage can be calculated:

$$\text{Transmission Coefficient} = \frac{4Z_1Z_2}{(Z_1 + Z_2)^2}$$

$$= \frac{4 \cdot 1.5 \cdot 45}{(1.5 + 45)^2}$$

$$= 0.125$$

$$\text{Reflection Coefficient} = \left(\frac{Z_2 - Z_1}{Z_1 + Z_2}\right)^2$$

$$= \left(\frac{45 - 1.5}{1.5 + 45}\right)^2$$

$$= 0.875$$

Using these calculated coefficients, the percentage of transmitted and reflected ultrasonic energy at each material interface can be determined:

Interface 1.	% Transmission	= 100% * 0.125
		= 12.5%
	% Reflection	= 100% * 0.875
		= 87.5%
Interface 2.	% Transmission	= 12.5% * 0.125
		= 1.56%
	% Reflection	= 12.5% * 0.875
		= 10.94%
Interface 3.	% Transmission	= 10.9375% * 0.125
		= 1.37%
	% Reflection	= 10.9375% * 0.875
		= 9.57%

From these calculations, 12.5% of the total ultrasonic energy will transmit into the steel structure from the water at the first material interface while 87.5% of the total energy will be reflected back toward the probe. At the following boundary, 1.56% of the total ultrasonic energy will transmit back into the water and 10.94% will internally reflect at the backwall boundary (1.56 + 10.94% = 12.5%). In a repeated process, the third material boundary will result in 1.37% of the total ultrasonic energy transmitting into the water and back toward the probe, while 9.57% will continue to propagate within the steel specimen.

In the situation of non-normal incidence, a portion of the wave will reflect, and a portion will transmit and undergo refraction. The reflected wave will propagate from the boundary at an angle equal in

magnitude to the incident angle from the normal. The refracted wave will propagate through the second medium at an angle deviating from the direction of the incident wave. The interaction of the incident wave at a boundary can be represented by the illustration shown in Figure 7, where θ_i is the angle of incidence, θ_r is the angle of reflection and θ_{ref} is the angle of refraction.

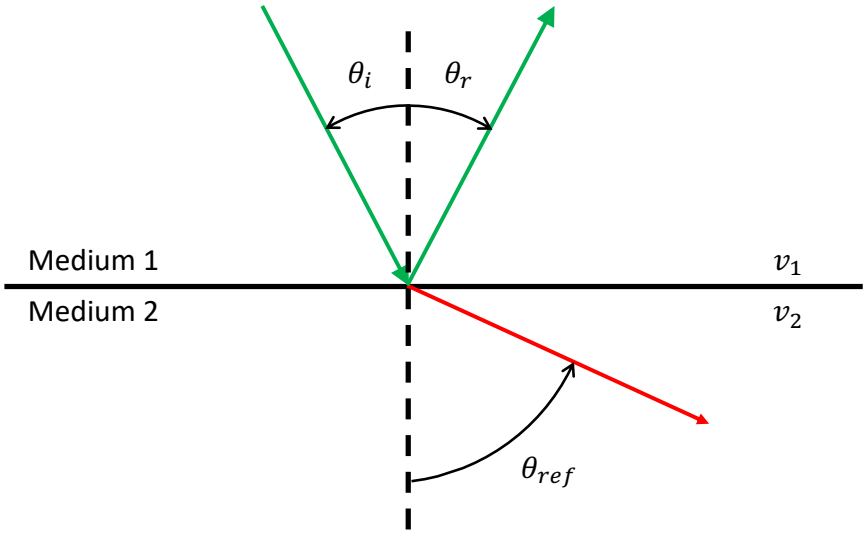

Figure 7: Schematic representation of oblique incident soundwave at the interface between two media

The relationship between the incident and refracted angle is known as Snell's Law [10]. This relationship can be expressed as Equation 2.14:

$$\frac{\sin\theta_i}{v_1} = \frac{\sin\theta_{ref}}{v_2} \tag{2.14}$$

At the boundary, both the reflected and refracted waves may undergo mode conversion if the interface is between two solid media (as gas and liquid media cannot support transverse waves). The mode

converted waves from a longitudinal incident wave can be visualised in Figure 8, where v_{L_1} represents the longitudinal wave velocity in medium 1, v_{L_2} is the longitudinal wave velocity in medium 2, v_{T_1} is the transverse wave velocity in solid medium 1, v_{T_2} is the transverse wave velocity in solid medium 2, θ_1 is the angle of incidence and reflection of the longitudinal wave, θ_2 is the angle of reflection of the transverse wave, θ_3 is the angle of refraction of the longitudinal wave and θ_4 is the angle of refraction of the transverse wave.

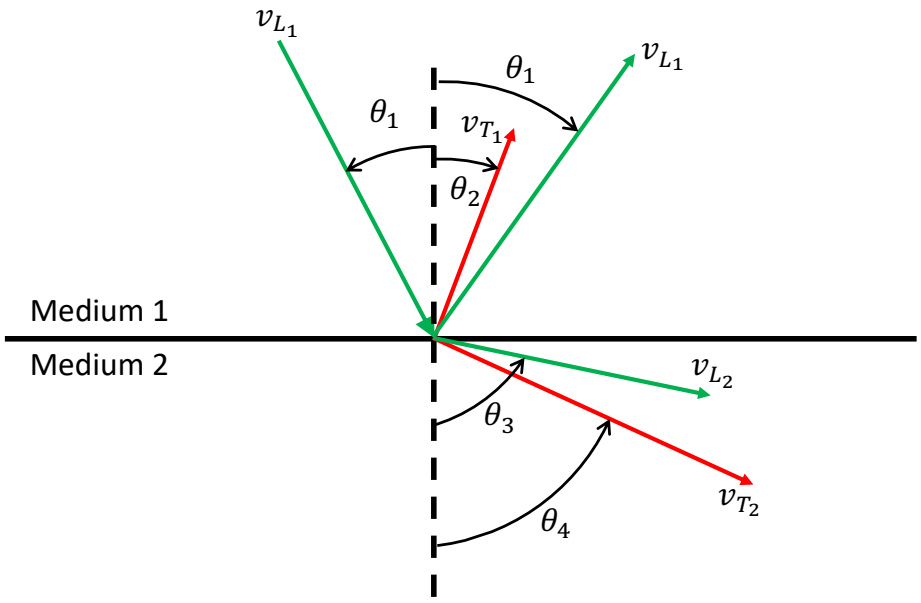

Figure 8: Schematic representation of oblique incident soundwave at the interface between two solid media with resulting mode conversions

Regardless of any mode conversions that occur at the boundary, Equation 2.12 can still be used to calculate all reflection and refraction angles for a specific incident angle, given the propagation velocities in both media. However, not all incident angles will have a refracted longitudinal or transverse wave. At high angles of incidence, the waves will propagate as Rayleigh/surface waves [27].

The incident angles at which the longitudinal and transverse wave modes disappear within the second medium are known as critical angles. These critical angles for each wave mode can be calculated from Equation 2.12, by setting the refraction angle to 90^0, using the appropriate refracted wave mode velocity, and solving for the incident angles.

2.1.5 Interference

Ultrasonic propagation may involve the interaction of multiple ultrasonic waves. During these interactions, the waves will sum together to form a new wave. There are two forms of interference: constructive and destructive interference.

Constructive interference can be defined as the sum of two waves of equal phase, which when combined, results in a wave of greater amplitude. To illustrate this concept, Figure 9 shows the merging of two low amplitude waves (in red) with in-phase peaks to form a high amplitude wave (in blue).

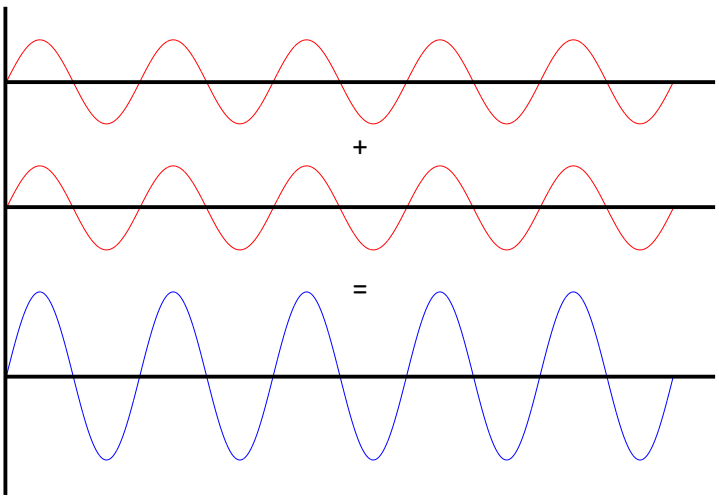

Figure 9: Schematic illustration of constructive wave interference

By contrast, destructive interference is the merging of two waves that are out-of-phase with one another. This produces a reduced or dampened response than either of the waveforms individually. Figure 10 shows the null response (in blue) generated from sum two waves (in red) that are 180^{o} out-of-phase.

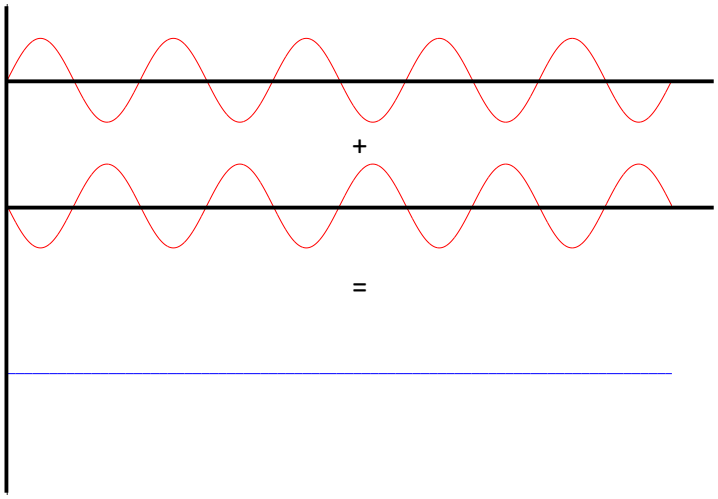

Figure 10: Schematic illustration of destructive wave interference

2.1.6 Transducers

Transducers are devices that convert one form of energy to another [28]. In the case of an ultrasonic transducer, electrical waves are converted to ultrasonic waves and *vice versa*.

The most common type of ultrasonic transducer uses piezoelectric crystals. These deform when a voltage is applied (piezoelectric effect) and accumulate electric charge when mechanically stressed (converse piezoelectric effect) [29]. The frequency at which a transducer transmits and receives ultrasound is equal to the ratio of the piezoelectric sound velocity to twice the thickness of the crystal [24]. A schematic diagram

of the internal structure of a single element ultrasonic transducer is illustrated in Figure 11.

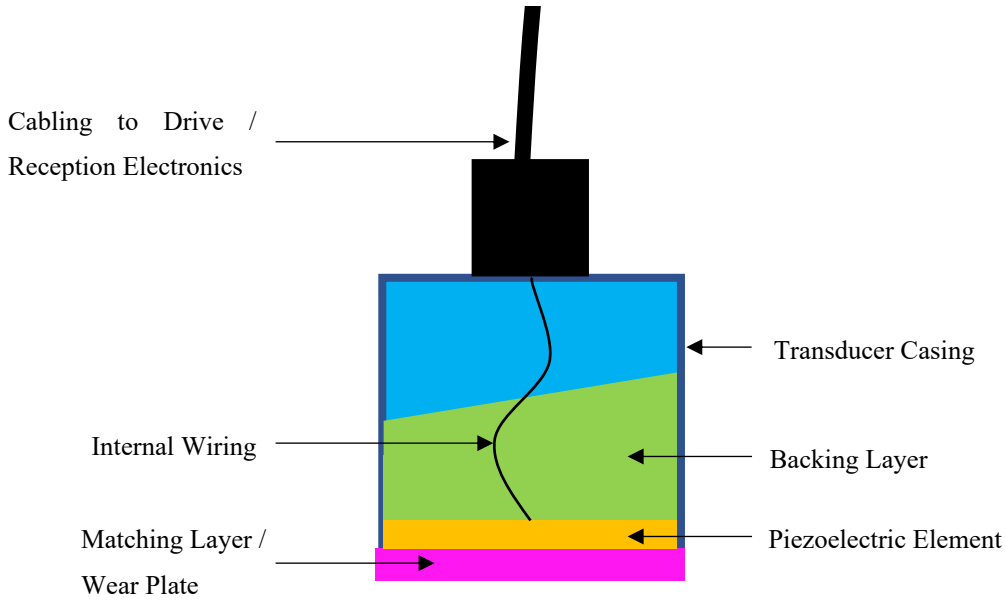

Figure 11: Schematic of a single element ultrasound transducer

In Figure 11, the piezoelectric material can be seen to be sandwiched between a backing layer and a matching layer, with connecting wires to instrumentation. In exciting the piezoelectric element, ultrasound of varying frequencies is generated and not just a single desired frequency. The backing layer is used to influence the centre frequency and the bandwidth of propagated frequencies about that centre frequency.

It accomplishes this by dampening specific frequencies generated by the piezoelectric layer. The damping capabilities of a backing layer depend on its acoustic impedance relative to the acoustic impedance of the active element. Transducers that have a backing layer and an active element with matching acoustic impedances will highly damp the active

element, creating broad bandwidth wavefront that increases the axial resolution of the inspection but at the expense of sensitivity. By contrast, transducers with increasing discrepancy between the acoustic impedances will have reduced damping capability, producing narrower bandwidths that have increased inspection penetration but at the expense of axial resolution [30].

The matching layer is included to improve the acoustic impedance matching between the piezoelectric material and the propagation medium. This increases the transmission of ultrasound into the desired material, as previously discussed in Section 2.1.4 [24]. In addition to optimising the transmission of ultrasound, the matching layer also acts as a protective layer for the piezoelectric element when moved across the surface of a specimen. Similarly, the casing protects the internal components of the transducer while in use and also provides electrical shielding.

2.1.7 Ultrasonic Fields

When an ultrasonic transducer is excited, a sound field is generated. A 2-dimensional schematic representation of this sound field is shown in Figure 12, where α is the beam spread angle of the probe.

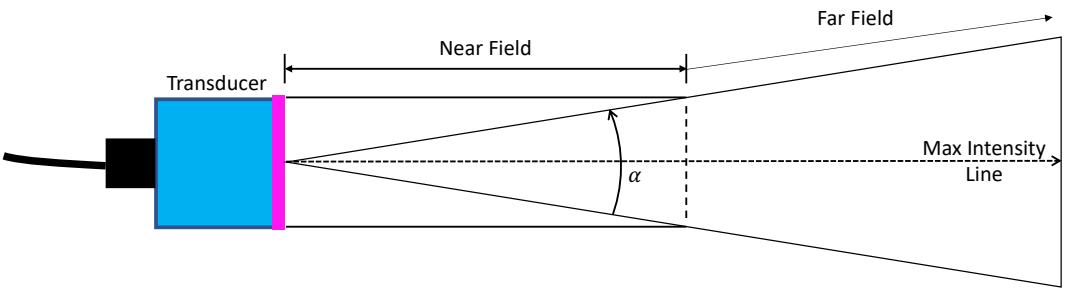

Figure 12: 2-dimensional schematic of the sound field of a transducer

The sound field can be divided into two key sections: the near field and the far field. Within the near field, the ultrasonic beam maintains a cylindrical shape of diameter equal to that of the transducer [8] with the amplitude fluctuating due to constructive and destructive interference. The length of the near field, NF, can be calculated from Equation 2.15, where D is the diameter of the transducer and λ is the wavelength of the propagating ultrasound.

$$NF = \frac{D^2}{4 \cdot \lambda} \tag{2.15}$$

Calculating NF is important due to the inconsistent amplitude in the near field. To illustrate the amplitude fluctuation within the near field, Figure 13 shows the axial response from a single element disk transducer:

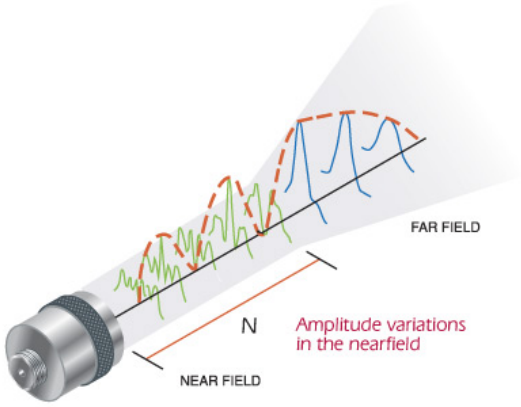

Figure 13: Axial response from a single element disk transducer [31]

Within the near field region, shown in Figure 13, the red trace following the largest amplitudes fluctuates significantly through increasing depth. Therefore, applying amplitude-based measuring techniques in this region is inappropriate because a fixed size defect

would produce inconsistent responses with increasing depth. The last maximum amplitude is considered as the end of the near field and the beginning of the far field, which is recognised as the natural focus of the transducer [10].

Once in the far field, the ultrasonic beams begin to diverge, and the sound fields follows a conical shape. Using Equation 2.16, the half angle beam spread, $\frac{\alpha}{2}$, can be calculated for a Gaussian beam.

$$\frac{\alpha}{2} = \sin^{-1}\left(\frac{1.22 \cdot \lambda}{D}\right) \tag{2.16}$$

The calculated divergence angle represents the spread from the maximum acoustic centreline to where the amplitude response has decreased by half [32].

2.2 Conventional Ultrasonic Testing

There are a variety of ultrasonic methods that can be used for fault and defect detection. The simplest and most fundamental technique is conventional Ultrasonic Testing (UT). Execution of this technique can be carried out using one of three probe arrangements:

Single Element Probes, as shown in Figure 14, contain one piezoelectric crystal that both transmits ultrasound and captures returning echoes.

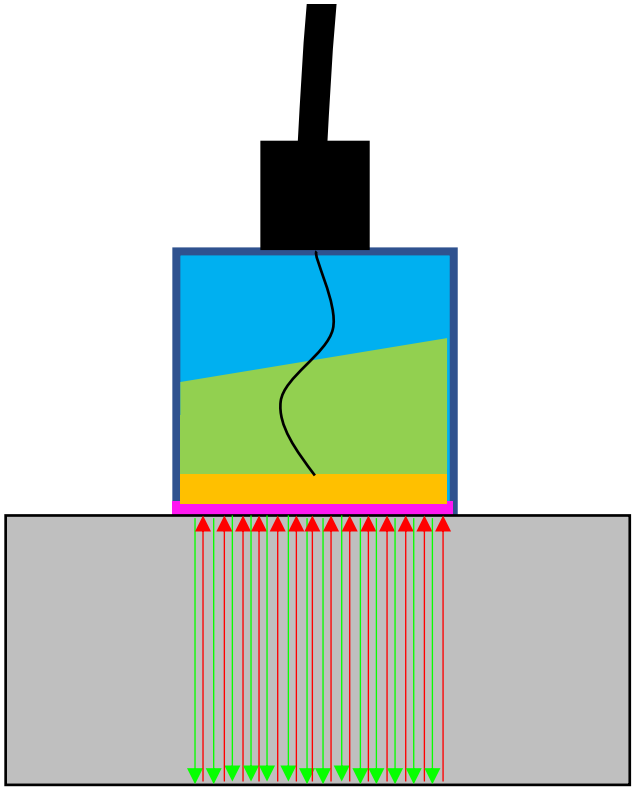

Figure 14: Schematic diagram of a conventional UT inspection using a single element probe

Single element transducers typically pulse longitudinal waves perpendicular to the surface of the structure. Based on the theory discussed in Section 2.1.4, the ultrasonic waves will reflect back toward

the probe from a defect or backwall assuming normal or near normal incidence, as shown in Figure 14. This type of setup is known as Pulse-Echo (P-E). In a scenario where a defect was orientated parallel or near parallel to the propagating wave, ultrasonic energy would either not be reflected or would be reflected away from the probe.

The results from this type of scan are normally presented as the energy response of the transmitted and received vibrations of the piezoelectric element as a function of time. This display type is known as an A-scan (Amplitude-scan). Figure 15 shows an example of an A-scan response from a thickness measurement inspection, using a similar setup to that shown in Figure 14.

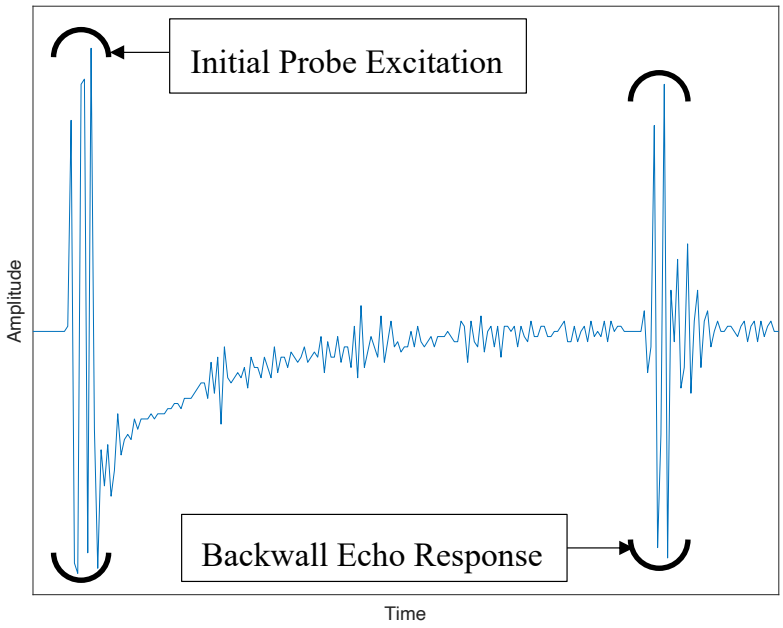

Figure 15: A-scan data representation for thickness measurement

Displaying amplitude as a function of time, as illustrated in Figure 15, allows an operator to calculate the thickness of a material based on the ultrasonic Time-of-Flight (TOF). The TOF is taken as the elapsed

time for generated ultrasound to propagate through a specimen, internally reflect at a defect/backwall boundary and return back to the source. The boundaries used to estimate the magnitude of the time of flight can be taken as the time locations of the highest peaks from both the probe excitation portion of the response and the backwall echo portion. The highest peaks approach is not the only approach used for determining the TOF; for example, within corrosion mapping, the TOF is measured based upon the time between the leading edges of the excited pulse and the response echo.

From Equation 2.17, the length of the sound path, d_{SP}, can be determined, where v_L is the longitudinal velocity of the specimen and t_{TOF} is the TOF of the propagated wave.

$$d_{SP} = \frac{1}{2} \cdot v_L \cdot t_{TOF} \tag{2.17}$$

From Figure 14, the TOF is the time taken for the ultrasonic beam to reach the far wall (one green arrow) and return to the transducer (one red arrow). Therefore, Equation 2.17 includes division by two to calculate the material thickness (represented by a single arrow in Figure 14).

The A-scan is the simplest and most fundamental presentation of an ultrasonic inspection. Combined with Equation 2.17, to calculate sound path, this forms the basis for additional display methods such as S-scan (discussed in Section 2.3.1).

Through-transmission inspection is an alternate setup that incorporates two single element transducers in a Pitch-Catch (P-C) configuration, i.e. where one transmits and the other receives. Typically, the transducers are setup on opposite surfaces of the specimen [33] as shown by Figure 16:

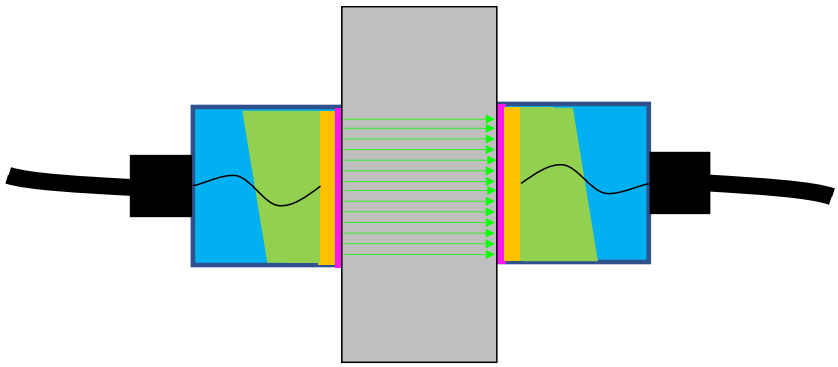

Figure 16: Schematic diagram of through-transmission inspection using two single element probes

The P-C setup can also be applied to cylindrical components. Both transducers can be placed on the same surface at different radial positions and ultrasound propagated through the structure from one probe to the other. The acquired TOF from this type of inspection setup represents the distance between the two probes and not twice the thickness as it does with P-E. Therefore, the half multiple must be removed from Equation 2.17.

As well as thickness measurement, the P-C configuration also allows for the detection of defects which can be identified through the reduction or loss of signal from the receiver probe. Typical material examples include highly attenuating materials such as specific composites and austenitic steels. However, the disadvantage of this

technique is that is requires access to both sides of a structure to perform it.

Dual Element Probes, as shown in Figure 17, contain two independent crystals; one to transmit the ultrasonic pulse and the other to receive any responses.

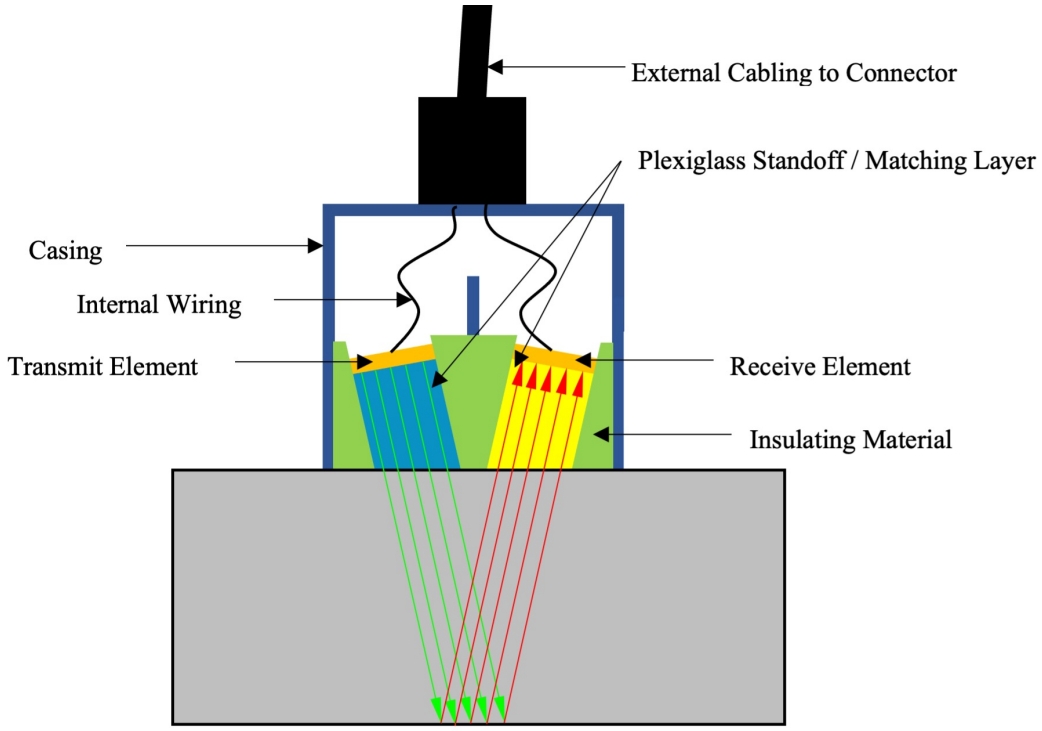

Figure 17: Schematic diagram of a conventional P-E UT inspection using a dual element probe

These types of probes are used for thickness measurement of thin structures and to enhance the capability of detecting and sizing defects close to the near surface of the inspection specimen [8]. By having independent transmitting and receiving elements that are completely isolated from one another, reverberations from one element cannot be picked up by the other.

The inclusion of a large standoff matching layer within these probes means that more of the fluctuating near field would occur within the probe. This subsequently reduces the potential dead zone volume created in the near surface caused by the reverberations of the initial element excitation, as shown in Figure 15 [34].

Further improvements to the resolution are made through the elements being angled slightly toward one another. By angling the elements, it maximises the amount of wave energy that could be picked up by the receiving element.

Angled Probes, as shown in Figure 18, incorporate a single element probe mounted on an angled wedge.

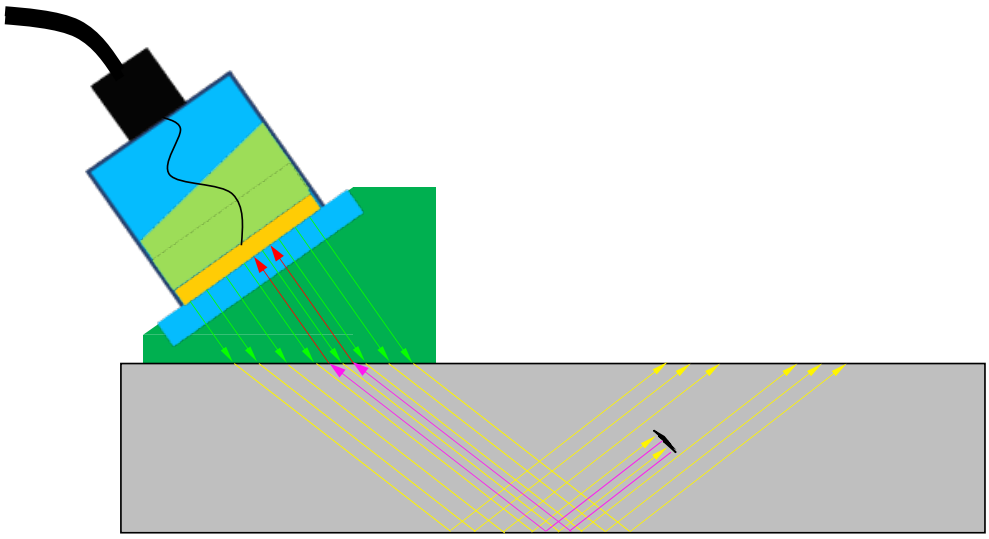

Figure 18: Schematic diagram of a conventional P-E UT inspection using an angled single element probe

The angled single element probe operates in the same way as a standard single element probe with the exception that refraction angles and acoustic impedances have to be considered due to the angled wedges. As discussed in Section 2.1.4, the refraction angle of the

propagating wave depends on the ratios of acoustic impedances between the materials at the boundary interface, i.e. the wedge and the specimen under inspection. Regardless of the probe, wedges are designed to acoustically match specific materials in order to generate a specific refraction angle.

Typically, wedges are designed for incidence above the critical angle, thus generating only mode-converted transverse waves in the material to be inspected. With the shear wave mode type having a slower sound velocity, compared with longitudinal waves, balancing of Equation 2.6 requires a smaller wavelength for a given propagation frequency. Since defect sizing is proportional to the wavelength of the propagating wave, shear waves have the advantage of better detection of smaller defects compared with longitudinal waves.

Similar to single and dual element transducers, the angled probes can also be arranged to perform a P-E inspection. This setup is particularly effective at inspecting volumes without having to position a probe directly above the region of interest. Furthermore, the angled approach provides greater inspection coverage from a single position than either of the single/dual element setups.

In addition to P-E inspection setups, angled probes can also be setup in a P-C configuration. With both probes in contact with the same surface of the specimen, they are positioned with a fixed distance between them. A schematic diagram of a P-C setup is shown in Figure 18.

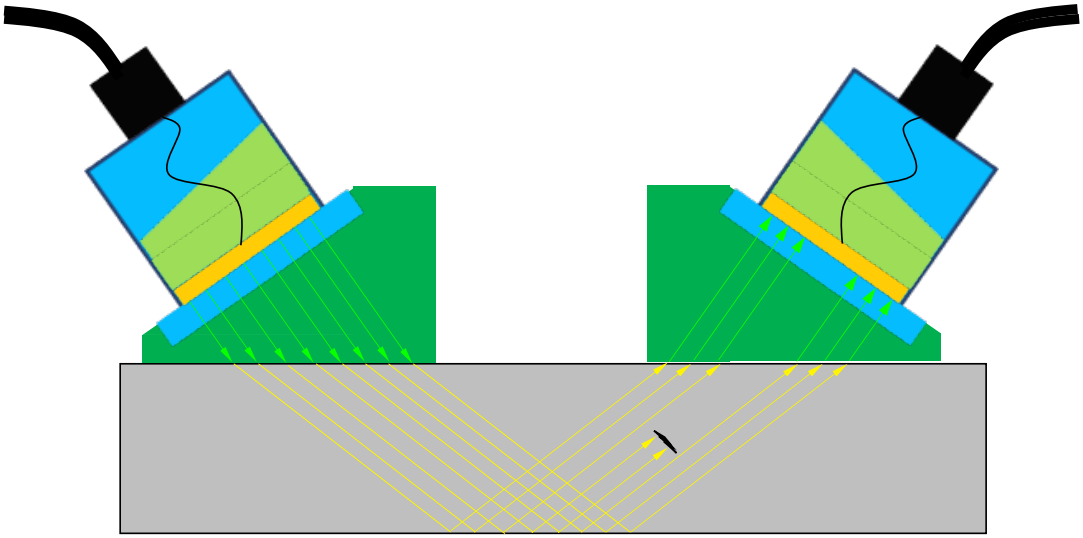

Figure 19: Schematic diagram of a conventional P-C inspection using an angled single element Probe

As with the through-transmission approach, identifying the presence of a defect can be performed using the setup illustrated in Figure 19, through the drop in the amplitude of the A-scan response.

All three probe types can be coupled directly to the surface of a structure, implementing a TOF approach to detect and size potential defects. In manual (non-encoded) inspections, the detection and characterization of defects cannot be done post-inspection for any of these probe types. Location and characterisation of defects requires analysis of the A-scan. This is done in real time as the probe is being moved across the surface of the structure under inspection. A skilled operator requires both a steady hand and the ability to track and interpret the observed echoes. As the probe traverses the specimen, the inspector is required to interpret changes in the signal in order to identify potential defective areas from an understanding of how flaw characteristics will manifest in the echo signals. In some circumstances, the probe can be mounted with a wheel encoder to aid in keeping the probe steady and

tracking its position across the surface to capture A-scan data. Table 1 details the preferred transducer type to detect specific flaw types and the detectable and scalable changes (relative to the DAC line, discussed later in Section 3.6.1) on an A-scan that would be used to characterise them.

Table 1: A-scan properties for flaw characterization [26]

Defect	A-scan Properties
Porosity	For clustered porosity, the single/dual element probe is preferred, and low amplitude spikes above the noise floor and beneath the DAC curve would be observable. Figure 20 presents an example of detected clustered porosity: 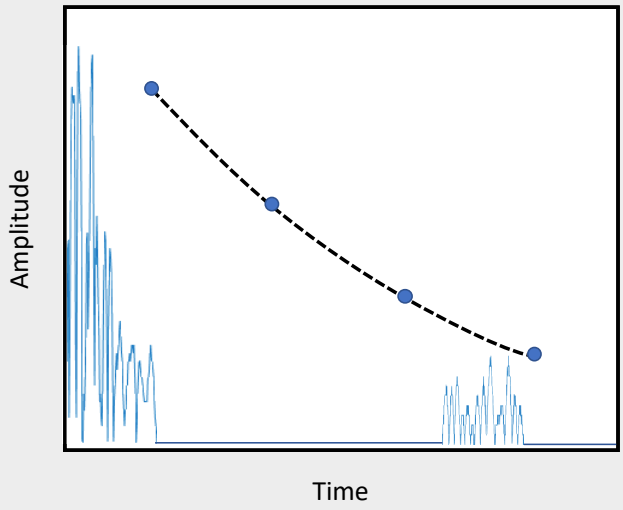 *Figure 20: A-scan data representation for clustered porosity relative to DAC curve* Unlike clustered porosity, remote pores, if detected, will result in individual low amplitude spikes below the DAC curve similar to that shown in Figure 21:

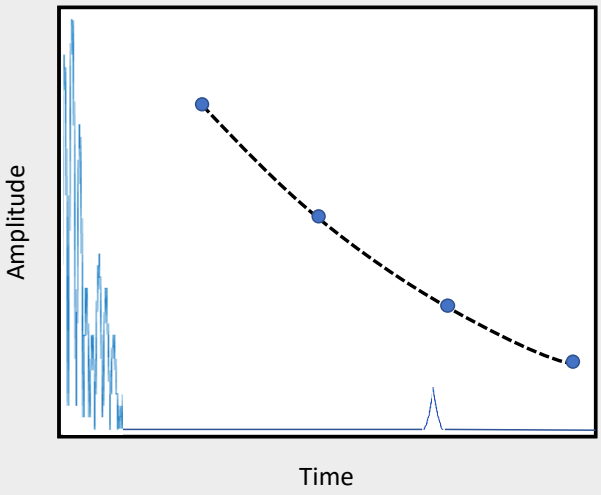

Figure 21: A-scan data representation for isolated pore relative to DAC curve

Planar Defects

Planar defects such as lack of fusion (LOF) and crack-like defects would most likely be detected using an angled probe. If detected, a LOF defect would present itself as a large amplitude spike that would break the DAC curve as shown in Figure 22:

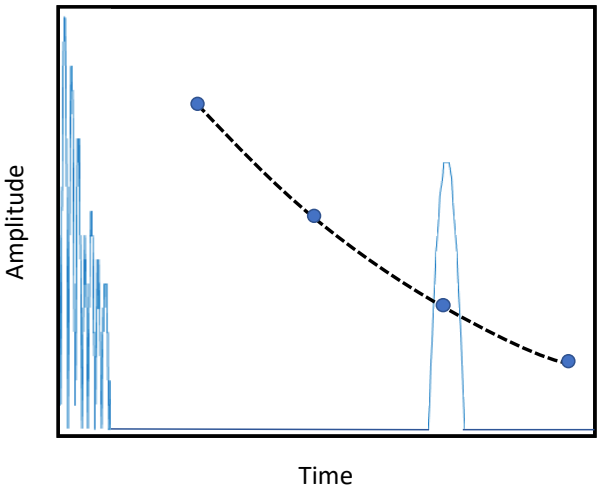

Figure 22: A-scan data representation for LOF defect relative to DAC curve

Its detection is based on its orientation being perpendicular/near perpendicular to the propagation angle. The same approach applies for detecting crack-like defects;

	however, their captured response can vary significantly depending on the inspection angle relative to the orientation of the crack's branches/facets. To illustrate one example, Figure 23 shows the A-scan that could be acquired from a crack-like defect, where large amplitude responses that break the DAC curve are acquired from different crack branches/facets: 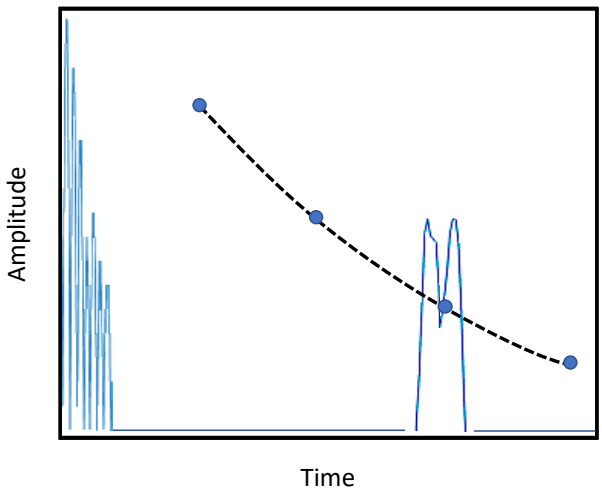 *Figure 23: A-scan data representation for crack-like defect relative to DAC curve* The inspection process would be repeated using another angled probe of a different incident angle to avoid missing a crack due to its orientation.
Corrosion	It is preferred to measure corrosion using a single/dual element probe. Large patches of corrosion would appear as a large amplitude spike relative to the DAC curve, similar to that shown in Figure 22, occurring before the back-wall echo. Alternatively, an indication for corrosion is a loss of backwall signal. Smaller cases of corrosion, such as pitting, are more difficult to detect as they are likely to produce low amplitude response due to their small surface area. As a result, they can be hard to distinguish from a backwall echo.

2.3 Phased Array Ultrasonic Testing

One of the major advantages of phased array probes is their ability to produce a diverse range of beam types and maximise the potential of locating, sizing and characterising defects. This ability of Phased Array Ultrasonic Testing (PAUT) to create different beam types offers improved flexibility in inspection setup and enhances volumetric coverage in the region of interest. Therefore, a single array can simplify the inspection process by having the capability to replicate multi-probe inspection systems. Phased array transducers contain an array of piezoelectric elements, typically ranging in number between 10 and 128 [35].

Phased array approaches are being applied in an increasing number of areas and industries, creating more interest in its research and development. Examples include: 2-dimensional arrays [36], small-scale array technologies [37], sparse arrays [38] and custom array designs [39]. A commonly used array type within NDT applications is the linear phased array. The example of a linear array illustrated in Figure 24 has 16 elements with elevation, H, width, w, and pitch, p, and a full array aperture length, L.

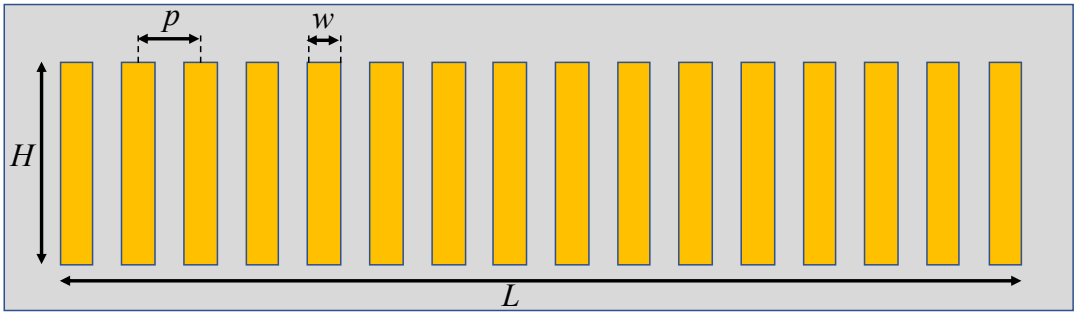

Figure 24: Schematic diagram of a 16-rectangular-element 1-D linear phased array probe

The associated drive and reception electronics, required for array probes, allow for implementing different techniques through a variety of excitation schemes. One such technique is called beam steering, where calculated time delays are applied between the excitation of different individual or groups of elements. This allows for the creation of angled inspection wavefronts away from the normal. This increases the potential coverage area that can be achieved by a probe and improves the probability of detecting a flaw that may not be appropriately orientated to reflect a signal back to the probe.

The centre frequency, width and pitch of the elements affect the capability of the array to beam steer. Based on Equation 2.16, decreasing the centre frequency and/or the width of the elements and/or the pitch between each element will increase the array's ability to beam steer to greater angles from the normal. However, side lobes will begin to occur within the sound field at element widths smaller than one wavelength of the centre frequency of the array [40]. This is due to greater beam spread generated from a smaller element and/or a more compact arrangement of elements.

Increasing the number of elements within the array will increase the full array aperture length, increasing the length of the near field and therefore the probe's penetration capabilities [41] as discussed in Section 2.1.7. In addition, increasing the number of elements will also reduce beam spread, improve focussing capabilities, and enhance sensitivity [40].

In a linear probe, the element elevation can also be referred to as the passive aperture, due to its fixed dimension. In general, the magnitude of the elevation should be approximately equal to or greater than 10 times the wavelength of the centre frequency of the array [42].

Based on these properties, two popular setups used throughout industry for weld inspection are sectorial scanning and linear scanning. In both of these techniques, elements can be excited either individually or in groups to transmit, to receive or both. The ability to address each element individually or as a group provides great versatility in the way a specimen can be inspected.

2.3.1 Sectorial Scanning

Sectorial scanning is an effective pulse-echo phased array technique for scanning large specimen volumes with a single scan. With a range of incident angles to potentially interact with a defect, this method aims to minimise the possibility of missing defects regardless of orientations. The technique involves the generation of delay laws to excite the elements of a fixed sub aperture, to create a fan of wave fronts, propagating at pre-determined angle steps. This technique can be implemented with or without a wedge, depending on the requirements of the inspection.

As an illustration, Figure 25 shows a sectorial scan with seven different angles generated from a 9-element aperture centred on element eight. The centre lines of each angled beam are shown in green. For probe contact sectorial scan scenarios, the recommended sweep range is approximately -30^0 to 30^0 [43].

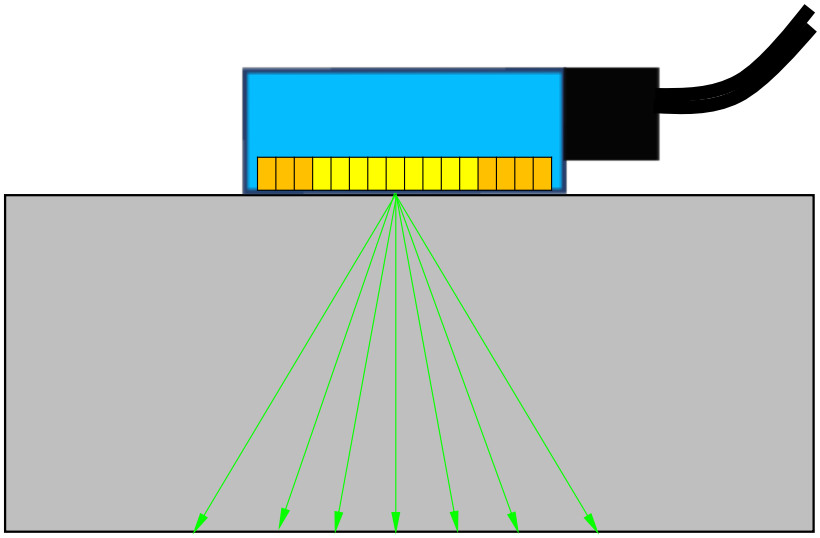

Figure 25: Schematic diagram of sectorial scanning PAUT using 9-element sub-aperture

Prior to developing an inspection setup, such as Figure 25, a number of parameters must be considered to balance maximising the inspection coverage area while minimising the likelihood of an unreliable scan. The first involves quantifying the coverage required for the inspection and determining whether available probes can meet the demands. The maximum beam steering angle for a chosen aperture, θ_{st}, can be calculated using Equation 2.18 [44], where λ is the wavelength of the ultrasound in the test material and e is the element width.

$$\sin\theta_{st} = 0.514 \cdot \frac{\lambda}{e} \tag{2.18}$$

Based on calculations using Equation 2.18, if additional angle coverage is required, the probe can be mounted on an angled wedge. Figure 26 shows a 16-element probe mounted on an angle wedge performing a simple sectorial scan using a 9-element sub-aperture, centred on element eight. For wedge-mounted probes, the sectorial scan

scenarios have a recommended refracted sweep range within the range of 30^0 to 70^0 [43].

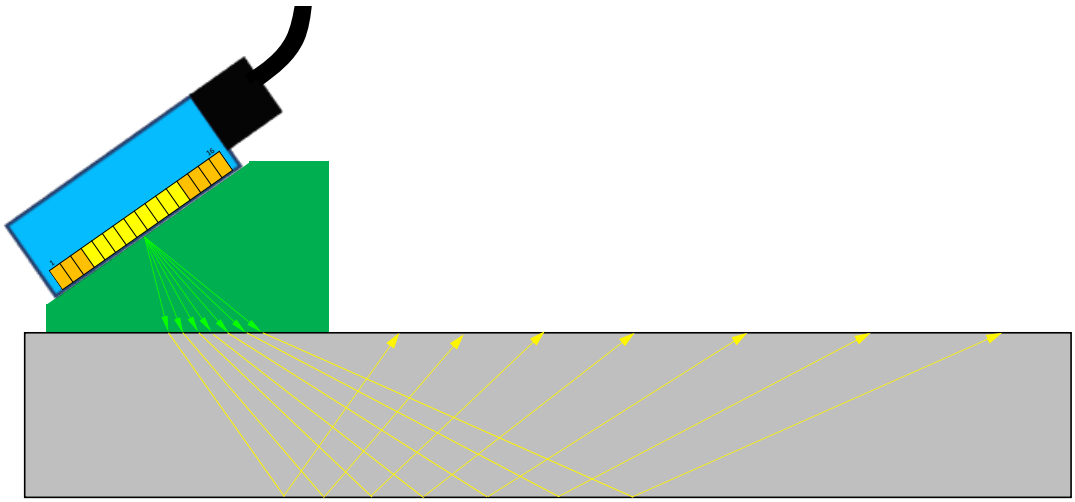

Figure 26: Schematic diagram of a 9-element wedge-mounted sectorial scanning PAUT

Figure 26 demonstrates that using a wedge significantly increases the potential coverage area that can be attained. However, it is also clear that there are significant gaps between each of the seven angle centrelines, which could result in missed defects.

This can be addressed by increasing the number of angle sweep steps (i.e. decreasing the magnitude of the increment sweep angle step). This reduces the possibility of not missing defects. However, increasing the number of angle steps to acquire coverage will demand a reduced scan speed for the Phased Array Controller (PAC) to meet the processing demands of more delay laws.

The PAC parameter setting that determines the speed at which a scan can be carried out at is the Pulse Repetition Frequency (PRF). The PRF indicates the rate at which the PAC pulsers are fired. Higher PRFs

allow for quicker scanning and data acquisition. Lower PRFs are used for battery conservation and limiting unwanted interference between outgoing and returning signals in long sound path inspections [45].

In addition to increasing the number of angles, increasing the number of inspections to be carried out can also affect the scan speed. PACs have the ability to perform more than a single inspection setup for a single scan pass. They can include both sectorial and/or linear scanning setups, with various inspection angle ranges (in sectorial) and number of generated virtual apertures (in linear, discussed in Section 2.3.2). Therefore, a compromise is required between the inspection coverage demands, the capabilities of the probe (and wedge), and application of delay laws and the inspection scan speed. An effective balance is achieved when the probe scan speed is slower than the period of the PAC to capture the data from all the generated inspection setups which is proportional to the defined PRF value.

When this balance is achieved, phased array equipment can be very effective in diagnosing the location and orientation of defects. A schematic of the specimen geometry can be superimposed on to acquired scan data to assist in visualising defect location. Using this overlay can help with defect location and characterisation, for example distinguishing between flaws such as toe cracks, root cracks, and LOF defects. Defect definitions will be discussed further in Section 3.2. To illustrate this, Figure 27 shows an S-scan (Sector-scan) of a weld inspection using sectorial scanning:

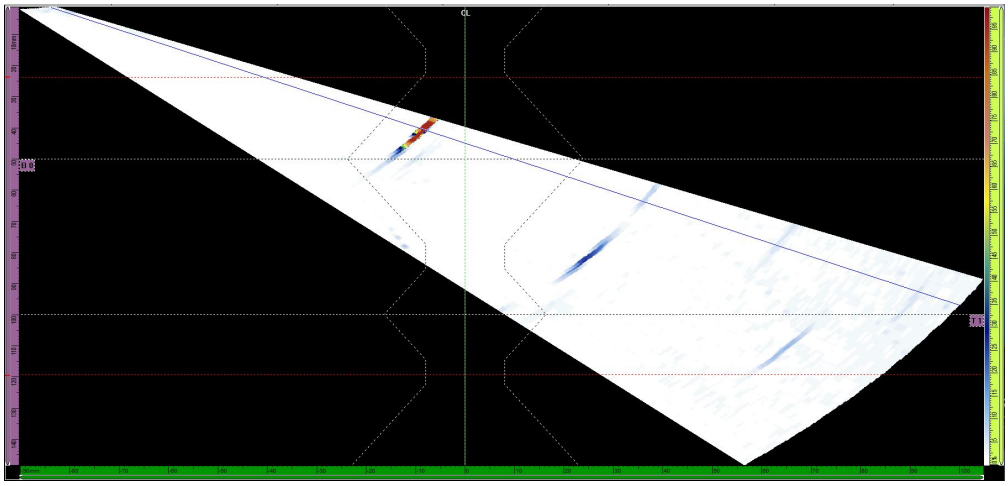

Figure 27: S-scan data representation of sectorial scan from OLYMPUS Omniscan MX2

An S-scan is a cross-sectional image generated from stacked, colour-coded A-scans. When electronically sweeping the ultrasonic beam through a designated range of refracted angles, an A-scan is acquired for each individual angle [46]. The cross-sectional image of an S-scan image shows the responses captured at a specific probe position within an inspection, from the perspective of a side on view, parallel to the probe coverage.

From the S-scan, shown above, the red response indication demonstrates the technique's ability to detect defects. As with conventional UT, the amplitude and signal dynamics are used to characterise defects. As previously noted, to aid in defect characterisation and location, the scan type can have a schematic diagram of the weld geometry outline superimposed on the scan data. For example, from its high amplitude and the location of the defect being close to weld fusion face, this defect would most likely be characterised as a LOF defect.

It has to be noted that not all indications on a scan image are defects. Depending on the geometry of the structure being inspected, structural features such as weld caps and tapered backwalls can return amplitude responses. Furthermore, not all defects produce high amplitude responses, such as porosity (further discussed in Section 3.2.2).

Figure 25, Figure 26 and Figure 27 all show that with increasing propagation distance, the relative distance between propagation angles also increases. This demonstrates a limitation in the ability to size defects using sectorial scans, as part of a defect could remain undetected. Despite its limitations, when fitted with an encoder module, phased array measurement positions can be tracked. The methodology is effective for defect detection, defining internal defect orientation, defect characterisation and its position can be detailed relative to a known marker on the specimen in doing so, the defect can be diagnosed.

2.3.2 Linear Scanning

Linear scanning PAUT is a common P-E approach used in many industries due to its versatility for corrosion mapping, composite material inspections, acquiring volumetric ultrasonic coverage within a specimen and sizing detected defects [1].

Unlike the sectorial scan approach that uses a single sub-aperture to propagate ultrasound through a sweep of angles, linear scans can utilise the full aperture of the probe by sequentially exciting fixed length sub-apertures to generate ultrasound at a fixed angle. Each sub-aperture can also be referred to as a Virtual Probe Aperture (VPA).

To illustrate the sequential excitation of sub-apertures, Figure 28 shows (from top to bottom) the progression of a 5-element active sub-aperture (yellow) as it is sequentially stepped along the full aperture of a 16-element probe. This results in the generation of 12 VPAs. When the sequence reaches the final scanning step, the whole process is continuously repeated.

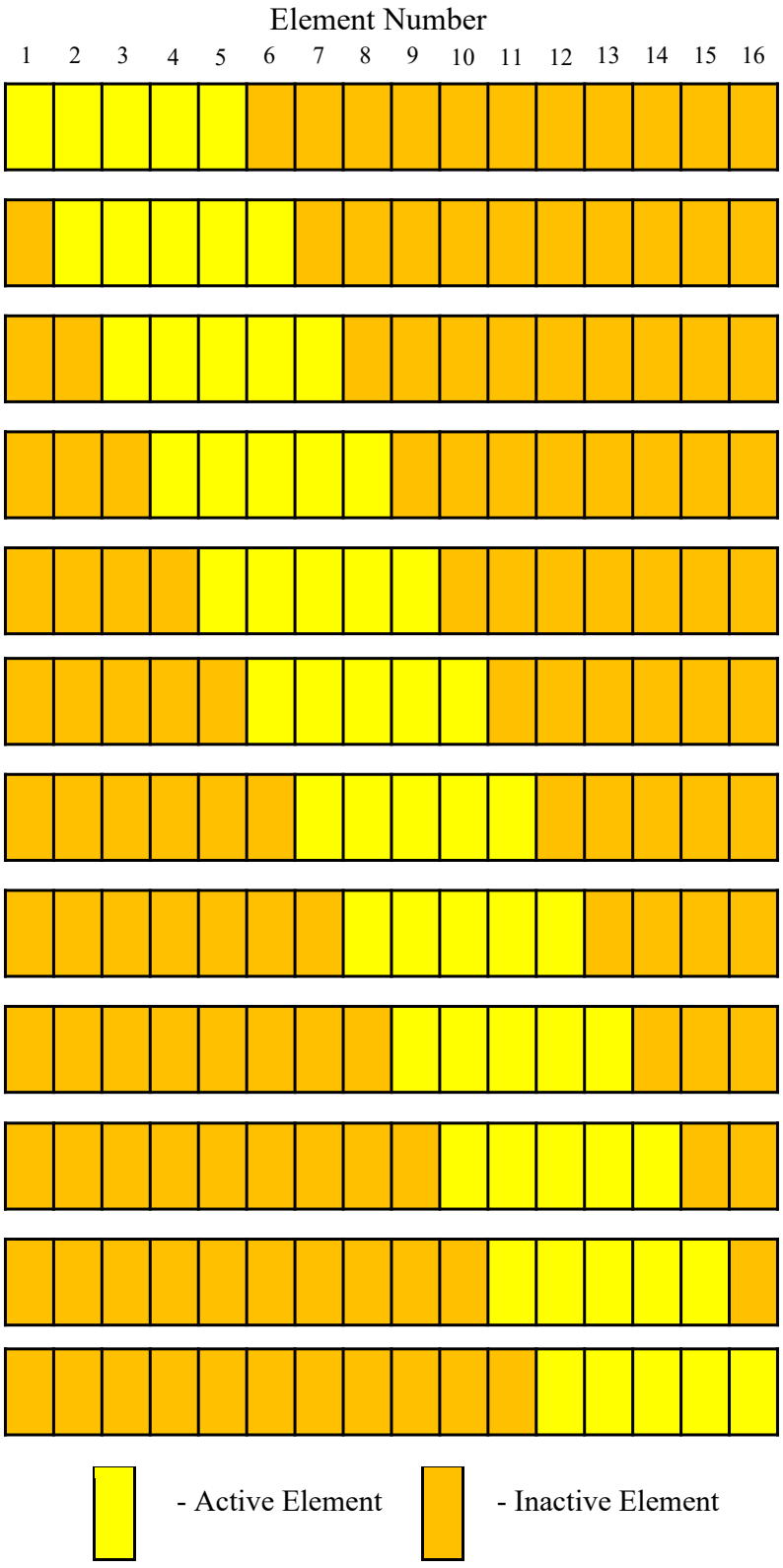

Figure 28: Schematic diagram of sequential excitation of 12 VPAs of five elements within linear scanning

It must be noted that, as shown in Figure 28, the activation of a sub-aperture does not mean that all elements are excited simultaneously. The activation of individual delay laws to specific elements allows a sub-aperture to beam steer its centreline beam at a desired angle. For example, when the first sub-aperture of elements one to five are made active, the underlying delay laws could be that the elements are excited sequentially from element five to element one.

Implementation of a sequential excitation of sub-apertures, like that shown by Figure 28, are illustrated in Figure 29, where a wedge-mounted probe is performing the linear scanning inspection setup of a twelve 5-element sub-apertures into a sample specimen.

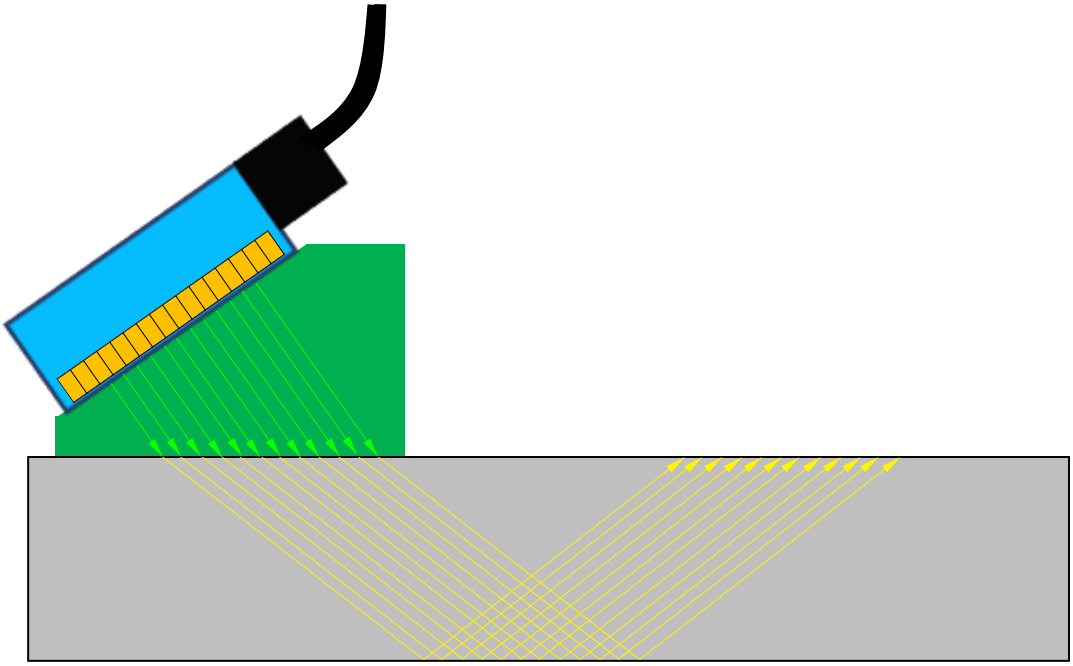

Figure 29: Schematic diagram of angled linear scanning PAUT using 12 VPAs of five elements

Figure 29 shows a schematic of an unfocussed linear scanning PAUT setup where the propagation centrelines for all the apertures are parallel in both the wedge and inspected structure. Similar to a sectorial

scan, linear scanning setups are typically presented as an S-scan. As an example of a linear scanning S-scan, Figure 30 shows a linear scan of the same defect as in Figure 27:

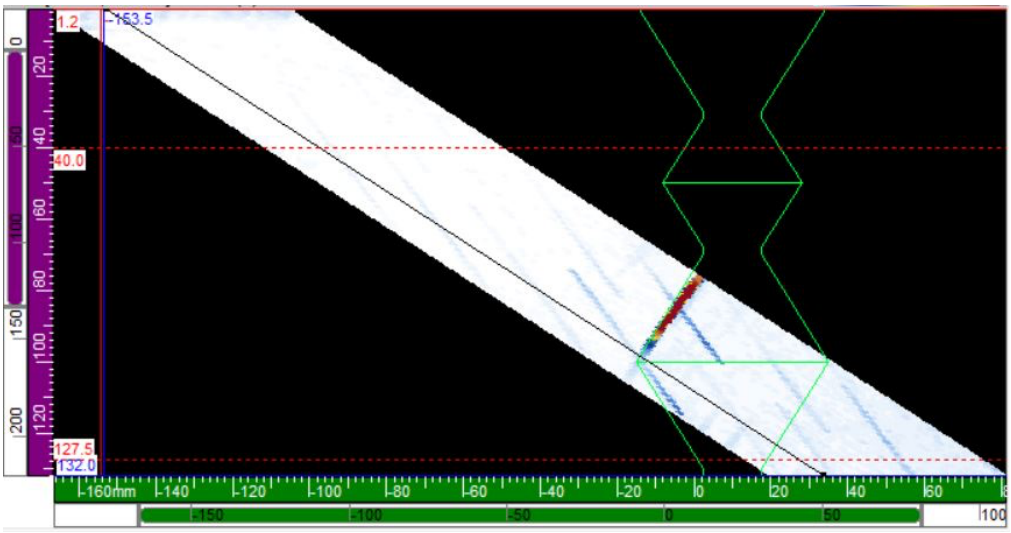

Figure 30: S-scan data representation of angled linear scan from OLYMPUS Omniscan MX2 captured using an OLYMPUS Omniscan MX2 attached with a 5MHz 60-element linear array PipeWizard probe and 55^0 Rexolite wedge

The response acquired using a linear scanning S-scan, above, is very similar to the response from the sectorial scanning setup. The high amplitude defect is found in a similar location. By comparison to the sectorial scanning, the linear scanning approach can more appropriately characterize and size detected defects. This is due to the more even coverage generated with constant spacing maintained between the centrelines of the sub-apertures, regardless of the depth. Due to the constant gap between sub-aperture centre lines, the defect shown above, maintains a linear shape. The sectorial scan response, by comparison, had a much more curved response due to the changes in angle across the coverage area. Again, based on the defect's high amplitude response, its shape and its location in the weld face, it would most likely be characterised as a LOF defect.

Despite the differences in appearance of defects and coverage, both linear and sectorial scanning setups share similar limitations. Defects orientated parallel to the centreline beams of each sub-aperture or angle are unlikely to be detected, as discussed in Section 2.2. In addition, the capabilities of the PAC have to be taken into consideration when generating a scan setup. A balance has to be found between coverage requirements, scan speed, number of delay laws required and penetration depth.

Another scan display that can be used for PAUT inspections is the C-scan. An example of this is shown in Figure 31:

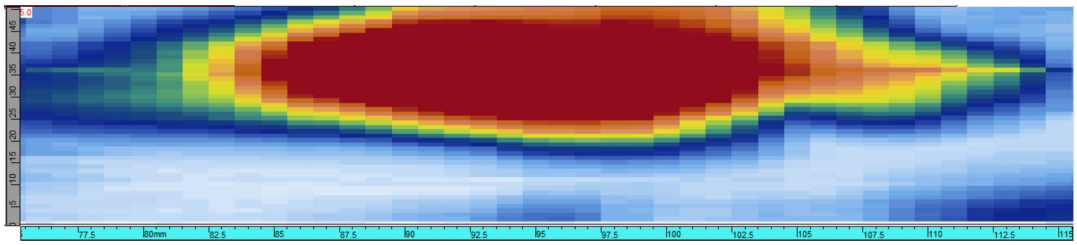

Figure 31: C-scan data representation of angled linear scan captured using an OLYMPUS Omniscan MX2 attached with a 5MHz 60 element PipeWizard probe and 55^0 Rexolite wedge

A C-scan presents a plan view of an inspection. The plane of the image is perpendicular to the angle of ultrasound propagation in the material. This scan type shows the maximum amplitude responses for each active aperture at each scan position. This can be used for defect length and width sizing, discussed later in Section 3.2.

2.4 Time of Flight Diffraction

Time of Flight Diffraction (TOFD) is an ultrasonic inspection technique that detects and sizes defects by identifying and measuring the diffracted signals radiating from their tips [47]. TOFD uses a pitch/catch setup requiring two transducers, one to transmit and the other to receive, as shown in Figure 32.

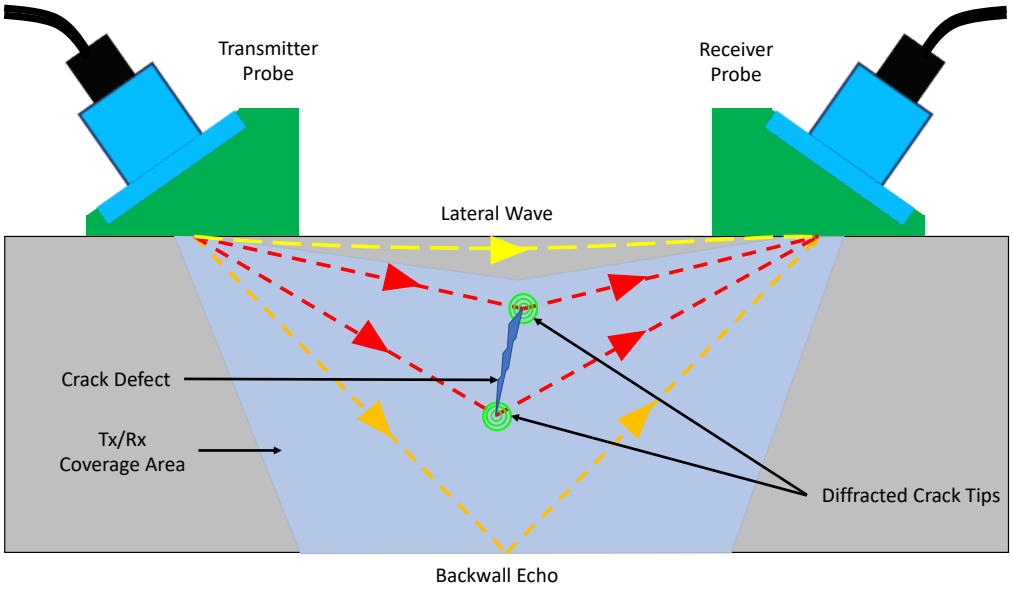

Figure 32: Schematic diagram of TOFD inspection setup

In a TOFD inspection, three wave types propagate through the specimen: a refracted longitudinal wave, a refracted transverse wave and a lateral wave. The lateral wave is a type of longitudinal wave that propagates along the surface of the structure [48]. At the same time, longitudinal and transverse wavefronts propagate through the material at different refracted angles [49], as explained in Section 2.1.4. If either of the sub-surface waves hits a defect, the tips of the defect will vibrate, producing diffracting signals. The receiver will detect these as well as the lateral wave and back-wall reflection.

As with conventional UT and PAUT, encoders can be used to record the distance scanned and assist with more accurate positioning and length sizing [50]. TOFD scans are typically presented in the form of a B-scan. Similar to an S-scan, B-scans also provide a side-on cross-sectional view of the internal structure but from a perspective parallel to the inspection direction.

Depending on the requirements of an inspection, parameters including the material thickness, the coverage volume and the focal depth affect the optimum transducer frequency and diameter, and the Probe Centre Separation (PCS) between the transmit and receive probes. As discussed previously, the frequency determines how sensitive the inspection setup is to detect and size defects; the probe diameter will vary the beam spread and therefore the inspection coverage; and the PCS will alter the intersection the transmit and receive probes.

Figure 33 shows an example of a B-scan generated from an encoded TOFD inspection of a simple butt weld sample. Visible and labelled are three defects, defect tip diffractions, the lateral wave and backwall reflection.

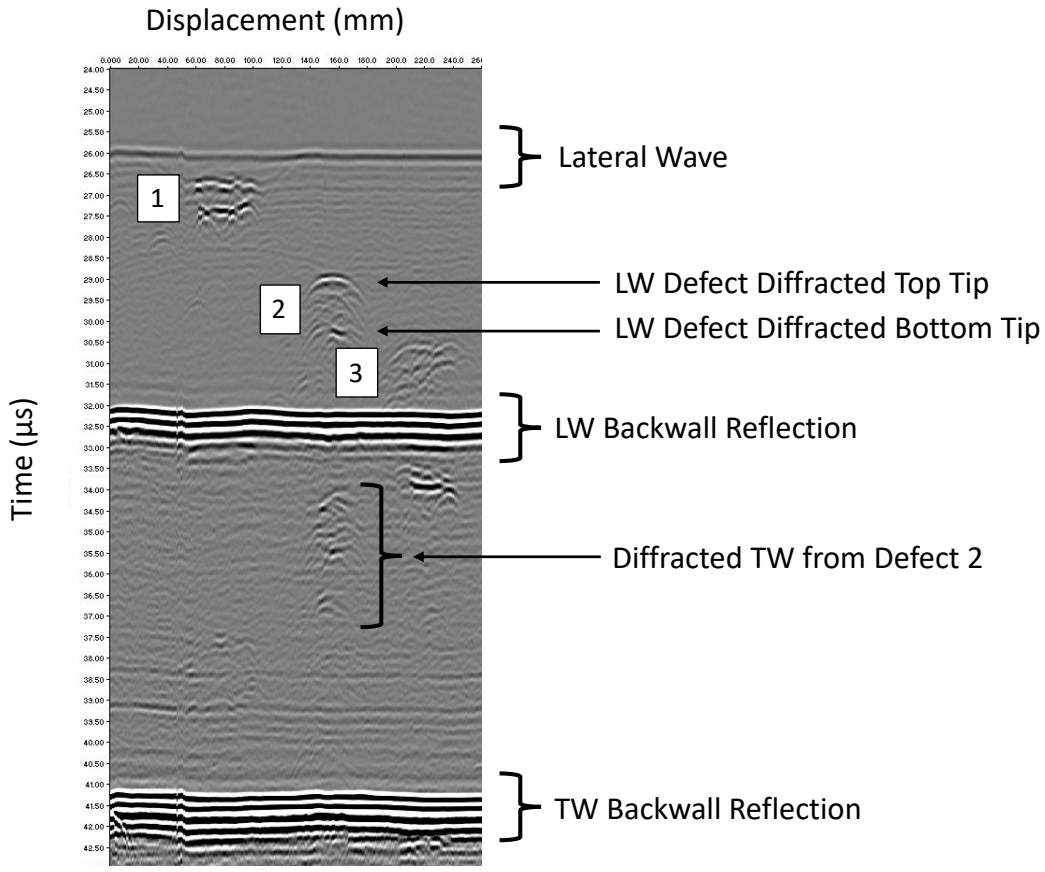

Figure 33: TOFD inspection B-scan of three defects captured using TUV Rheinland Sonovation with 10 MHz TOFD probes in 60^0 Rexolite wedges

TOFD is a very effective inspection approach for the detection and sizing of crack-like defects. Through wall height is measured from the differences in TOF between the signals that arise from the crack tips [51]. Unlike conventional UT and PAUT techniques, the detection and sizing of defects does not depend on the orientation of the defect. Conventional UT and PAUT are reflectivity-based techniques; they are thus very angle dependent and require defects to be perpendicular or near-perpendicular to the incident wave direction for detection and sizing. Diffraction-based techniques, by comparison, result in defects producing near omni-directional responses. Therefore, detection and sizing using TOFD is independent of defect orientation.

TOFD has two major limiting factors. The first key disadvantage is that propagation of the lateral wave creates a dead zone at the near surface. A dead zone also occurs at the backwall, shown in Figure 34:

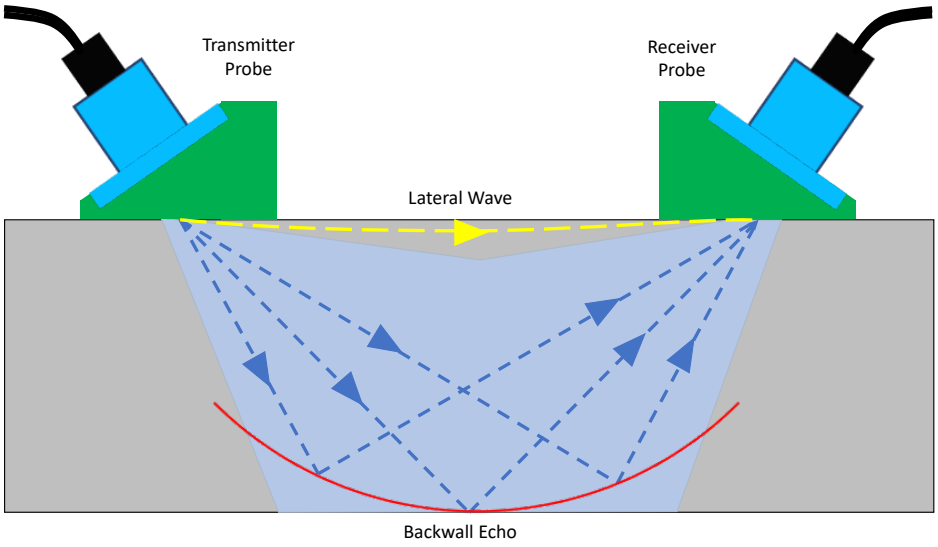

Figure 34: Schematic diagram of the TOFD backwall dead zone

The red elliptical line, shown above, represents the locations where any ultrasound path between probes will have the same TOF as the centre axis back-wall echo (BWE) [52]. As a result, TOFD offers limited capability to detect and size defects at the backwall of a structure, as well as the near surface. This potential backwall blind zone can be mitigated by performing offset scans to either side of the centreline scan. The second disadvantage is that the technique requires two probes which, can be problematic depending on the PCS and the surface accessibility for probe placement – particularly where structures with complex geometries are to be considered.

2.5 Summary of Review

Of these three probe types, the angled probe transducer setup is the more commonly used methodology for the inspection of a weld. The angling of the beam allows for defects within the weld to be detected through reflections from the back-wall as shown in Figure 18, as well as direct inspections. By comparison, transducers transmitting with normal incidence to the structure surface (single/dual element transducers) may struggle as the surface directly above/below the defect may have an uneven surface [5]. Therefore, within weld inspection, the two normal incidence probe setups are best suited for thickness testing, corrosion mapping and locating porosity within the HAZ using reflector edge scanning [53].

Despite TOFD's being a commonly used approach for weld inspection through its capabilities of detection and sizing regardless of defect orientation, it is limited in detecting and sizing near-surface defects and those positioned with the same TOF as the back-wall. Furthermore, it requires a transmitter and receiver probe straddling the weld which is a potential issue for complex geometry structures. To overcome these issues, TOFD scans are commonly complemented by PAUT scans.

Therefore, PAUT is the preferred approach for further research. Of the propagation methods, sectorial scanning PAUT is very good at locating and providing sufficient clarity to allow defect characterization defects, but it is not the most effective at being able to size a flaw. For that reason, linear scanning PAUT, with its more appropriate sizing capabilities, is the more preferred technique for further development.

3 Weld Inspection Overview

As important as it is to understand the fundamental principles and applications of ultrasound (as discussed in the previous chapter), it is equally essential to understand the structural and material properties of the media being investigating using ultrasound. This chapter will present an overview of welds and the standardised processes to inspect them. It will discuss weld geometries and defect-types, the standards set out to create a weld inspection setup, and how different ultrasound technique datasets are analysed and sentenced.

3.1 Weld Geometry Types & Features

Welding is a fabrication process whereby two individual components, typically metallic, are joined together using heat and/or pressure [54]. An example of a welded joint, or weldment, is shown in Figure 35 where the two parent materials represent the two individual components and the filler material represents the fusion volume.

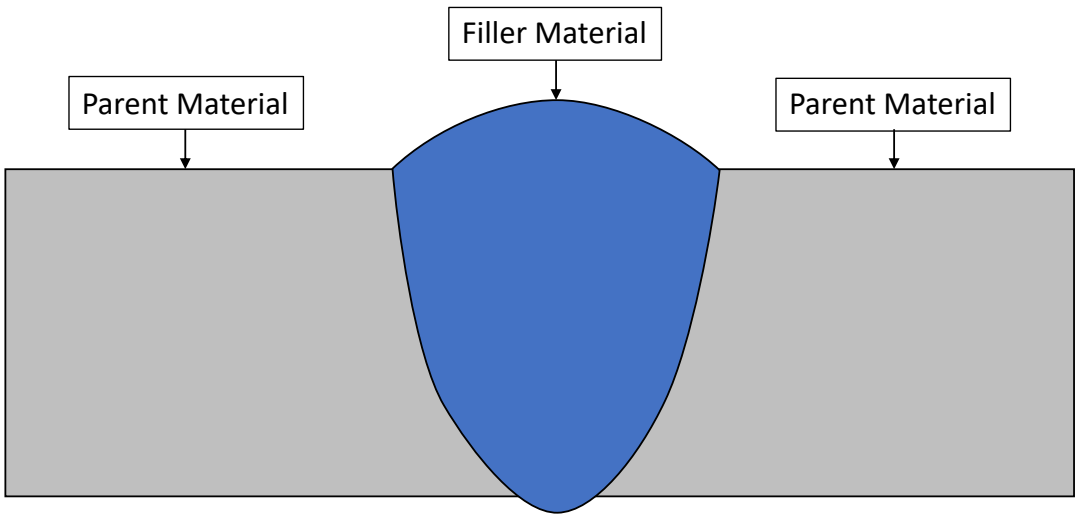

Figure 35: Schematic diagram of a single run full penetration simple single-U butt weld

Depending on the welding process, the filler material defined in Figure 35 can be formed solely from melting the parent materials or a consumable filler material can be added during the course of the welding operation. Selection of the consumable filler material requires careful consideration as it has to be compatible with the parent materials. The selected filler material has to show matching chemical and mechanical properties, its durability to undergo heat treatment, and allow inspection techniques to be applied effectively [55].

3.1.1 Square Groove Weld

The methodology of how the weldment volume is generated depends on the geometry of the weld and the thickness of the parent materials. For thinner and simpler geometry welds or weld processes implemented with shallow penetration capabilities, a single-pass approach can be used. The weldment shown in Figure 36 illustrates a single-pass weld process applied to a square groove joint.

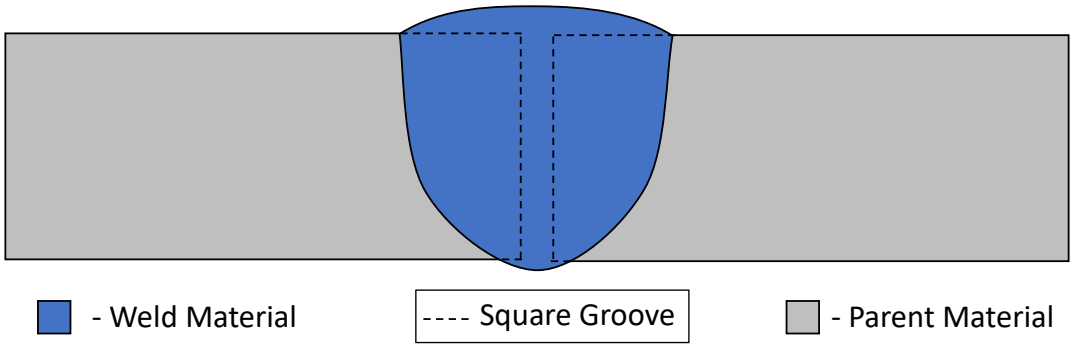

Figure 36: Schematic diagram of a simple square groove weld setup

To ensure complete penetration to fuse the two parent materials together, the material thickness of the square groove weld geometry is limited to approximately 6 mm [55]. Due to this small thickness and the shape of the square groove joint, it is not possible to do a multi-pass on

this type of weld geometry. The parent materials provide no groove nor have a sufficient gap between them to allow a weld torch to be manoeuvred.

3.1.2 Single V Weld

The single-V groove weld illustrated in Figure 37 demonstrates a multi-pass welding setup. Geometries that are thicker and more complex will require welding techniques with deeper penetration capabilities and a multi-pass approach [56]. Within the groove between the two parent materials, the filler material is generated from 16 weld passes; the numbers represent the order in which the weld pass was carried out.

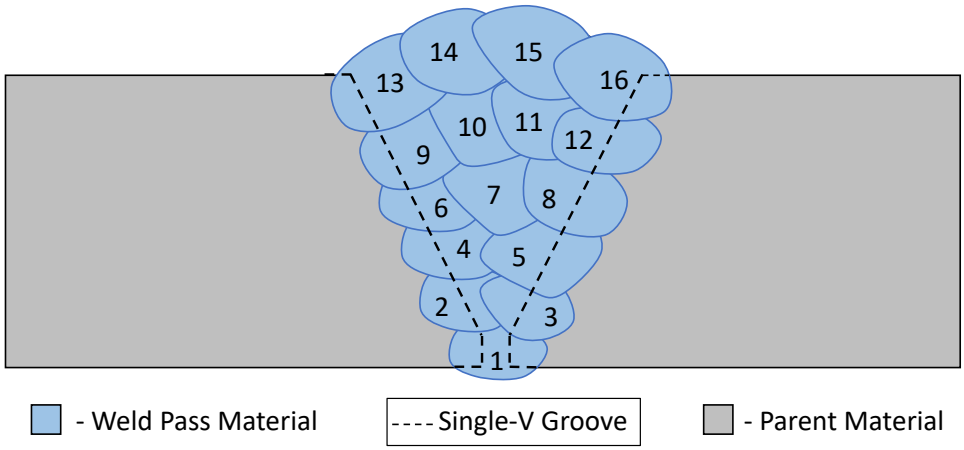

Figure 37: Schematic diagram of a multi-run full penetration simple single-V butt weld, where the numbers indicate the passes of the welding torch

Due to the groove, there is greater accessibility to steer the weld torch so that it may enhance root penetration and reduce the potential for lack of fusion defects [57]. The large volume of the groove between the parent materials will require the welding technique used to merge the two components with a consumable filler material.

Specific volumes and areas within the weld structure need to be identified in order for an operator to accurately locate and report a defect. Defining these allows the position of defects to be detailed relative to specific parts of the weld.

Figure 38 defines specific points and areas of interest for a full penetration single-V butt weld:

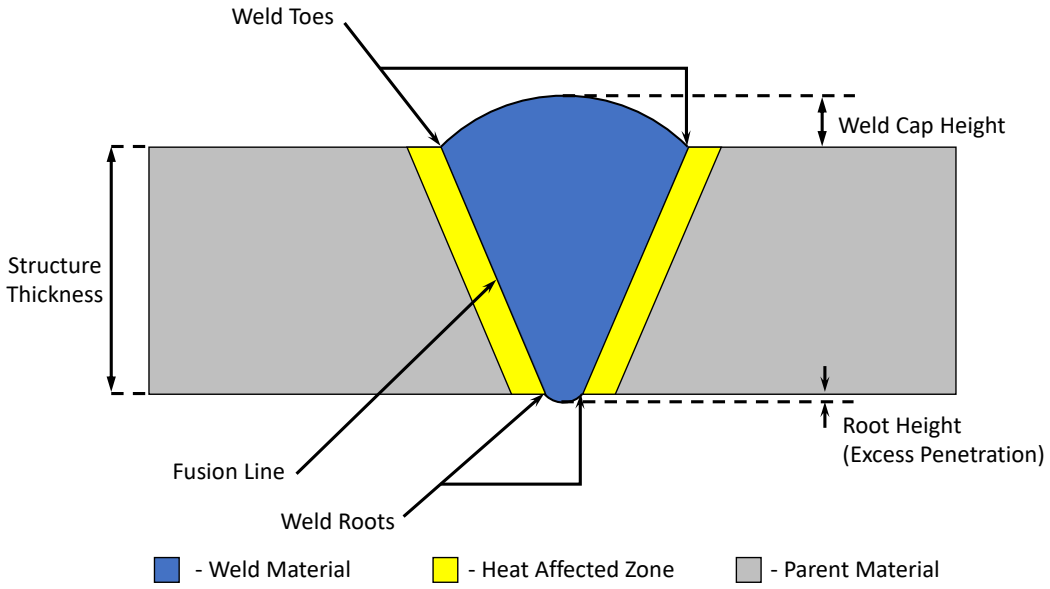

Figure 38: Schematic diagram of a simplified single-V butt weld joint

Unlike the detailed multi-pass welding illustration shown in Figure 37, Figure 38 shows a smooth outline of a single-v butt weld geometry shape. The area between the parent and weld filler material, is the Heat Affected Zone (HAZ). This is a region of the parent material that has been metallurgically affected due to the high temperatures of the weld process, potentially resulting in reductions in mechanical properties [58]. The fusion face is the boundary line of the HAZ with the weld material [54]. From the fusion face, the width of the HAZ extends approximately 10 mm [59].

In accordance with specified tolerances, both penetration beyond the thickness of the parent materials at the base of the weld and excess deposit at the top of the weld are acceptable. The weld toes are the surface boundary edges of the fusion face, along with the junction points of the weld cap. The weld roots are also boundary edges of the fusion face; those that are located furthest into the weldment [60].

3.1.3 Double V Weld

The design of a weld geometry is fundamentally based on the mechanical requirements of the in-service task it is required to carry out. The mechanical requirements that primarily influence the geometry of the weld are the loading demands. These can manifest in a variety of different ways based on the type (compressional, tensional, bending, torsional or shearing [61]) and the occurrence of application of the load (static or cyclic). Although square groove and single-V weld geometries are commonly used across many industries, another weld geometry widely used, especially for thicker structures, is the double-V weld, as shown by Figure 39:

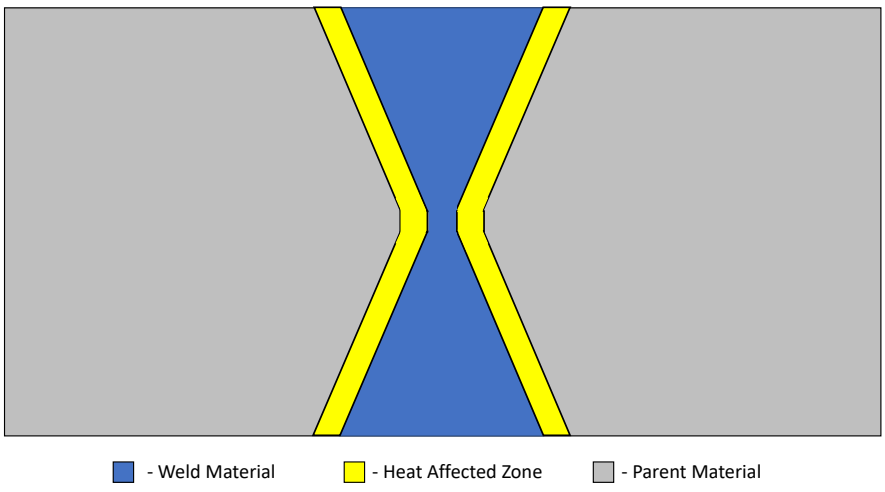

Figure 39: Schematic diagram of a simple double-V butt weld joint with flattened weld caps

Unlike square groove or single-V butt welds that are welded from a single side of the parent materials, the double-V butt weld is welded from both sides of the parent materials. As a result, this weld has four weld toes at the surfaces and four weld roots completely contained at the centre of the geometry.

The double-V weld, by design, uses significantly less weld filler material which reduces the amount of thermal energy required to be inputted into the weld volume. Consequently, this reduces the probability of shrinkage and angular distortion. This reduction is due to greater balance within the geometry of the weld, resulting in less thermal stress through the thickness of the material [62, 63].

Another design variation aimed at reducing the probability of defects arising is the removal of weld caps, as shown in Figure 39. Grinding the weld caps to align the weld faces with the thickness of the parent material reduces the stress levels surrounding the weld toes and roots of the weld and reduces the possibility of defects arising there [54, 64]. The requirement to remove or leave a weld cap will depend on the standard dictating the procedure for manufacturing and dressing the weld. In relation to the assets that QinetiQ Rosyth provide expertise to inspect, assets with and without a weld cap will be inspected.

3.1.4 Complex Geometry Welds

Adhering to the design specifications becomes increasingly more important when:

- the severity of a welded component's operation becomes increasingly critical
- there is limited surface accessibility during in-service inspection
- the complexity of the weld geometry increases

The weld joint types illustrated by Figure 36, Figure 38 and Figure 39 can all be considered as simple butt weld geometries. Butt weld geometries can become increasingly complex based on their location relative to physical features. A full definition of a complex geometry butt weld, in relation to Defence Standard 02-773, is:

"where at least one surface is non-parallel to its opposing surface and where the cross-sectional profile deviates from that of a simple butt weld. In many cases, the weld itself will be of a similar designation to that of a more common plain butt weld; with similar weld preparation angles, root and nose details. The complexity of inspection results from significant change in plate thickness either side of the weld or close proximity to features (chamfers, fillets or attachments) which make standard inspection procedures impractical." [59]

Based on the definition above, examples of complex geometry welds include tapered double-V butt weld as illustrated in Figure 40 and the Tee-butt joint shown in Figure 41:

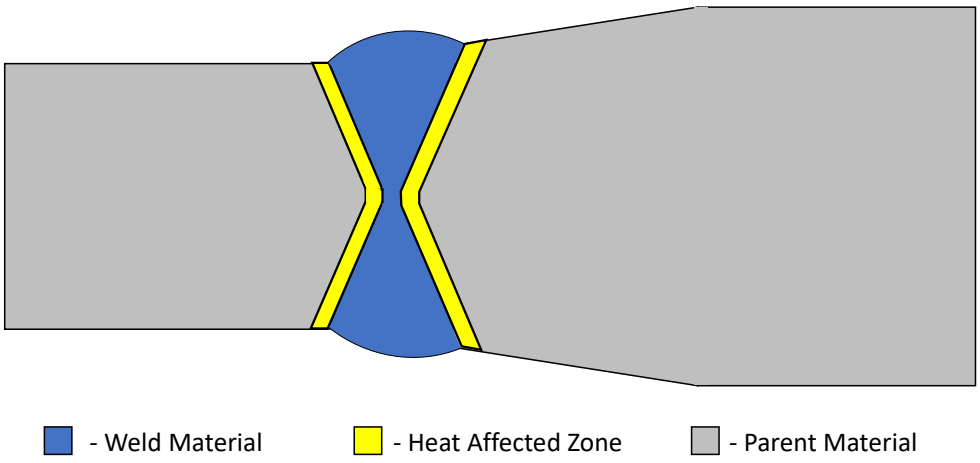

Figure 40: Schematic diagram of a tapered double-V butt weld joint

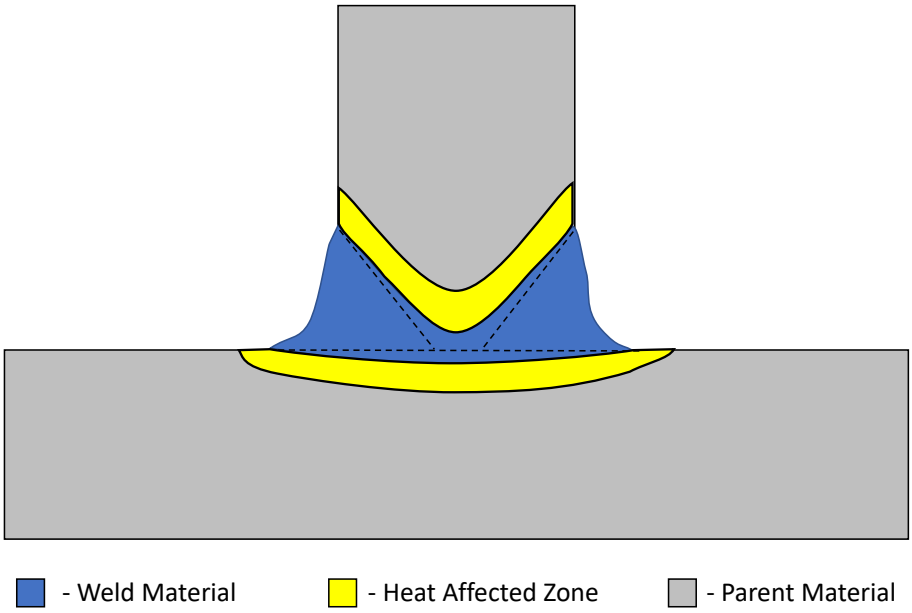

Figure 41: Schematic diagram of a full penetration tee-butt weld joint

During the manufacturing phase, all surfaces surrounding both of the complex weld geometries, above, are accessible, maximising the number of setup possibilities to acquire inspection coverage. However, within the in-service phase, certain limitations can prevent repeating the same inspection process including:

- environmental factors preventing access for inspectors (e.g. nuclear radiation, extreme temperatures, toxic air pollution, etc.)
- reduced surface accessibility or probe manoeuvrability to acquire the required inspection coverage due to interfering structures
- shortened timescales due to minimizing an assets offline period

These factors are also applicable in simple butt-weld geometry inspections. This results in alternate inspection setups being implemented and/or multiple inspection techniques used in conjunction with one another, in order to acquire similar percentage coverage.

3.2 Weld Defects

During both the manufacture and in-service inspection phases, a range of different defect types can occur. Certain defects only occur during the manufacturing phase, and some only occur while the structure is in-service.

Many of the potential defects that happen during the manufacturing stage are more probable to arise than others, due to individual factors or a combination thereof. The occurrence of each defect can be caused by a variety of factors. Some result from poor welding technique, some from the weld materials being contaminated by debris or foreign substances and some are due to environmental factors. Some factors stem from a lack of welding experience, specific welding techniques being implemented, particular materials being used and/or the surrounding environment of the location of the fusion.

Defect faults found within the in-service phase are typically caused by the deterioration of a structure's mechanical properties through cyclic loading over a prolonged time frame. Other factors that can cause defects to develop during in-service include sudden changes in operating conditions and impact damage due to failures of surrounding structures.

Flaws can also stem from the known and unknown abnormalities initiated during the manufacturing phase. Based on the UK Defence Standard acceptance criteria for the type of defect and its size (discussed in Section 3.4), those defects were either too small to be detected or are sufficiently small that no action/repair was required. If they have grown

to measurable levels, these defects are documented and regularly observed during the in-service inspection process. Most defects detected during the manufacturing stage will either be repaired prior to being rolled-out into service or scrapped. Some of these defects and their causes are given in Table 2, below:

Table 2: Common Faults arising in welds during manufacturing

Potential Fault	Properties & Cause
Undercut	Due to arc travel speed being too high, quick solidification occurs causing surface tension to draw the molten metal away from the edges and toward the centre, where the bead stacks up resulting in a groove along the toe of the weld [65, 66] .
Inclusions	These are foreign materials trapped within the weld material or at the joint between the weld material and parent material. Inclusions can occur if the welding area and equipment is inadequately cleaned after each welding pass [66].
Lack of Root Penetration	Due to low amperage to the welding torch, the weld bead does not penetrate through the complete thickness of the parent material in Single-V welds. In Double-V welds, the weld beads at the root of each V do not interpenetrate [67].

With the focus of this thesis being on in-service inspection, three defect types that are commonly detected during the in-service phase are LOF, porosity and cracks. There are multiple ways in which these defects can initiate: they can either remain undetected from the manufacture phase, or if detected during manufacture, passed acceptance standards and require further monitoring; or can arise during the in-service stage can arise due to fatigue or from sudden impact.

3.2.1 Lack of Fusion Defects

LOF defects occur during the fabrication of a weld and are commonly due to poor welding technique. Typically, the weld pool is too large because of slow travel speed and/or the weld filler has been added ahead of the arc [68]. Poor welding technique can also include insufficient torch current and improper electrode angle [68, 69]. Alternate reasoning for LOF defects to arise include incorrect joint positioning, such as narrow root gap or large root face, and magnetic arc blow, where the welding arc deflects due to changes in the magnetic field surrounding the arc [66, 70]. This causes the weld filler material to have poor adhesion to either the parent material(s) or to previous weld passes.

The schematic in Figure 42 demonstrates ways this defect can orientate itself within a weld, where LOF defect 1 is located on the fusion face between the parent material and the weld while LOF defect 2 is located between two weld bead layers:

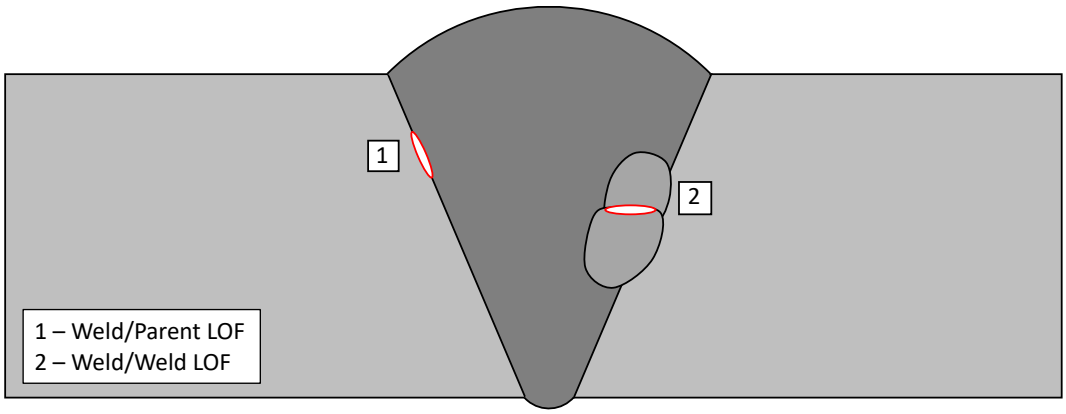

Figure 42: Schematic diagram of LOF defect within a weld

3.2.2 Porosity Defects

Porosity is the development of small gas bubbles/pores that occur in the centre of the hardened weld filler. There are multiple causes for porosity, including atmospheric exposure to the weld pool from lack of gas shielding, damp electrodes/fluxes, too large arc length, or contaminants such as moisture/oil on the surface of the material [66].

Depending on the extent of the cause, porosity can develop and present itself within a weldment in different ways: uniform, clustered or linear. Uniform and clustered porosity types are illustrated in the schematic diagram in Figure 43:

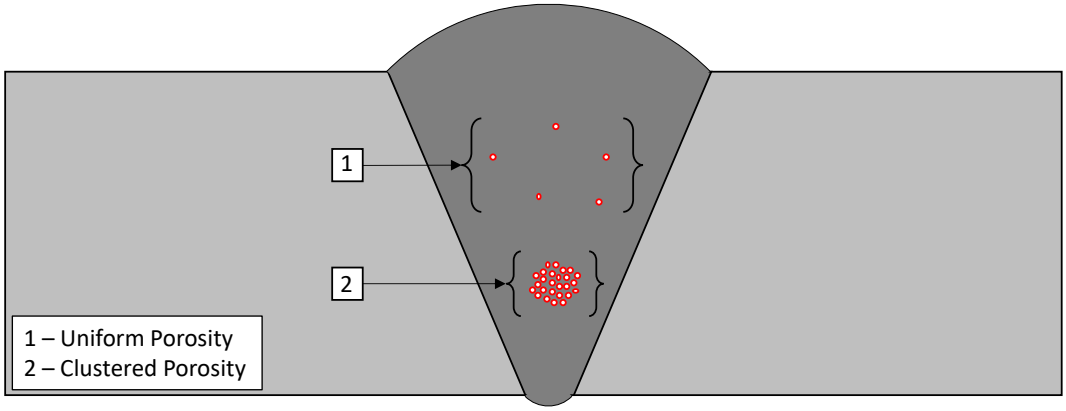

Figure 43: Schematic diagram of uniform/clustered porosity within a weld

As shown above, uniform porosity is the uniform distribution of individual pores within the volume of the weld material. By contrast, clustered porosity is a localised group of pores closely grouped together as shown in area 2 above. Linear porosity can be described as the alignment of numerous pores along the length of the weld as shown in Figure 44.

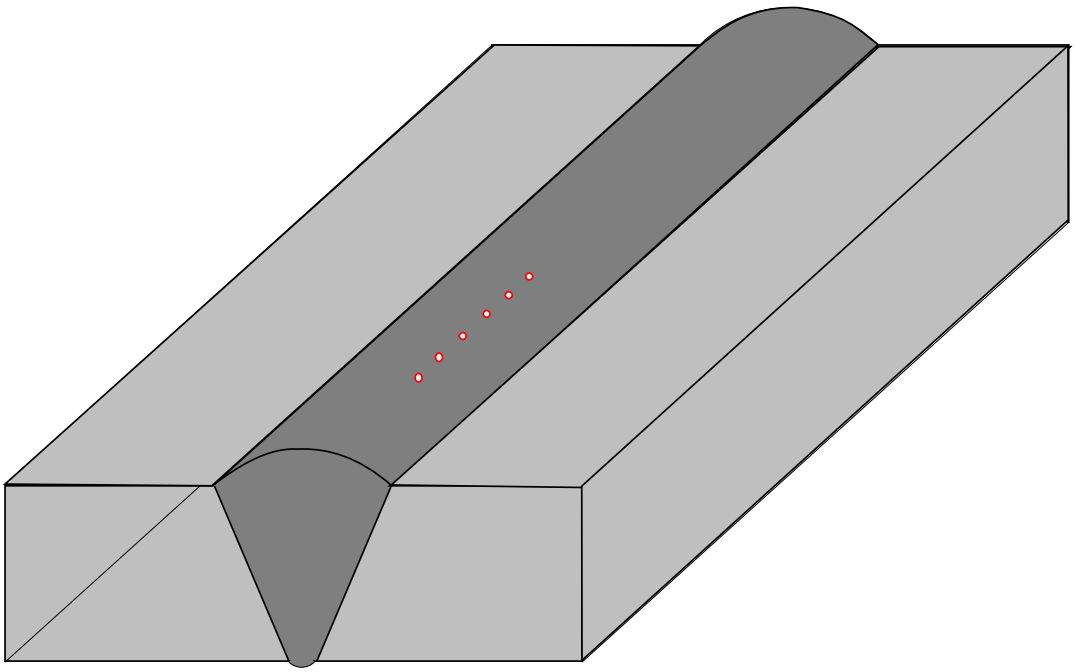

Figure 44: Schematic diagram of linear porosity within a weld

The shape of each pore is typically spherical, but can be cylindrical [71]. As a result of their point like nature, the interaction of ultrasound with individual pores will result in an omni-directional reflection.

3.2.3 Crack-like Defects

Cracks are caused by elevated magnitudes of stress within an area of the weld. The stress can be instigated from irregularities or improper technique during manufacture, or fatigue over time during service can cause discontinuities to grow into cracks. In addition, such defects can be positioned in or between weld beads and/or in the Heat Affected Zone (HAZ).

The schematic diagram in Figure 45 illustrates the different ways in which cracking can manifest and orientate itself within a weldment:

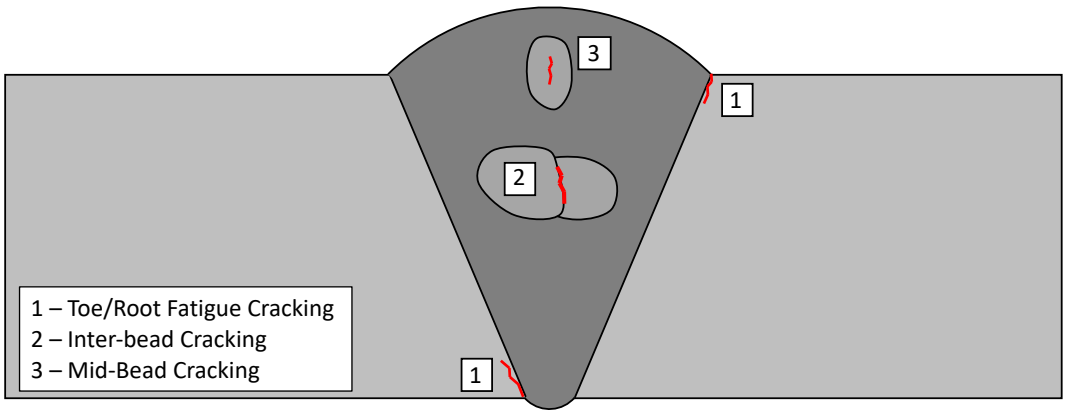

Figure 45: Schematic diagram of internal cracking defects within a weld

Toe and root fatigue cracking occur during the in-service phase as a result of the areas having high stress concentrations. These would typically be surface breaking cracks and would require repair, as discussed in Section 3.4.

Inter-bead and mid-bead cracking commonly occur due to a variety of different reasons; welding speed, incorrect post-weld treatment and shrinkage. As illustrated in Figure 45, inter-bead cracking presents itself as two weld beads separating; while mid-bead cracking, also known as centreline cracking, is separation in the centre of a given weld bead [72]. Deriving from the manufacturing stage, another cause for both crack types to occur is Hydrogen Induced Cracking (HIC). HIC occurs due to the diffusion of hydrogen atoms into the weld material and filler material during manufacture. Cracking transpires from the increased concentration of hydrogen atoms combining within the material to form hydrogen molecules. These molecules cause a pressure increase within the structure and reduce the structure material's ductility and tensile strength, resulting in a crack [73]. Omission or incorrect application of post-weld treatments and processes results in residual

stresses within the material reaching unacceptable levels that increase the probability of crack-like defects forming.

Many of these defects are related to the effects of unsuspected or changing properties of the welding materials and/or environment. They can also cause another type of defect: HAZ cracking, which occurs outside the weld area. The remaining types of faults that can occur are normally due to human error by the welder, including misalignment of the parent materials, arc striking and burn-through.

3.3 Defence Standards for Welds and Inspections

The motivation for the research in this thesis is to investigate how the in-service weld inspection process can be improved to optimize inspection strategy for thicker structures (>16 mm) and complex geometries. Due to the research being carried out in collaboration with QinetiQ, all work is carried out in accordance with the UK Defence Standards. The relevant UK Defence Standards for the manufacture and inspection of welded structures are:

- Defence Standard 02-706: *Welding & Fabrication of Ship Structure for HM Submarines and Ships not in Class*

- Defence Standard 02-729: *Requirements for Non-Destructive Examination Methods (Part 5: Ultrasonic)*

- Defence Standard 02-773: *Minimum Non-Destructive Examination Acceptance Standards for Welds in HM Submarines and Surface Ships not in Class*

According to Defence Standard 02-729, the preferred inspection approach for butt-weld geometries is TOFD. In the case of simple butt-weld joints, the preferred setup is to apply TOFD from both surfaces. Probe selection for a TOFD inspection setup is given as a table providing recommended probe size, frequency, wedge angle and focus depth appropriate to various plate thickness ranges.

Based on the plate thickness, chosen wedge angle and chosen focus depth, another table is used to select the PCS value. The PCS

values can also be calculated from the following formula, where D is the desired focal depth and θ is the refraction angle of the probe setup [74]:

$$PCS = 2D \cdot \tan\theta \quad (3.1)$$

As the name implies, PCS is defined as the distance between the centre of the transmit and receive probes used within TOFD. It is important to use the correct PCS for an inspection setup as it is aimed at acquiring maximum coverage and effective resolution.

Depending on the ratio of the material thickness to the width of the weld, the number of TOFD scans to be applied on each surface will vary. This is regardless of whether all surfaces or only one surface is accessible. For plate thicknesses where only one TOFD scan is required, the scan will be centred along the centreline of the weld. When two scans are required, they will be centred at offsets on either side of the weld centreline. For three scan setups, one probe centreline will be aligned with the weld centreline and the other two will be offsets on either side of the weld. The magnitude of the offsets from the centreline for two and three scan scenarios are either 5 or 10 mm depending on the thickness of the plate [52]. The purpose of these offsets is to mitigate the effect of backwall blind zones that may be experienced by single scan setups.

When only a single surface is accessible, TOFD inspection of simple geometry butt-welds must be supplemented by phased array linear scanning inspection. This is to cover the TOFD dead zones at the near (scanning) surface and far (backwall echo) surfaces, as discussed in Section 2.4 [52]. Nominally, the near surface dead zone coverage is

acquired using a full-skip $45^0 \pm 2^0$ beam and the backwall dead zone coverage using a half-skip $60^0 \pm 2^0$ beam.

To avoid missing defects that are potentially parallel to the inspection beam profile, the phased array setup is carried out on both sides of the weld face. The desired extent of the coverage is 100% overlap of the phased array inspections from each side of the weld face, with coverage across the complete width of the weld, plus an additional 20 mm to inspect both HAZs. An example, provided within Defence Standard 02-729 of a combined TOFD and phased array butt weld inspection is shown in Figure 46:

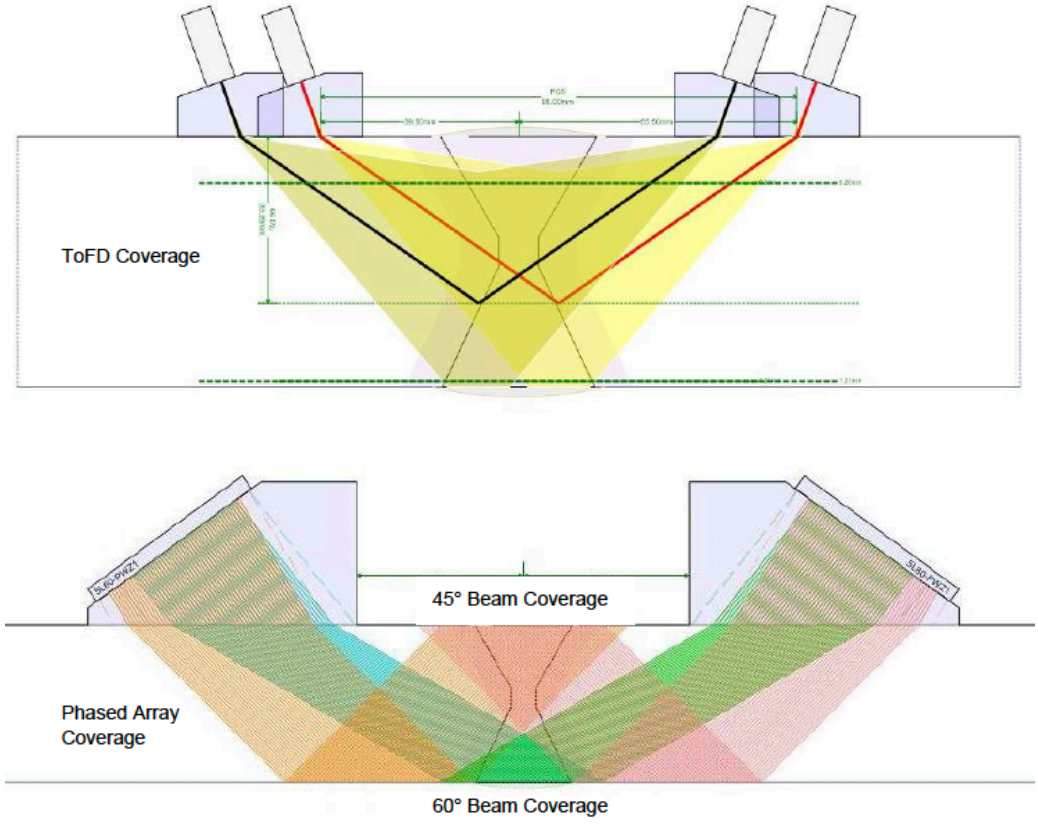

Figure 46: Schematic diagram of defence standard single side access butt weld inspection [52]

Due to the thickness of the weld shown above, two TOFD inspections are required with equal offsets from the weld centrelines. For the areas of the weld geometry not marked in yellow in the TOFD inspection, the phased array setups acquire the necessary coverage at the near and backwall dead zones and the HAZs.

For complex geometry butt welds, TOFD is still the preferred method. On occasions when full surface accessibility is available, TOFD inspections must be supplemented by phased array linear scanning and other techniques for surface-breaking crack detection.

For the increasingly more complex scenarios where TOFD cannot be implemented, coverage must be established using a combination of phased array linear scanning and surface-breaking crack detection techniques.

3.4 Weld Defect Sentencing Criterion

As previously mentioned, UK Defence Standard 02-773 is the MOD NDE acceptance standard for the examination of welds in submarines and surface ships. For ultrasonic inspection techniques, it details whether a defect's size, relative position or amplitude response calls for it to be disregarded, rejected, repaired or reported for further analysis.

Using the preferred method, TOFD, the acceptance standards are applicable to high strength steels of thicknesses equal to or greater than 16 mm. For all welds, all surface breaking cracks are rejected and require repair; point reflectors with no measurable through thickness height or length can be disregarded [59].

For detected defects within different weld types, the sentencing criteria for TOFD is broken down based upon the location of the defect. Depending on position relative to weld features of the weld such as plate surface, weld toes, or weld root, the defect will be sentenced accordingly.

For butt weld joints, the sentencing begins based on whether a defect has at least one of its detected diffracted tips located within 5 mm of the plate surface or if both are further than 5 mm from the plate surface. The following table details the actions to be taken within each scenario, where 't' is the thickness of the parent material (specifically the thinner plate thickness when plates of different thickness are being welded):

Table 3: UK defence standards for TOFD inspection of butt weld joints [59]

Defects with One Tip ≤ 5 mm to Plate Surface	
Indication	**Action/Sentence**
Through Thickness Height > 3 mm or t/5	Rejection
Single Continuous Defect Through Thickness Height > 2 mm & Defect Length > 30 mm or 2t	Rejection
Single Continuous Defect Through Thickness Height: 2-3 mm & Defect Length > 20 - 30 mm	Record within Inspection Report
Combined Length of Defect Indications Through thickness height > 2 mm & Combined Defect Length > 100 mm per 1000 mm Weld length*	Rejection
*for welds < 1000 mm - Adjust Combined Length proportionally	

Defects with One Tip ≤5 mm to Plate Surface	
Indication	**Action/Sentence**
Through Thickness Height > 5 mm or t/5	Rejection
Single Continuous Defect Through Thickness Height > 2 mm & Defect Length > 50 mm or 2t	Rejection
Single Continuous Defect Through Thickness Height: 4-5 mm & Defect Length > 40 - 50 mm	Record within Inspection Report
Combined Length of Defect Indications Through thickness height > 2 mm & Combined Defect Length > 200 mm per 1000 mm Weld length*	Rejection
*for welds < 1000 mm - Adjust Combined Length proportionally	

Applying the criteria above to sentence the LOF defect from Figure 50 as an example; the detected tips of the defect can be measured using the cursors to be greater than 5 mm from the plate surface. The through thickness height of the defect can be measured to be 6.5 mm, which means the defect would be rejected and require repair.

Two defect indications are sentenced together as a single defect if the separation distance between them is less than 1.25 times length of the longer defect. To demonstrate, Figure 47 illustrates a schematic of the combined length achieved between two defects indications based on the ratio of the longer defect length to the separation distance.

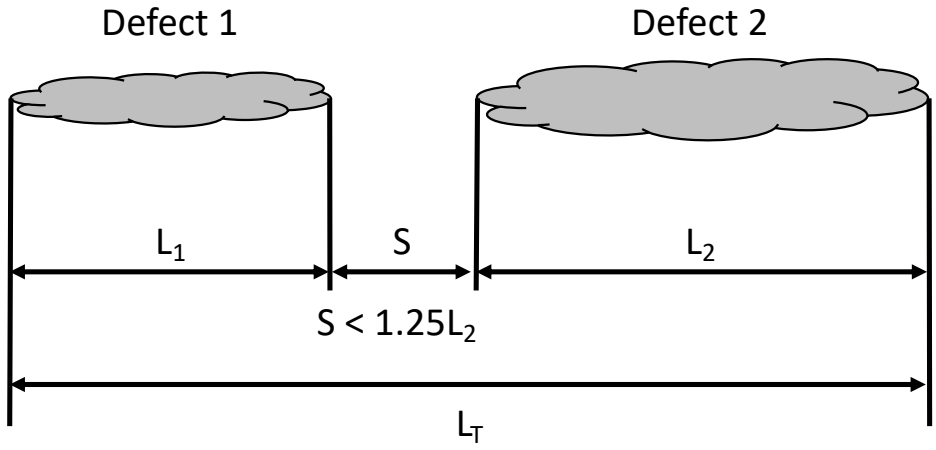

Figure 47: Schematic diagram of combined defect length from adjacent defects

The sentencing criteria for these defects relative to length of the weld is adjusted proportionally for smaller lengths of weld. For example, any combined length of indication defects located within a 500 mm long weld would be rejected if they exceeded 50 mm for one tip within 5 mm of the surface and 100 mm if both tips were further than 5 mm from the surface.

Clustered porosity follows similar sentencing criteria to a combined length of defect indications. Repairs are only required if the length of the porosity exceeds 100 mm if located near the surface and 200 mm if buried within the body of the weld for any 1000 mm length of weld [59]. However, it has a differing restriction in that the through thickness height does not exceed half of the thickness of the plate. If porosity is detected, and no repair is required, it should still be recorded for future reference.

By comparison, uniformly distributed porosity will be rejected if it causes more that 1% loss of area for any given 150 mm weld length. This is measured based upon the allowable number of point reflectors for a given thickness of weld. In the circumstance that a particular indication of measurable length or through thickness height is measured within a band of uniformly distributed porosity, the indications are sentenced in accordance with the standards set out in Table 3. If passed on that basis, further analysis would be performed to calculate the area taken up by the porosity. This would be used to estimate the reduction in maximum allowable number of point reflectors for any given 150 mm length of weld. Using the reduced maximum of point reflectors, the number of point reflectors would be counted and sentenced accordingly.

In the scenarios where PAUT is required to supplement a TOFD inspection due to impracticalities caused by limited surface access and/or complex geometry, an additional set of sentencing standards are enforced. Due to PAUT being a reflectivity-based detection method, its acceptance standards are based on the sentencing criteria for manual/conventional ultrasonic inspection techniques. The amplitude

responses of indications are measured using the logarithmic unit, decibels (dB). The amplitude response can also be expressed as a percentage of the Full Screen Height (FSH) of the inspection equipment, calculated from the decibel response using Equation 3.2:

$$\%\ Response\ = 100 \cdot \sqrt{10^{\frac{dB\ Response}{10}}} \tag{3.2}$$

For butt weld geometries, the following table details the acceptance criteria for indications detected using conventional UT and PAUT techniques.

Table 4: UK defence standards for conventional UT/PAUT inspection of butt weld joints [59]

Indication	Action/Sentence
Reflectivity ≥12dB below DAC or TCG	Accepted
Reflectivity ≥12dB above DAC or TCG	Rejection
Reflectivity < 12dB above DAC or TCG: Single continuous defect: Length < 1t or 38 mm & Indicated Total Length of Defects: Length < 2t per 30t length* *for welds <30t mm - Adjust Combined Length proportionally	Accepted
Reflectivity <12dB below or equal to DAC or TCG: Single continuous defect: Length < 2t or 76 mm & Indicated Total Length of Defects: Length <4t per 30t length* *for welds <30t mm - Adjust Combined Length proportionally	Accepted
Indication transverse to major axis of weld: 1. Reflectivity > DAC or TCG 2. Reflectivity <12dB below or equal to DAC or TCG 3. Reflectivity ≥12dB below DAC or TCG	 Rejection Accepted Accepted

The reflectivity amplitudes are relative to the respective calibration processes, Distance Amplitude Correction (DAC) for conventional UT and Time-Corrected Gain (TCG) for PAUT as discussed later in Section 3.6.

To ensure consistency between the TOFD and PAUT inspections of the same LOF defect, these acceptance criteria can be applied to the linear scanning PAUT inspection of the same LOF defect shown in Figure 51 and Figure 52. Based on the 392% screen height amplitude response, this would result in an immediate rejection due to being greater than 12 dB above the 80% screen height TCG calibration line.

3.5 Advanced UT Weld Inspection Equipment

Weld inspection equipment can vary across companies and industries depending on factors such as its capabilities, its cost and the preferences of the user. Throughout the lifespan of any welded structure, all of the inspections carried out on it will not always be performed using the same equipment. This could be as a result of different companies, being contracted to inspect a given structure at different points in the structure's lifespan using different inspection equipment from one another. Examples of this occur when the company who inspects a structure at manufacture will be different to the company who inspects it once it has been deployed and in-service. Alternatively, throughout the lifespan of a structure, improvements to inspection technologies may convince companies to upgrade their equipment between scheduled inspections. Regardless of what equipment is used to carry out an inspection, the important aspect is that the equipment meets the requirements of the governing standards. In the case of this thesis, the relevant standards being adhered to are the UK Defence Standards.

QinetiQ Ltd provides recommendations for UK Defence Standard in-service inspection setups, offering expertise in performing specialised inspections and provide third party analysis to captured inspection data. To maintain consistency, QinetiQ aim to use the same ultrasonic testing equipment used by the primary in-service inspections contractor for the Ministry of Defence (MOD). For phased array inspections, the Olympus OmniScan MX2 (Evident, Tokyo, Japan) is used; and for TOFD inspections the specified equipment is the TUV Rheinland Sonovation TUV Rheinland, Oosterhout, Netherlands) running Sonavision software with additional automated defect sentencing technology.

3.6 UT Calibration Processes for UK Defence Standards

The calibration process of an ultrasonic technique involves the adjusting of the measurement system settings to ensure its sensitivity and accuracy for detecting and sizing defects are in accordance with a referenced standard. The appropriate calibration setup depends on the ultrasonic technique and setup required. Across conventional UT, PAUT and TOFD, each technique has its own range of calibration techniques that can be applied.

Common to all ultrasonic setups, an essential calibration process relates to quantifying the material velocity of the structure under inspection, prior to any sensitivity calibration. This can be achieved by measuring the TOF for a known thickness of the material being inspected. The velocity can then be calculated using Equation (2.17), discussed in Section 2.2.

In reference to UK Defence Standard 02-729 Part 5: Ultrasonic, the remainder of this section will provide definitions to the sensitivity calibration practices used specifically for conventional UT, linear/sectorial scanning PAUT and TOFD. The calibration processes discussed are commonly used throughout industry. Other standards such as the British Standard (BS), International Organization for Standardization (ISO) and American Society of Mechanical Engineers (ASME) recognise these processes [75].

3.6.1 Distance Amplitude Correction for Conventional UT

Distance Amplitude Correction (DAC) is a commonly used calibration technique for a conventional UT setup. A DAC is a curve acquired by measuring the amplitude responses of multiple Side-Drilled Holes (SDHs) of equal size at varying distances away from the probe. The normal procedure for setup is that the gain of the flaw detector is adjusted so that the response of the shallowest SDH is set to 80% FSH [76]. For the remaining SDHs, at their respective depths, the gain setting is kept constant and the maximum response for each is acquired. An example of a generated DAC curve is shown in Figure 48:

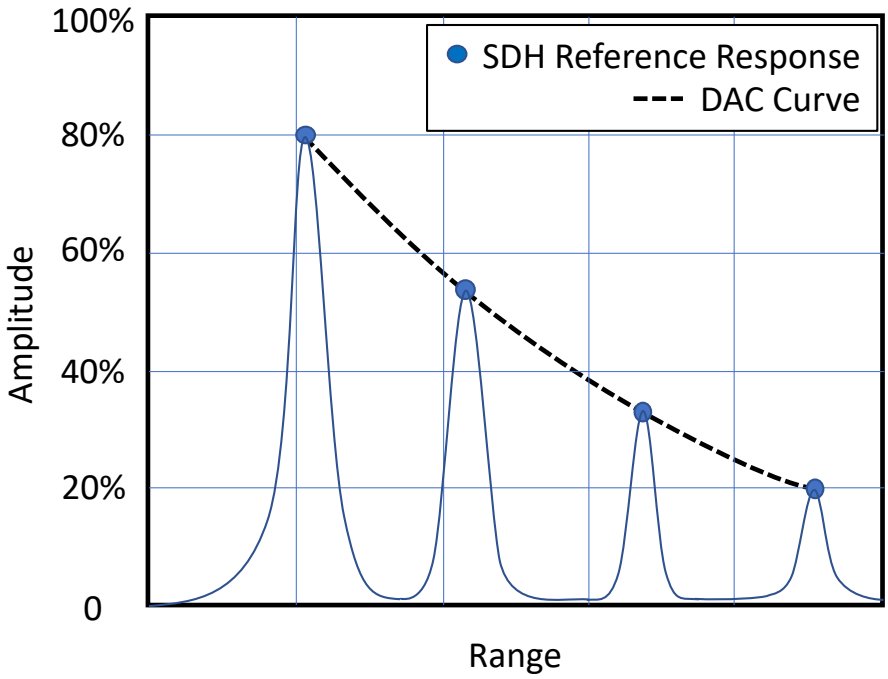

Figure 48: DAC curve generation from SDH amplitude responses

As shown, the curve is generated through the linear/spline interpolation of the SDH reference responses [77]. This process is necessary to approximate the amplitude response that would be captured for a SDH positioned intermediary to two of the measured SDHs.

3.6.2 Time Corrected Gain Calibration for PAUT

TCG is a commonly used calibration technique used for linear scanning and sectorial scanning PAUT setups. According to the British Institute of Non-Destructive Testing (BINDT), a TCG can be defined as:

"a method of compensating for a reduction in signal amplitude with increasing depth from reflectors of equal area. This is achieved by increasing the system gain with time so that the signals appear of equal amplitude."

Figure 49 provides a visual representation of this definition compared with a DAC curve:

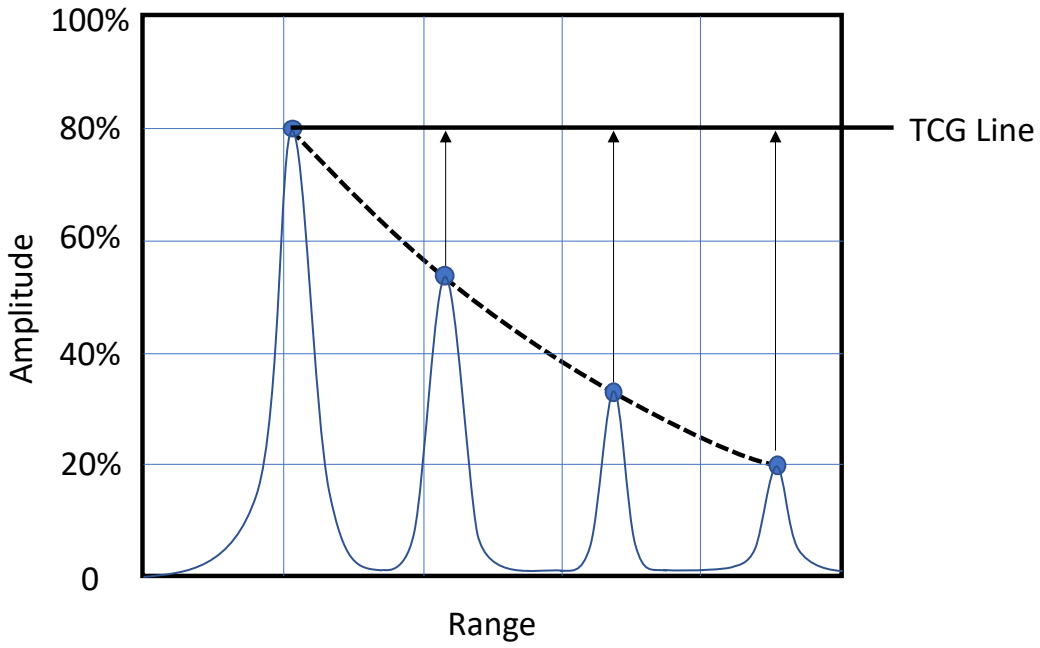

Figure 49: Implementation of a TCG calibration to an A-scan [78]

From Figure 49, as the amplitude response from identical defects decreased with increasing range, increasing levels of gain are applied to normalise the responses to a specified percentage response height.

For both linear scanning and sectorial scanning phased array setups, the process is repeated for all active apertures/angles of the respective scanning setup. This ensures that identical reflectors at all depths produce the same amplitude response across all apertures/angles.

This is particularly important for phased array scanning setups with wedge-mounted probes as the sound path length for each active aperture or angle within the wedge will vary. For active apertures or angles that have larger sound paths within the wedge, greater attenuation will occur resulting in more gain being required to compensate and normalise the reduction in signal.

3.6.3 Time of Flight Diffraction

Having selected the parameters, such as the probe frequency, probe size, wedge angle and PCS, for a TOFD inspection, based on the material and sample thickness; the gain settings of the equipment are set so to meet the following:

- Noticeable acoustic grain scatter beyond the TOF of the lateral wave that is at least 6 dB higher than the amplitude of the electronic noise prior to the lateral wave TOF
- The percentage amplitude of the lateral wave response is set within the range of 10-40% FSH without over-saturating the reflected BWE

The calibration processes for a TOFD inspection in accordance with the UK Defence Standards is to ensure that 50 mm of uninterrupted BWE signal is acquired when scanning a 60 mm long notch. Further

dimensions of the notch are that it is 1-2 mm wide with a 60^0 include angle vee-tip and is 0.2T (T = plate thickness) in depth.

Furthermore, a depth calibration is carried out to convert the TOF between the probes to depth. The conversion is calculated using trigonometric formulas due the non-linearity of the scan image. Modern inspection equipment can complete this conversion by positioning parabolic cursors at the lateral wave and the tips of reflector echoes at known depths or the backwall echo. This calibration would be carried out within a 200 mm radius of the inspection setup. In addition to calibrating, the TOF of the lateral wave and backwall would be recorded to be used as datum values when analysing structures with weld caps and rough surfaces. This process would be repeated after the inspection to verify the TOFs of the lateral wave and BWE to ensure that the PCS did not significantly change [52].

3.7 Defect Detection & Characterisation

3.7.1 Lack of Fusion

To illustrate how a LOF defect appears in TOFD inspections and how it is characterised and measured, Figure 50 is a zoomed-in D-scan image of Defect 1 from Figure 33:

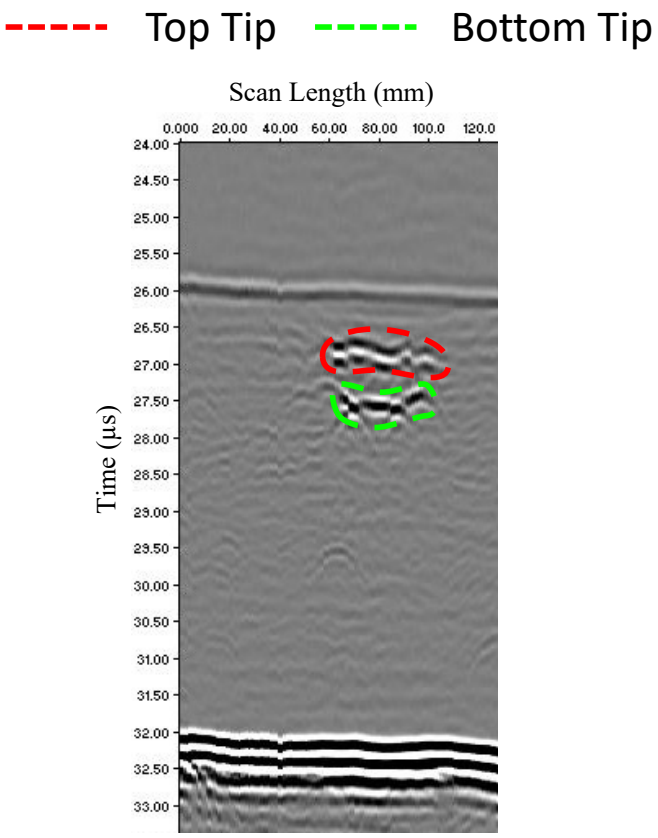

Figure 50: TOFD D-scan image of a LOF defect using TUV Rheinland Sonovation with 10 MHz TOFD probes in 60° Rexolite wedges

A D-scan display can be defined as the cross-section view of a structure that is perpendicular to both the scanning surface and the projection of the beam axis relative to the scanning surface [79]. A LOF defect is recognised within a TOFD inspection by unbroken top and bottom tips for the full length of the defect, as shown in the scan image above. The through-thickness height of the defect can be measured using hyperbolic cursors. The phases of the BWE and lateral wave are

determined by observing the order of the alternating black and white bands and checking that the BWE and the lateral wave have inverted orders. The cursors are positioned with one on the top tip on the same phase as the BWE and one on the bottom tip with the same phase as the lateral wave [59].

In the case of the BWE and top tip, the cursor would be positioned on the white portion of the tip, while the cursor would be positioned on the black tip for the bottom tip. The through-thickness height of the defect can then be calculated by multiplying the difference in TOF of the top and bottom tips with the longitudinal velocity of the material. Using the same cursors, the length of the defect can be measured by positioning the centre of each hyperbolic cursor at either end of the defect. A PAUT inspection of a LOF defect can be seen in the S-scan and C-scan images in Figure 51 and Figure 52:

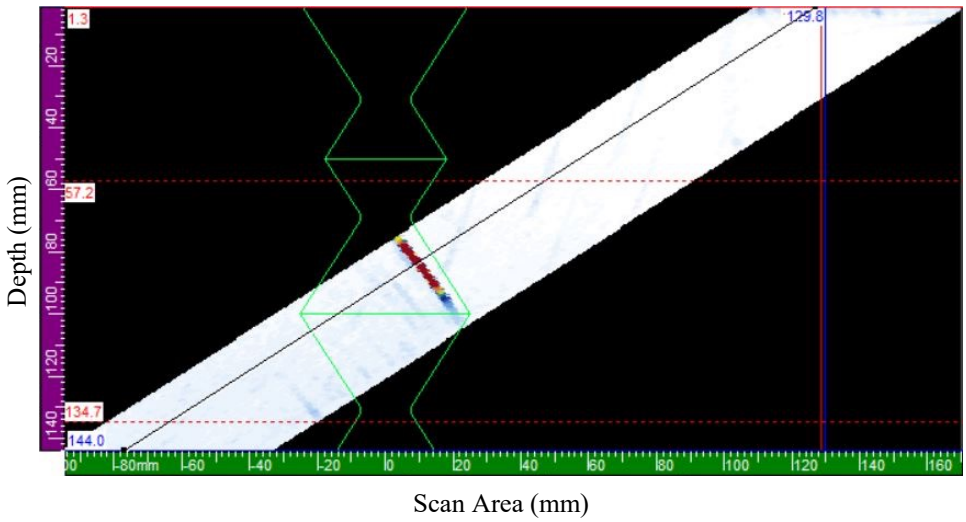

Figure 51: PAUT S-scan image of a LOF defect captured using an OLYMPUS Omniscan MX2 attached with a 5MHz 60 element linear array PipeWizard probe and 550 Rexolite wedge

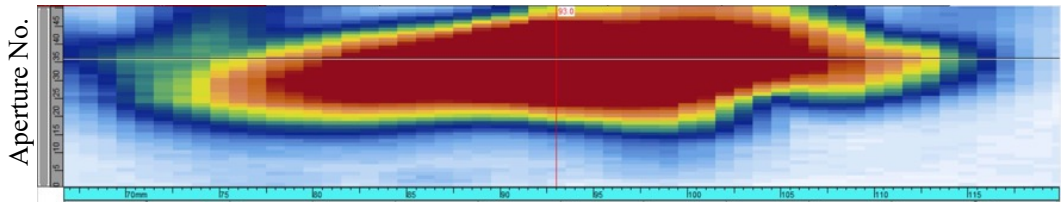

Figure 52: PAUT C-scan image of a LOF defect captured using an OLYMPUS Omniscan MX2 attached with a 5MHz 60 element linear array PipeWizard probe and 550 Rexolite wedge

Unlike a TOFD scan, the S-scan from a linear scanning PAUT setup can provide clarity in the identification of a LOF defect based on its location and its reflectivity. This defect can be characterised as a LOF due to its close proximity to the fusion face based upon the superimposed weld overlay within Figure 51. Further justification can be made based on the heavily saturated percentage screen height responses for most apertures along most of the length of the flaw as shown in Figure 52.

For a continuous defect such as a LOF defect, the length and through-thickness height can be measured using a 6 dB drop method. This method involves locating the most outer scan positions where the percentage amplitude of the defect does not drop below 6 dB or 50% of the maximum amplitude of the defect.

As PAUT is a reflectivity-based technique, there are limitations in the 6 dB drop method that hinder the complete certainty that the location of the amplitude drop is the edge of the defect. These limitations include:

- The true edges of a defect being orientated in such a way that the beam is not reflected back toward the probe, resulting in the true size of the defect being larger than measured
- the probe being unintentionally angled away from the desired scan direction as it moves through the scan length [80]
- the area of the defect at the edge may drop below the lower detection limit of half a wavelength [81]

3.7.2 Porosity

An example of the appearance of porosity in a TOFD scan is shown in Figure 53:

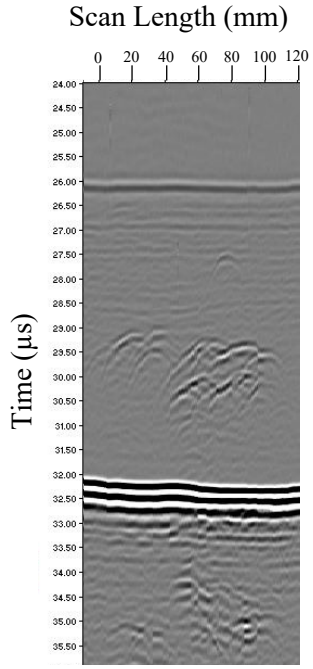

Figure 53: TOFD D-scan image of a clustered porosity defect using TUV Rheinland Sonovation with 10 MHz TOFD probes in 600 Rexolite wedges

The indications shown in Figure 53, can be characterised as a porosity type defect because the responses are act like point reflectors, with a lack distinction between the top tip and the bottom tip for each

individual indication. Without clear separation between the two tips, it is difficult to quantify any through-thickness height of the individual indications.

This particular porosity defect would most likely be characterised as clustered porosity based on the numerous point-like reflections occurring at multiple depths at the same scan position. Had the defect been uniformly distributed porosity, the individual point-like indications would have been scattered throughout the inspection volume. Similarly, had the defect been linear porosity, individual point-like indications would have been aligned at the same depth within the inspection volume, along the scan length.

For a PAUT inspection, the responses acquired within the S-scan and C-scan images for a porosity type defect are illustrated in Figure 54 and Figure 55:

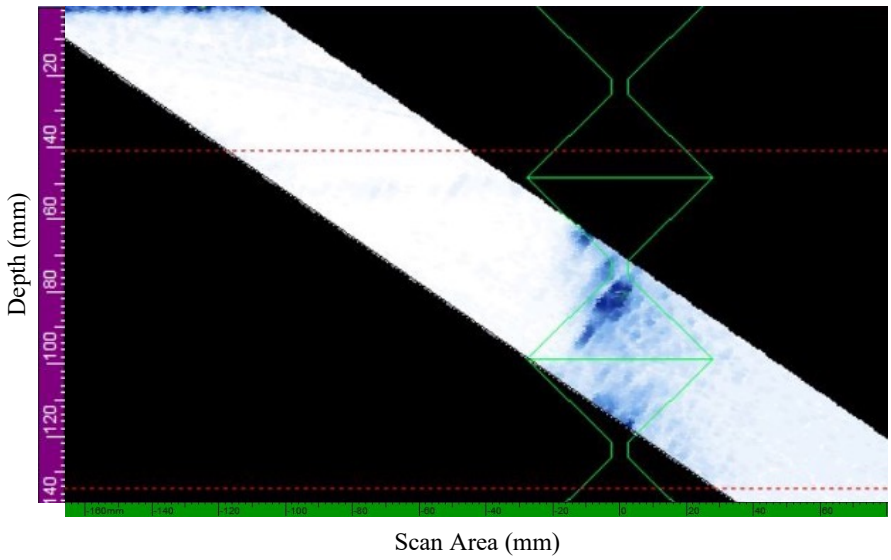

Figure 54:PAUT S-scan image of a clustered porosity defect captured using an OLYMPUS Omniscan MX2 attached with a 5MHz 60 element linear array PipeWizard probe and 550 Rexolite wedge

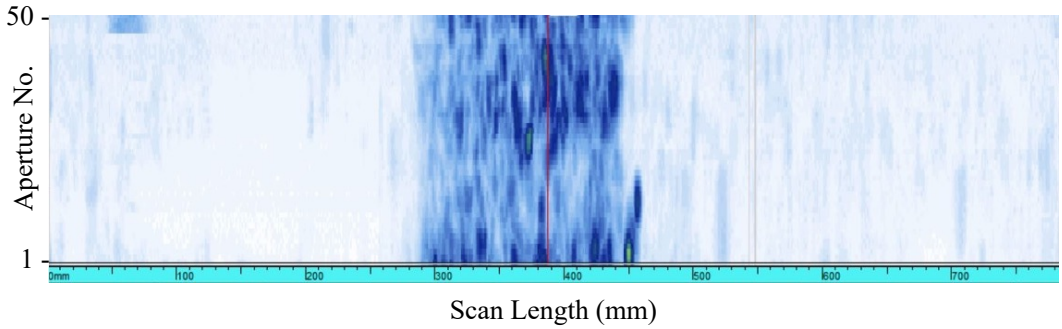

Figure 55: PAUT C-scan image of a clustered porosity defect captured using an OLYMPUS Omniscan MX2 attached with a 5MHz 60 element linear array PipeWizard probe and 550 Rexolite wedge

The point reflector nature of porosity visible in the TOFD inspection can also be seen within both the S-scan and C-scan images presented above. As previously mentioned, due to the pores being spherical, they scatter the ultrasonic beams omnidirectionally. As a result, the probe will detect a portion of the reflections from each of the pores. However, the magnitude of the response will be a low amplitude response by comparison to the responses from a LOF defect.

The defect shown in Figure 54 and Figure 55 is a clustered porosity defect. The hazy area within the S-scan represents many individual indications, at varying thickness positions, that have been detected along the scan length defined in the C-scan image. Similar to the TOFD scans, had there been a random assortment of indications, it would have been uniform porosity and had several pores been aligned, it would have been characterised as linear porosity. Another factor that causes the reduction in amplitude response of some pores is that due to the omnidirectional scattering pattern from the reflection of the pores, some ultrasonic energy is internally reflected between the pores and does not reach the probe.

Similar to the sizing method used for LOF defects, the length of the defect is based on a 6 dB drop in amplitude from a known maximum. However, unlike LOF defects that are continuous, the 6-dB drop is taken from the most outer local maximum amplitude response rather than the global maximum of the defect. In this case that would be the pore that produces the last most significant response.

3.7.3 Crack-like Defect

To illustrate how a crack-like defect can appear within a TOFD scan, Figure 56 shows the D-scan images captured for the same defect within a double-V butt weld. The three images represent scan data acquired for the centre of the probe pair setup being aligned to (a) the weld centreline, (b) 10 mm offset to the right of the weld, and (c) 10 mm offset to the left of the weld.

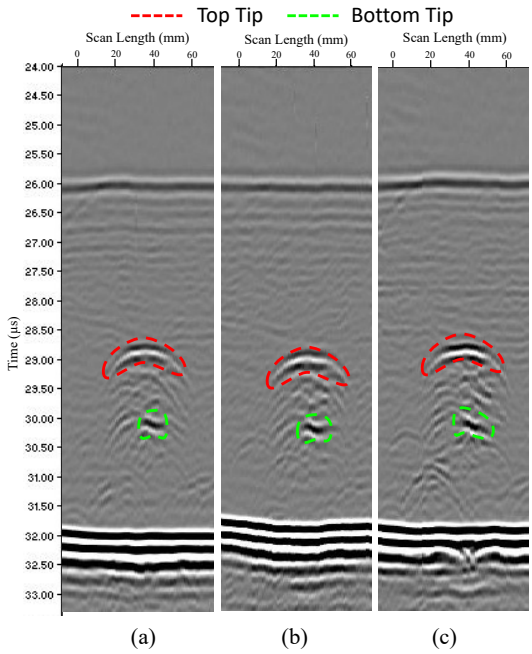

Figure 56: TOFD D-scan image of a crack-like defect (a) centreline (b) offset right (c) offset left using TUV Rheinland Sonovation with 10 MHz TOFD probes in 60° Rexolite wedges

From the indications shown above, a top tip and a bottom tip can be detected. Unlike the LOF defect, from Figure 33, where the tips are elongated and jagged along the full length of the defect, indicating a defect edge; this defect shows a single arc for both tips indicating single points of crack tip diffraction. More evidence to suggest that this defect is crack-like is the small indications in between the top and bottom tips, which suggest the jagged edges of branches of a crack. The process of identifying the phase change between the top and bottom tips, as applied for LOF defects, is applied in the same manner for cracks.

Despite TOFD's limitations in defining a defect's exact position within a weld, by acquiring multiple scans of a weld using different scan offset positions, the location of a defect relative to the centreline can be determined. In the case of the three scans of the crack-like defect shown in Figure 56, it can be determined that the crack is a centreline crack due to all three scans showing clear detection of the crack. Had the defect only appeared in two or only one of the three scans, the side of the weld on which it is located could be determined.

As an example, Figure 57 illustrates the D-scan images, acquired at the same probe scan positions as before, for a surface breaking crack at the remote surface of a welded structure:

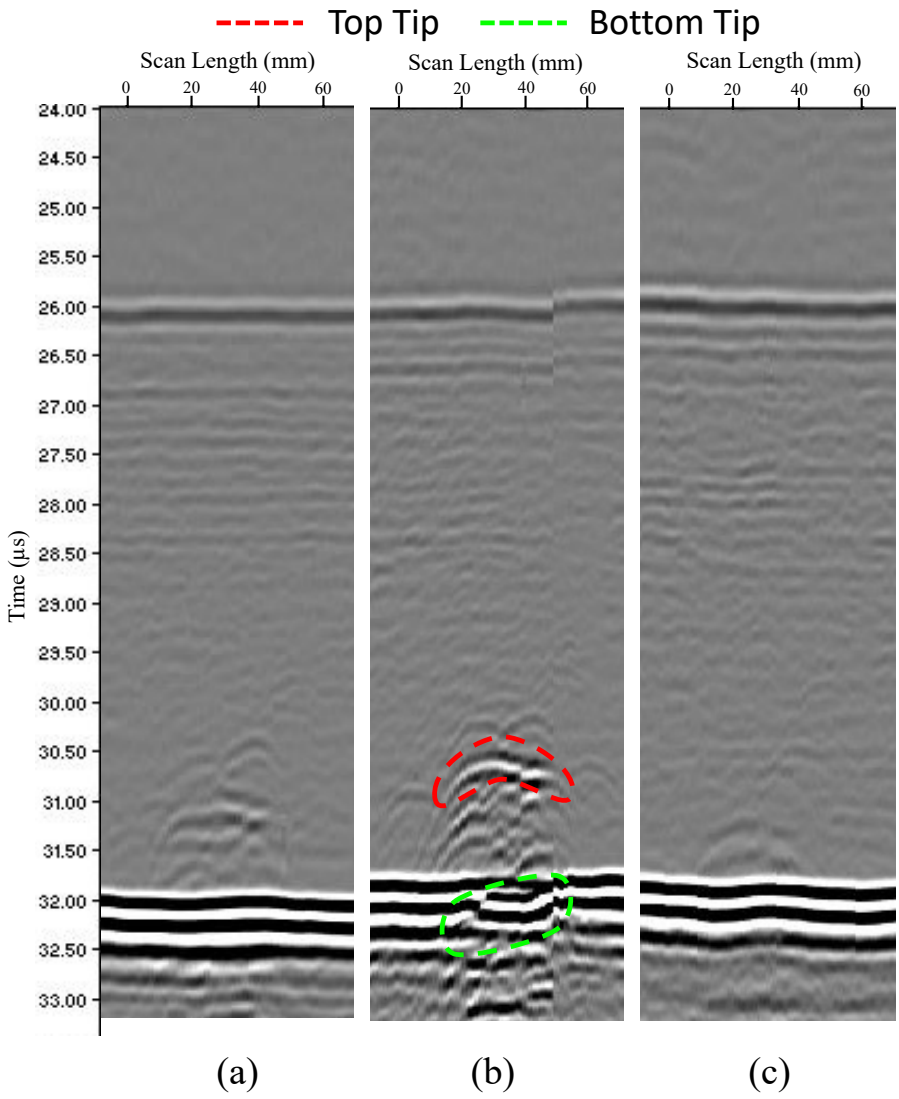

Figure 57: Locating crack position from TOFD D-scan images using (a) centreline (b) offset right and (c) offset left probe setup positions, using TUV Rheinland Sonovation with 10 MHz TOFD probes in 600 Rexolite wedges

From the three scan images shown above, it is clear to see that the defect is located to the right-hand side of the weld centreline based on the response within Figure 57 (b). The top tip can be identified prior to the backwall. The bottom tip is located within the backwall reflection and as a result it is difficult to pinpoint its exact position. However, it can be verified that it does exist, based on the clear ripple that can be seen within the backwall reflection caused by the diffraction of the

bottom tip. In addition, multiple potential branches/jagged edges can be assumed based on the numerous small indications that are detected between the two tips. By comparison, from Figure 57 (a) and (c), there is very little indication of a defect existing near the backwall of the welded structure.

Distinction between LOF defects and cracks using PAUT can be made based on a variety of factors such as; the location of the detected flaw, the amplitude response of the flaw, the geometry of the amplitude responses and when the flaw was first detected relative to manufacture/in-service events.

Based on Figure 45, a manufacture-related crack-like defect can be located anywhere within the weld volume or HAZ as a result of improper welding technique, poor post-weld treatment and shrinkage. As previously mentioned, during in-service, cracks will be most prominent in areas of high stress concentrations and weak fusion such as the weld toes and roots; whereas LOF defects are typically located on the fusion faces and in between the weld beads of adjacent weld passes.

PAUT amplitude responses depends on the size and orientation of the LOF or crack defect. Typically, with complete ultrasonic coverage of the volume with propagation from near perpendicular directions, LOF defects will have a significantly higher amplitude response. This is due to the likelihood that crack defects will have a more multifaceted structure reducing the possibility of normal incidence of the propagating wave front with the defect [82].

Depending on the size of the individual facets along the length of the crack relative to the inspection wavelength of the ultrasound, some of the incident ultrasound beams will be reflected back toward the probe better than others. This will result in the noticeable differences in amplitude response that can help characterise the defect as a crack [83].

Again, due to the uncertainty in the geometry of a crack, sizing it requires a similar approach to the methodology used for sizing a porosity type defect. Instead of locating the highest response from the outermost pore, the 6-dB drop is applied to the response of last most significant facet of the crack.

Due to the branched and faceted nature of a crack-like defect, as demonstrated in Figure 57, presenting and characterising one using a linear scanning PAUT requires imaging from multiple scan positions and perspectives. The S-scan and C-scan images shown within Figure 58, Figure 59, Figure 60 and Figure 61 illustrate the responses acquired at four steps of the inspection of a crack-like defect:

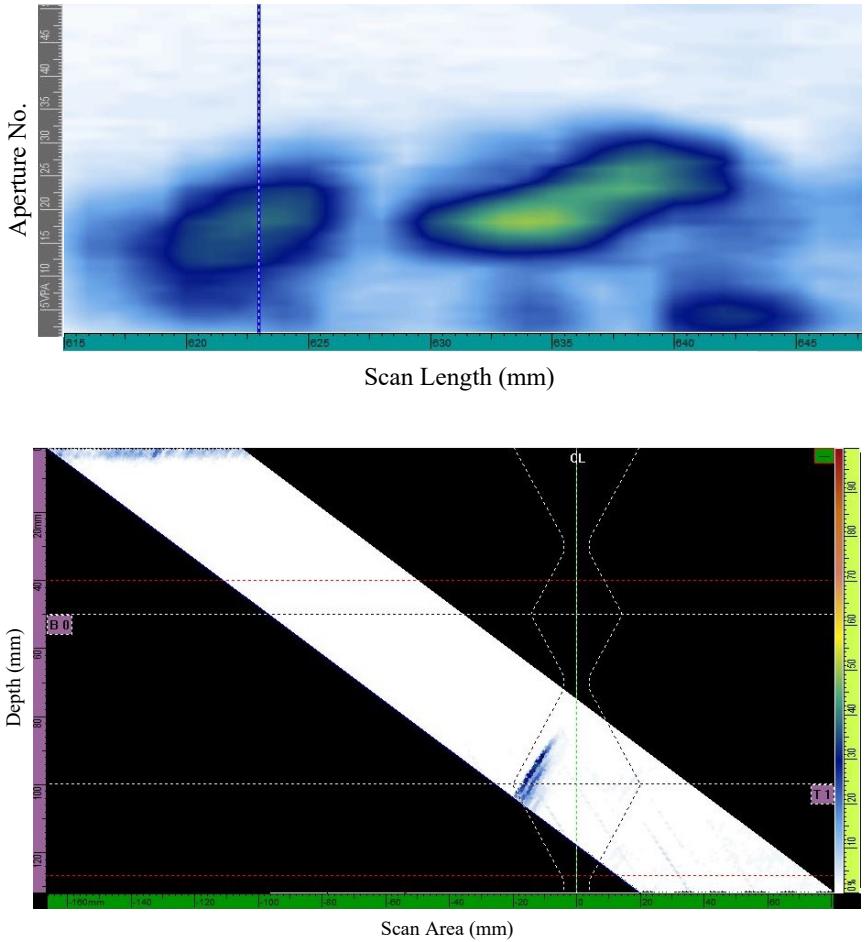

Figure 58: PAUT C-scan and S-scan images of crack-like defect at first position captured with an OLYMPUS Omniscan MX2 and a 5 MHz 60-element PipeWizard array with 55^0 rexolite wedge

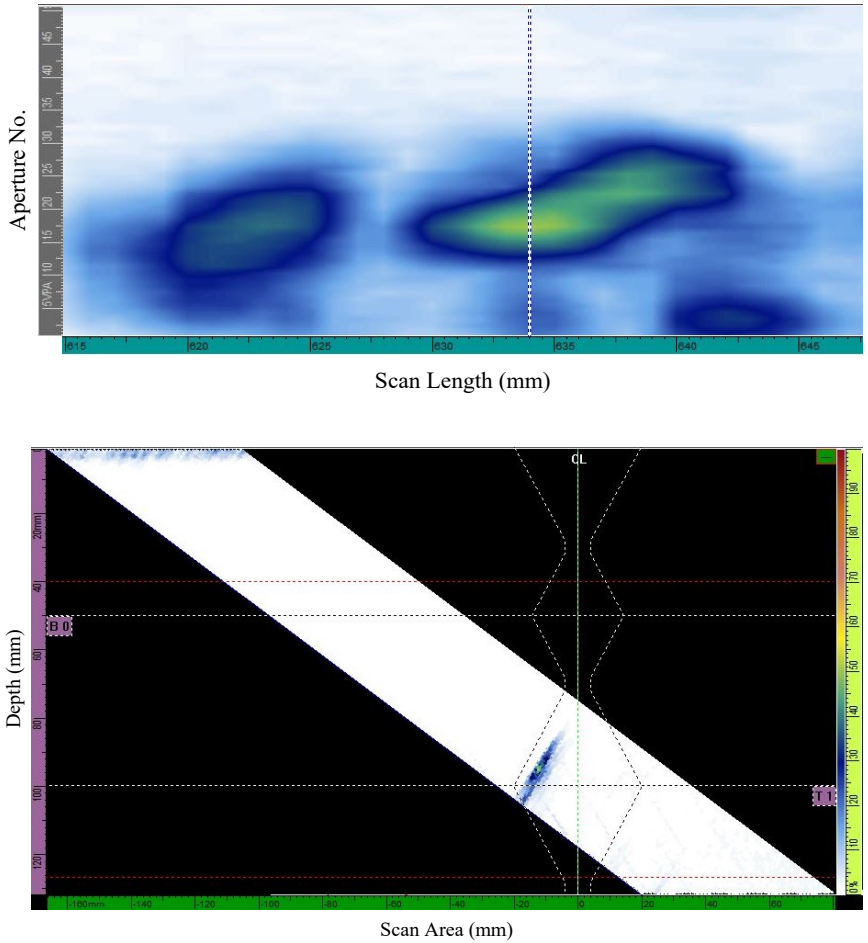

Figure 59: PAUT C-scan and S-scan images of crack-like defect at second position captured with an OLYMPUS Omniscan MX2 and a 5 MHz 60-element PipeWizard array with 55^0 rexolite wedge

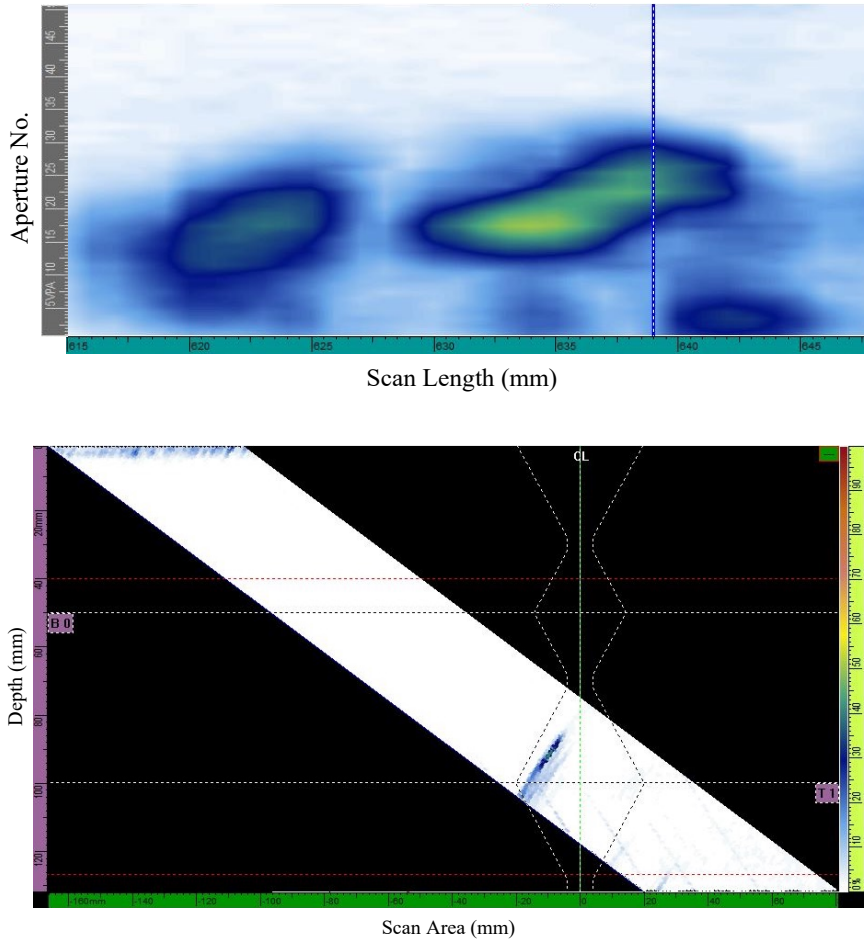

Figure 60: PAUT C-scan and S-scan images of crack-like defect at third position captured with an OLYMPUS Omniscan MX2 and a 5 MHz 60-element PipeWizard probe with 55^0 rexolite wedge

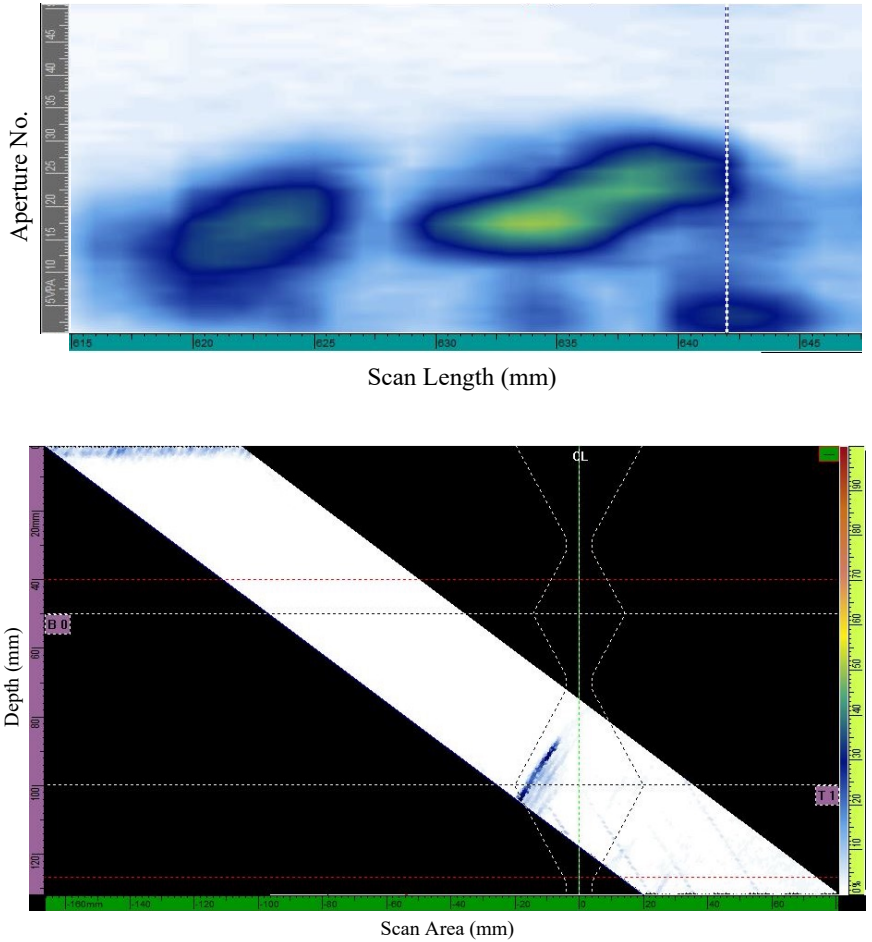

Figure 61: PAUT C-scan and S-scan images of crack-like defect at fourth position captured with an OLYMPUS Omniscan MX2 and a 5 MHz 60-element PipeWizard probe with 55^0 rexolite wedge

Progressing through each of the cursor locations highlighted in each of the C-scan images shown above, the corresponding S-scan images give improved definition to the change in structure of this particular indication. Due to the multi-faceted nature of a crack, different branches will have different surface areas and orientations. This results in the differences in amplitude response of the scan data, indicated by the colour variations. In this instance, the maximum response from this defect in 50% FSH, captured in Figure 59, which is significantly lower than the response from the LOF defect, as shown in Section 3.7.1. In a similar way to sizing a LOF defect, a crack-like defect can be sized using the 6dB drop method. The only difference is that due to the multi-faceted nature of the defect, the method is not applied relative to the highest global amplitude response of the defect, but relative to the highest outer local peak amplitude in each direction.

Despite the C-scan appearing to show several independent indications, the sentencing criteria from Section 3.4 would considers the three individual indictions as a single flaw, based on Figure 47. Therefore, the length of this defect would be sized as 28mm using the 6dB drop method from the highest amplitude response located at each end of the flaw.

Based on the TOFD inspection of this flaw alone, the indication would be considered as a surface-breaking crack and therefore rejected. This sentencing is reinforced by the locational findings within the S-scans. As previously mentioned, defects appear at this location due to it being at an area of high stress concentration. They can occur during the

manufacture stage or while in-service, potentially caused by elevated thermal stresses or through-life fatigue [72, 84].

Had the weld geometry been inspected solely by UT or PAUT techniques, the Defence Standards would require the weld geometry to be inspected using multiple angles, typically 45^0, 60^0, and 70^0. In this instance, only one inspection angle was used (60^0) due to PAUT supplementing the TOFD inspection. It is important to note that if the PAUT inspection data solely been considered, the detected flaw would have been accepted according to Table 4 due to its low amplitude response. However, had all inspection angles been implemented, the amplitude response of the defect on another inspection angle may have been more prominent.

This highlights the limitation faced by reflectivity-based inspection techniques, such as UT and PAUT, where multiple inspection angles are required to maximise detectability and reflectivity. Therefore, by not detecting and/or sizing a potential defect correctly could have severe consequences; demonstrating the importance of implementing multiple inspection techniques and /or setups.

4 CIVA Modelling, Validation & Calibration

Throughout various industries, modelling packages are becoming more prominent in being implemented to support NDT inspections. Included within that are platforms that are capable of modelling various ultrasonic inspection setups, such as the PAUT and TOFD techniques discussed in the previous chapter. This chapter will introduce the concept of ultrasonic weld inspection modelling, which will include a background into various simulation approaches and packages. This will be further supplemented with an evaluation of a selected platform to assist in the inspection requirements/standards discussed in the previous chapter.

4.1 Weld Inspection Modelling

The use of modelling tools has become increasingly more important to better understand how a system operates based on underlying theory and specified variable boundaries. The benefits of modelling can be summarized by:

"The benefit of mathematical modelling codes for modern NDT is well-known, as they are increasingly applied to simulate ultrasonic experiments in real-life inspection. They yield valuable information on the propagation of ultrasound and its interaction with defects and allow for visualization of sound fields and sensitivity zones of ultrasonic transducers." [85]

Diederichs' definition above emphasises the need for modelling tools to aid in the inspection of welds, especially for investigations into welds within complex geometry structures. Modelling has evolved over

time to better suit the needs of engineers to solve more complex problems.

Modelling began as a process of geometric calculations creating scale drawings and using ray tracing to represent the propagation of a wave between different points on a surface. Later, mathematical modelling began to be used where systems were approached using a process of mathematical reasoning and calculations. As more complex problems arose, this modelling technique required the processing power of computers to rapidly solve equations and calculations, which then opened the door to graphical representations, allowing both fundamental theories to be expressed visually and more complex problems to be solved [85].

Within ultrasonic inspection, modelling provides a range of advantageous capabilities:

- Based on fundamental theory, it can be used for educational/training purposes to provide visual representation of how ultrasonic waves may behave within a material.

- Re-creation of an inspection scenario based on the geometry of the system and the equipment used. This allows for a better understanding of how the system might react when repeated using different variable magnitudes and limits.

- Better operator preparation for carrying out an inspection regarding placement of equipment based on wave propagation.

This will help reduce inspection costs, minimise potential exposure to potential hazardous environments, and aid in the identification of inspection blind zones.

- Provision of approximated results comparable to the responses acquired from a real inspection as to predict what response should be achieved.

- Research and development of new probes and techniques to be applied in the inspection of welds for defects.

Presently, there are a variety of different modelling packages used within industry. Because of their versatility, modelling packages provide their users with tools that can be applied in a variety of different projects and investigations. Different software packages are specific to particular aspects of the weld inspection process. Some packages, such as Eclipse Scientific BeamTool (Ontario, Canada) have advanced ray-tracing capabilities to better visualise and improve the design of a weld inspection setup based on coverage mapping and beam computation [86].

Others, such as OnScale FEA (OnScale Inc., Atlanta, GA, USA), and Abaqus FEA (Dassault Systemes Simulia Corp., Providence, RI, USA) are Finite Element Analysis (FEA) packages that can be used to model the transduction process and detection of ultrasound by various modalities (piezoelectric, capacitive, magnetostrictive, laser). FEA implements a process of creating a range of matrix equations to represent the mass and stiffness effects of a component. The structure is

represented by a number of finite elements with an associated mathematical formula based upon the geometrical description of the structure. Each of these elements are interconnected by a polynomial curve or surface [87]. The modelling process investigates the interaction of these elements based upon a specified external influence, using the associated mathematical formulae for each node. Despite different FE software packages basing their simulation process on the same fundamental theory, in finding the solution to an identical problem, different FEA software packages follow different schema.

Comparing the approaches of the two stated FEA platforms, both primarily use structured meshes of quadrilateral elements for 2D models and hexahedral elements for 3D models. Similarly, both packages have the ability to use implicit and explicit differential equation solvers. Implicit solvers determine a solution by using the current system state and the system state at a later time, requiring the solver to consider how each node interacts with all other nodes at each timesteps [88]. Explicit solvers, by contrast, determine the unknown state of a system at a future time step through a function of the current known system state. The solver achieves this by disregarding the interactions between nodes, which simplifies the number of calculations related to the dynamics of wave propagation and optimises computation time [89].

Where these platforms differ is in the structured meshing process, as OnScale specifically adopts a Cartesian mesh. Being the simplest form of a structured mesh, the mesh is generated against a rectangular grid of points that align with a Cartesian coordinate system. By having a mesh that follows a repeated pattern, it simplifies the calculations

required and therefore minimises the computation time. For models with rounded or chamfered boundaries, a higher density mesh will be required to ensure accuracy, which will also increase computation time. By Abaqus FEA having a standard structured mesh approach, a more representative mesh can be made for models with complex boundaries/edges as the shape of the geometry can be followed more closely [90].

For this thesis, in collaboration with QinetiQ, the chosen modelling package is CIVA. CIVA is a semi-analytical NDT simulation suite developed by CEA-LIST: Laboratoire d'Intégration de Systèmes et des Technologies, the French Alternative Energies and Atomic Energy Commission. The Laboratory for Integration of Systems and Technology (LIST) research institute is one of CEA's three technological research divisions.

Semi-Analytical Modelling (SAM) is a methodology that compromises between the facile computation of ray tracing and the accuracy of FEM. Unlike FEM, where the entire system is recreated as a mesh of elements, SAM packages like CIVA only generate meshes around the transducer and included flaws within a component, computing within a specified sensitivity zone rather than the entire system. Where FEA will complete the analysis by discretising the entire component into a mesh of elements, CIVA generates ultrasonic rays based on the pencil method and models the interaction of the incident rays with the flaw using approximation algorithms such as Kirchhoff or Geometrical Theory of Diffraction (GTD) [91, 92]. The drive for using semi-analytical modelling is to acquire accurate quantitative

approximations for an inspection setup, that can be acquired using FEM, while reducing the potential computation time.

With a drive to provide analysis into the performance of inspections within an industrial context, the ultrasonic module of CIVA provides huge flexibility in the design of inspection setups to be simulated. Within the specimen builder, 2D and 3D structure geometries can be constructed from pre-built templates (e.g. basic plates, nozzles, tapers) or custom-designed using the in-built CAD environment. Specimens designed on external CAD packages can also be imported into CIVA.

The material parameters can also be modified to best replicate a specimen include density, wave velocities, whether it is homogeneous or heterogeneous, isotropic or anisotropic and/or comprises grain structure definition. The modelling platform also allows for a range of flaw types such as planar flaws, cylindrical flaws, spherical inclusions and notches. To inspect those flaws, an in-built library of probes and wedges from the major probe manufactures (OLYMPUS, GE and Phoenix) can be selected, or a custom probe and/or wedge design can be implemented. Factors related to the pulsed waveform, the pulsing sequence and the scan paths can also be specified. Within the simulation settings, the boundaries of the simulation can be set: the scan type (e.g. direct, half-skip, full-skip, etc), the flaw interaction algorithms, sensitivity zones, and calibration settings. Defining these boundary settings allows for certain assumptions to be made within the simulation and for unrelated aspects of the structure to be ignored resulting in faster computation times.

4.2 CIVA Simulation Process

The computation of a CIVA simulation is broken down into two stages: beam computation and application of defect approximation algorithms. The beam computation process within CIVA applies the pencil method, which is used to predict the elastodynamic fields in anisotropic, heterogeneous and complex geometry structures from element sources [93].

A pencil can be described as a cone of the elementary rays diverging from a point source located on the surface of a transducer [94]. A pencil propagation matrix is used to approximate the wave front curvature along the axial ray path while accounting for the beam divergence, transmission/reflection coefficients at boundaries, attenuation, time of flight and wave polarization [95]. A pencil is calculated between the point source located on the transducer surface and an observation point specified within the specimen structure. An example of a pencil and its evolution across multiple boundaries can be seen in Figure 62:

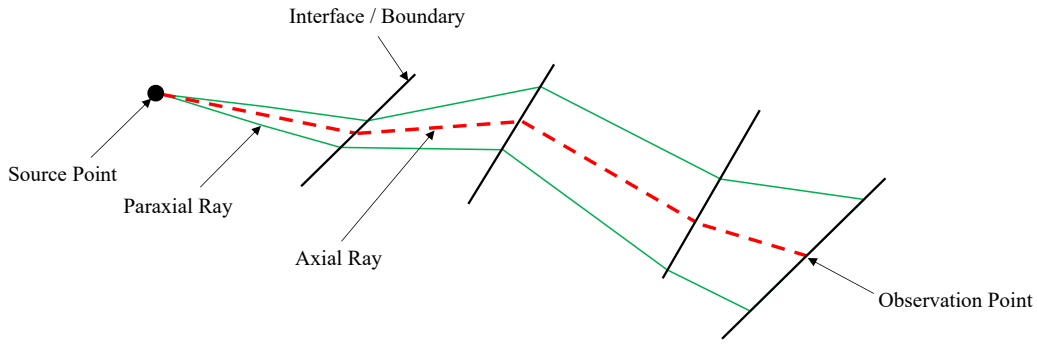

Figure 62: Schematic diagram of a pencil as utilised in CIVA [96]

To visualise the application of a single pencil within a specimen, Figure 63 illustrates the divergence of a single pencil from a point source located in the centre of a single element, wedge-mounted probe that would be used to calculate the field at a specific point within a structure (marked by the black spot):

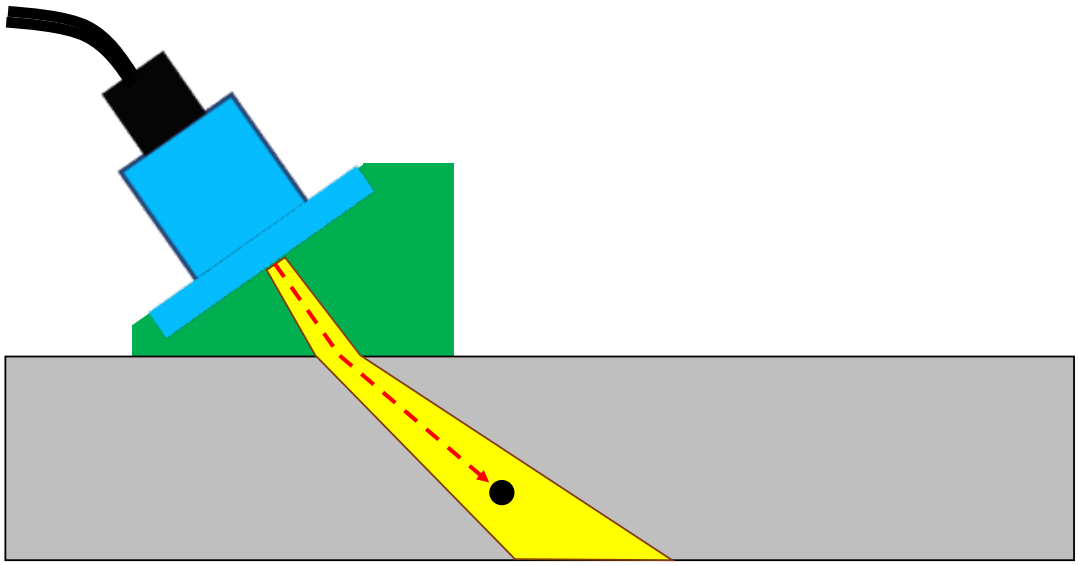

Figure 63: Schematic diagram of the pencil method for a single pencil

The field at a specific computation location is calculated through the summation of the contributions from a discretised series of source points across the face of the transducer [95, 97]. For the probe setup used in Figure 63, Figure 64 shows the contributions from three-point sources that would make contributions toward the calculation of the field at the specified coordinate marked by the black spot based on the divergence of their individual pencils:

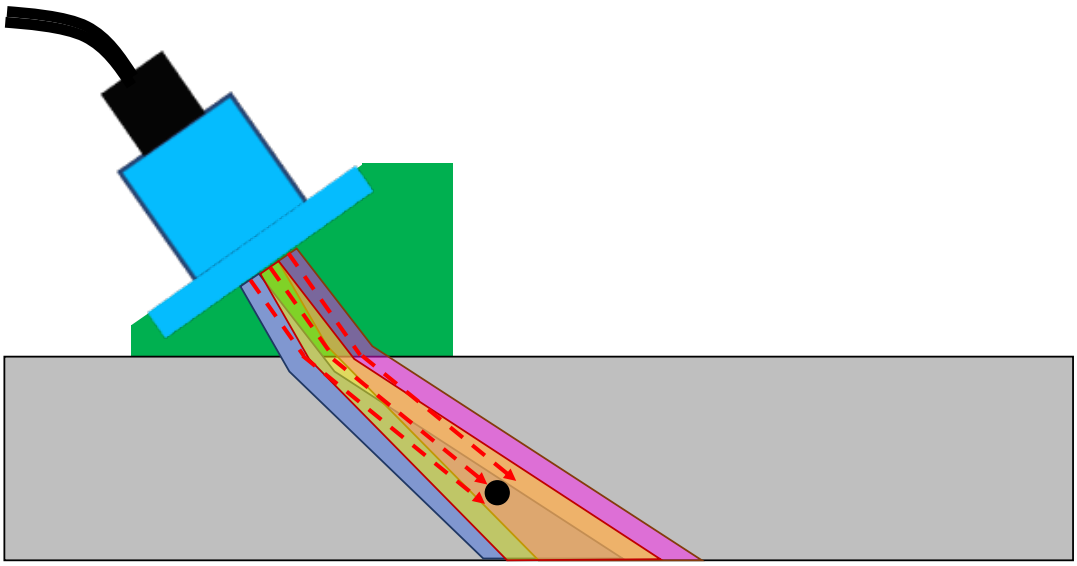

Figure 64: Schematic diagram of pencil method for multiple pencils

The contributions of each individual point source at the specified coordinate are summed to acquire the impulse response that is then convoluted with the input signal of the transducer in the frequency domain. This allows the amplitude and TOF to be acquired from the resulting displacement signal [96].

This process is repeated, and the amplitude and TOF for all coordinates within the ultrasonic field of the transducer are calculated. For each coordinate, its generated amplitude response is based on an internal quantity known as a CIVA Reference Amplitude (CRA). Despite CIVA's manual providing information on the underlying theory to how it simulates beam computation and its defect interaction algorithms, a 'black box' approach is adopted to protect the exact calculations it uses. Therefore, it is unknown how the magnitude of this property is determined based on the input settings to the simulation. Despite this 'black box' approach, the outcomes of the work being

presented are adaptable to any future changes that may be made by the manufacturer.

Once the approximated wave front at the location of flaw has been calculated, a defect approximation algorithm can be applied to determine the scattering of the wave by the flaw [98]. The default algorithm to be applied is dependent on the flaw type and the inspection technique specified within the simulation setup. Algorithms have been pre-selected by CIVA to produce the most accurate representation of a flaw's response and scattering profile.

For some defect types, alternate approximation algorithms can be implemented, however all simulated flaw types investigated within this thesis will use the default option. Three of the approximation algorithms implemented by CIVA and used within this thesis are the Kirchhoff Approximation (KA), GTD and Separation of Variables (SOV).

To give a general overview of the approximation algorithms, KA is commonly used algorithm within NDT modelling [99]. Its approach models the echoes due to specular reflections from planar flaws and crack-like defects [100]. These defects can be generated as rectangular or CAD generated multi-faceted defects within CIVA. The algorithm predicts how the incident wave interacts with a flaw by representing the incident surface as a discretized mesh of facets [101]. On the insonified side of the flaw, it can be assumed that each elementary surface can be considered as an infinite tangent plane to the surface where the total displacement is the sum of the incident and reflected waves [102]. On the reverse surface of the flaw, the field is assumed to be zero [103, 104].

At any location, preferably as close to the incident wave path as possible, the scattered wave can be quantified by the integral of a Green's function and total displacement product [99, 101, 102]. This process is repeated for all discrete elements of the flaw. Experimental validation has shown that the approach is most accurate when the height of the flaw is greater than the wavelength of the inspection wavefront [105]. Additionally, studies of the algorithm have shown that it is increasingly more accurate at normal incidence between the wavefront and flaw [99].

Consequently, the KA approach is not a suitable algorithm to implement for a SDH defect. The rounded nature of the geometry reduces the available surface area that is normal to the incidence wave. Therefore, the ratio of the incident wavelength to the defect becomes unfavourable for KA. Furthermore, to predict the amplitude response from a cavity-type defect, like SDHs, another wave type that has significant influence has to be considered. Creeping waves propagate around the surface circumference of SDHs, but KA only predicts the response from specular reflections on the insonified portion of the defect surface. A more suitable approximation algorithm that accounts for the creeping wave around SDHs is SOV.

SOV overcomes limitations faced by the KA approach in approximating the amplitude responses from cylindrical cavities [92]. It is an analytical modelling approach that implements series functions to represent the scattered waves. Terms within the series are expressed as products of complex exponential functions and Hankel functions. Coefficients within these series can be quantified based on the boundary conditions at the surface of the flaw. The echo at an observation point,

relative to the centre of the flaw, can be calculated by applying Huygens' principle of spherical wavefronts from point sources [106] to replace the scattered cylindrical waves of the Hankel functions [100].

When simulating the ultrasonic field and its interactions with flaws, CIVA can perform its computations in 2D or 3D. 2D computation simulates the beam and its interations with flaws within a chosen inspection plane that represents a slice of the volume being inspected at a given inspection location. the transducer will be approximated as a 2D extrusion and the flaw interaction will solely be evaluated along the intersection line of the inspection plane and the flaw surface. This type of computation is suitable for simple symmetric planar flaw geometry inspections. For more complex inspection simulations including non-symmetric defects, 3D computation is required.

3D computation simulates the beam and its interations with flaws within the entire volume beneath the probe at a given inspection location. Flaw interactions are evaluated across the entire surface of the flaw that intersects with the propagating wavefront line and not just a line.

Overall, 3D computation is the preferred option as it produces a more accurate simulation of the beam propagation and interaction with flaws. Consequently, 3D simulations require longer computation times so 2D computations are recommended for initial validation.

4.3 CIVA Simulation Analysis

Once an inspection simulation setup has been configured, it can be saved and initiated. The simulation can be run directly within the model setup or can be included as part of a batch of simulation setups that will be processed sequentially. Running in batch mode is particularly useful as it allows for continued use of the CIVA platform while other simulations are running in the background. Alternatively, CIVA can perform parametric studies. These allow for a range of simulations to be run with a selected parameter being varied through a stepped range of magnitudes. This function has huge potential when varying flaw angle, tilt and orientation to acquire the flaw positioning that best replicates the response amplitudes and defect sizing of a physical inspection.

To demonstrate how the inspection setup simulation data is generated, Figure 65 presents the CIVA Graphical User Interface (GUI) of a linear scanning PAUT inspection simulation setup. The scan direction of the probe is perpendicular to the horizontal component of the wave propagation direction (x-axis). The instrumentation setup, above, incorporates a 60 element 5 MHz OLYMPUS PipeWizard probe (5L60-PWZ1) mounted on an OLYMPUS PipeWizard wedge (SPWZ1-N55S-IHC-RevC). The pulsing sequence was setup to generate 50 VPAs of 11 elements with a refraction angle of 60^0. The inspection refraction angle of 60^0 was chosen to ensure conformability with the Defence Standard requirements mentioned in Section 3.3. The specimen is a 60 mm thick carbon steel specimen with two 6 mm through-thickness rectangular flaws (representing a LOF-type defects). Both flaws are angled at 30^0 from the vertical and the centre of each is positioned 50

mm from the top surface. With the sole purpose of this simulation being to demonstrate how CIVA simulated data is generated and outputted, a 2D computation is implemented with no attenuation properties.

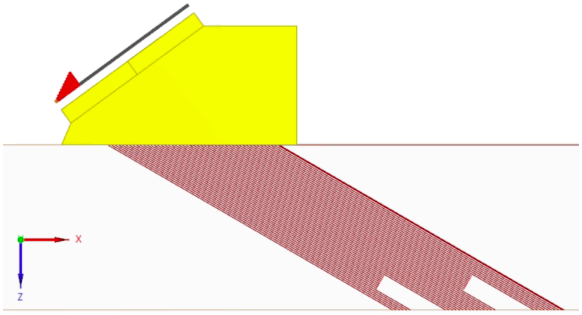

Figure 65: Schematic of linear scanning PAUT inspection setup in CIVA

On completion of an inspection simulation, the results are displayed within a data analysis page showing various scan views including A-scans, C-scans and variations of S-scan (depending on the inspection type). Figure 66 presents the data analysis page of the simulated results showing a selection of scan displays, primarily C-scan and S-scan:

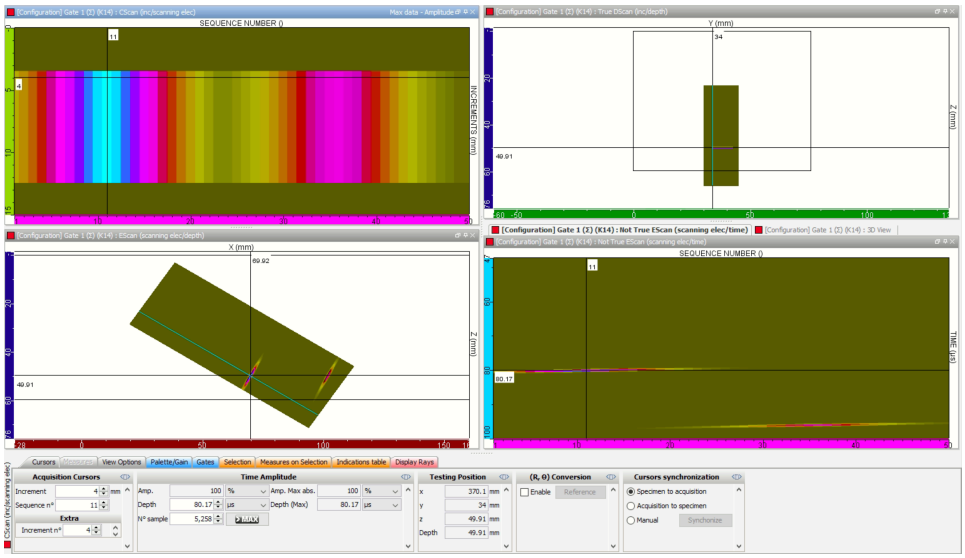

Figure 66: CIVA simulation data analysis display

As previously noted, the data analysis tab above relates to the linear scanning PAUT inspection simulation of the two rectangular (LOF-type) defects. In this instance, the top left scan display is a C-scan of the simulation, the top right display is a D-scan, the bottom left display is a S-scan, and the bottom right is an S-scan orientated vertically. The data analysis tab is not limited to presenting its results using these scan views. A variety of other display options are available such as A-scan and importing multiple scan views into a 3D model.

Within the different views, cursors can be positioned to acquire the data response amplitudes at specific scan coordinates. When the cursors on one scan view are adjusted, the displayed data and cursor positions on other scan views will automatically update. The data can also be exported to a text file for analysis using alternative software platforms.

As previously mentioned, the percentage amplitude response of all the scan data coordinates is set in reference to the co-ordinate with the largest CRA, which is given a 100% FSH response (see Section 0). Adjusting the cursors within the C-scan of Figure 66 to locate the highest amplitude response (light blue/turquoise in colour on the S-scan) and maximising the S-scan image to full screen, the data analysis page will display as shown in Figure 67:

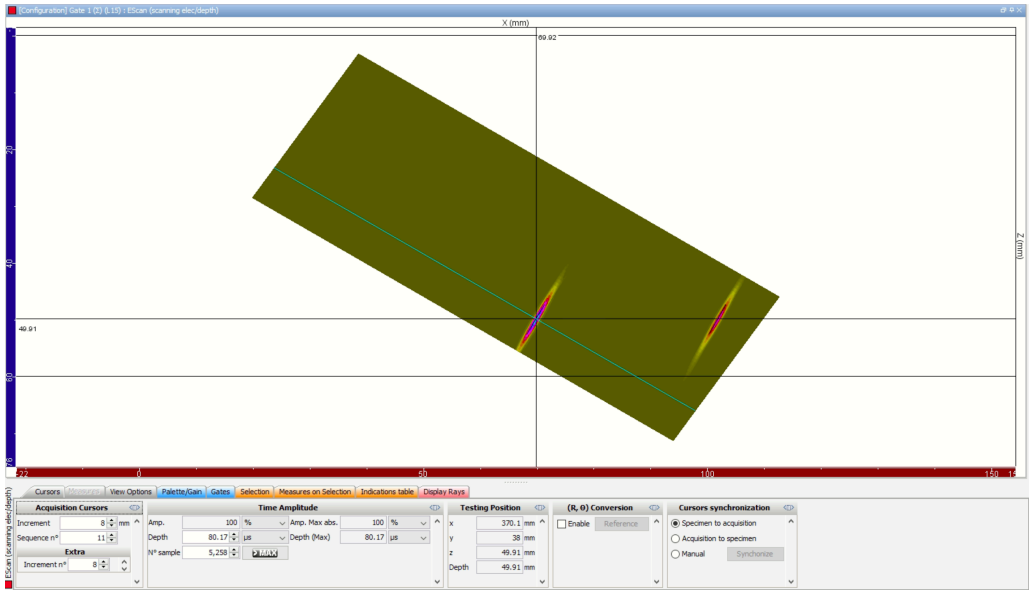

Figure 67: CIVA simulated S-scan of two LOF-type flaws

Depending on the PAC equipment used, S-scan displays can have repeating mirrored outlines of the weld geometry with each backwall reflection. CIVA has the capability of reflecting the responses to remain within the boundaries of the structure being inspected. By doing this, the user can better visualise the location of responses.

In addition to the various views and cursor manipulation to analyse the simulated responses, CIVA has the additional functionality of allowing the user to calibrate the simulated setup. The calibration methodology to be used is dependent on the type of inspection setup used, as discussed in Section 3.6. CIVA also has its own basic calibration methodology that calibrates all amplitude responses relative to a specific CRA amplitude. In addition to this approach, standard calibration techniques, such as DAC and TCG, are available for conventional UT and PAUT inspection setups.

4.4 CIVA Simuation Validation

To verify that the relative amplitude responses for identical defects at multiple depths in an experimental setup can be replicated by CIVA, a custom carbon steel validation block containing multiple SDH and FBH reflectors was manufactured. This process involves quantifying the attenuation coefficients of the probe wedge (Rexolite) and the carbon steel to incorporate as part of the CIVA simulation. Repeating the same process for SDH and FBH reflectors ensures that CIVA can effectively replicate the conditions of different defects being approximated using different approximation algorithms. As previously discussed in Section 4.2, the preferred approximation algorithms were selected for each defect type: SOV for SDH reflectors and KA/GTD for FBH reflectors.

4.4.1 Carbon-Steel Validation Test Specimen

A schematic of a custom-built carbon-steel block with SDH and FBH reflectors is shown in Figure 68:

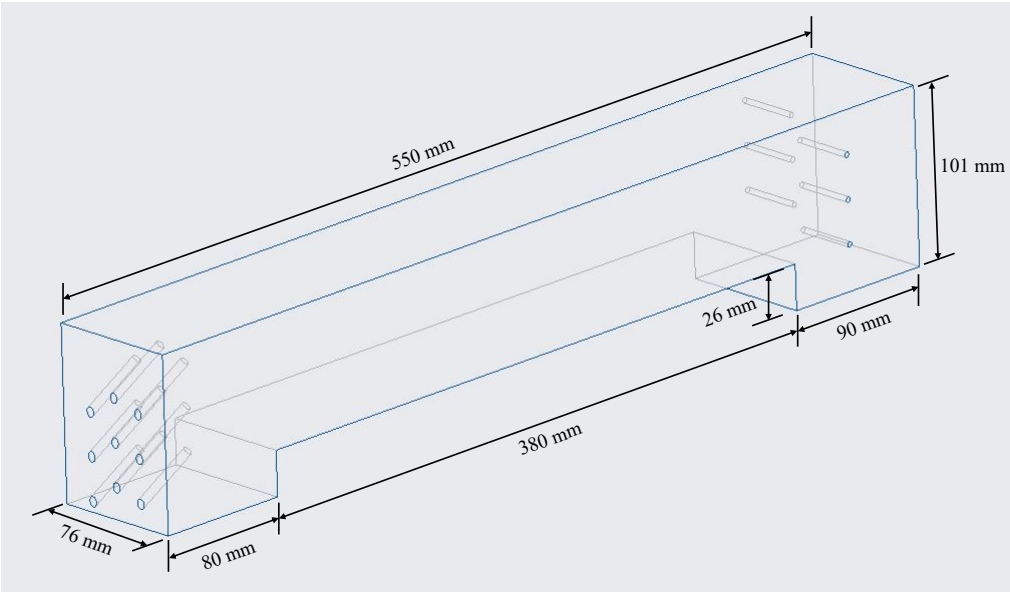

Figure 68: Schematic diagram of a custom-built carbon-steel block

The primary dimensions of the block are 550 mm length, 101 mm height and 76 mm wide. Prior to any SDH/FBH reflectors being drilled, a rectangular cut-out from the remote surface was made on the centre section of the block to a depth of 26 mm. As the material is carbon steel, the longitudinal and transverse wave velocities can be approximated to be 5900ms^{-1} and 3240ms^{-1} [1, 107]. These approximated values were further checked and verified against backwall and SDH echoes appearing at the correct depths.

On the right-hand side of the block, as illustrated in the schematic shown in Figure 68, six 3 mm diameter SDHs were drilled to half the width of the block, with three on each side. The depths of the SDHs were at 12.5 mm intervals starting at 12.5 mm from the top surface to 75 mm from the top surface.

On the left-hand end of the block, nine 5 mm diameter FBHs were drilled into the side of the block at an angle toward the top surface such that the bottom of each hole is at 30^0 from the vertical. These were manufactured by using a standard drill bit to drill holes to the respective measured depths, before a specialised flat-bottomed drill bit was used to create the flat bottom finish. This angle was chosen to create normal incidence when inspected by a 60^0 refraction angle PAUT setup that complies with Defence Standard requirements [52]. Coincidently, this also improves the efficacy of the Kirchhoff approximation when predicting the amplitude responses of FBHs, as mentioned in Section 4.2.

The nine FBHs are grouped into three columns of three, with the depths between each vertically adjacent FBH being 25 mm. This interval was chosen to ensure that each FBH would have a distinct response that would not interfere with responses from other FBHs when examined. The depths of the shallowest three FBHs of each column are 12.5, 17.5 and 25 mm. Table 5 presents a comprehensive list of all possible SDH and FBH depths that can be achieved, depending on whether a half-skip or full-skip setup is being implemented to inspect the SDHs and FBHs:

Table 5: Custom-built carbon-steel block reflector depth list

	SDH depths (mm)	FBH depths (mm)
Half-skip	12.5, 25, 37.5, 50, 62.5 & 75	12.5, 17.5, 25, 37.5, 42.5, 50, 62.5, 67.5, 75
Full-skip	87.5*, 100*, 112.5, 125, 137.5 & 150	87.5*, 92.5*, 100*, 112.5, 117.5, 125, 137.5, 142.5, 150

The motivation behind the design and construction of the block was that off-the-shelf calibration blocks and test samples do not provide the same quantity of angled reflectors at the preferred surface area and depths. By having the cut-out step, makes possible the SDH and FBH depths marked by an asterisk (*) in Table 5. Without the step, the jump in reflector depth from the half-skip to the full-skip would have been 75 mm to 112.5 mm for both the SDHs and FBHs. As a result, the six SDH depths of the block can create up to twelve appropriately spaced TCG points by scanning both the top and bottom surfaces, from both half-skip and full-skip approaches. Moreover, 18 FBH depths can be investigated

with twelve of the FBHs at a corresponding SDH depths in the block and a further six FBHs at depths intermediate to those SDH depths.

4.4.2 Rexolite/Steel Attenuation Experimentation

Using the same instrumentation and pulsing setup from Section 4.3, the custom carbon steel block was scanned to capture the amplitude responses from SDHs at depths 50, 75, and 100mm. Replicating the same pulsing sequence of 50 VPAs of 11 elements with a refraction angle of 60^0, responses from the three SDH depths could be achieved by scanning the block in the following manner:

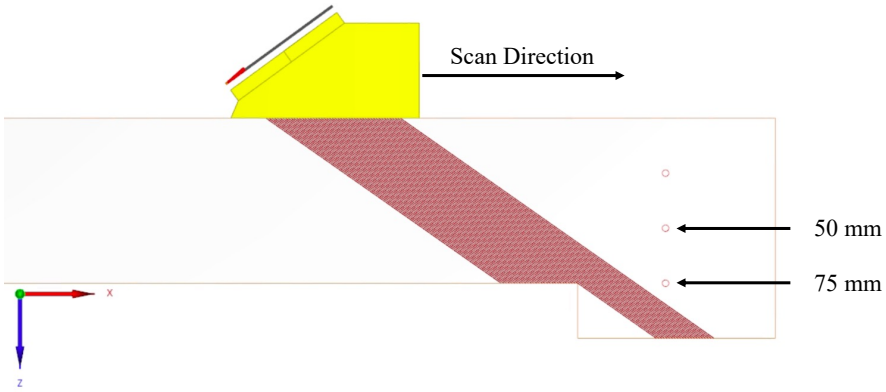

Figure 69: Schematic of experimental setup on the validation block performing a direct scan of two SDHs at depths of 50 and 75 mm depths

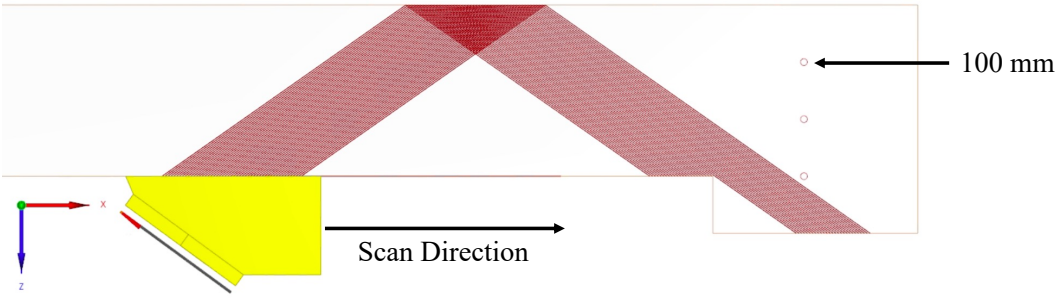

Figure 70: Schematic of experimental setup on the validation block performing a half-skip scan of a SDH at depth of 100 mm

Figure 69 and Figure 70 present the scan setups implemented experimentally to capture responses across all apertures for SDHs at depths of 50, 75 and 100 mm. This was achieved by performing two scan setups. This first scan acquires the responses for the 50 and 75 mm SDH depths directly. The second scan implements a half-skip on to the SDH at a 25 mm depth (from the top surface) to replicate an equivalent direct scan of an SDH at a 100 mm depth.

When capturing the data for these three SDHs, the overall system gain of the Omniscan MX2 instrumentation used was adjusted such that the response from the shallowest SDH (50 mm) on the first aperture was set to 100% screen height. Table 6 presents the percentage amplitude responses at the three SDH depths for given aperture numbers between 1 and 50:

Table 6: Experimental percentage amplitude response data for given aperture numbers captured using Omniscan MX2 of SDHs at 50, 75 and 100 mm depths

Experimental - Amplitude Response (%)							
		Aperture					
		1	10	20	30	40	50
Depth (mm)	50	99.81	78.63	60.36	45.76	33.63	28.06
	75	39.1	31.63	25.4	17.6	14.36	11.4
	100	16	12.1	10.4	8.2	6.3	5.2

Within each aperture column, there is a decrease in amplitude response which can be associated with the increasing impact of attenuation linked with increasing sound path within the carbon steel. Similarly, across each SDH depth row, there is a decrease in amplitude reponse linked with the increasing impact of attenuation linked with increasing sound path within the Rexolite wedge.

Calculating the attenuation coefficients of the steel and Rexolite can be achieved by quantifing the differences in decibel response between SDH depths and aperture numbers relative to sound path lengths through the respective materials.

Regardless of what aperture scans the three SDHs at 50, 75 and 100 mm, the sole reason for the difference in amplitude response between them is the additional distance travelled by the sound within the steel. This can be established due to the portion of the sound path within the Rexolite wedge remaining constant when comparing responses on the same aperture. This is based on the assumption that the three SDHs are identical and will reflect ultrasound in the exact same manner. To calculate the difference in decibel response, the following equation can be implemented [17], where A_1 is the amplitude response from the first reflector, A_2 is the amplitude response of the second reflector A, and ΔI is the change in sound intensity:

$$\Delta I = 10 \cdot log \frac{{A_2}^2}{{A_1}^2} = 20 \cdot log \frac{A_2}{A_1} \tag{4.1}$$

Based on the data presented in Table 6, Table 7 presents the difference in decibel response, calculated using Equation 4.1, for each SDH depth relative to the amplitude response acquired from the shallowest SDH on that given aperture:

Table 7: Calculated experimental decibel differences in amplitude response data for SDH depth relative to the amplitude acquired on the shallowest SDH for that given aperture

Experimental - Normalised Amplitude Response (dB)							
		Aperture No.					
		1	10	20	30	40	50
Depth (mm)	50	0	0	0	0	0	0
	75	-8.139946	-7.9097817	-7.5183103	-8.299467	-7.3914485	-7.8236563
	100	-15.901081	-16.256058	-15.274318	-14.933443	-14.547726	-14.641686

The attenuation coefficient for steel can be approximated by quantifying these decibel reductions with respect to the additional sound path distance covered within the steel relative to the sound path of the shallowest SDH depth. Between the 50 and 75 mm depth SDHs, the additional sound path is 100 mm, while the difference in distance between the 50 and 100 mm SDH depths is 200 mm. Accounting for these sound path length differences, Table 8 presents the calculated attenuation coefficients for steel based on experimental data captured:

Table 8: Calculated experimental attenuation coefficients for steel based on the decibel reduction experienced with respect to additional sound path distance covered

Experimental - Attenuation Coefficient (dB/mm)							
		Aperture No.					
		1	10	20	30	40	50
Depth (mm)	50	0	0	0	0	0	0
	75	0.08139946	0.07909782	0.0751831	0.08299467	0.07391449	0.07823656
	100	0.07950541	0.08128029	0.07637159	0.07466722	0.07273863	0.07320843

Averaging the calculated values across all apertures for SDH depths 75 and 100 mm generates an attenuation coefficient of 0.077 dB/mm.

A similar process can be repeated to determine the attenuation coefficient of Rexolite by analysing the difference in amplitude response between apertures for the same SDH depth. Table 9 presents the difference in decibel response, calculated using Equation 4.1, for each aperture relative to the amplitude response acquired on the first aperture at a given SDH depth:

Table 9: Calculated experimental decibel differences in amplitude response data for increasing aperture number relative to the amplitude acquired on the first aperture for a given SDH depth

Experimental - Normalised Amplitude Response (dB)							
		Aperture No.					
		1	10	20	30	40	50
Depth (mm)	50	0	-2.0717156	-4.3684965	-6.7737608	-9.4489438	-11.021728
	75	0	-1.8415513	-3.7468608	-6.9332818	-8.7004463	-10.705438
	100	0	-2.4266922	-3.7417329	-5.8061226	-8.0955887	-9.7623328

The attenuation coefficient for Rexolite can be approximated by quantifying these decibel reduction relative to the additional sound path distance covered within the Rexolite relative to the sound path of the first aperture. The additional sound paths travelled between apertures are:

- Between apertures 1 and 10, the additional sound path is 13.6 mm.
- Between apertures 1 and 20, the additional sound path is 28.6 mm.
- Between apertures 1 and 30, the additional sound path is 43.6 mm.
- Between apertures 1 and 40, the additional sound path is 58.8 mm.
- Between apertures 1 and 50, the additional sound path is 73.8 mm.

Accounting for these sound path length differences, Table 28 presents the calculated attenuation coefficients for Rexolite based on experimental data captured:

Table 10: Calculated experimental attenuation coefficients for Rexolite based on the decibel reduction experienced with respect to additional sound path distance covered

Experimental - Attenuation Coefficient (dB/mm)							
		Aperture No.					
		1	10	20	30	40	50
Depth (mm)	50	0	0.15233203	0.15274463	0.15536149	0.16069632	0.1493459
	75	0	0.13540818	0.13100912	0.15902022	0.14796677	0.14506014
	100	0	0.17843325	0.13082982	0.13316795	0.13768008	0.13228093

Averaging the calculated values between apertures 10 and 50 for all SDH depths generates an attenuation coefficient of 0.15 dB/mm. The measured values of attenuation for steel and Rexolite both present similarity to the expected attenuation values 0.07 dB/mm and 0.2 dB/mm for 5 MHz propagation [43].

4.4.3 CIVA Simulation vs. Experimental - SDH

To replicate the experimental data capture performed in Section 4.4.2 for the 50, 75 and 100 mm SDH reflectors within CIVA, Figure 71 presents a schematic of the same phased probe/wedge combination performing a direct scan of the three SDHs.

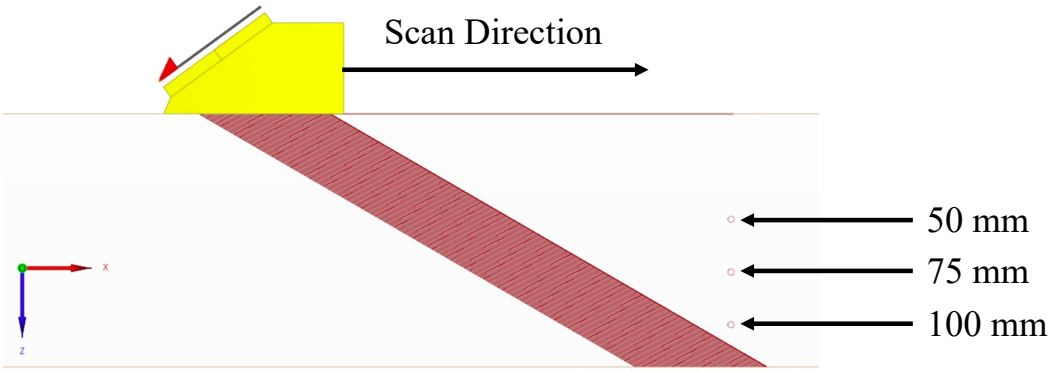

Figure 71: Schematic of CIVA simulation setup performing a direct scan of three SDHs at depths of 50, 75 and 100 mm depths

The simulation setup was executed using the same pulsing parameters and optimised to collect all of the necessary data within a single model execution. Simulation settings included the calculated attenuation coefficients of 0.077 and 0.15 dB/mm incorporated for steel and Rexolite, the negation of backwall reflections to reduce the need for unwanted calculations, and running 3D computation for accurate comparison against experimental values. As mentioned, the approximation algorithm used to simulate the beam interaction with the SDH reflector was SOV. Table 11 presents the CIVA simulated percentage amplitude responses at the three SDH depths for each of the given aperture numbers between 1 and 50:

Table 11: SDH percentage amplitude response data for given aperture numbers from CIVA simulation (with attenuation) of experimental Omniscan MX2 setup

3D Simulation / Steel Att (0.077 dB/mm) + Wedge Att (0.15 dB/mm)							
% Response		Aperture					
		1	10	20	30	40	50
Depth (mm)	50	100	75.54	57.14	42.06	31.42	19.87
	75	25.35	19.46	15.09	10.82	8.13	5.24
	100	7.31	5.64	4.29	3.15	2.39	1.53

Figure 72 presents a comparison of the CIVA amplitude response approximations, while implementing the experimental attenuation coefficients in the simulation, on each aperture at each SDH depth against the experimentally acquired data:

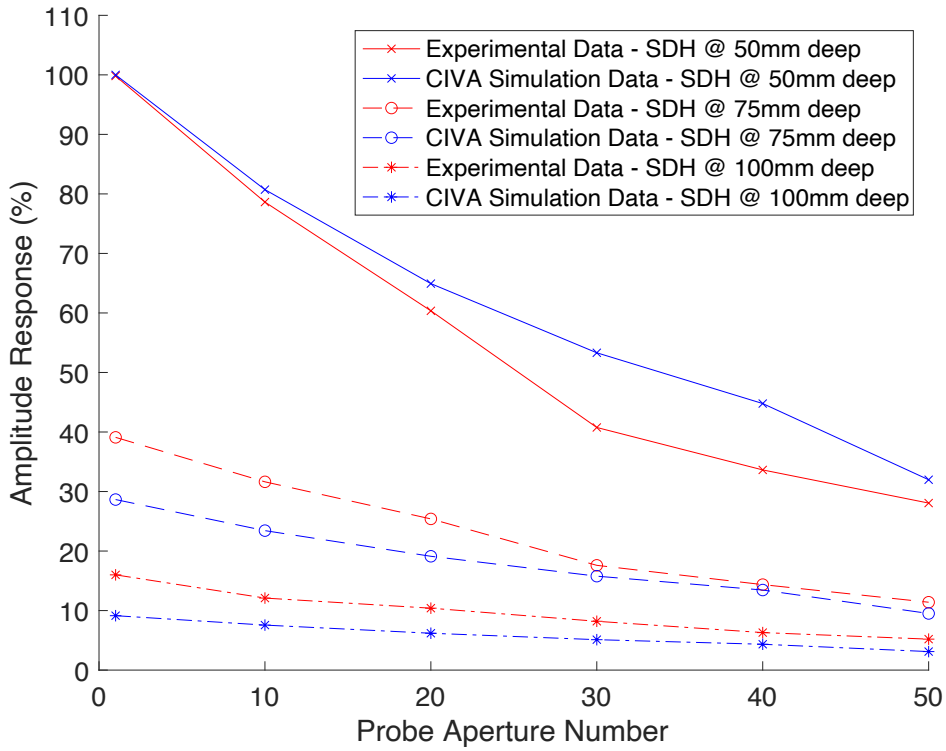

Figure 72: Comparison of experimental and CIVA simulation amplitude response data (using experimental attenuation coefficients) scanning SDHs at 50, 75 and 100 mm depths

Analysis of Figure 72 finds that despite the simulated scan data following the same trend as the experimental data, it does not accurately replicate what is acquired physically. To understand the root cause of why the simulation's approximations are not fully representative of the experimentally captured data, the simulation was repeated but without attenuation being considered. Table 25 presents the SDH percentage amplitude responses approximated from the CIVA simulation of the

experimental setup that does not incorporate attenuation coefficients for the Rexolite or steel:

Table 12: SDH percentage amplitude response data for given aperture numbers from CIVA simulation (without attenuation) of experimental Omniscan MX2 setup

3D CIVA Simulation / No Attenuation							
% Response		Aperture No.					
		1	10	20	30	40	50
Depth (mm)	50	100	95.18	95.22	89.89	87.21	70.23
	75	60.38	59.18	57.94	56.15	53.95	43.91
	100	40.48	40.45	39.79	38.12	37.09	30.4

Figure 73 presents a comparison of the CIVA amplitude response approximations, while neglecting attenuation in the simulation, on each aperture at each SDH depth against the experimentally acquired data:

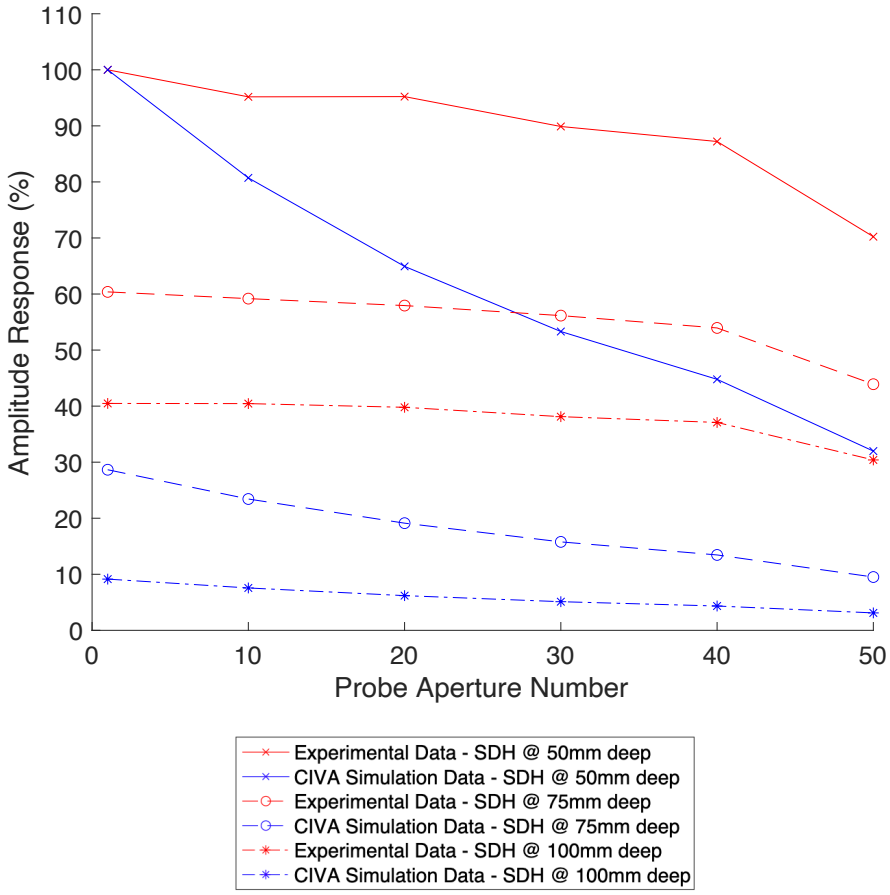

Figure 73: Comparison of experimental and CIVA simulation amplitude response data (neglecting attenuation) scanning SDHs at 50, 75 and 100 mm depths

As expected, these amplitude responses do not demonstrate any similarity to the experimentally acquired amplitude responses. It can be observed from these approximations that despite attenuation not being considered as part of the simulation, there is a decrease in amplitude response relative to both the increasing SDH depth and across apertures for the same SDH depth. Where attenuation is associated with the reduction in amplitude caused by the scattering effect from a material's microstructure; these reductions are associated with CIVA's approach in approximatimg the acoustic behaviour of the beam from the specified probe parameters. As explained in Section 2.1.7, the beam profile of the

probe is calculated by parameters such as the excitation frequency, crystal size and crystal shape.

To ensure that the simulation is representative of the experimental setup, the attenuation approximated within the simulation has to be comparable to the calculated attenuation experienced within the experimental setup. From the data in Table 11, the underestimation of the amplitude responses relative to the experimental data highlights that the attenuation coefficient of the simulation is too high. As a reduction in amplitude is observed in a simulation without attenuation, an equivalent energy loss needs to be calculated and considered within the simulation.

From the data in Table 25, an equivalent energy loss representative of the acoustic profile of the beam can be calculated and deducted from experimental attenuation coefficients. Using the same process as before to calculate attenuation coefficients for the steel and Rexolite in the experimental setups, the normalised amplitude responses relative to the shallowest SDH are shown in Table 13 and the normalised amplitude responses relative to the first aperture are shown in Table 14:

Table 13: CIVA simulated decibel differences in amplitude response data for SDH depth relative to the amplitude acquired on the shallowest SDH for that given aperture

3D Simulation / No Attenuation - Normalised Amplitude Response per aperture (dB)							
		Aperture No.					
		1	10	20	30	40	50
Depth (mm)	50	0	0	0	0	0	0
	75	-4.3821378	-4.1274148	-4.3149937	-4.0872324	-4.1714967	-4.0791846
	100	-7.8551899	-7.4325435	-7.5790848	-7.4511698	-7.4261891	-7.2729817

Table 14: CIVA simulated decibel differences in amplitude response data for increasing aperture number relative to the amplitude acquired on the first aperture for a given SDH depth

3D Simulation / No Attenuation - Normalised Amplitude Response per SDH depth (dB)							
		Aperture No.					
		1	10	20	30	40	50
Depth (mm)	50	0	-0.429086	-0.4254365	-0.9257724	-1.1886743	-3.0695466
	75	0	-0.174363	-0.3582924	-0.630867	-0.9780332	-2.7665934
	100	0	-0.0064396	-0.1493313	-0.5217522	-0.7596734	-2.4873384

Using the appropriate soundpath lengths, Table 15 presents calculated energy loss coefficients within the steel and Table 16 presents calculated energy loss coefficients within the Rexolite:

Table 15: Calculated CIVA simulated energy loss coefficients representing acoustic behaviour of beam within steel based on the decibel reduction experienced with respect to additional sound path distance covered

3D Simulation / No Attenuation - Energy Loss Coefficient (dB/mm) - Steel							
		Aperture No.					
		1	10	20	30	40	50
Depth (mm)	50	0	0	0	0	0	0
	75	0.04382138	0.04127415	0.04314994	0.04087232	0.04171497	0.04079185
	100	0.03927595	0.03716272	0.03789542	0.03725585	0.03713095	0.03636491

Table 16: Calculated CIVA simulated energy loss coefficients representing acoustic behaviour of beam within Rexolite based on the decibel reduction experienced with respect to additional sound path distance covered

3D Simulation / No Attenuation - Energy Loss Coefficient (dB/mm) - Rexolite							
		Aperture No.					
		1	10	20	30	40	50
Depth (mm)	50	0	0.03155044	0.0148754	0.02123331	0.02021555	0.04159277
	75	0	0.01282081	0.0125277	0.01446943	0.01663322	0.03748772
	100	0	0.0004735	0.00522137	0.01196679	0.01291962	0.03370377

For clarification, these coefficients are not a form of attenuation and do not carry the same exponential reduction in amplitude properties with increasing soundpath. Instead, each are representative of the energy loss associated with the behaviour of the acoustic beam along the given soundpath length of each aperture within the given material.

To illustrate, all wave propagation within the Rexolite wedge, negating attenuation, for all apertures is within the probe's near field. Figure 74 presents the CIVA beam computation simulation setup (excluding attenuation) of the same probe (without wedge) propagating into a 300 mm deep Rexolite block and the resulting acoustic behaviour of the beam:

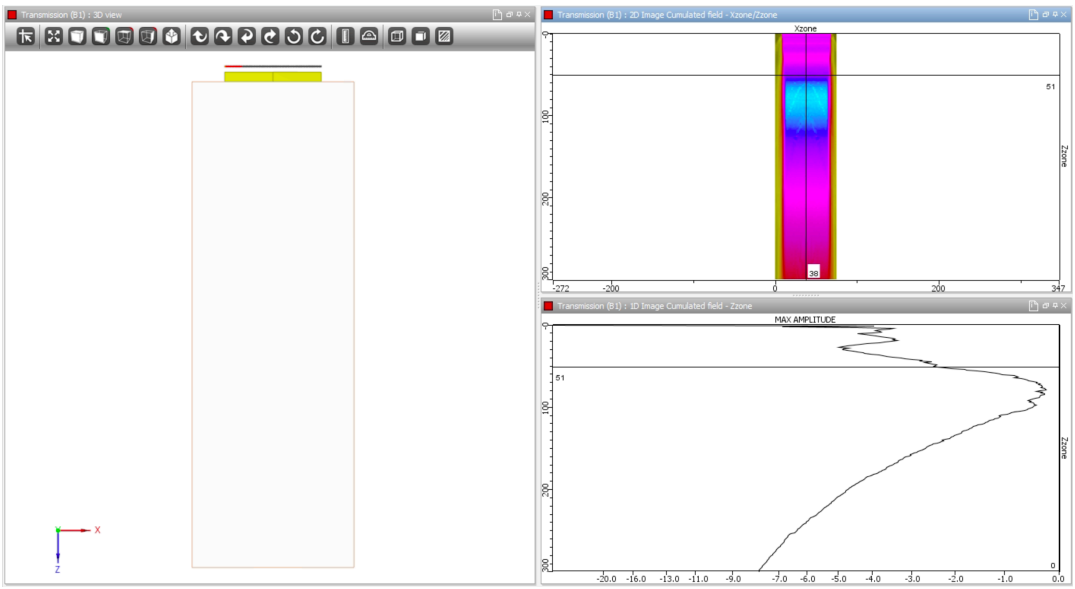

Figure 74: CIVA simulated beam computation setup of probe (without wedge) propagating into a 300 mm deep block of Rexolite with results highlighting the depth of longest soundpath within wedge (on aperture 50)

The marked depth within the analysis section of the acoustic beam profile of the probe at 51 mm deep shown in Figure 74 highlights the

longest soundpath length within the wedge (aperture 50). With the simulated focal point of the 11 element aperture being approximated at 80 mm deep, it can be deduced that the beams within the wedge for all apertures are within the near field. As such, the propagating wave is fluctuating which can be observed in the simulated beam amplitude profile. This is also shown by the significant differences in magnitude of the calculated energy loss coefficients within Figure 16 for Rexolite.

To correctly account for the energy loss associated with the acoustic behaviour of the beam for individual apertures inspecting a defect, each soundpath would have to be adapted independently. However, this would require individual simulations of each aperture such that the attenuation coefficients incorporated within the simulation can be adapted to account for the energy loss associated with the beam profile. As such an average of the simulated energy loss coefficients across all apertures and defect depths can be taken. Based on the energy loss coefficients calculated in Table 16 for Rexolite, the energy loss coefficient can be equated to be 0.02 dB/mm.

Repeating a similar process for the steel, an acoustic profile of the beam can be computed. Unlike the Rexolite which looked at a longitudinal wave mode, the propagation within the steel is a shear wave mode. To generate the acoustic profile of the shear wave propagation within the steel, a beam computation analysis of the actual inspection setup was implemented as shown in Figure 75:

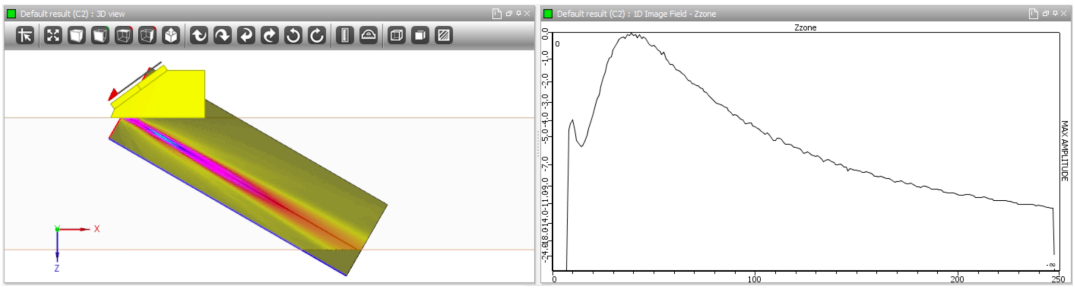

Figure 75: CIVA simulated beam computation of inspection setup on aperture 1 presenting the acoustic behaviour of the beam within the steel

The focal point of the setup for aperture 1 occurs at a depth of approximately 16 mm from the top surface of the depth. As this is aperture has the shortest soundpath through the Rexolite, it will have the deepest focal point within the steel of all apertures. Therefore, all defect responses (at 50, 75 and 100 mm depths) will occur within the far field where the propagating wave has stabilised. This can be concluded as the amplitude response of the beam, beyond the focal point, can be observed to gradually reduce in amplitude at a steady rate with no drastic fluctuations. This is reflected in the consistency of the energy loss coefficients calculated in Table 15.

Despite the amplitude response trend within Figure 75, following a near exponential reduction in amplitude, it must be reiterated that this response is independent from the properties associated with attenuation. The calculated energy loss coefficients represent the average reduction in amplitude across a given soundpath length where the magnitiude of energy loss can fluctuate at various points depending on the acoustic behaviour of the beam.

Facing the same issue to incorporate the individually calculated energy loss coefficients for the steel within the CIVA simulation for each

aperture, an average of the coefficients calculated in Table 15 can be generated. This equates to an energy loss coefficient of 0.02 dB/mm for the steel.

Deducting the calculated energy loss coefficients from the experimentally acquired attenuation coefficients used in the initial simuation creates the new attenuation coefficients of 0.135 and 0.037 dB/mm for the Rexolite and steel respectively. Rerunning the CIVA simuation of the experimental setup scanning three SDHs with these newly calculated coefficients generates the percentage amplitude responses shown in Table 26.

Table 17: SDH percentage amplitude response data for given aperture numbers from CIVA simulation (with adapted attenuation coefficients) of experimental Omniscan MX2 setup

3D Simulation / Steel Att (0.037 dB/mm) + Wedge Att (0.13 dB/mm)							
% Response		Aperture					
		1	10	20	30	40	50
Depth (mm)	50	100	78.1	61.71	46.42	35.93	23.47
	75	39.97	31.8	25.18	18.95	14.65	9.7
	100	17.82	14.35	11.32	8.62	6.68	4.42

Figure 76 presents a comparison of the CIVA amplitude response approximations, while implementing the adapted attenuation coefficients in the simulation, on each aperture at each SDH depth against the experimentally acquired data:

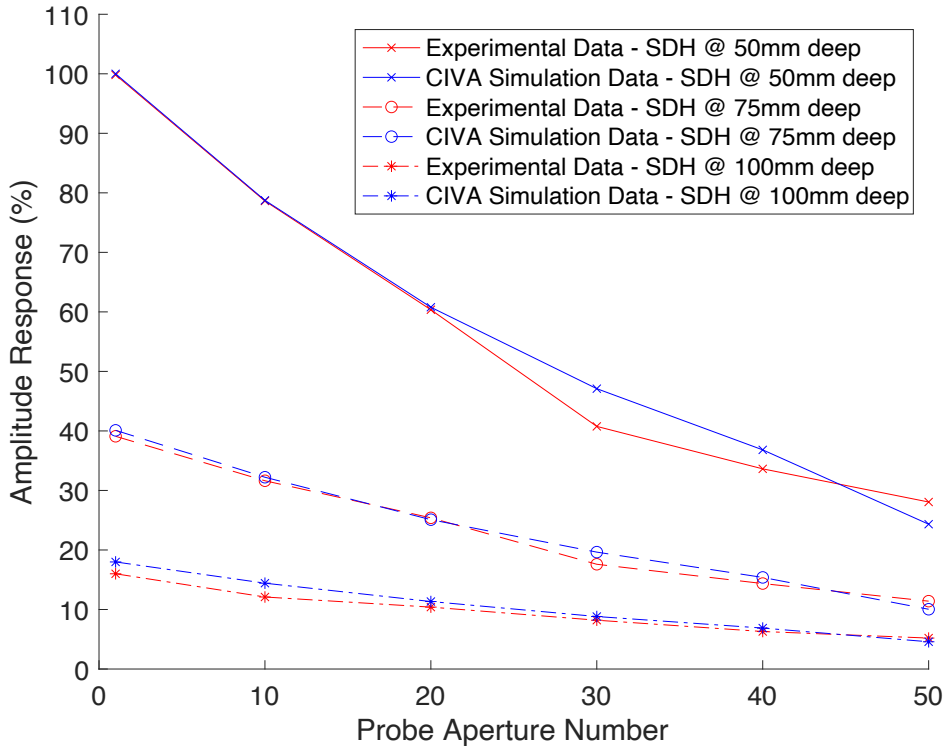

Figure 76: Comparison of experimental and CIVA simulation amplitude response data (using adatpted attenuation coefficients) scanning SDHs at 50, 75 and 100 mm depths

Comparison of these percentage approximations against the experimental values in Table 6 and Figure 76 shows effective replication. This validates that CIVA can accurately simulate the amplitude responses of defects that require the SOV approximation algorithm, such as SDHs. The CIVA simulation approach to incorporating attenuation can be further validated by quantifying the theoretical attenuation reductions, based on the adapted attenuation coefficients. The subsequent results should align with the relative difference in amplitude response between the CIVA simulation incorporating no attenuation and the simulation incorporating the adapted attenuation coefficients.

As such, Table 18 presents the total sound path distances within the Rexolite and steel for each aperture:

Table 18: Total sound path distances travelled within the Rexolite wedge and steel sample for each respective aperture of the given setup

Total Sound Path Distances (mm)							
Material	SDH Depth (mm)	Aperture					
		1	10	20	30	40	50
Rexolite	-	28.2	41.8	56.8	71.8	87	102
Steel	50	200	200	200	200	200	200
	75	300	300	300	300	300	300
	100	400	400	400	400	400	400

Using the adapted attenuation coefficients of 0.13 and 0.037 dB/mm for the Rexolite and steel, the reductions in amplitude of the CIVA simulation accounting for attenuation can be theoretically approximated by summing the products of each coefficients with the distance travelled within the respective material medium:

Table 19: Theoretical signal reduction of for each aperture at SDH depths of 50, 75 and 100 mm assuming attenuation coefficients of 0.13 and 0.037 dB/mm for Rexolite and steel

Theoretical dB Loss (dB) - 0.037/0.13 dB/mm							
		Aperture					
		1	10	20	30	40	50
Depth (mm)	50	11.066	12.834	14.784	16.734	18.71	20.66
	75	14.766	16.534	18.484	20.434	22.41	24.36
	100	18.466	20.234	22.184	24.134	26.11	28.06

For comparison, the relative difference between the no attenuation simulation and adapted attenuation simulation can be calculated based on the data presented in Table 12 and Table 17. As previously mentioned, all data points within the output of CIVA simulations will

have a calculated CRA value which will have an associated percentage value relative to the data point with the largest CRA value in that simulation output. Despite the presented percentage amplitudes between the tables showing some similar magnitude, they are percentage amplitudes relative to two different data point CRA magnitudes.

The maximum CRA value for the no attenuation simulation is 0.219 which was approximated for the 50 mm SDH on aperture 1. The maximum CRA value for the adapted attenuation simulation is 0.06135 which was approximated for the 50mm SDH on aperture 1. Calibrating the adapted attenuation simulation relative to the CRA magnitude of the maximum response of the no attenuation simulation, the following table presents the decibel loss for each SDH depth on each SDH:

Table 20: dB loss of adapted attenuation simulation responses relative to the no attenuation simulation for each aperture at SDH depths of 50, 75 and 100 mm assuming attenuation coefficients of 0.13 and 0.037 dB/mm for Rexolite and steel

CIVA dB Loss (dB)							
		Aperture					
		1	10	20	30	40	50
Depth (mm)	50	11.1	13.2	15.2	17.7	19.9	23.6
	75	19	21	23	25.5	27.7	31.3
	100	26	27.9	30	32.3	34.6	38.1

To allow these calibrated CIVA dB losses to be comparable against the theoretical dB loss, the reductions in amplitude observed within no attenuation simulations, as calculated earlier, have to be corrected for. The reduction corrections for a no attenuation simulation can be shown in Table 21:

Table 21: dB reduction corrections for no attenuation simulations for each aperture at SDH depths of 50, 75 and 100 mm

3D Simulation / No Attenuation Reduction Correction (dB)							
		Aperture					
		1	10	20	30	40	50
Depth (mm)	50	0.0	-0.4	-0.4	-0.9	-1.2	-3.1
	75	-4.4	-4.6	-4.7	-5.0	-5.4	-7.1
	100	-7.9	-7.9	-8.0	-8.4	-8.6	-10.3

Summing the values of Table 20 and Table 21 will generate the magnitudes in Table 22, which are the relative reductions in amplitude linked directly to the incorporation of the attenuation coefficients within the simulation:

Table 22: Corrected dB loss of adapted attenuation simulation responses relative to the no attenuation simulation for each aperture at SDH depths of 50, 75 and 100 mm assuming attenuation coefficients of 0.13 and 0.037 dB/mm for Rexolite and steel

Corrected CIVA dB Loss (dB)							
		Aperture					
		1	10	20	30	40	50
Depth (mm)	50	11.1	12.8	14.8	16.8	18.7	20.5
	75	14.6	16.4	18.3	20.5	22.3	24.2
	100	18.1	20.0	22.0	23.9	26.0	27.8

Comparison of these values against the theoretical reductions in signal amplitude calculated based on the adapted attenuation coefficients can be presented in Figure 78:

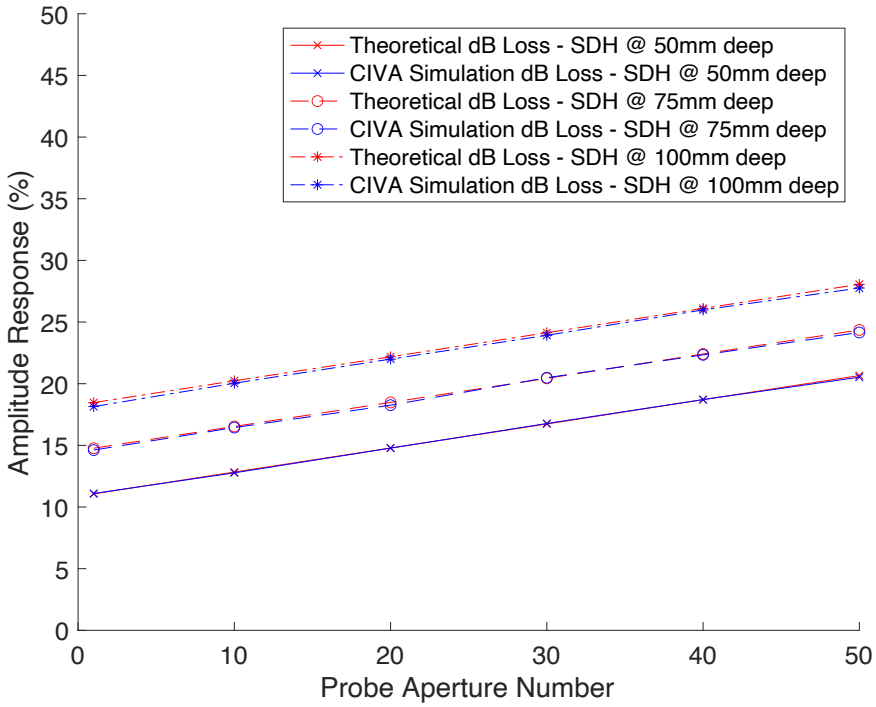

Figure 77: Comparison of theoretical and CIVA simulated dB loss associated with the adapted attenuation coefficients

It can be observed from Figure 78 that the inclusion of the attenuation coefficient within a CIVA simulation generates reduced outputs relative to CIVA simulation with no attenuation accounted for that align with the predicted theoretical loss in amplitude response. This is deduced due to the equivalence between the simulated and theoretical dB losses.

This also highlights that CIVA simulations do not require attenuation coefficients to be defined and included within the setup of the simulation. Instead, the calculated reductions in amplitude for given attenuation coefficients or even the measured reductions in amplitude acquired from a scan can be included within simulation post-processing.

4.4.4 CIVA Simulation vs. Experimental - FBH

To ensure that CIVA can replicate the experimental amplitude responses of alternative defects, three FBH reflectors of the validation block were scanned using an identical setup to that used for scanning the SDHs in Section 4.4.2. The importance of this is to validate the application of a different, commonly-used, approximation algorithms recommended for alternate defect types. A schematic diagram of the scan setup is shown in Figure 78:

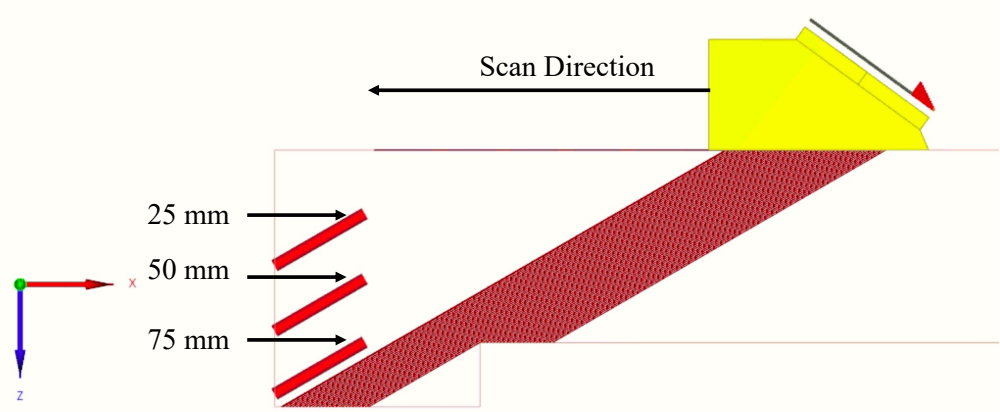

Figure 78: Schematic of experimental setup on validation block performing a direct scan of three FBHs at depths of 25, 50 and 75 mm

The gain settings of the Omniscan MX2, used to capture the amplitude responses, were adjusted such that the response from the shallowest FBH and on the first aperture were set to 100% screen height. From the scan setup shown, the percentage amplitude responses can be seen in Table 23:

Table 23: FBH experimental percentage amplitude response data for given aperture numbers captured using Omniscan MX2 of FBHs at 25, 50 and 75 mm depths

Experimental Data (FBH)							
% Response		Aperture No.					
		1	10	20	30	40	50
Depth (mm)	25	100	79.43	61.66	47.32	35.89	23.17
	50	39.36	30.90	24.27	18.41	14.13	8.81
	75	16.22	12.16	9.33	7.16	5.07	3.05

Attempting to replicate these amplitudes, Figure 79 presents the simulation setup of three FBHs at the respective depths of 25, 50 and 75mm:

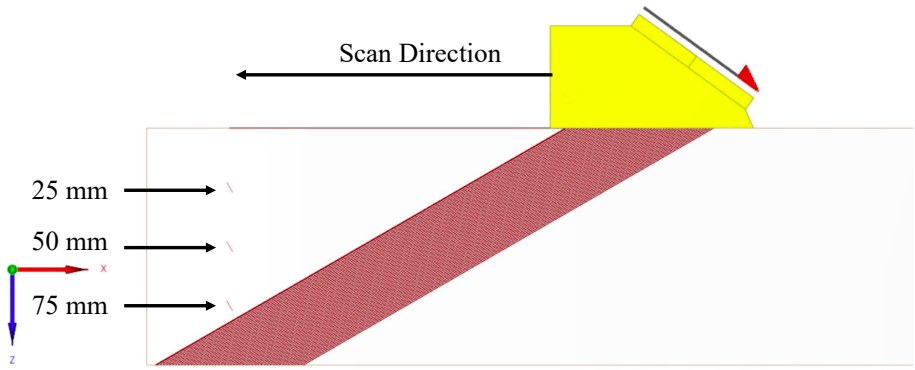

Figure 79: Schematic of CIVA simulation setup performing a direct scan of three SDHs at depths of 25, 50, and 75 mm depths

Like before, the scan setup was executed using the same pulsing parameters of 50 11-element apertures. The simulation was optimised to collect all of the necessary data within a single model execution, negating backwall reflections and running 2D computation. The simulation settings included the attenuation coefficients determined in Section 4.4.3, of 0.037 and 0.13 dB/mm for steel and Rexolite. As mentioned, the approximation algorithm used to simulate the beam

interaction with the FBH reflector was KA/GTD. Table 28 presents the percentage amplitude responses approximated by CIVA for the FBHs at multiple depths across the designated aperture numbers:

Table 24: FBH percentage amplitude response data for given aperture numbers from CIVA simulation (with amended attenuation) of experimental Omniscan MX2 setup

3D FBH Simulation / Steel Att (0.037 dB/mm) + Wedge Att (0.13 dB/mm)							
% Response		Aperture No.					
		1	10	20	30	40	50
Depth (mm)	25	100	80.51	62.54	48.23	36.93	24.87
	50	36.74	28.68	21.75	16.55	12.59	8.20
	75	13.38	10.44	8.01	6.12	4.72	3.06

Figure 80 presents a comparison of the CIVA amplitude response approximations, while implementing the adapted attenuation coefficients in the simulation, on each aperture at each SDH depth against the experimentally acquired data:

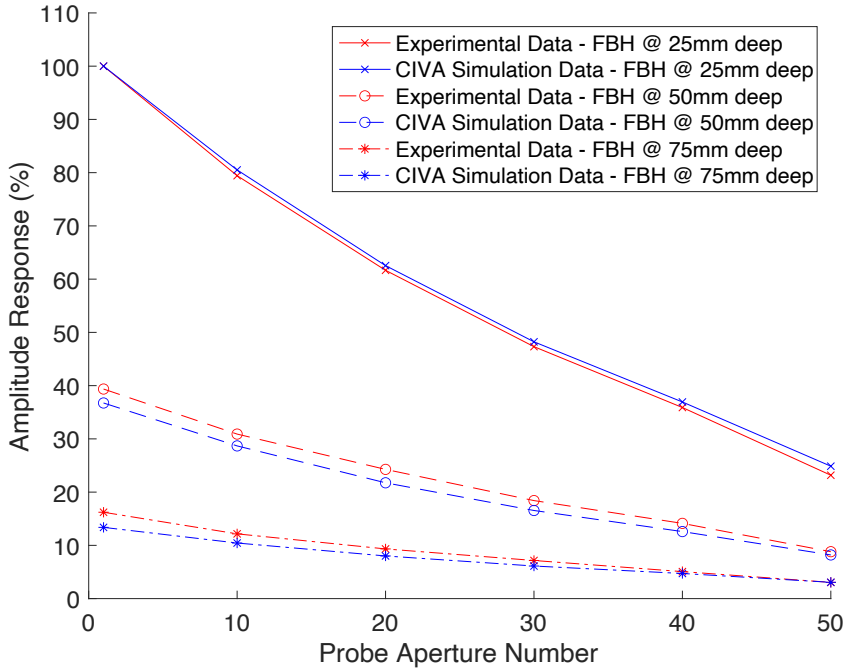

Figure 80: Comparison of experimental and CIVA simulation amplitude response data (using experimental attenuation coefficients) scanning FBHs at 25, 50 and 75 mm depths

The simulated results presented in Figure 80 demonstrate how the approximated results closely mimic the experimental acquired data. This validates that CIVA can replicate the experimental amplitude responses of more than one defect type. The importance of this is that it highlights the accurate approximation of defect amplitude responses using alternative approximation algorithms; in this case Kirchhoff and GTD.

4.5 Basic Calibration of CIVA Simulations

As discussed in Section 3.6, the calibration approaches for reflectivity-based techniques use the amplitude response from SDHs as reference. The calibration of a setup occurs at the highlighted step within the following simplified flow chart of the physical inspection process:

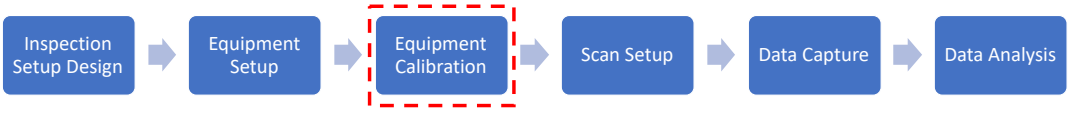

Figure 81: Flow chart of physical PAUT inspection process

In a similar manner, the recommended calibration approach to be applied within CIVA aims to replicate the calibration process by repeating the inspection simulation with a chosen flaw being replaced by a SDH at the exact same depth and position. The flow charts, illustrated in Figure 82 and Figure 83, give an overview of the two approaches of calibrating an inspection simulation:

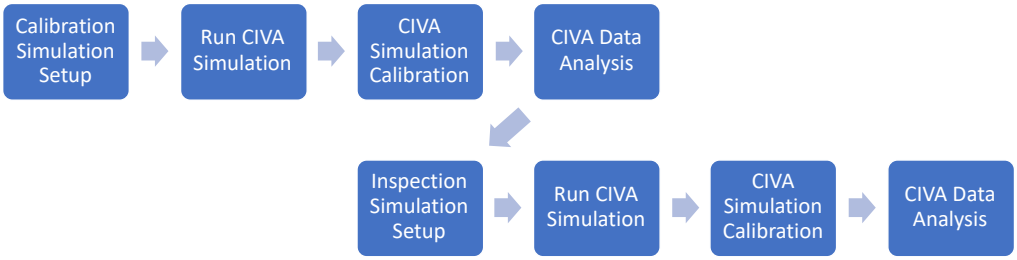

Figure 82: Basic CIVA calibration process flow chart (pre-inspection simulation)

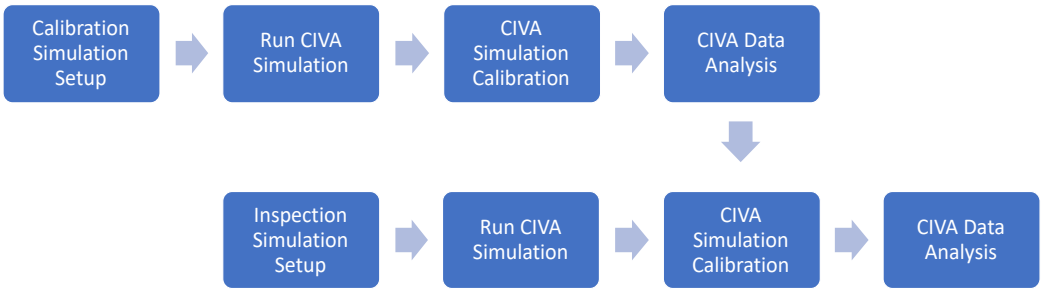

Figure 83: Basic CIVA calibration process flow chart (post-inspection simulation)

Comparing the second two flow charts to that in Figure 81, the pre-inspection simulation calibration process is a more appropriate replica. However, regardless of which calibration procedure flow chart is implemented, similar results should be achieved. Both processes, shown in Figure 83, calibrate the inspection simulation in reference to a SDH calibration simulation, based on the internal CRA value.

As discussed in Section 4.3, each discrete coordinate of the simulated field of the transducer within the inspection specimen is assigned a CRA. The coordinate calculated to produce the largest amplitude reflection is assigned the largest CRA. With regards to a percentage response, this coordinate is set to 100% FSH and the percentage of all other coordinates is calculated relative to the largest CRA.

From a repeated simulation incorporating a SDH, the CRA associated with the largest percentage amplitude response for the SDH can be acquired. This value is then used to calibrate the inspection simulation using the Gain/Color tab within CIVA's data analysis page, shown by Figure 84:

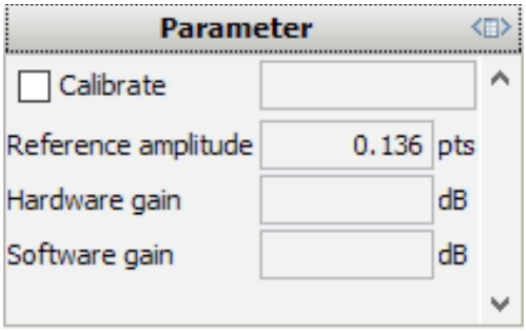

Figure 84: Gain/Color tab within CIVA data analysis

In the tab GUI shown above, the Calibrate tick box is selected and the CRA value associated with the highest response from the SDH, is inputted into the respective box. To demonstrate the application of this calibration technique, Figure 85 shows a schematic of the same inspection setup from Figure 65 with the rectangular flaws replaced by 3 mm SDHs at the same locations:

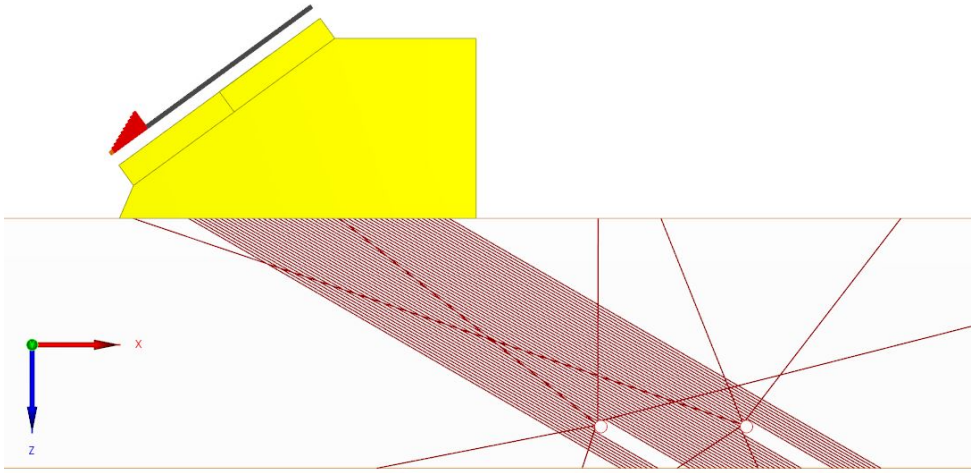

Figure 85: Schematic of CIVA calibration simulation setup for a linear scanning phased array inspection

For the inspection setup in Figure 65, there are two identical flaws on different apertures. Therefore, to appropriately calibrate each of them, the calibration simulation must have both flaws replaced by SDHs to acquire the corresponding CRAs. In completion of a 2D simulation

with attenuation not being accounted for, Figure 86 shows the maximised S-scan image of the repeated simulation with the rectangular flaws being replaced by SDHs:

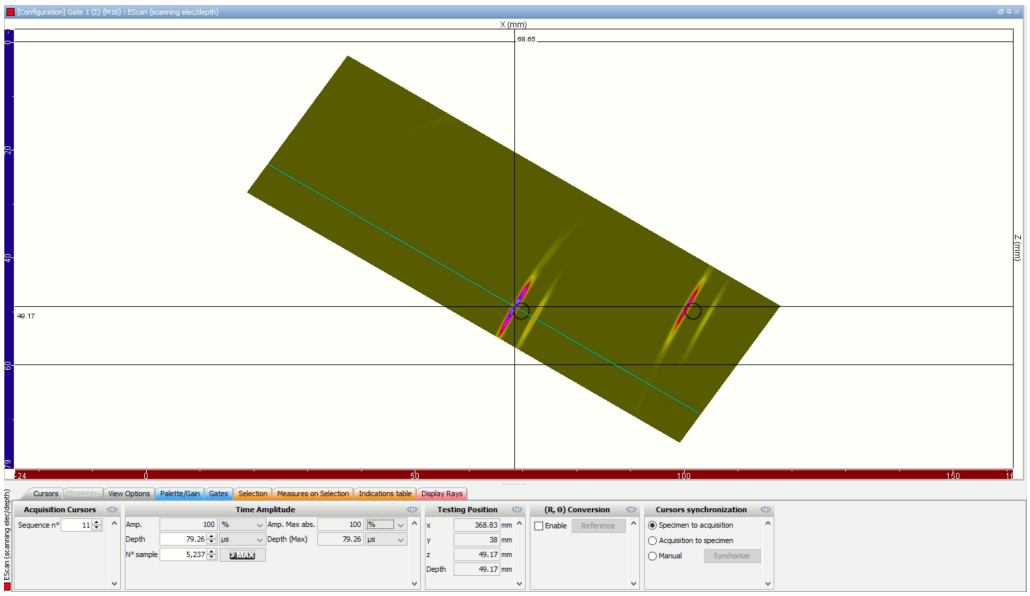

Figure 86: Simulated S-scan image of inspection setup with SDHs flaws

Locating the highest percentage response coordinates associated with each SDH, the CRAs (of 0.135 on aperture 11 and 0.13 on aperture 36) can be extracted. Each CRA is entered into the Palette/Gain tab (Figure 84) of the inspection simulation (Figure 66) and the software calculates the new percentage amplitude response of all data points in reference to the inputted value. The resulting effects on the S-scan data for each CRA value are highlighted by Figure 87 and Figure 88:

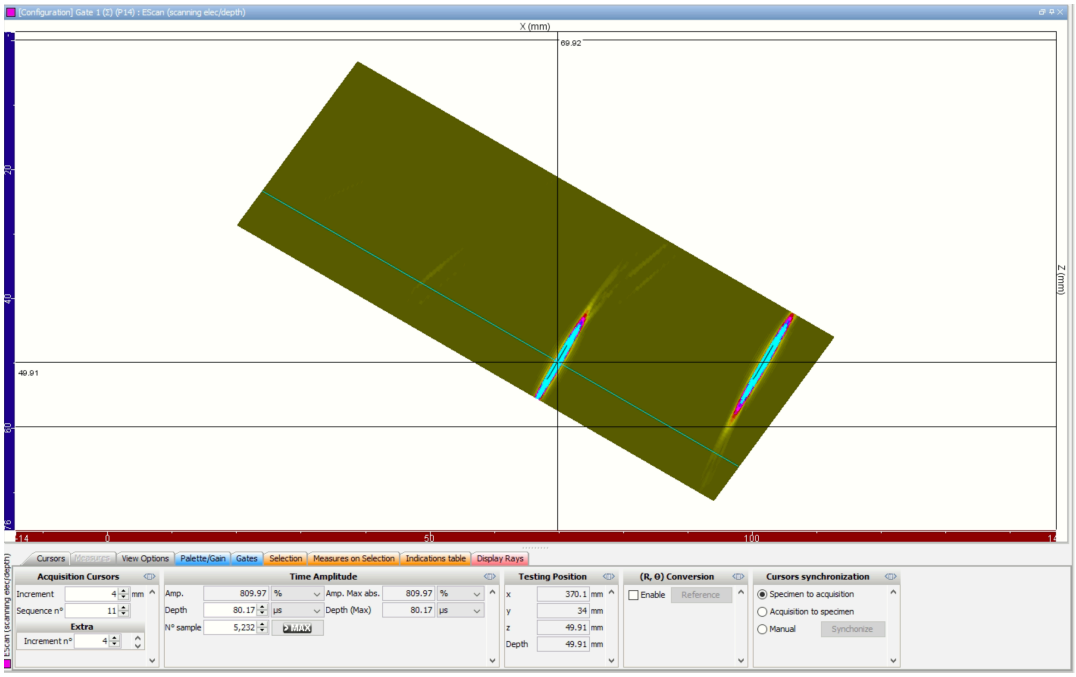

Figure 87: Calibrated S-scan of CIVA simulated LOF flaw inspection relative to SDH on aperture 11

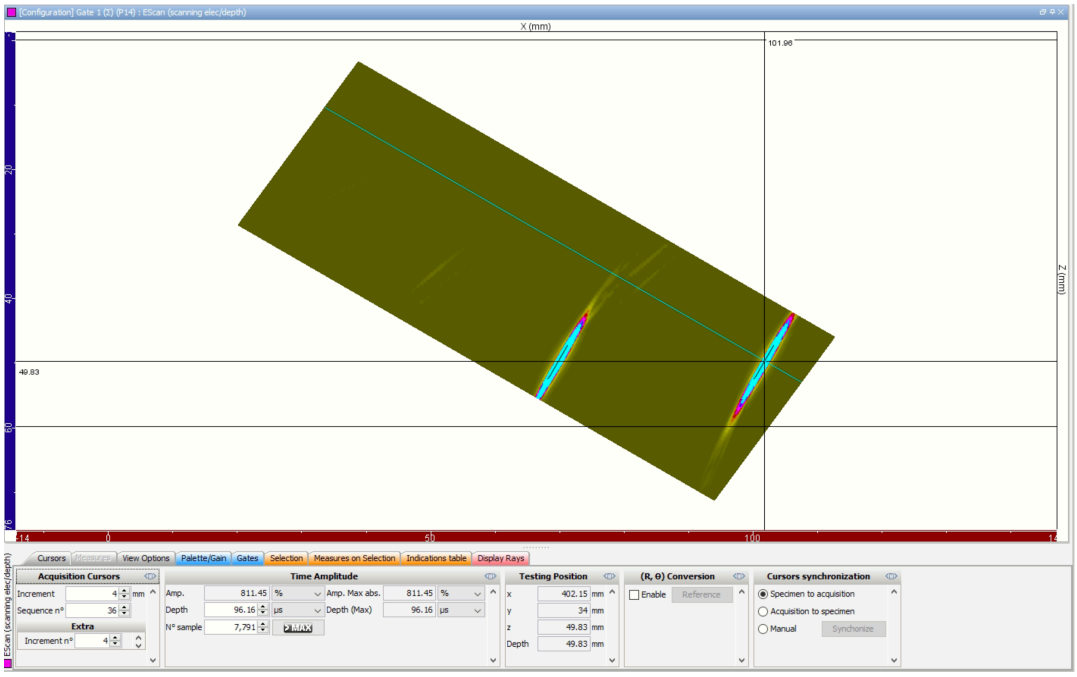

Figure 88: Calibrated S-scan of CIVA simulated LOF flaw inspection relative to SDH on aperture 36

In Figure 87, where the inspection setup is calibrated using the CRA relative to the SDH on aperture 11, the amplitude response of the flaw on the same aperture is 809.97%. By comparison, where the chosen CRA is relative to the SDH on aperture 36, the amplitude response of the flaw on the same aperture is 811.45%. Despite a magnitude change in the highest amplitude response, the colour palette remains unchanged with each colour shade being associated with a percentage amplitude response between 0% and 100%. For any amplitude responses that return greater than 100%, the coordinate will appear as the same colour shade as a 100% amplitude response. In both calibrated simulation results cases, the inputted CRAs cause the amplitude responses across the entire face of each flaw to spike. This can be seen from the large turquoise coloured response highlighted at each flaw location.

Having independently calibrated each of the amplitude responses for the two flaws in the inspection simulation relative to their respective SDHs based on the acquired CRAs from the calibration simulations, the flow chart detailing the basic calibration process, presented in Figure 83, has been completed.

4.6 Limitations of Basic Calibration Approach

In its simplicity, the basic calibration approach has several limitations in its ability to effectively replicate the calibration process carried out for a physical inspection setup. As previously described in Section 3.6.2, the standard calibration approach for PAUT techniques such as linear scanning and sectorial scanning is to apply a TCG. In applying a TCG, all active apertures/angles are calibrated to produce identical amplitude responses from identical reflectors at selected depths, with linear interpolation used to calibrate the responses between those depths.

The basic calibration approach, by comparison, only calibrates the amplitude response of the coordinates located at a specific depth and on a designated active aperture. As shown in Section 0, to normalise the amplitude response of an identical flaw on an alternate aperture, the corresponding SDH CRA has to be attained. As only one CRA can be inputted to calibrate the inspection setup, the calibrated image cannot replicate a TCG calibrated inspection.

Consequently, this does not make it an appropriate calibration methodology for performing through-thickness flaw sizing on any flaw. Due to one active aperture/angle at a single depth being calibrated, the corresponding CRA would not be appropriate to calibrate the response acquired on a different aperture/angle or depth, which may occur at a different sound path depth. Therefore, the basic calibration approach does not appropriately replicate the TCG calibration process required for a PAUT setup.

4.7 In-built TCG Calibration for CIVA Simulations

At the beginning of this project, no TCG functionality was available. Within an update to CIVA 2020 in 2021, an in-built TCG function was added to approximate the additional gain settings generated within a TCG calibration. The TCG is setup within two sub-tabs of the calibration tab as part of the Simulation Settings, as shown in Figure 89:

(a): Specimen sub-tab

(b): Reflector sub-tab

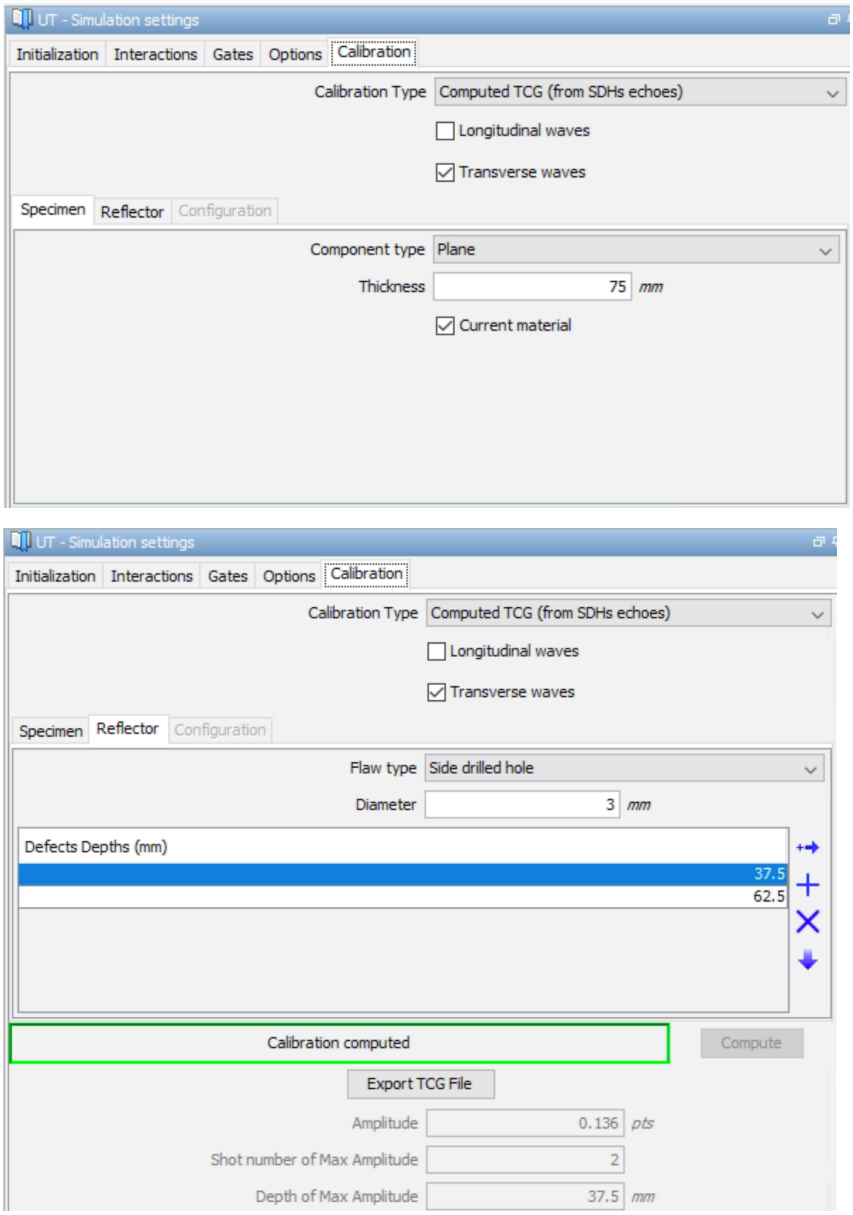

Figure 89: Sub-tabs of calibration tab within CIVA inspection simulation settings

From the Calibration Type dropdown menu, selecting “Computed TCG (from SDHs echoes)” allows the user to auto-generate a specimen containing identical flaws at various depths to create the TCG settings to be applied to the inspection simulation. The thickness and material type of the calibration specimen are specified in the Specimen sub-tab while the flaw type, dimensions and depths are set in the Reflector sub-tabs. Once inputted, the “Compute” button will calculate the TCG settings for the array settings applied at each reflector depth. Based on the inputs shown in Figure 89, of two 3 mm SDH at depths of 37.5 and 62.5 mm, Figure 90 shows the TCG settings calculated for the first aperture of the linear scanning PAUT setup used in the previous section:

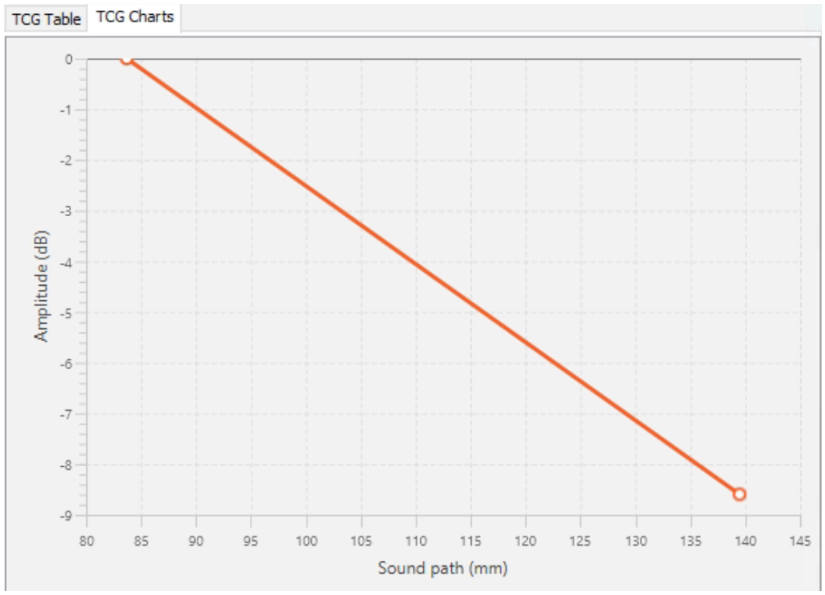

Figure 90: Approximated TCG settings curve using in-built CIVA TCG settings

Once generated, the gains settings for each active aperture can be viewed using the slider at the bottom of Figure 90 and will be applied as part of the inspection simulation. Alternatively, the TCG settings can be exported into a file and applied to the simulation output using CIVA’s

TCG signal processing options within the analysis tab. By saving a file of the TCG settings, the user can apply the settings to other inspection simulations using the same array settings setup. In addition to applying the TCG file within the analysis tab, the settings can be imported and included as part of the inspection simulation. This is achieved by selecting the "Imported TCG" option from the Calibration Type dropdown menu option, in Figure 89.

As a result, Figure 91 shows the data analysis page for the inspection simulation setup from Figure 65 with the in-built TCG settings applied:

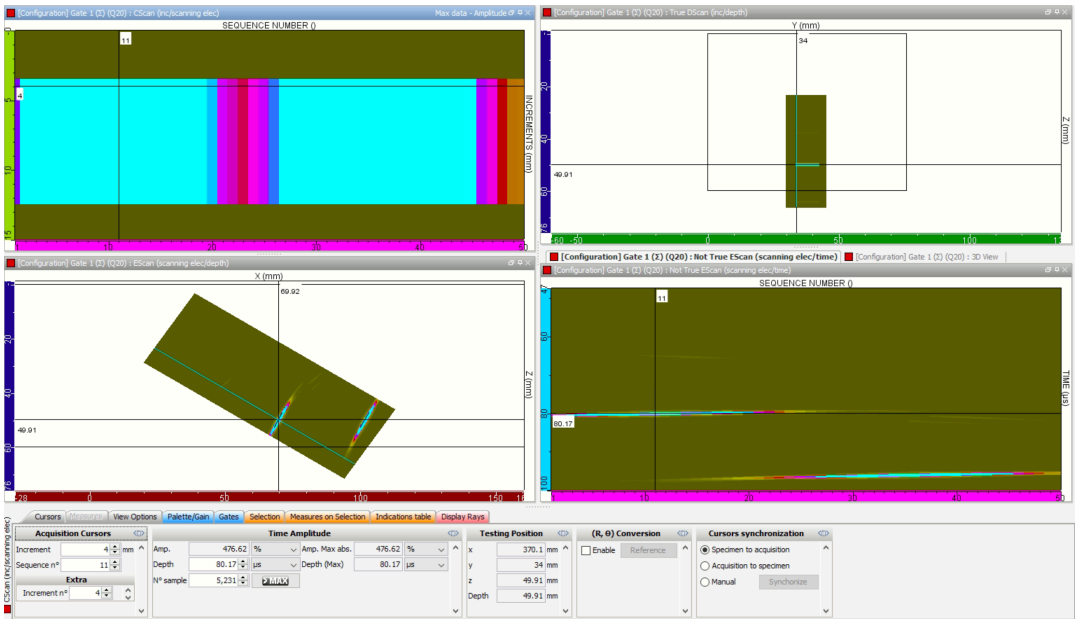

Figure 91: CIVA simulation data analysis page with in-built TCG settings applied to a PAUT inspection of LOF-type flaws

The results from the data analysis page, presented in Figure 91, show that the peak response of the rectangular flaw on aperture 11 has been approximated to 476.62% while the other rectangular flaw on aperture 36 has been approximated to 484.37%. In applying the TCG

file generated by the in-built function, the amplitude responses of both flaws have been normalised to similar levels. Unlike the basic calibration approach, by applying this approach has generated a single image with all volume coordinates being calibrated relative to a SDH at the corresponding depth and on the respective aperture.

4.8 Limitations of CIVA's In-built TCG Calibration

The in-built TCG function has several limitations. The main restriction faced is that it does not calculate and apply gain settings that are relative to an 80% FSH response from a SDH at designated depths. Knowing that the default simulation approach by CIVA is to assign the coordinate with the highest approximate CRA to 100%, negative gain would be required to lower the response to the desired amplitude of 80% FSH. However, from the approximated TCG settings curve in Figure 90, 0 dB of gain is added for the first SDH depth on the first aperture. Therefore, the predicted output when applying the in-built TCG is to normalise all responses across all apertures and SDHs to 100% FSH.

To verify this, Figure 92 shows the S-scan image of the SDH inspection in Figure 85 when calibrated using the approximated TCG gain settings calculated using the in-built TCG function:

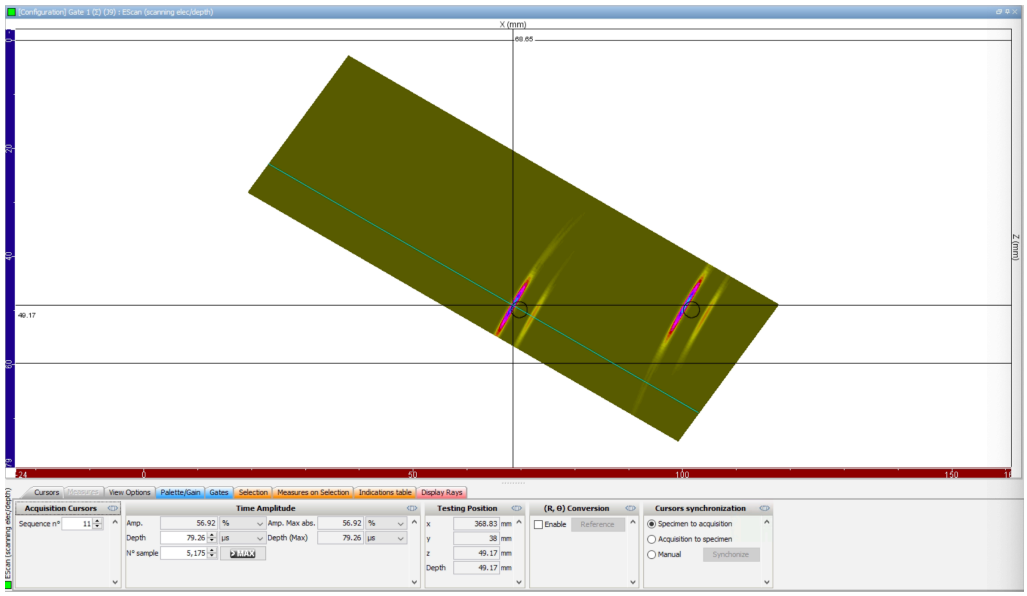

Figure 92: CIVA simulation data analysis page with in-built TCG settings applied to PAUT inspection of SDHs

The amplitude responses for each of the SDHs in Figure 92 were approximated to be 56.92% on aperture 11 and 57.84% on aperture 36. Despite the in-built function showing its capability of normalising the amplitude responses to approximately the same FSH; the TCG gain settings have been approximated to calibrate the amplitude responses to produce a FSH response closer to 57%.

Alternatively, a TCG calibration file based on the TCG gain curve settings from an experimental setup could be created and imported into CIVA. However, the complication with this approach is that the overall system gain of an experimental setup is attuned to having the largest uncalibrated amplitude response from a SDH, on any aperture, set to a specific screen height percentage, which is typically less than 100%. To then normalise the amplitude responses to the same FSH on every other aperture and for each SDH depth, the gain settings specify the additional gain required relative to the system gain of the PAC. As a result, the same issue is faced with the experimental gain settings typically calibrated to specify additional gain rather than negative gain.

Consequently, in not being able to calibrate all responses from a SDH for all apertures to the same FSH, it would be inappropriate to make comparisons against experimental data of the same setup. As shown in Section 4.7, the in-built TCG is capable of normalising the amplitude responses across identical flaws (different from SDHs) within an inspection. However, as will be discussed later, comparison of simulation data with experimental data of the same inspection showed that the calibrated simulation data does not effectively approximate the amplitude response of a flaw.

5 Custom TCG Calibration of CIVA Simulations

To improve on the capabilities of the calibration approaches described in the previous Chapter, this chapter presents the development of a custom TCG approach. This includes the experimental and simulated inspections of the custom-made carbon-steel test specimen with manufactured known reflectors, mentioned previously, to further enhance its efficacy.

5.1 Development of a Custom TCG Calibration

The limitations faced by both CIVA calibration methodologies to appropriately calibrate a linear scanning PAUT inspection can be overcome. By following the flow chart procedure presented in Figure 93, a custom TCG calibration approach can be implemented:

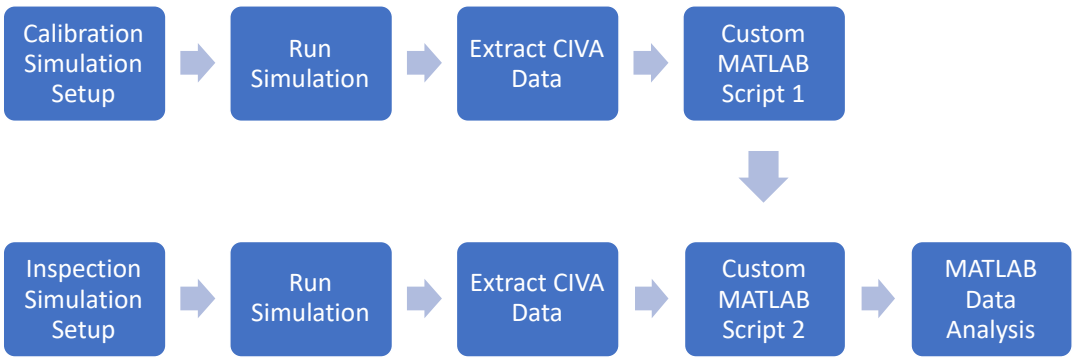

Figure 93: Flow chart of implementing a custom TCG calibration process

The process described in Figure 93 has the data from the calibration and inspection simulations extracted and imported into MATLAB for TCG calibration replication and data analysis. By comparison, the flow charts presented in Figure 83 have the data from

the calibration simulation extracted and used on the inspection simulation within the simulation setup or data analysis pages of CIVA.

After the A-scan data has been extracted from both simulations, the data from the SDH calibration simulation is passed through a Custom MATLAB Script (CMS-1) [Appendix 7.1]. Defining parameters of the inspection setup, the script generates a table of CRAs that are associated with the maximum response for each SDH depth on each aperture. These CRAs represent the reference values which would produce a 100% response from the associated SDH for the given aperture.

This table is then imported into a second Custom MATLAB Script CMS-2 [Appendix 7.2] alongside the extracted inspection simulation data. The table of CRAs is interpolated to acquire the CRAs for depths in between the SDH depths to create a calibration matrix. The calibration matrix is then divided by 0.8 to produce the CRAs that are associated with a SDH producing an 80% response. All data points of the inspection simulation are then calibrated by the CRA from the calibration matrix that corresponds to the relative depth and aperture.

TCG calibration is applicable to both linear scanning and sectorial scanning inspection setups. However, this thesis focuses on the development of a custom TCG for linear scanning PAUT setups. As previously discussed, the priority is inspection setups being carried out in accordance with Defence Standard 02-729 Part 5 [52]. Linear scanning PAUT inspection setups are selected to both supplement TOFD inspections and for inspecting complex weld geometries.

5.1.1 Custom MATLAB Script 1 - SDH CRA Generator

On the completion of a calibration simulation, the A-scan data for all apertures can be exported into a single text file. From this file, the CRAs defining the peak amplitude response from each SDH on each active aperture can be quantified and saved within a table.

To demonstrate how the table of CRAs is generated, Figure 94 shows the same probe and wedge combination used in Section 4.3 to inspect three 3 mm SDH at depths of 37.5, 62.5 and 87.5 mm within the steel validation block described in Section 4.4.1:

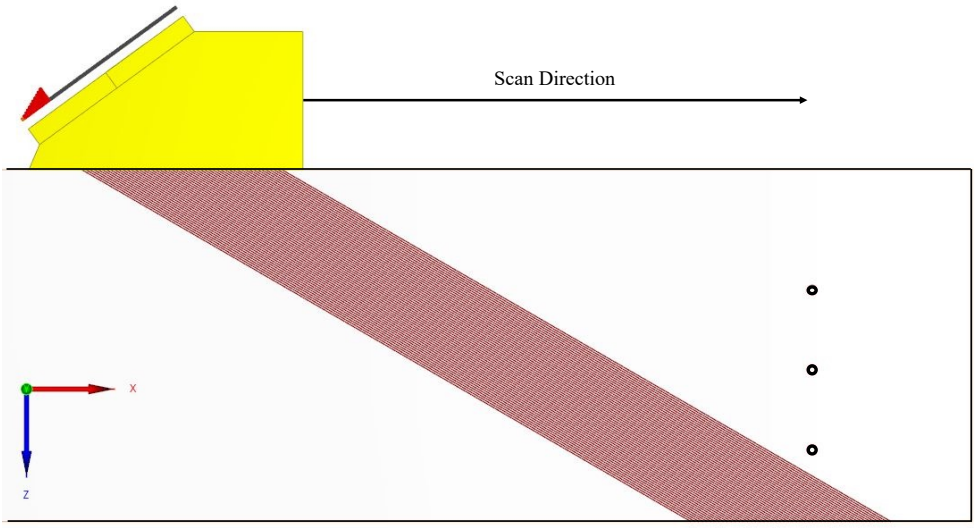

Figure 94: Schematic of CIVA calibration simulation setup of three SDHs at depths of 37.5, 62.5 and 87.5 mm

This simulation was run using 3D computation and attenuation coefficients accounted for with magnitues as calculated (0.037 dB/mm for steel and 0.13 for Rexolite). The A-scan CRA and decibel (amplitude) data for all apertures is exported from the data analysis page and into a single text file. This text file is imported into CMS-1, and a loop function within the script extracts the CRA data associated with the

largest responses from each aperture on each scan step. The extracted data can then be used to generate a C-scan image.

To demonstrate CMS-1's ability to recreate the C-scan image based on the A-scan data, Figure 95 present the C-scan image produced by CIVA and CMS-1 for the calibration simulation from Figure 94:

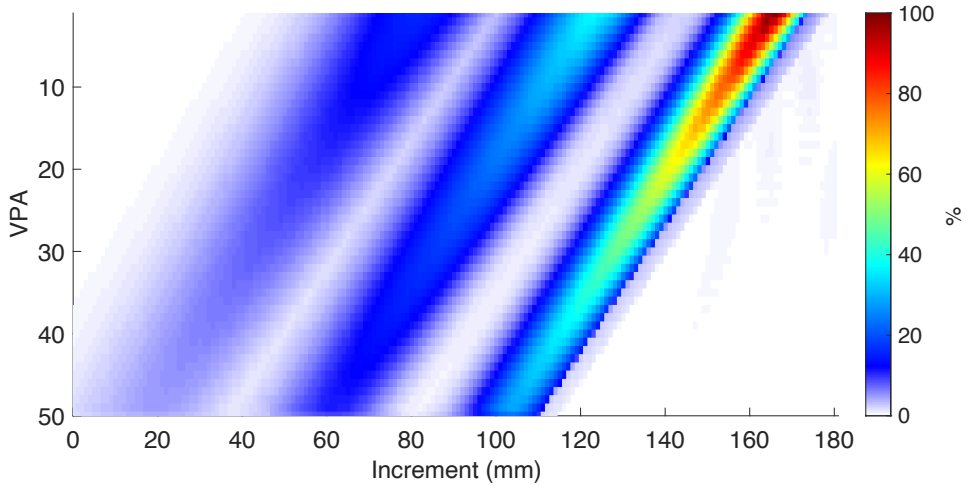

Figure 95: CMS-1 recreation of CIVA-generated C-scan of SDHs

After defining the inspection setup parameters within CMS-1, the TOF from each probe element to each volume coordinate along the wave propagation centreline within the wedge and structure can be calculated. Inspection setup parameters include material longitudinal/transverse velocities, probe/wedge dimensions, refraction angle, scan step size and active aperture size. Aligning the imported A-scan data of each aperture on each scan step with its corresponding coordinate, the depth associated with each of the data points in the C-scan can be quantified.

Implementing a peak detection function, the CRAs associated with the maximum response of each SDH for each aperture can be generated. For the calibration simulation shown in Figure 94, Table 25

presents the CRAs extracted for the first five active apertures at the average depth those responses were acquired at, across all apertures:

Table 25: Example of the outputted CRA table from CMS-1

Active Apertures	SDH Depths (mm)		
	36	60.5	85
1	0.10262	0.038371	0.016129
2	0.099816	0.036928	0.015957
3	0.097645	0.036186	0.015578
4	0.094515	0.035324	0.015079
5	0.092374	0.034511	0.014589
...	...	...	...

CRA tables, such as Table 25, are saved as Excel files, so that they can be imported into CMS-2. On this occasion, the three selected SDHs were simulated together in a single model setup to generate the CRAs in Table 25. However, CMS-1 has the functionality to build a table of CRAs based on multiple calibration simulations. Each time CMS-1 is run, a check is carried out to determine whether a file containing a CRA table for an identical setup has already been created.

If a previous file is not found, a new file is created. If one already exists, it is imported and the CRAs from the new calibration file are added. On occasion, more than one calibration simulation may have been carried out. A scenario where that may be the case is if the text file exported from a single calibration simulation is too large to be imported into MATLAB. Alternatively, multiple simulations may be needed if the position of one calibration SDH causes interference the signal from another. Interference can be referred to as casting a dead zone shadow over another SDH or the edge of the response constructively interfering with another flaw.

5.1.2 Custom MATLAB Script 2 - TCG Calibration

CMS-2 follows the same import process as CMS-1 but using the inspection simulation data, rather than the calibration simulation data. The calibration table generated from CMS-1 (such as Table 25) is also imported and linear interpolation is applied to acquire the relative calibration CRAs for depths intermediate of SDH depths for each aperture at given step size.

Linear interpolation is carried out to replicate an experimental calibration to acquire the gain settings to be applied to indications at depths intermediate to the depths of the calibration SDHs. The interpolation step size is limited by the time step of the imported A-scan data. By choosing an interpolation step that is too small, there may not be an A-scan time step that aligns with that depth while too large an interpolation step may result too many rounded A-scan time steps aligning with that depth and responses being overlapped.

Performing the interpolation creates a calibration matrix of all CRAs for each depth on each designated aperture to be applied to the inspection simulation. For all calibration matrices within this thesis, the interpolation step size was selected to be 0.5 mm. At this point, the CRAs represent the SDHs giving a 100% amplitude response, rather than an 80% FSH response. Prior to applying the calibration matrix to the inspection simulation, its CRAs must be adjusted to produce the amplitude responses relative to a SDH at 80% FSH, to adhere to UK Defence Standard 02-729 Part 5 [52]. All the values in the calibration matrix are adjusted by dividing the CRAs by 0.8.

After importing this inspection data text file into CMS-2, the CRA data can be extracted and organised into a 3D matrix. The matrix is structured such that each layer represents each active aperture with each column being the A-scan for each scan step and each row correspond to each time step.

Identical to CMS-1, after defining the inspection setup parameters, the TOF from the centre of each active aperture to each volume coordinate along the wave propagation centreline within the wedge and structure can be calculated. The amplitude response at each coordinate is calibrated relative to the CRA, from the calibration matrix, at the depth and on the aperture that the coordinate is located on. With the A-scan data calibrated and the coordinates for each time step on each aperture and on each scan step calculated, another 3D matrix can be generated to represent individual S-scans for each aperture.

When performing a TCG calibrated experimental scan, only the indications found beyond the depth of the shallowest calibration SDH depth can be measured. Therefore, any simulated amplitude indications occurring at a depth shallower than the first SDH calibration depth, the percentage response cannot be considered and are subsequently set to zero. Similarly, for any indications located beyond the deepest SDH calibration depth, the amplitude response is relative to the gain setting of the deepest SDH. This is a standard outcome when implementing a TCG on a PAC such as an OmniScan MX2 in the field. To replicate this, any simulated indication amplitudes beyond the deepest SDH calibration depth are calibrated against the deepest calibration CRA on the respective aperture.

5.1.3 Performance Results & Evaluation

A common methodology to verify that an effective TCG has been generated is to re-scan the calibration. To confirm the validity of a TCG calibration, the amplitude responses should be as expected (in this case 80% FSH). For clarity, in relation to the flow chart from Figure 93, this example uses the SDH scan as both the calibration and inspection simulations. Therefore, the amplitude responses from each of the SDHs should be 80% FSH. As mentioned, from the 3D matrix is of S-scans for the individual apertures of an inspection scan. Performing a calibration check on the calibration simulation setup shown in Figure 94; Figure 96 illustrates an example of a calibrated sector scan (S-scan) of the calibration block generated from CMS-2 for aperture 25:

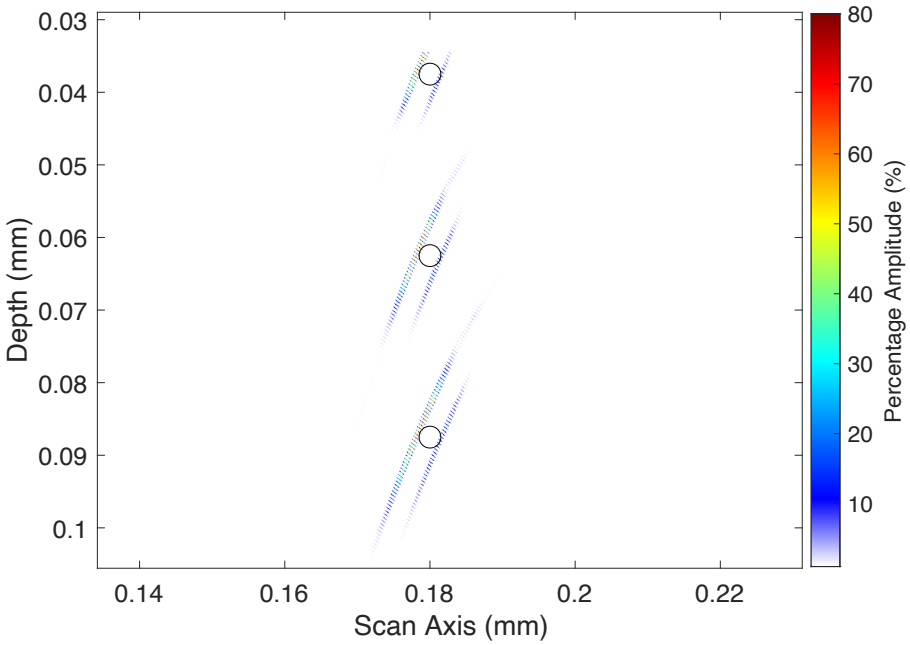

Figure 96: Zoomed calibrated S-scan of three SDHs at depths of 37.5, 62.5 and 87.5 mm for aperture 25 from CMS-2

Similar to that Figure 96, Figure 97, Figure 98 and Figure 99 show the comparison of the uncalibrated CIVA data against the CMS-2 calibrated responses for each SDH depth across all apertures:

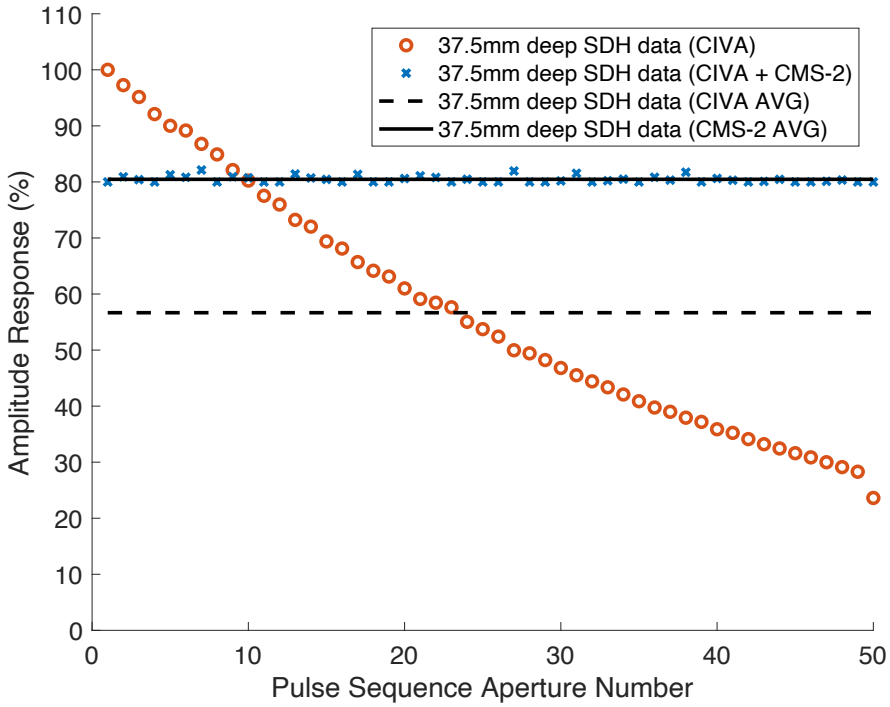

Figure 97. Implementation of CMS-2 TCG calibration to 37.5 mm deep SDH

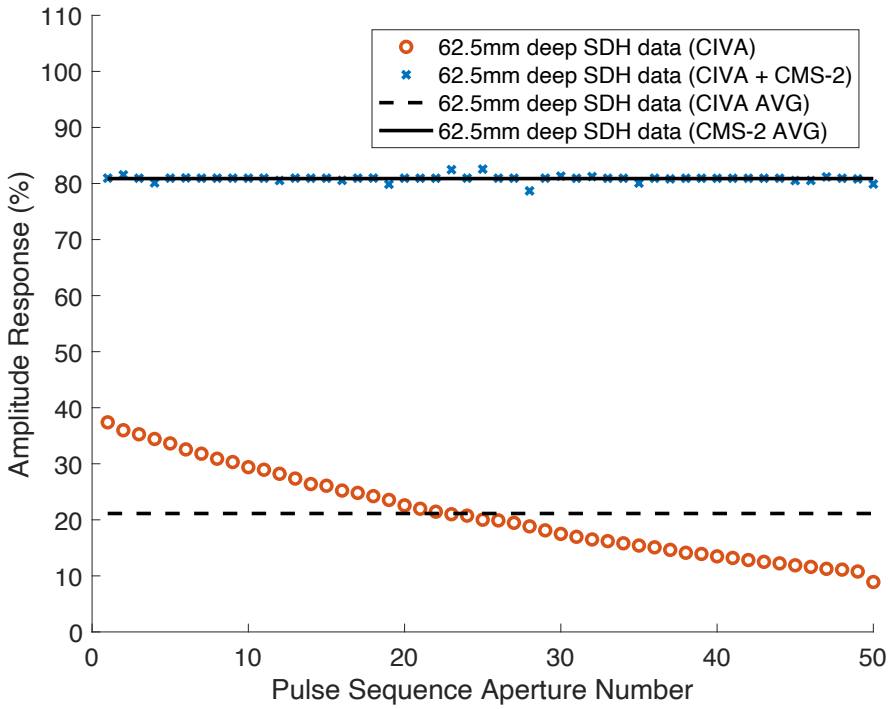

Figure 98: Implementation of CMS-2 TCG calibration to 62.5 mm deep SDH

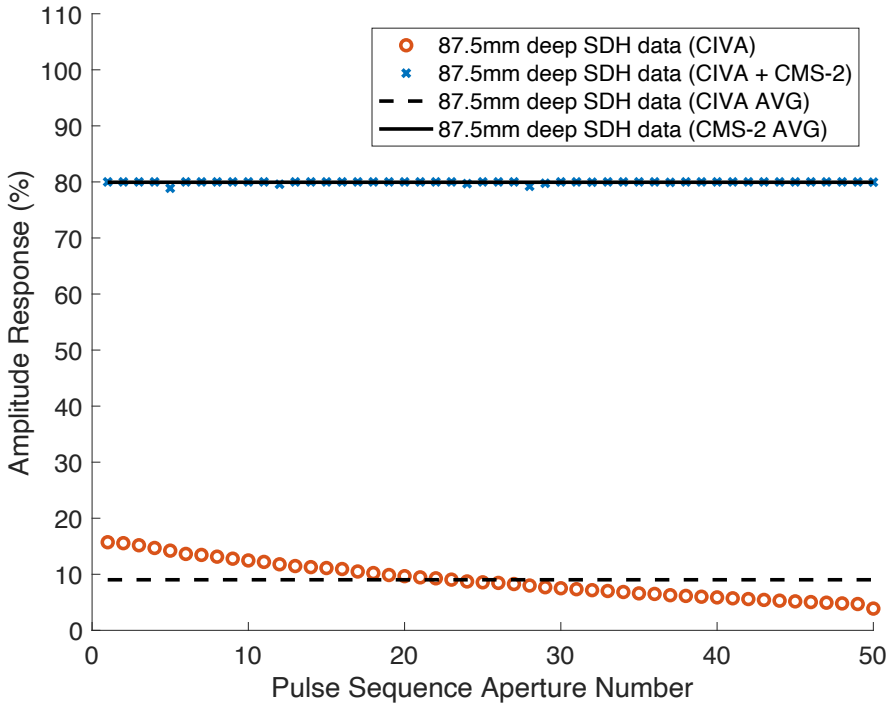

Figure 99: Implementation of CMS-2 TCG calibration to 87.5 mm deep SDH

Across the three figures, as expected it can be clearly seen that with increasing SDH depth, the average amplitude response of raw uncalibrated data (orange circles) across all apertures decreases. Closer analysis of the uncalibrated response data for each SDH depth independently shows a smaller decrease in amplitude with increasing aperture number. By comparison, the CMS-calibrated data demonstrates the percentage responses been normalised for all active apertures at each SDH depth to 80% FSH.

Aggregating the average amplitude responses from Figure 97, Figure 98 and Figure 99, Figure 100 presents a comparison of average uncalibrated amplitude response data with the average calibrated amplitude response data for each SDH depth:

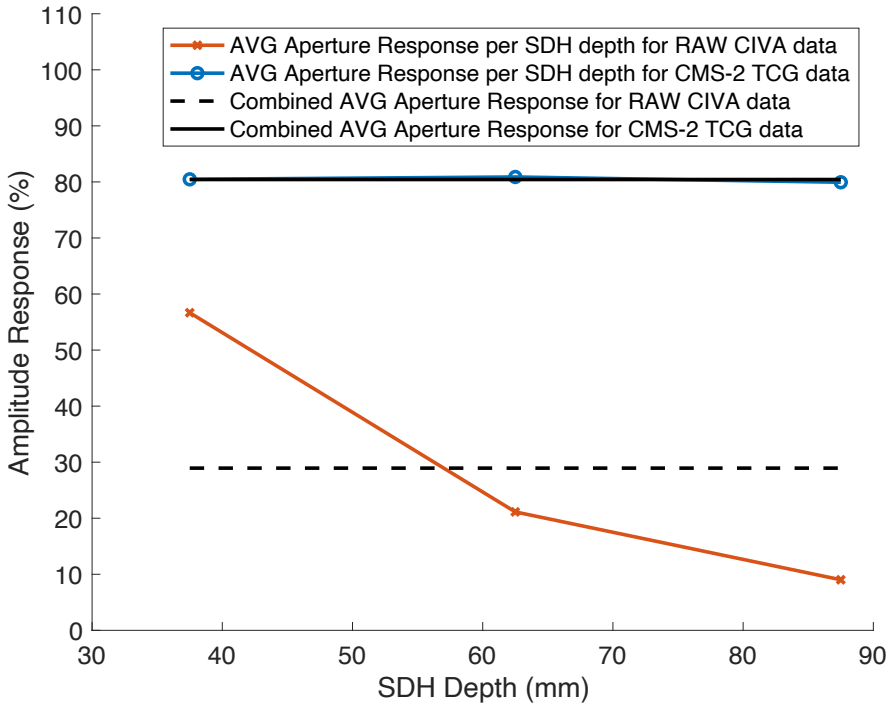

Figure 100: Average CMS-2 TCG calibrated responses across all active apertures per SDH (accounting for attenuation)

Figure 100 clearly shows the average calibrated amplitude response across all the SDH depths to be 80.43% FSH, which aligns with the desire outcome of TCG calibration to 80% amplitude response. This approach is not solely applicable to simulations accounted for attenuation. Repeating the same simulation setups with 3D computation without accounting for attenuation, Figure 101 presents a comparison of the average uncalibrated amplitude response data with the average calibrated amplitude response data for each SDH depth:

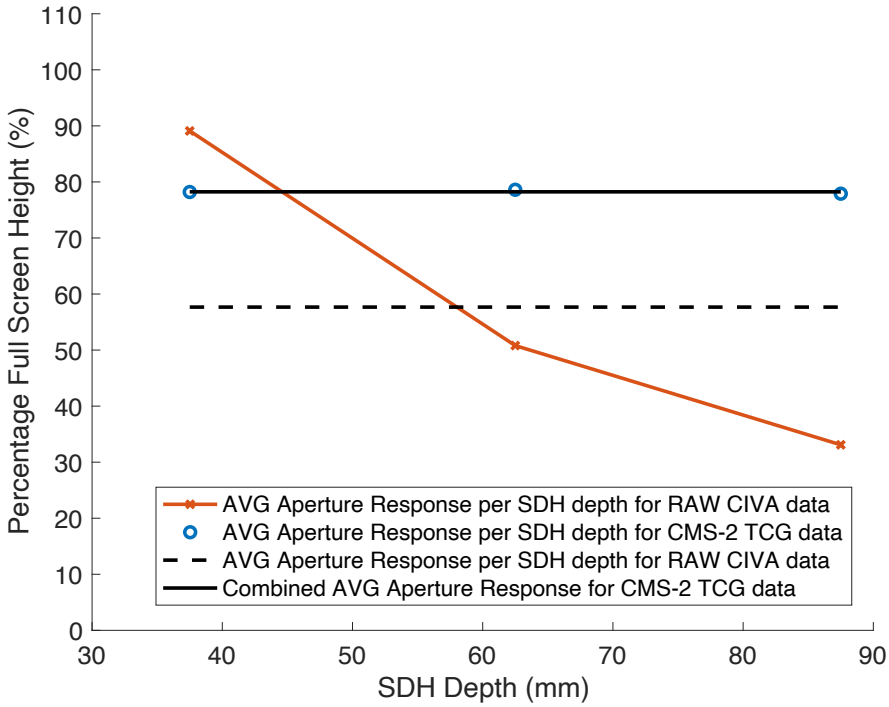

Figure 101: Average CMS-2 TCG calibrated responses across all active apertures per SDH (not accounting for attenuation)

As shown in Figure 101, the average calibrated amplitude response across all the SDH depths to be 78.23% FSH. It therefore demonstrates the capability of effectively implementing a TCG to CIVA simulations regardless of whether attenuation is accounted for or not.

Two potential limiting factors that could affect the CMS's ability to acquire an exact 80% FSH calibrated response include:

- Differences between the averaged SDH depth, used to create the CRA table outputted from CMS-1, and the actual depth of the maximum response for each active aperture

- The scan step of the probe during the calibration simulation was set to 1mm. Therefore, as each aperture centreline

scanned over the SDH, the size of the scan step may have prevented normal incidence from occurring with the SDH. This results in a reduced amplitude response caused by increased scattering by the SDH. To determine whether a smaller scan step improves performance, the simulation setup for was repeated using a 0.25 mm scan step. To reduce simulation time, this simulation was commutated in 2D. Figure 102 presents a comparison of the outputs from the CMS-2 TCG when 0.25 mm and 1 mm scan steps are implemented:

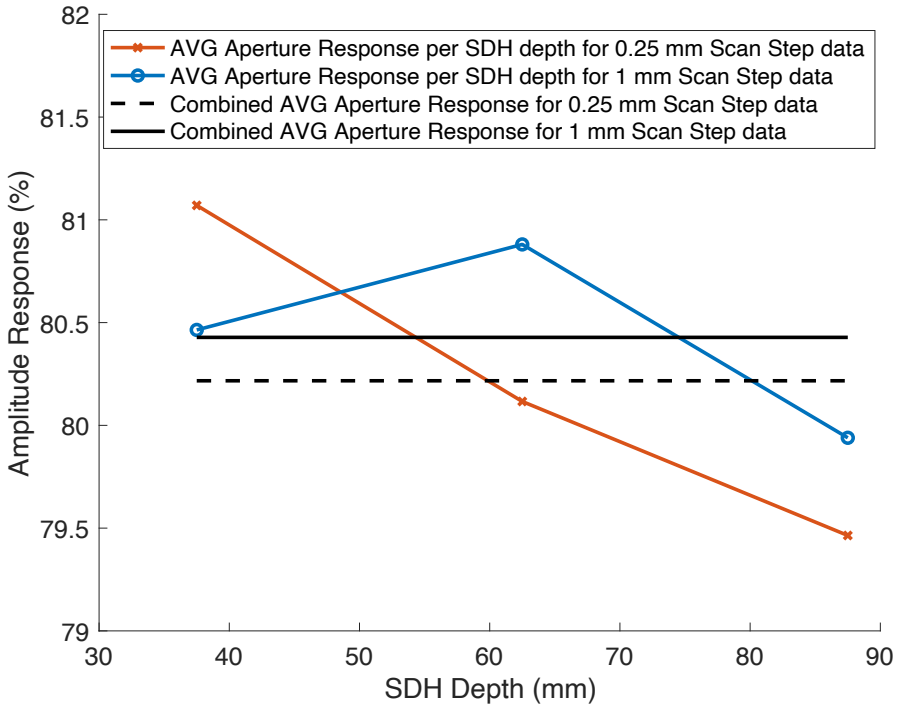

Figure 102: Performance comparison of average CMS-2 TCG calibrated responses between 0.25 mm and 1 mm scan steps

Despite a smaller scan step being used, the performance in implementing the TCG is very similar, where

the combined average for the 0.25 mm scan step is 80.22%. Despite the 0.25 mm scan step over halving the percentage error of the average response (from 0.538% to 0.275%) relative to 80% screen height target, the performance of the 1 mm scan step is sufficient. Furthermore, by simulating four times as many scan steps, this significantly increases simulation time, file size and processing time for no improvement in performance.

When carrying out a physical TCG calibration, the calibrated responses may not normalise to exactly 80% FSH either. This can potentially be linked to limitations in minimum gain step of the system when calibrating or variations in probe positioning/orientation and coupling efficiency when rescanning. Despite the margin of error from the 80% being left to the discretion of the inspector, the upper and lower amplitude response bounds are typically set to 75% and 85% FSH, respectively, for an SDH.

Therefore, the custom calibration process presented in this Chapter can be considered a successful application of a TCG for SDH reflectors. However, further investigation is required to determine how effective the approach is at normalising the amplitude responses from alternate flaw types and if the predicted amplitude responses align with experimental scan data - this will form the basis of the next Chapter of the thesis.

5.2 Custom Test Specimen Inspection Setup in CIVA

As previously mentioned, for this thesis, linear scanning PAUT will be carried out in accordance with Defence Standard 02-729 [52]. Therefore, when investigating a backwall dead zone/remote surface using a 60^0 inspection angle, the PAC would be configured to record data from one half-thickness before the backwall to one half-thickness after the backwall [52].

As an example, a 50 mm thick butt weld would require its first TCG point to be at or shallower than 25 mm and its last TCG point at or beyond 75 mm. Applying these example boundaries to the inspection setup of the custom-built validation block, the amplitude response from reflectors within this depth range, specifically the FBHs at 37.5, 42.5, 50, 67.5 and 75 mm, can be approximated. Using the same pulsing sequence described in previous sections for a 60^0 inspection angle of 50 11-element apertures, the three inspection setups in Figure 103, Figure 104 and Figure 105 were simulated within CIVA:

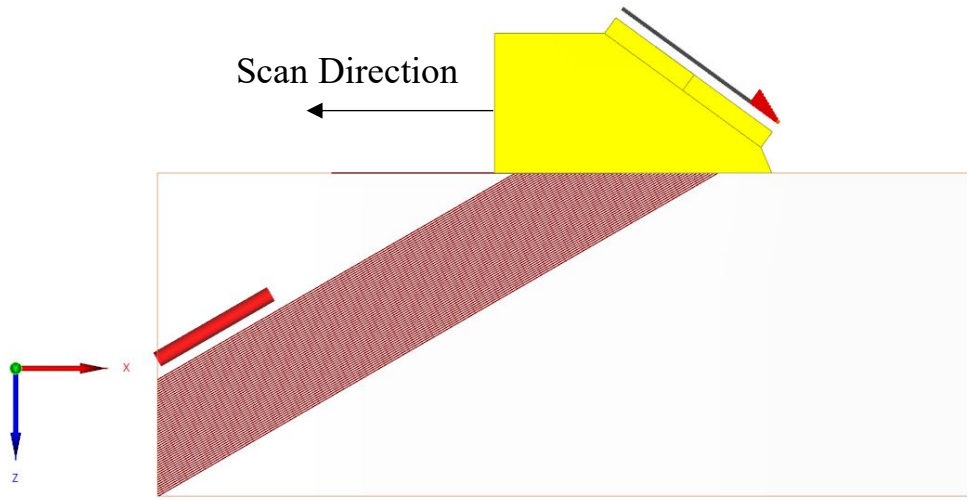

Figure 103: PAUT inspection setup of 37.5 mm deep FBH in CIVA

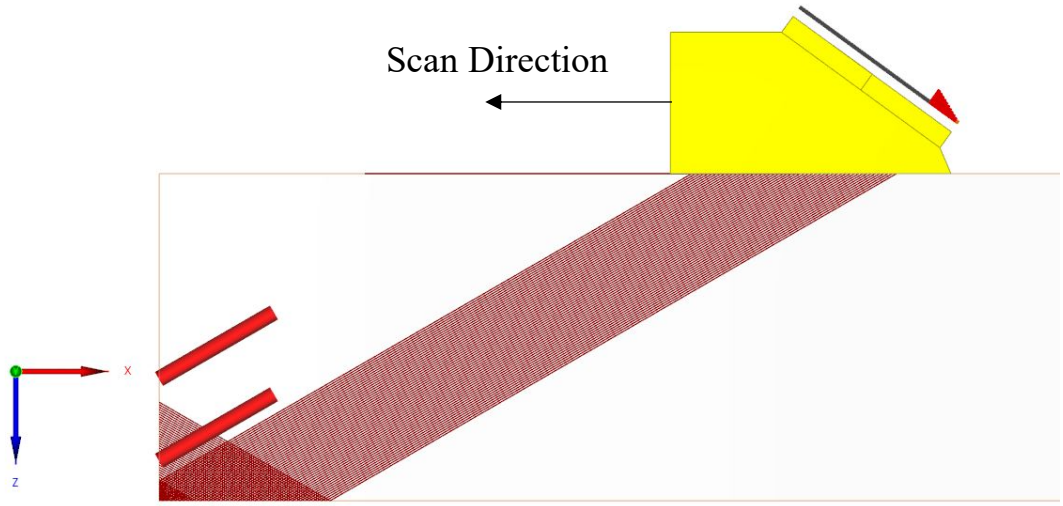

Figure 104: PAUT inspection setup of 42.5 mm and 67.5 mm deep FBHs in CIVA

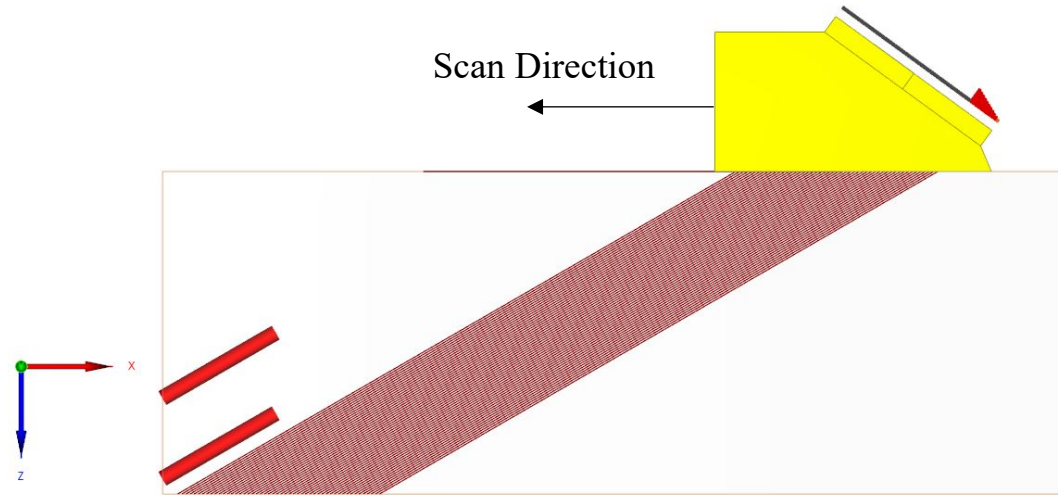

Figure 105: PAUT inspection setup of 50 mm and 75 mm deep FBHs in CIVA

Like the simulations presented in Section 5.1.3, these simulations were completed for both combinations of 3D computation with and without attenuation accounted for (using the same attenuation coefficients, where applicable).

5.3 Custom TCG Calibration of FBH data

To ensure effective calibration, equally spaced TCG points using 3 mm SDHs at 25, 50, 75 and 100 mm depths were selected, thus covering the first FBH depth, beyond the deepest FBH depth and at two appropriately separated depths within the scanning region. Extracting the calibration response data for these selected SDH depths using CMS-1, the three inspection simulations were calibrated using CMS-2. The maximum amplitude response for each active aperture at each FBH depth can then be isolated to examine whether the inspection simulations of all FBHs produce comparable approximates to one another. Figure 106, Figure 107, Figure 108, Figure 109 and Figure 110 present a comparison of the raw (uncalibrated) CIVA response data with attenuation accounted for against the CMS-2 calibrated data for each active aperture at each FBH depth:

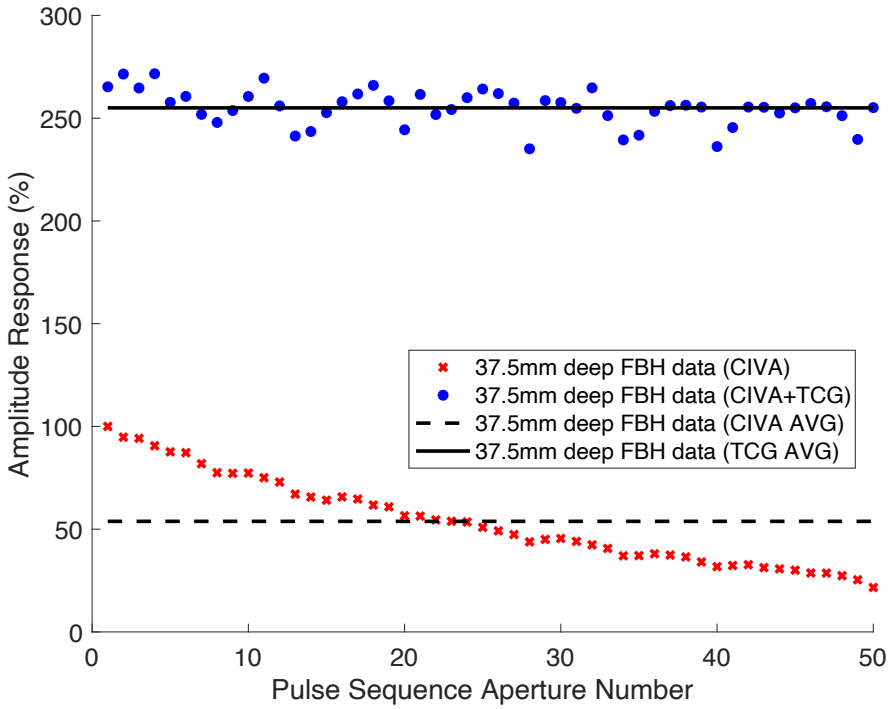

Figure 106: CMS-2 TCG calibrated response data for FBH at 37.5 mm depth (with attenuation accounted for)

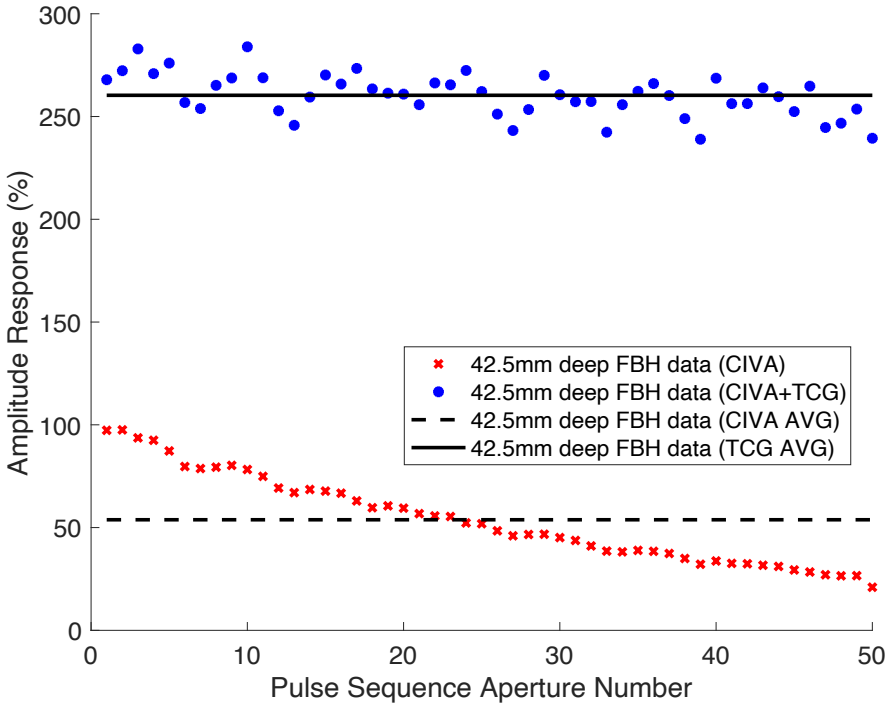

Figure 107: CMS-2 TCG calibrated response data for FBH at 42.5 mm depth (with attenuation accounted for)

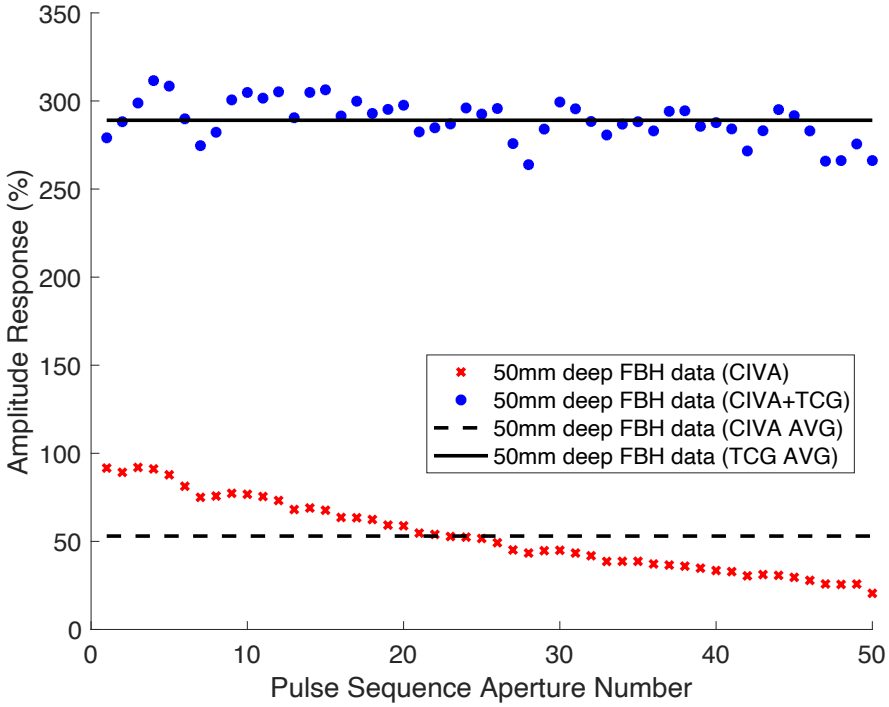

Figure 108: CMS-2 TCG calibrated response data for FBH at 50 mm depth (with attenuation accounted for)

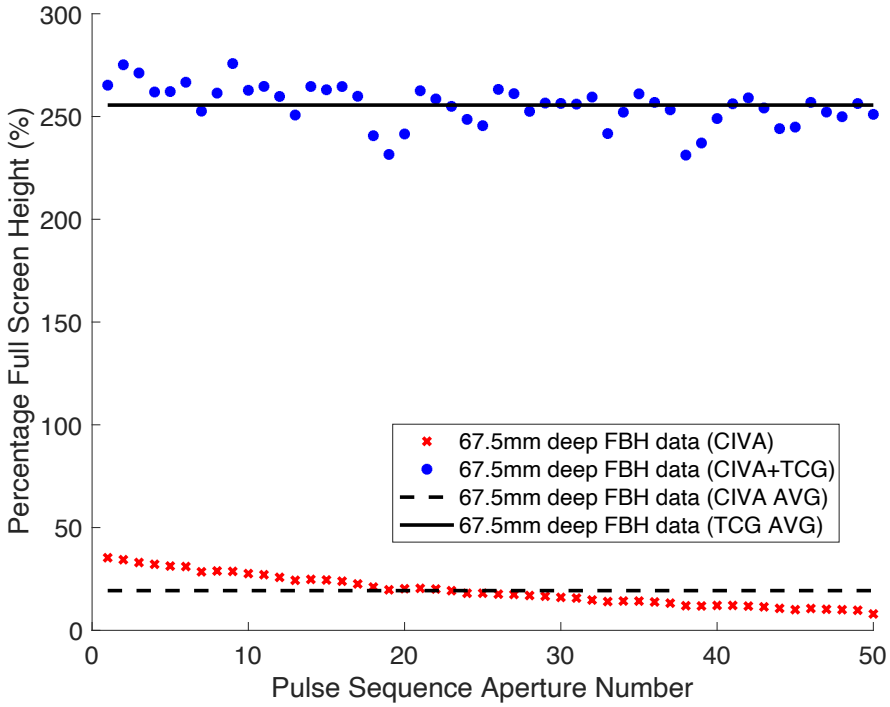

Figure 109: CMS-2 TCG calibrated response data for FBH at 67.5 mm depth (with attenuation accounted for)

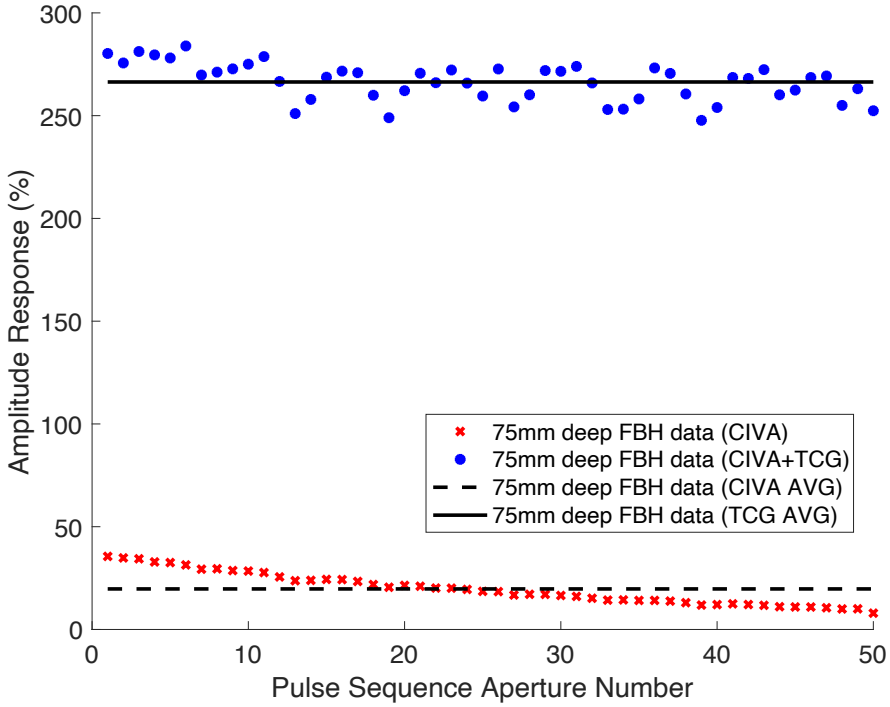

Figure 110: CMS-2 TCG calibrated response data for FBH at 75 mm depth (with attenuation accounted for)

Figure 111, Figure 112, Figure 113, Figure 114, and Figure 115 present a comparison of the raw (uncalibrated) CIVA response data with attenuation not being accounted for against the CMS-2 calibrated data for each active aperture at each FBH depth:

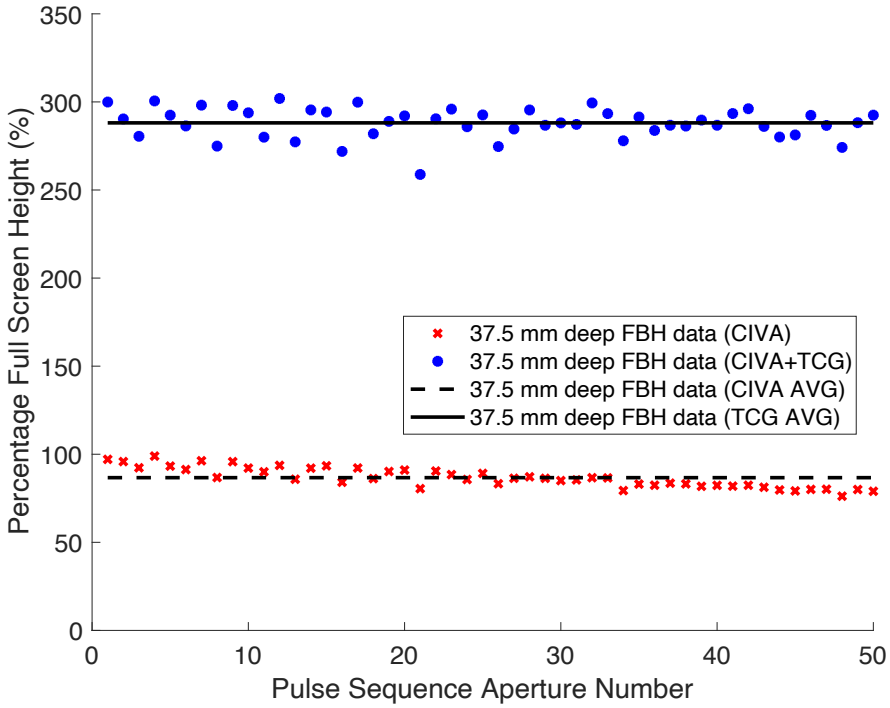

Figure 111: CMS-2 TCG calibrated response data for FBH at 37.5 mm depth (with attenuation not accounted for)

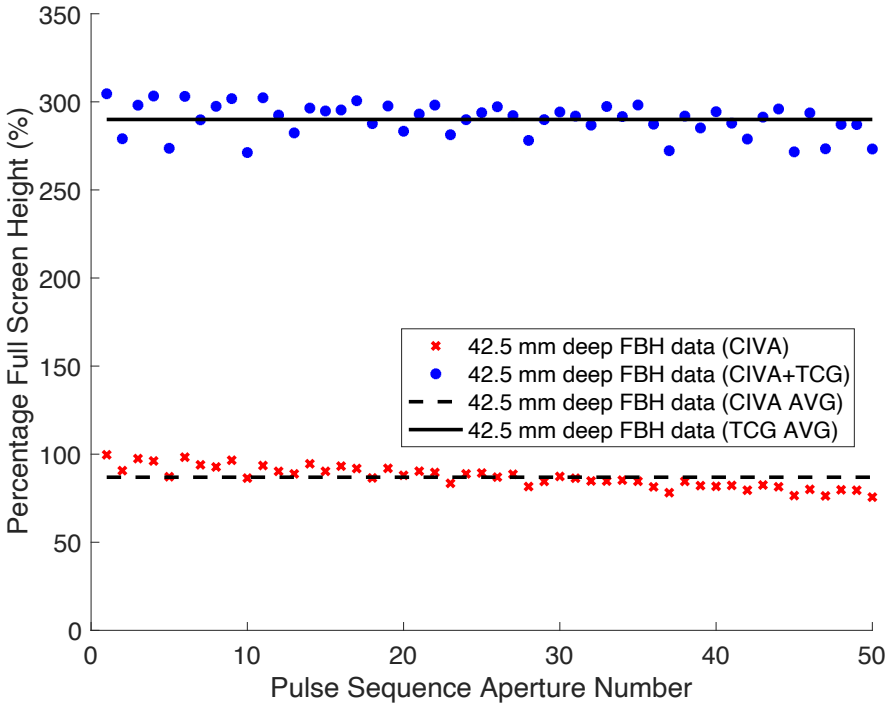

Figure 112: CMS-2 TCG calibrated response data for FBH at 42.5 mm depth (with attenuation not accounted for)

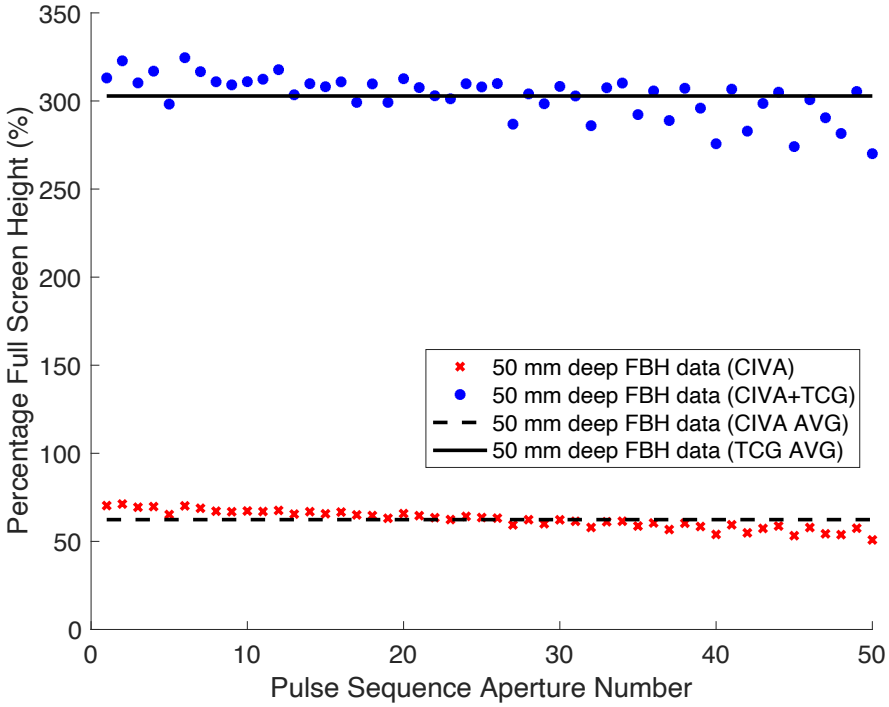

Figure 113: CMS-2 TCG calibrated response data for FBH at 50 mm depth (with attenuation not accounted for)

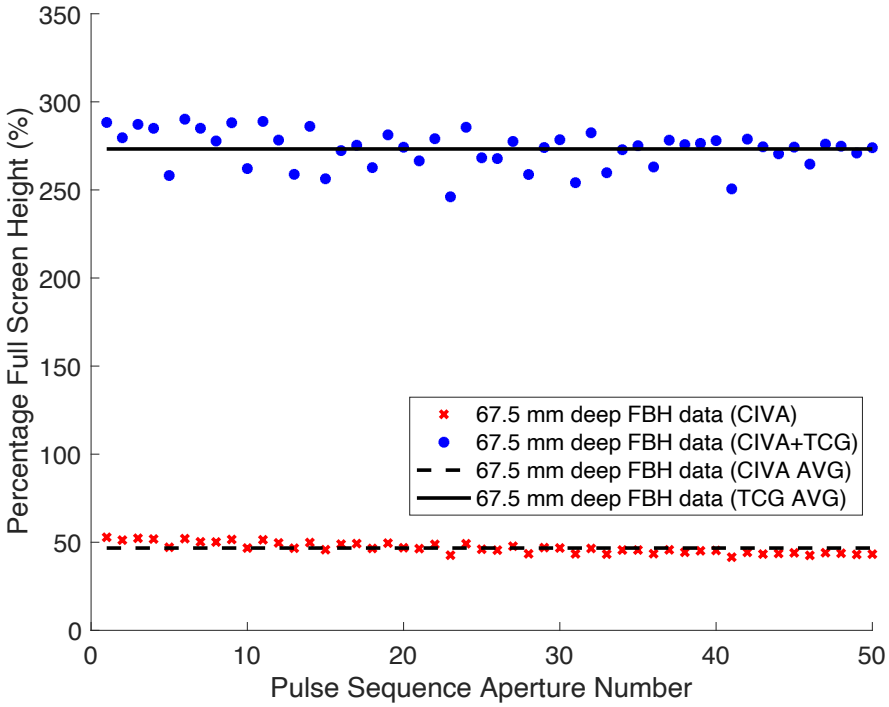

Figure 114: CMS-2 TCG calibrated response data for FBH at 67.5 mm depth (with attenuation accounted for)

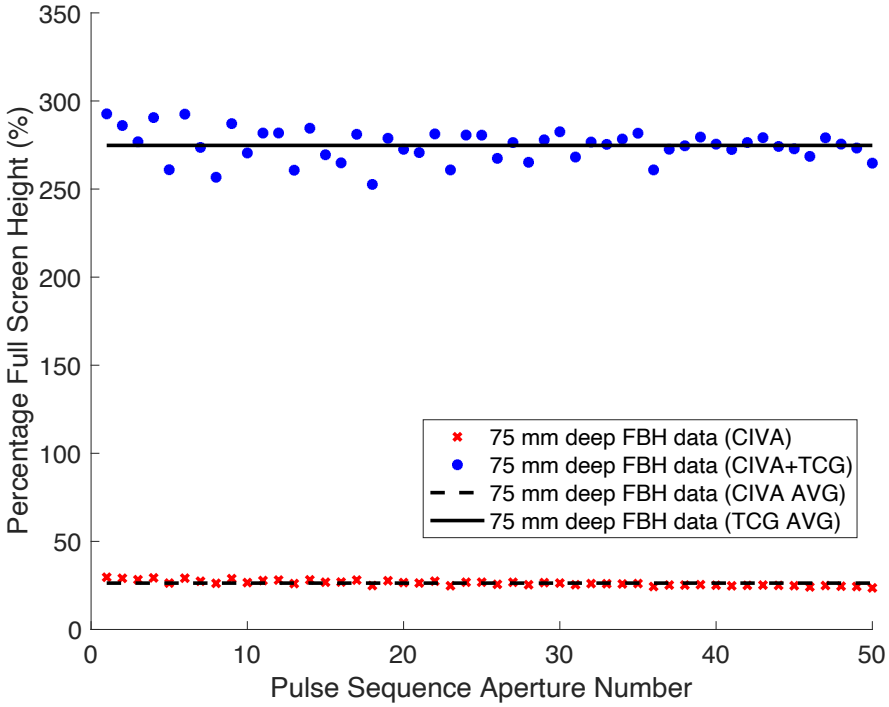

Figure 115: CMS-2 TCG calibrated response data for FBH at 75 mm depth (with attenuation accounted for)

Across the 10 figures shown above, the simulated amplitude response data from each of the FBHs, regardless of whether attenuation has been accounted for or not, have been calibrated to within acceptable percentage differences from one another. To verify whether the calibrated approximations are representative of experimental FBH response data, each of the physical inspections setups shown in Figure 103, Figure 104, and Figure 105 were created and carried out. Figure 116 presents the calibrated percentage amplitude response data acquired on apertures 1, 10, 20, 30, 40 and 50 for each FBH depth:

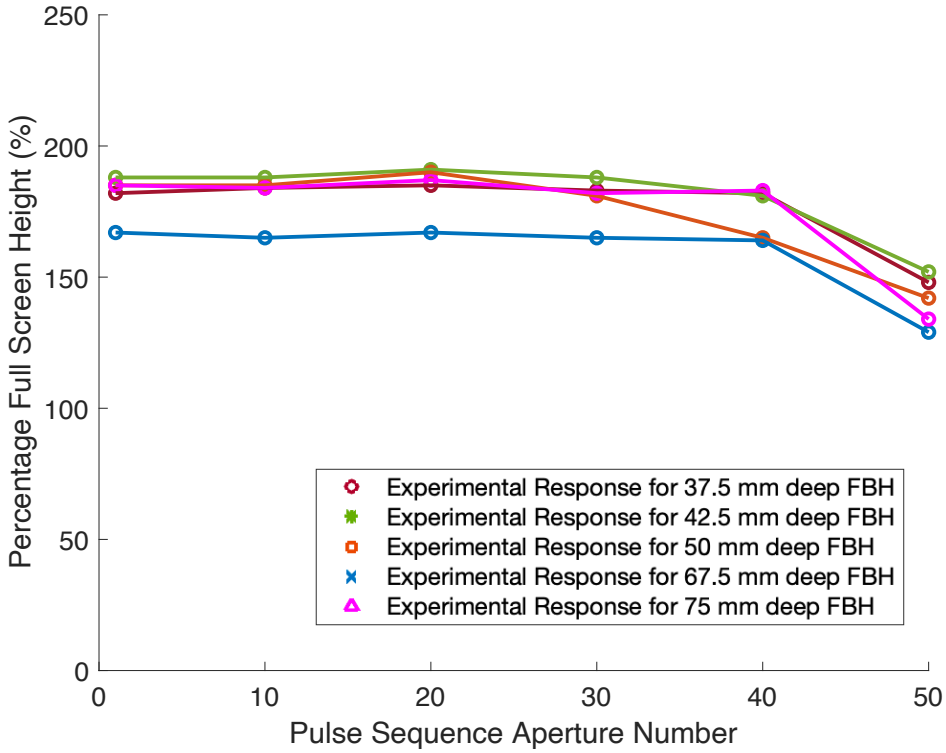

Figure 116: Experimental percentage responses from FBHs at various depths

It is clear from the comparison of Figure 116 with the previous 10 figures that there is a large discrepancy between the simulated and experimentally acquired data when comparing the average amplitude response across all apertures and for each FBH depth. The source of this

disparity is linked to the raw simulation data not being comparable to uncalibrated response data from a physical inspection setup. This is profoundly influential on the magnitudes of the CRAs used to implement the TCG and the compatibility of the calibration simulations with the inspection simulations.

Addressing the first issue, should the percentage amplitude responses curve acquired by SDHs in the calibration simulation not be representative of that acquired in a physical calibration procedure, then the simulated TCG would not be implemented accurately. Therefore, a sensitivity calibration is required, based on experimental, sensitivity calibrated SDH response data, to rectify the CRAs.

Regarding the second issue, the calibration and inspection simulations use two different approximation algorithms. The calibration simulation implements the SOV algorithm for SDHs while the FBHs in the inspection simulation are approximated using KA. As demonstrated in Section 4.4.3 and Section 4.4.4, the two approximation alorithms can appropriately simulate the two defect types respectively and acquire the relative amplitude responses between identical defects at different depths. Due to the different reflector types implementing different approximation algorithms, the CRAs of the two simulations are not calculated in a manner that are relative to one another. This is made clear by the simulated amplitude relationship between the SDHs and the FBHs not being representative of the physical inspection relationship. Therefore, applying the current version of the TCG calibration would not be appropriate.

5.4 Further Development of Custom TCG - Simulation Gain Calibration Enhancement

In any physical inspection scenario, the properties that define how waves propagate through the material and interactions at material boundaries are constant, regardless of what flaw geometry is being examined. The same properties and scientific principles that govern the investigation of a SDH would be applied to that of an FBH. Therefore, the amplitude responses of each flaw type can be compared relative to one another.

When replicating and simulating the inspections of these two flaw types in CIVA, two different approximation algorithms are used to predict the amplitude responses from the two flaw types. Irrespective of whether both algorithms are effective at replicating the dB responses of each flaw when compared with raw experimental data, it is critical that the relative percentage amplitude responses between the two flaw types are consistent.

As shown previously in Section 5.3, when calibrating the simulated inspection of FBHs based on SDHs, the relative amplitude responses are not accurately representative of those acquired experimentally. Therefore, additional factors must be applied to the raw CRAs of inspection simulations such that they are proportional to the CRAs of the calibration matrix to be appropriately representative of the experimental percentages of the SDHs against FBHs. This will create the required correspondence between the calibration and inspection simulations for improved amplitude response approximation. An approach to calibrate inspection simulation CRA data is to apply a gain

factor to the amplitude responses of the simulation based on the experimental amplitude responses of a known flaw across all apertures.

To illustrate the approach and demonstrate that expected amplitudes are achieved when applied, raw experimental FBH data relative to a SDH at 100% is used to calibrate the raw simulated inspection of the same FBH. This occurs prior to being made relative to the 80% FSH response of the same SDH, applied using a TCG. Figure 117 presents the raw percentage response data acquired from three amplitude responses on selected apertures for FBHs at 25, 50 and 75 mm depths with the system gain of the OmniScan adjusted to produce 100% FSH response for a SDH at the same corresponding depth:

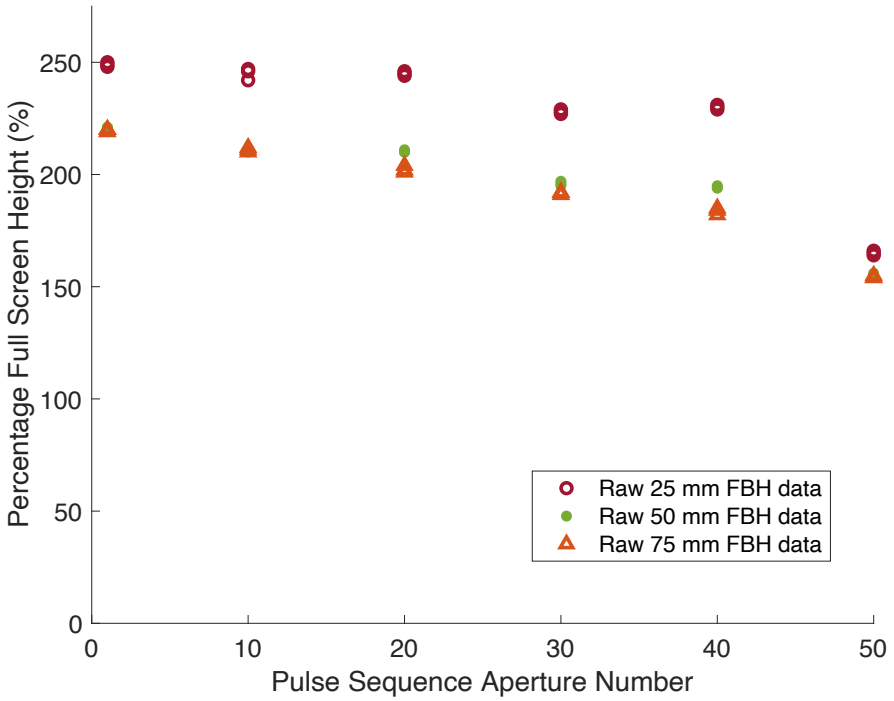

Figure 117: Experimental FBH percentage responses for SDHs at the corresponding depth with a 100% FSH response

Table 26 presents the average relative FBH amplitudes at each aperture number across the three SDH depths from Figure 117:

Table 26: Average FBH amplitude responses for experimental system gain settings when SDH response is at 100% FSH [108]

Aperture	1	10	20	30	40	50
(%)	230	222	219	205	203	158

Using these percentage amplitudes, the raw CIVA inspection simulation can be calibrated through the following steps, prior to a TCG calibration being applied:

1. The CRA data for each aperture is adjusted relative to the simulated 100% FSH response from a FBH at the respective depth from the calibration simulation. In a similar manner to acquiring the CRA data for SDHs, FBH CRA data can be acquired by passing inspection simulation data through CMS-1.

2. Quantifying the largest response on each aperture, all percentage amplitudes are divided by the largest response of their respective aperture (to acquire a decimal factor).

3. Each value is multiplied by the interpolated raw FBH percentages from Table 26 respective to its aperture.

4. After dividing each percentage value by 100, the data is multiplied by a matrix of CRAs for SDHs at 100% FSH on each aperture and at each respective depth. This ensures that the inspection data can

be TCG calibrated by the sensitivity calibrated SDH calibration matrix.

These steps were applied to the inspection data of the five FBHs and applying the TCG calibration to the sensitivity calibrated SDH calibration matrix. Figure 118 presents how experimentally calibrated simulation data through the updated TCG script (TCG 2 - with and without attenuation accounted for in simulation) compares with the results from the application of the initial TCG script (TCG 1- with and without attenuation accounted for in simulation), and the experimentally acquired data, for each of the selected apertures:

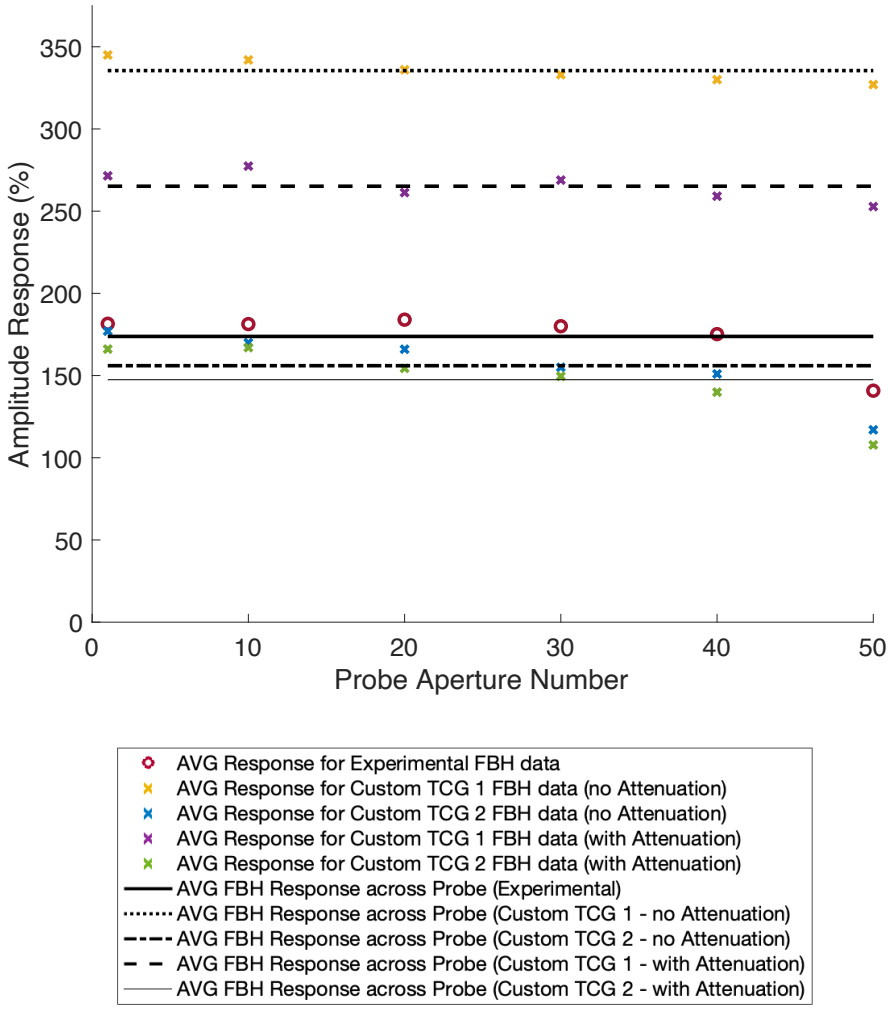

Figure 118: Comparison of averaged FBH data sets for calibrated experimental data, initial custom TCG data and updated custom TCG data (with and without attenuation accounted for in simulation) across all active apertures

Figure 118 shows that experimental sensitivity calibration data and raw experimental data can be combined into a simulated TCG to improve the approximation of the average percentage FSH response for FBHs at multiple depths and across all generated apertures. This statement is applicable to both simulation setup cases of with and without attenuation being accounted for. With the average FBH response experimentally being 173.8%, the average FBH response for the simulations without attenuation considered moved from 335.5% to 156%, and the simulations with attenuation considered moved from

265.2% to 147.5%. Between the two cases, the calibrated approximations from the no attenuation simulations performed better than the simulations with attenuation considered.

A potential factor is the difference in variance in calibrated data observed between the two differing simulation setups from the initial attempts at implementing the TCG (Figure 106 to Figure 115). The calibrated data within the simulations accouting for attenuation have a noticeably greater spread relative to the mean response by comparison to the no attenuation simulation calibrated data.

Consequently, this could potentially increase the likelihood of variations in application of the gain calibration enhancement. The calibrated percentage amplitude of the same coordinate in both simulation setups may differ slightly based on the raw amplitude relative to the largest in the simulation. Another reason to be considered is that there may still be some discrepancy in the attenation coefficients approximations made.

Further analysis of the data shows that there is a noticeable decrease in amplitude response between apertures 40 and 50. This could be associated with interaction from the wedge's side wall as it becomes increasing prominent with the increasing aperture number.

In must be noted that repetitions of the same physical inspection will not produce the exact same amplitude responses due to variations in couplant layer, probe orientation and pressure, element to element sensitivity, and flaw geometry. Therefore, it should not be expected that

the approximated amplitude response can ever be exact, despite the demonstrated improvements in the simulated amplitude response approximations using the updated simulation TCG against the experimental.

The intention for this approach is to obtain better agreement between the calibration and inspection simulations using a known flaw of known amplitude response. By using the experimental response data of a known flaw (such as an FBH relative to an SDH) to calibrate the inspection simulation; an inspection setup with other flaw types can be approximated relative to the known flaw. Further development to the calibration script and investigation of a known butt weld sample will demonstrate this capability.

5.5 Butt Weld Sample Inspection

CIVA has been shown to produce comparable results to experimental data across numerous areas for both UT and PAUT inspection setups [95, 109]. Where the methodology presented here differs from previous work is:

- The combination of settings for the simulation setups in the calibration and inspection simulations of this approach extend beyond what has already been investigated [3D computation mode of a full-skip shear wave inspection of thick steel (> 25 mm) using a linear scanning PAUT setup]

- This approach incorporates a custom TCG calibration for simulated linear scanning PAUT setups that fully replicates the experimental setup

- Other research papers have solely relied on the simulation approximations of calibration reflectors to calibrate inspection simulations. This approach incorporates the experimental amplitude response of two physical calibration reflectors to calibrate the inspection simulation.

To validate the proposed approach, a test sample containing defects of known size, position and characterization was inspected experimentally and simulated within CIVA for comparison. A planar view of the sample with several defects is shown in Figure 119:

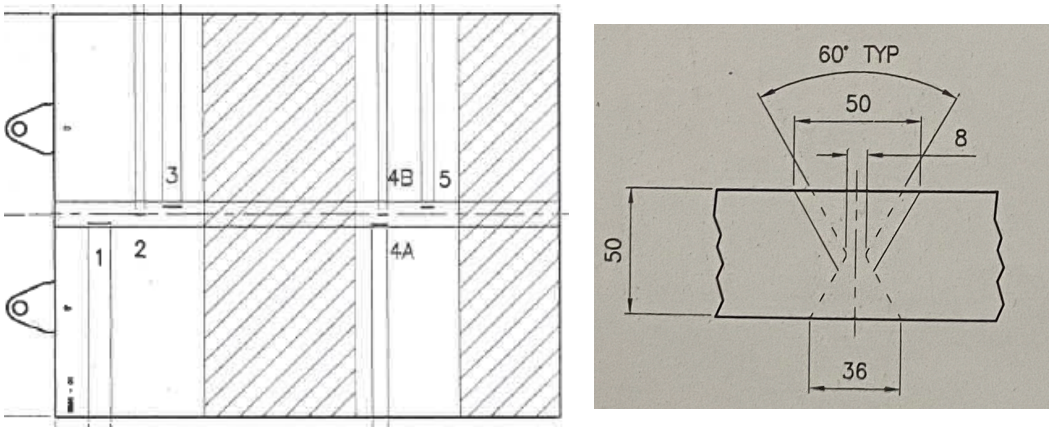

(a) (b)

Figure 119: Butt weld test specimen: (a) planar view, (b) weld geometry

The sample is a 997 mm long, 808 mm wide and 50 mm thick carbon steel plate weld joint sample. As with the manufactured block used in Section 4.4.1, typical carbon steel longitudinal and transverse wave velocities of 5900ms^{-1} and 3240ms^{-1} were used [1, 107]. These velocities were confirmed by measuring the TOF of known reflectors in a calibration block of the same material. As opposed to measuring the velocities using this sample, the adopted approach for acquiring velocities reflects what would be carried by inspectors when performing an in-situ inspection of an asset.

The specimen is a manufactured sample containing artificial defects both on the edge of the weld volume and within the weld volume material at each of the numbered locations along the length of the weld. The geometries, dimensions and positions of each defect are defined within a master drawing provided by the manufacturer based on the manufacturer's measurements using conventional UT. These defect sizes were also verified using TOFD by a PCN-qualified inspector at QinetiQ. Where measurement techniques such as radiography would

give a truer value of defect length, the scan history using ultrasonic techniques was sufficient for QinetiQ's requirements. Furthermore, the expense to ship for testing or implement radiography on-site was beyond the budgets and requirements of the project.

The inserted flaws are characterised as either LOF or crack-like defects located either within the weld material or at the parent material/weld material interfaces. The entire sample was replicated in CIVA, as shown in Figure 120:

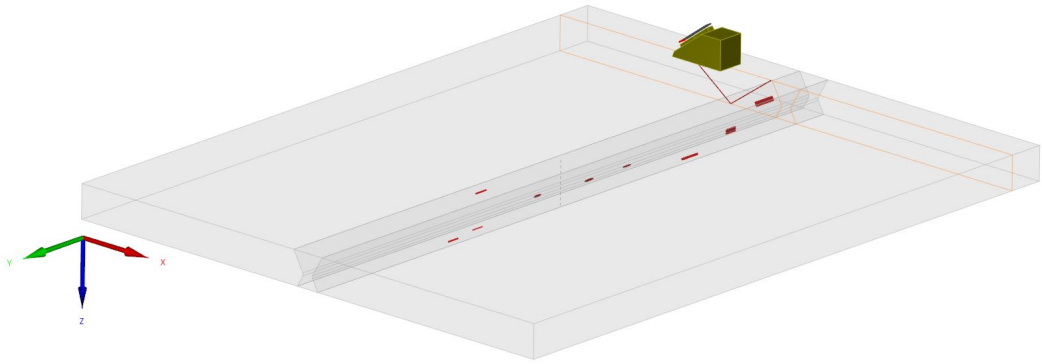

Figure 120: CIVA replica of butt weld sample

This study will focus on comparing the simulated linear scanning PAUT setup of two LOF defects, identical to the physical inspection scan carried out on the butt weld specimen. The decision to only compare the simulated and physical scans of the LOF defects was due to their simpler geometry when compared with crack-like defects. LOF defects have a simpler geometry compared to the random size and location of facets and branches stemming from a crack-like defect. Consequently, scatter from the rough, jagged geometry of a crack-like defect is difficult to predict and replicate within CIVA. By comparison, the geometry and surface area of a LOF defect is significantly more predictable.

To model a planar flaw within CIVA, it requires selecting the flaw type and entering the length and height. The flaw can then be positioned and orientated anywhere within the simulated structure. Therefore, using a planar flaw type, within CIVA, to replicate a LOF defect within CIVA will be suitable.

For the given sample, a scanning jig would be typically be considered due to the simplicity of conditions for setup. However, all scans were carried out manually to be representative of performing a scan in the field where the use of a jig may not be feasible. Experimental data capture will be performed using an OLYMPUS OmniScan MX2. As such, scan images for comparison against the experimental data will be taken as screenshots from the device due to inability to reformat in an alternate manner.

Based on the findings from Section 5.4, all the simulations of this study will be 3D computations with attenuation not being accounted for. The reasoning is that the reflective surface area of the flaws may be orientated normal to the propagating wave and thus 3D computation is required. Furthermore, negating attenuation within the calibration and inspection simulation setups yielded improved results relative to experimental data when compared against simulations accounting for attenuation.

5.5.1 Inspection Simulation Relativity Calibration

For the TCG calibration script to be applied consistently across independent inspection simulations, the simulated responses from a flaw under investigation must be made relative to the simulated response of a

FBH at the same depth. As the experimental amplitude responses of FBHs are used as part of the calibration process within the custom script, they must be used as a reference point for the raw CIVA inspection simulation data.

Therefore, by dividing all CRAs of the inspection simulation of an unknown flaw by the maximum response CRAs of FBHs at the same respective depths, a decimal factor can be applied to the experimental values used as an input to the calibration script. The matrix of CRAs for the FBH amplitude responses at all depths is acquired using a similar approach to that in Section 5.1.1 for the SDH CRA Generator. The data points for all VPAs at the chosen depths on the custom block, used prior, can be captured and interpolated. In applying this matrix to the raw CIVA inspection data, it is compatible with the settings of the calibration matrix for it to be appropriately calibrated.

After this process is applied, prior to simulated TCG, all the data can be appropriately calibrated. It must then be displayed as a C-scan so that the amplitude data of the calibrated simulation can be compared with the experimental scan data. As previously explained, the C-scan view displays the maximum amplitude acquired for each aperture at each scan step.

5.5.2 Defect 1 Geometry & Inspection Setups

As shown in Figure 121, the master drawing gives the first LOF flaw as a 3.9 mm through-thickness height planar defect, 45 mm in length, positioned 14.4 mm deep (relative to the top tip of the defect) and on the upper V weld face.

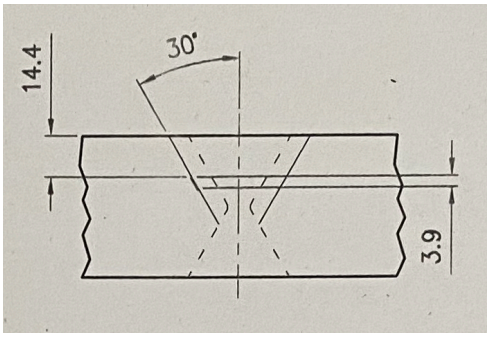

Figure 121: Butt weld LOF defect 1 dimensions

However, improved sizing capabilities of TOFD found that the defect was 6.5 mm in through-thickness height and 35 mm in length. The TOFD sizings of all defects investigated within this section were provided through internal QinetiQ inspection reports generated by a PCN-qualified inspector.

Using the TOFD-measured dimensions to recreate the flaw within CIVA, the same OLYMPUS PipeWizard probe/wedge combination and 50 11-element aperture setup, as used in previous sections, with the same calibration process must also be implemented. The flaw can then be inspected from both surfaces of the butt weld plate. From the remote surface (bottom surface in reference to Figure 121) the flaw can be inspected directly and from the top surface it can be inspected using a half skip, after a reflection from the remote surface. Figure 122 and Figure 123 illustrate the CIVA simulation probe positions setups that replicate the probe position setups of an experimental inspection:

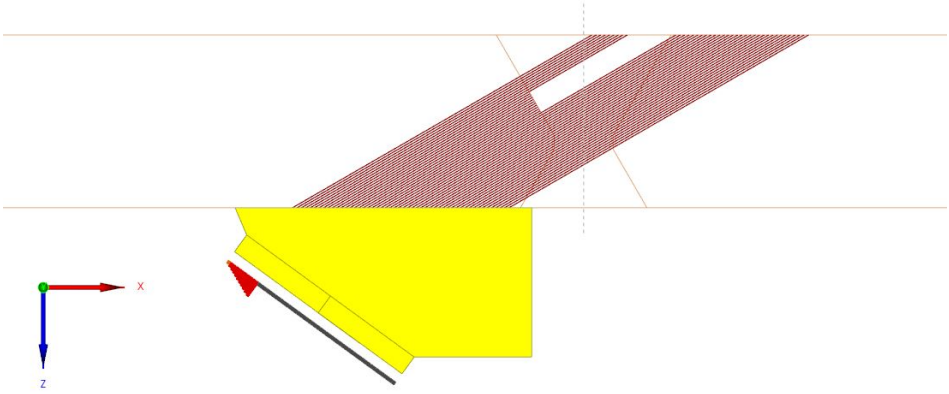

Figure 122: CIVA representation of remote surface direct 60^0 linear scanning PAUT inspection of planar flaw 1 in butt weld using a 15 mm probe offset

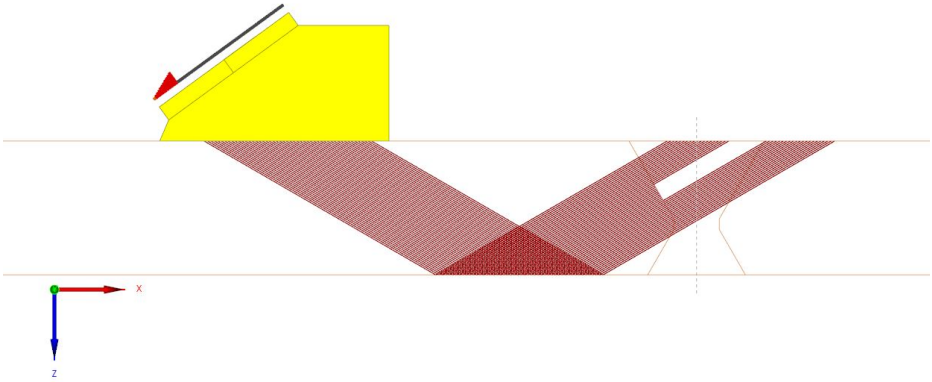

Figure 123: CIVA representation of top surface half-skip direct 60^0 linear scanning PAUT inspection of planar flaw 1 in butt weld using a 115 mm probe offset

In the direct inspection setup in Figure 122, the probe offset is set to 15 mm from the weld centre, relative to the front of the wedge (in yellow). The front of the wedge is the right-hand (straight) edge. To acquire the peak amplitude responses on different apertures, scans were also taken at probe offsets of 30 mm and 45 mm. Similarly, for Figure 123 the probe offset is set to 115 mm from the weld centre with additional scans taken at probe offsets at 130 mm and 145 mm. For each probe offset, three scans were carried out to average the captured amplitude responses.

5.5.3 Defect 1 Direct Inspection Analysis

From the three simulated scans inspecting the first LOF defect directly from the remote surface, Figure 124 shows the custom TCG calibrated CIVA simulation of the 15 mm probe offset inspection. Of the three repeats of experimental scanning for each probe offset, Figure 125 shows the experimental scan acquiring the highest amplitude response:

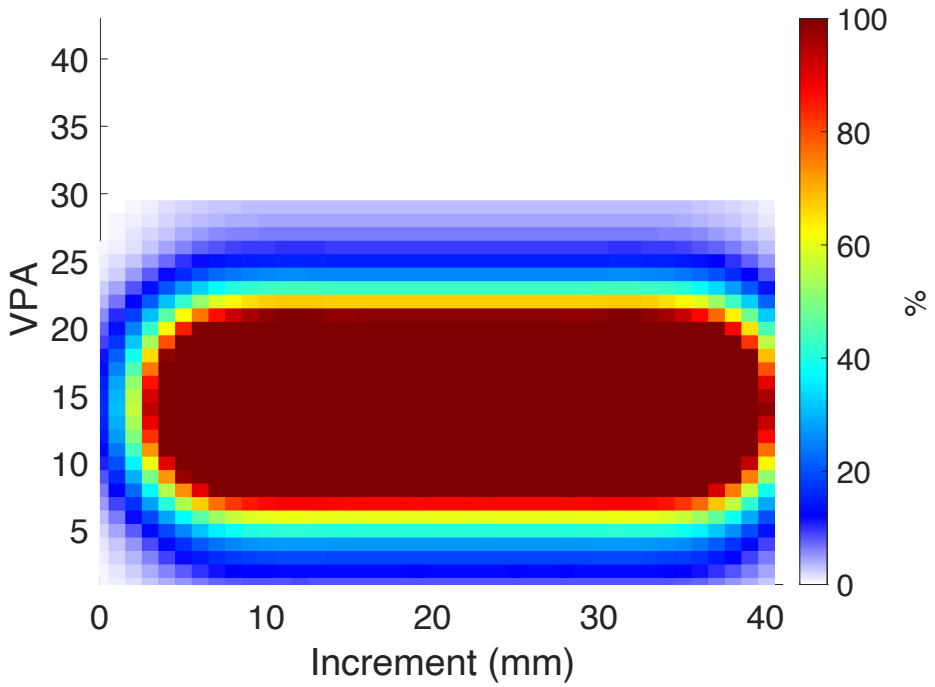

Figure 124: Custom TCG calibrated CIVA simulation data of remote surface direct inspection of LOF defect 1 in butt weld at 15 mm probe offset

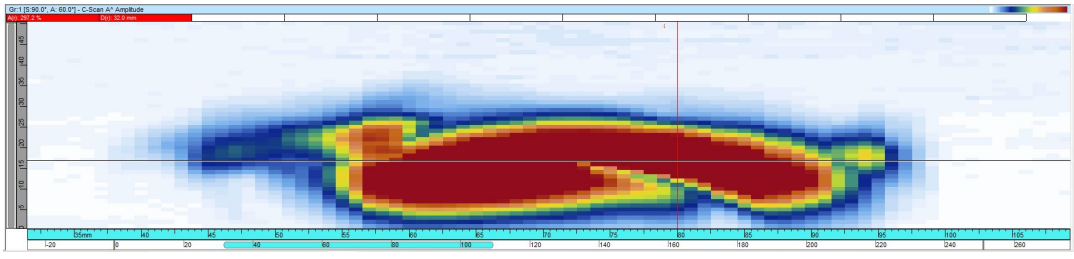

Figure 125: Experimental data of remote surface direct inspection of LOF defect 1 in butt weld at 15 mm probe offset captured using an OLYMPUS Omniscan MX2 attached with a 5 MHz 60 element linear array PipeWizard probe and 55^0 Rexolite wedge

Between Figure 124 and Figure 125, it can be seen that the simulated scan has achieved good replication of the experimental scan in relation to the size and shape of the flaw in a C-scan image. The same can be said when comparing the simulated and experimental results of the 30 mm and 45 mm probe offsets, which can be found in Appendices 7.2 and 7.4. Across the three probe offset scan comparisons, there are some slight differences in visual appearance which relate to the simplistic flaw geometry inputted into CIVA to replicate the scan. In the experimental scan the defect can be seen to have some crack-like branches (in the top left and right of the defect). These may have developed due to stresses related to repositioning/reorientating the sample from a crane and/or thermal stresses linked to environmental temperature fluctuations while located in a warehouse over multiple years. However, these features have not changed the primary amplitude response and would not change the sizing and sentencing of the defect utilising the approach outlined in the UK Defence Standards 02-773.

In a similar manner to the experimental scan data, the simulated results presented in Table 27 would be sentenced based on Table 4. In each probe offset case, the maximum amplitude response acquired would initially be compared against TCG ± 12 dB. If the amplitude response exceeds TCG + 12 dB, which in this case it does, the defect would be rejected. If the response was below that range, it would be accepted and if within that, sentencing would be relative to defect length.

Applying normal PAUT sizing techniques to raw simulated results have been shown to approximate the flaw sizes measured in an experimental environment. The issue dealt with in this section of the

thesis is the calibration of one CIVA simulation using one approximation algorithm relative to another to quantify flaw amplitude relative to a known reflector. In this case, the key aspects of comparison between the simulated and experimental scans are the percentage amplitude response and the VPA capturing the largest response.

Table 27 presents the highest experimental amplitude responses from each of the three scans at each probe offset and the VPA that each amplitude was captured on. Averages of these responses have been calculated and presented alongside the custom TCG calibration amplitude responses with the VPA they were approximated on; and the calibrated amplitude responses using the basic CIVA calibration approach (as mentioned in Section 0). Table 27 and Figure 126 present the acquired data to determine the effectiveness of the calibrated simulations:

Table 27: Experimental, CIVA calibrated and custom TCG calibrated data of remote surface direct inspection of LOF flaw 1 in butt weld at three probe offsets

Probe Offset	Experimental			CIVA Calibration		Custom Calibration	
	Scan No.	% Response	VPA	% Response	VPA	% Response	VPA
15 mm	1	247%	15	505%	15	300%	15
	2	297%	17				
	3	265%	18				
	AVG	304%	17				
30 mm	1	272%	28	488%	26	277%	26
	2	280%	27				
	3	293%	29				
	AVG	303%	28				
45 mm	1	259%	39	467%	38	268%	38
	2	257%	39				
	3	282%	39				
	AVG	290%	39				

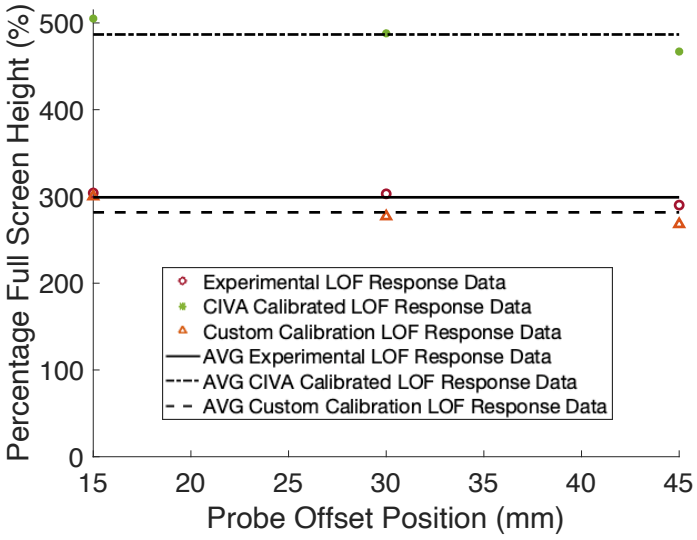

Figure 126: Comparison of experimental, CIVA calibrated and custom TCG calibrated data of remote surface direct inspection of LOF defect 1 in butt weld across three probe offsets

Prior to comparing the highest amplitude response captured for the experimental scans at each probe offset, it can be seen from Table 27 that the apertures capturing the maximum amplitude for each probe offset show slight variance. There are a variety of potential factors that could explain why the maximum amplitude is not captured on exactly the same aperture:

- the physical probe position may differ from the intended offset from the weld centre.
- the physical orientation of the probe may not be parallel with the weld centre
- lack of or uneven couplant
- wear and tear on the wedge
- differences in the location of the flaw in the simulation setup and the actual location of the flaw in the physical specimen.

A possible example of these factors can be seen in the 15 mm and 30 mm probe offset scan data where the maximum amplitude responses are captured on three different apertures. This could be linked to variations in applied couplant. Alternatively, the physical scans had the probe/wedge being scanned by hand and without the use of a scanning mount. Consequently, the specified offset distance could have been shifted in either direction by one or two millimetres.

Comparing the amplitude responses of the calibrated simulation data with the experimental data in Figure 126, the custom TCG calibration process has yielded a pronounced improvement in defect amplitude approximation. The basic CIVA calibration process is significantly over-sizing the amplitude response of the defect, producing an average response of more than 1.5 times the magnitude of the experimental data, while the custom TCG calibration is within 6% of the experimental scan data. This improvement is further enhanced by these simulated amplitude response approximations being captured on VPAs close to those that captured the experimental maximum amplitudes.

5.5.4 Defect 1 Half-skip Inspection Analysis

To investigate the top surface half-skip inspection of the first LOF defect, three simulations and three repeats of experimental scanning for each probe offset were again carried out. Figure 127 shows the custom TCG calibrated CIVA simulation of the 115 mm probe offset inspection and Figure 128 shows the experimental scan that acquired the highest amplitude response for the same scan setup:

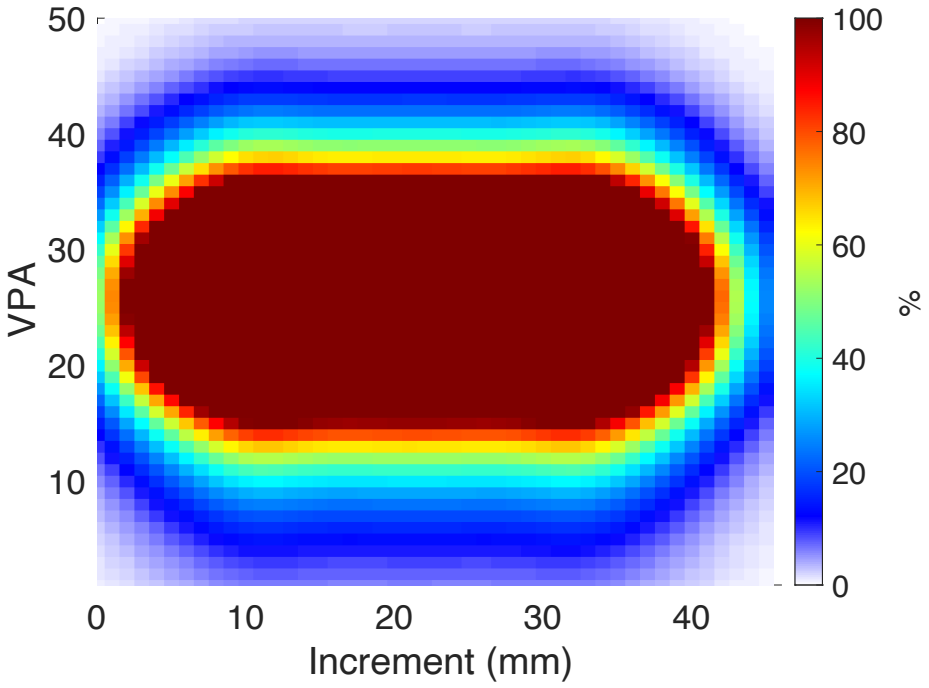

Figure 127: Custom TCG calibrated CIVA simulation data of top surface half-skip inspection of LOF defect 1 in butt weld at 115 mm probe offset

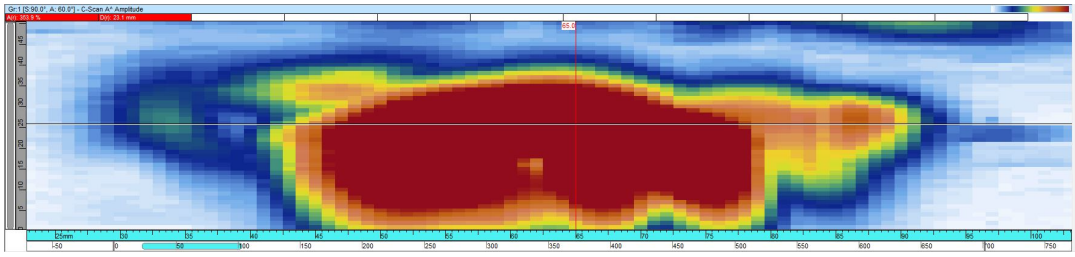

Figure 128: Experimental data of top surface half-skip inspection of LOF defect 1 in butt weld at 115 mm probe offset captured using an OLYMPUS Omniscan MX2 attached with a 5 MHz 60 element linear array PipeWizard probe and 55^0 Rexolite wedge

As before, the simulated and experimental results of the 130 mm and 145 mm probe offsets scans can be found in Appendices 7.5 and 7.6. Comparing the experimentally acquired scans with their simulated approximation images, the size and shape of the main body of the flaw has been replicated effectively. There are some slight discrepancies in the appearance; of the signals captured on apertures one to ten and the branches. The modelled flaw is an idealised LOF flaw without branches.

Table 28 summarises all the collated experimental and simulated inspection data with their respective capture apertures. Figure 129 presents a comparison of the simulation-approximated amplitude responses against their respective experimental data:

Table 28: Experimental, CIVA calibrated and custom TCG calibrated data of top surface half-skip inspection of LOF defect 1 in butt weld across three probe offsets

Probe Offset	Experimental			CIVA Calibration		Custom Calibration	
	Scan No.	% Response	VPA	% Response	VPA	% Response	VPA
115 mm	1	354%	26	1174%	26	372%	26
	2	292%	27				
	3	335%	27				
	AVG	354%	26				
130 mm	1	400%	39	1301%	38	361%	38
	2	400%	39				
	3	400%	39				
	AVG	398%	39				
145 mm	1	400%	48	1306%	49	305%	48
	2	400%	50				
	3	370%	50				
	AVG	400%	49				

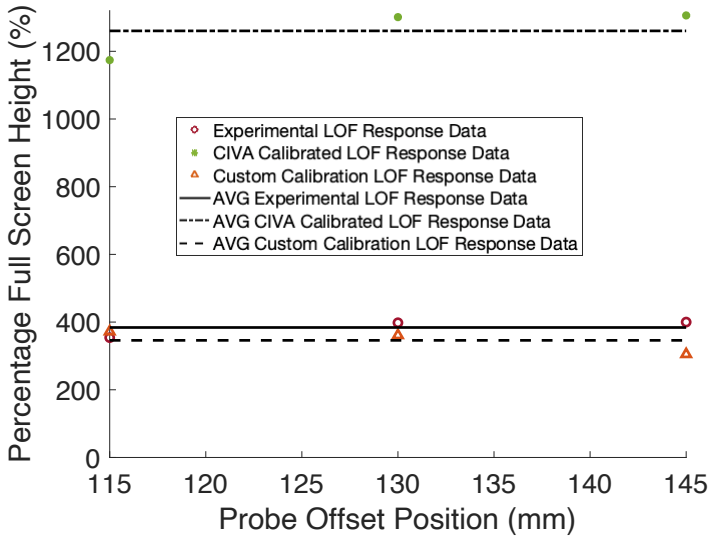

Figure 129: Comparison of experimental, CIVA calibrated and custom TCG calibrated data of top surface half-skip inspection of LOF defect 1 in butt weld across three probe offsets

Similar to the previous inspection setup, the basic CIVA calibration approach seriously overestimates the amplitude response of the LOF flaw for all three probe offset positions. The custom TCG calibration approach greatly improved the flaw amplitude approximations, while also acquiring the highest amplitude responses on the same apertures as the experimental scan data. In this inspection, the average amplitude response approximation of the custom TCG calibration approach was within 10% of the experimental scan amplitudes while the basic CIVA calibration approach was over three times higher.

As mentioned in the previous inspection results, the defect response can vary in amplitude due to a variety of factors such as couplant, physical probe/wedge position and orientation, and differences in flaw geometry between physical specimens and simulation. For the calibration setup considered here, there is another potential factor that may impede with approximation accuracy. It is linked to differences in attenuation between the butt weld test specimen and the custom test block specimen containing the FBHs reflectors, used for calibration. Despite the material of both carbon-steel samples having similar wave velocities, the attenuation of the butt weld sample, shown in Figure 119, and its accompanying calibration block may be slightly different from the custom test block, shown in Figure 68.

This may explain circumstances where the custom TCG calibration approach has slightly undersized the defect. In a simulation, where there is less randomness and variation to affect the outcome of the result, the expected result is an average amplitude response slightly

higher than the experimental. Furthermore, for increasingly deeper sound paths to flaws, linked to increased aperture numbers, Figure 126 and Figure 129 both show that the custom TCG calibrated amplitude responses have larger decreases in amplitude than the experimentally acquired data.

Where this can be accounted for is in the FBH amplitude responses relative to the 100% FSH response of 3 mm SDHs at varying depths. If the custom test block had been made of the exact same material as the butt weld test specimen, then different amplitude responses would be acquired for the FBH amplitude responses across all depths and apertures.

However, as shown by the experimental data for the two inspections analysed, the same inspection can acquire amplitude responses that vary by more than 10% of the maximum amplitude response across the repeated scans. Therefore, based on the results acquired thus far of approximating within 10% on the largest known sound path to be investigated, the approach would need to undergo further rigor. Had the inspection required the calibration of amplitude responses located on longer sound paths, then a review of the FBH amplitudes would be required.

5.5.5 Defect 2 Geometry & Inspection Setups

For the second of the two LOF flaws, the master drawing of the defect, as shown in Figure 130, states the defect has a 4.2 mm through-thickness height, is 35 mm in length, and is positioned 39 mm deep (relative to the top tip of the defect) on the lower V weld face.

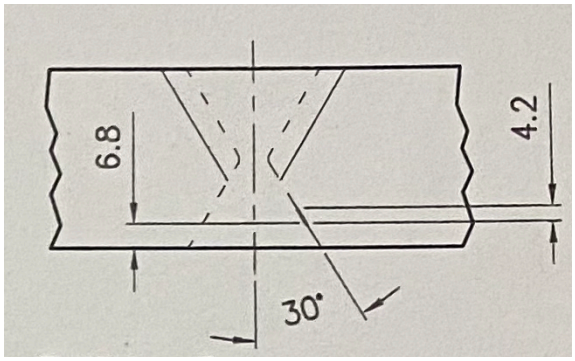

Figure 130: Butt weld LOF defect 2 dimensions

TOFD sizing of this defect gave a 2.5 mm through-thickness height, 32 mm in length, positioned 44 mm deep (relative to the top tip of the defect) and on the lower 30^0 angle weld face.

Replicating the PAUT probe/wedge setup, as before, and inputting the flaw dimensions based on the TOFD scan measurements, the inspection simulations can be undertaken from the top surface both directly and on the half skip. Figure 131 and Figure 132 illustrate CIVA simulations that replicate two of the probe position setups used to scan this flaw in the experimental scan:

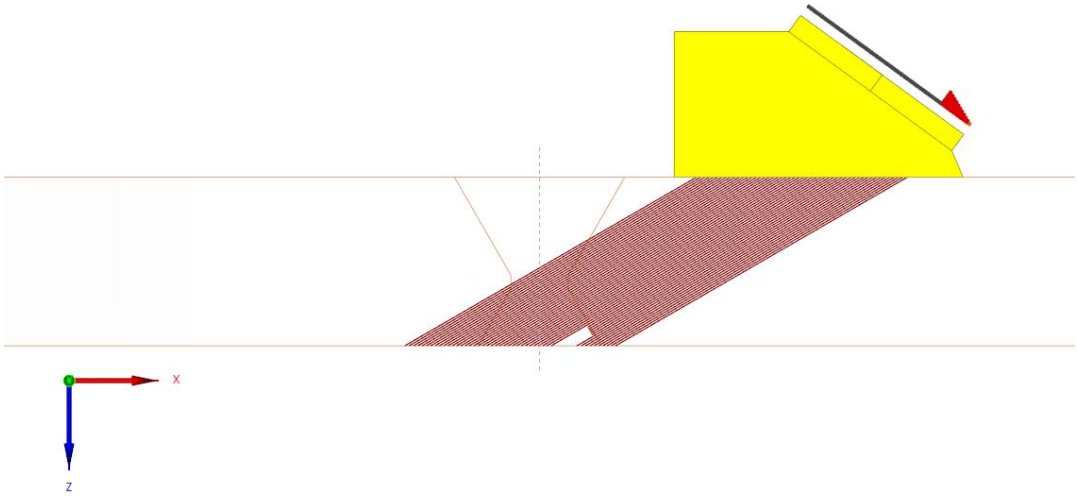

Figure 131: CIVA representation of top surface direct 60^0 linear scanning PAUT inspection of LOF defect 2 in butt weld using a 40 mm probe offset

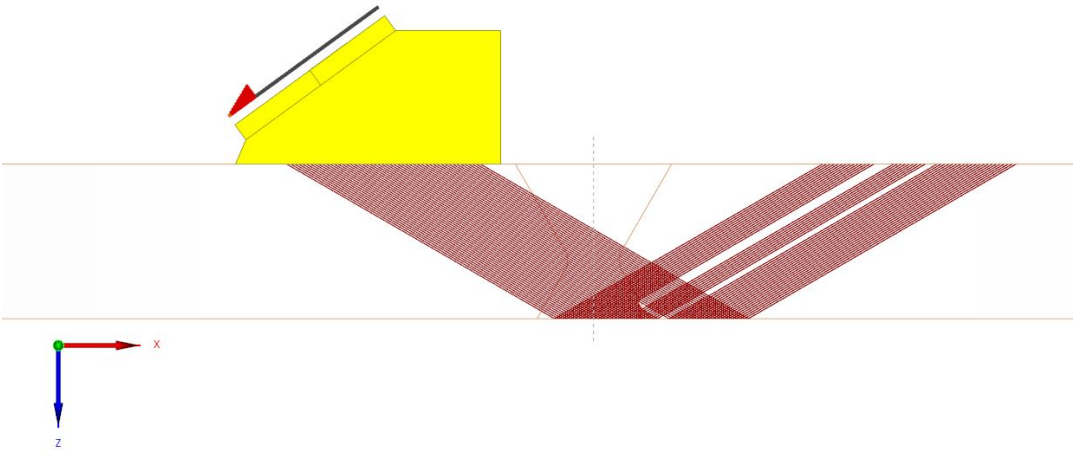

Figure 132: CIVA representation of top surface half-skip direct 60^0 linear scanning PAUT inspection of LOF defect 2 in butt weld using a 30 mm probe offset

For the direct inspection setup in Figure 131, the probe offset is set to 40 mm from the weld centre, relative to the front of the wedge. Additional scans were also taken at probe offsets of 50 mm and 60 mm. Similarly, for Figure 132 the probe offset is set to 30 mm from the weld centre with additional scans taken at probe offsets at 40 mm and 50 mm.

5.5.6 Defect 2 Direct Inspection Analysis

Three simulations were run and the experimental scans repeated three times for each probe offsets inspecting the second LOF defect directly from the top surface. Figure 133 shows the custom TCG calibration result of the 40 mm probe offset inspection and Figure 134 shows the equivalent experimental scan acquiring the highest amplitude response for that probe offset:

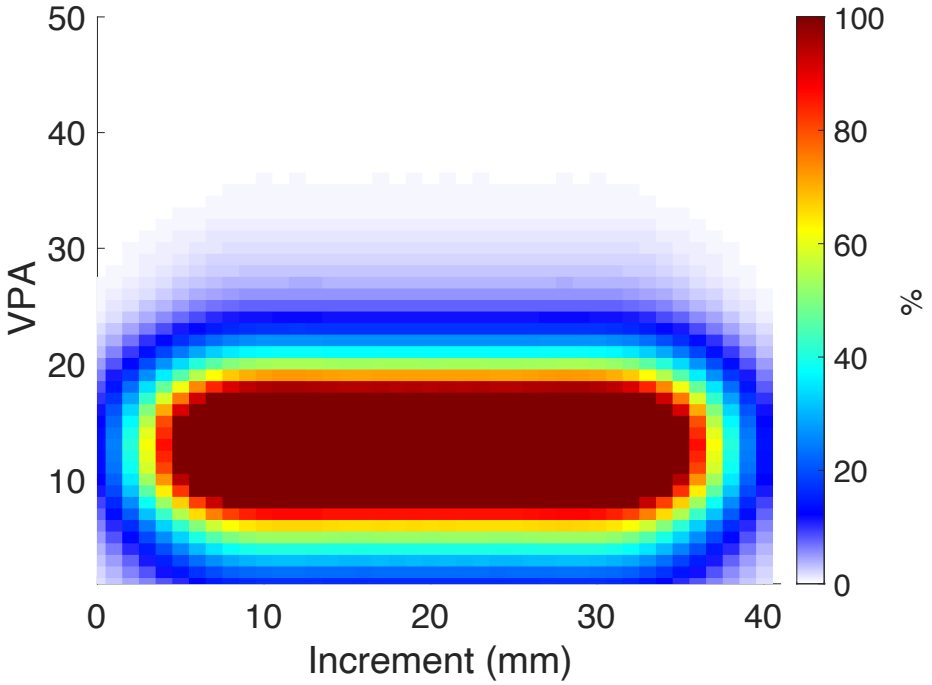

Figure 133: Custom TCG calibrated CIVA simulation data of top surface direct inspection of LOF defect 2 in butt weld at 40 mm probe offset

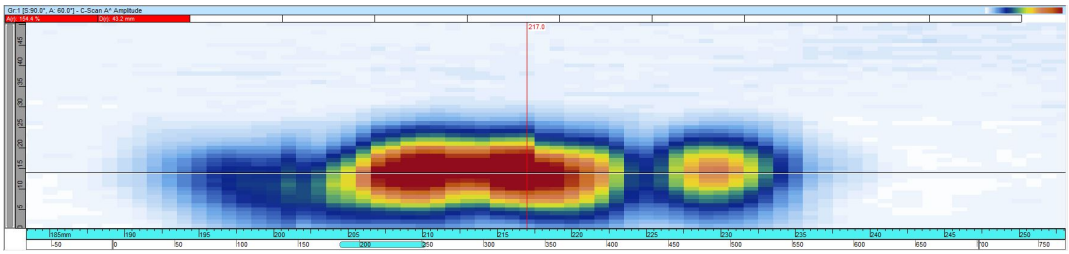

Figure 134: Experimental data of top surface direct inspection of LOF defect 2 in butt weld at 40 mm probe offset captured using an OLYMPUS Omniscan MX2 attached with a 5 MHz 60 element linear array PipeWizard probe and 55^0 Rexolite wedge

Comparing the two images of Figure 133 and Figure 134, as well as the other experimental/simulation probe offset scan data located in Appendices 7.7 and 7.8, the simulated inspection has replicated the size of the flaw very well. The simulation captures a good likeness to the experimental scan in the main portion of the flaw. However, there are some differences in shape toward the right-hand side of the flaw. This is most likely due to the physical flaw having a more complex geometry

than the modelled flaw. This could be investigated further by adjusting the geometry of the flaw within CIVA.

Table 29 shows all the collated highest amplitude responses from the experimental and simulated inspections, alongside their respective capturing apertures. Figure 135 presents a comparison of the simulation-approximated amplitude responses against their respective experimental data:

Table 29: Experimental, CIVA calibrated and custom TCG calibrated data of top surface direct inspection of LOF defect 2 in butt weld across three probe offsets

Probe Offset				CIVA Calibration		Custom Calibration	
	Scan No.	% Response	VPA	% Response	VPA	% Response	VPA
40 mm	1	142%	14	358%	13	174%	13
	2	154%	14				
	3	154%	14				
	AVG	150%	14				
50 mm	1	158%	22	332%	21	164%	21
	2	153%	20				
	3	151%	20				
	AVG	154%	21				
60 mm	1	106%	29	314%	29	154%	28
	2	149%	29				
	3	154%	29				
	AVG	136%	29				

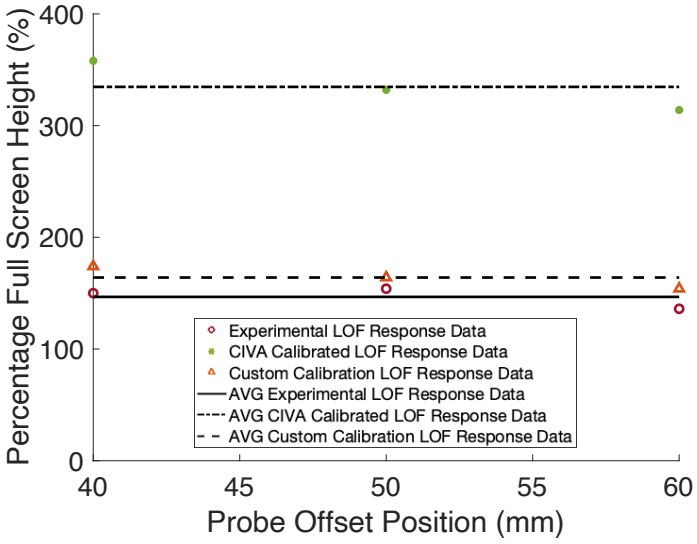

Figure 135: Comparison of experimental, CIVA calibrated and custom TCG calibrated data of top surface direct inspection of LOF defect 2 in butt weld across three probe offsets

As with the first LOF-type flaw, the amplitude response approximated using the basic CIVA calibration approach significantly overpredicts the amplitude response of the flaw in all three probe offset positions. The custom TCG calibration approach, by comparison, demonstrates an improved agreement of the flaw's amplitude approximations with the experimental scan data, including the location of the maximum amplitudes relative to the capturing VPAs. In this instance, the average amplitude response approximation of the custom TCG calibration approach was within 12% of the experimental scan amplitudes while the basic CIVA calibration approach was over twice the experimental amplitude response.

As previously explained, there are a variety of factors that can impact the amplitude response acquired for a flaw. Unlike the previous comparisons, the simulated approximations are higher in amplitude than the average experimental amplitudes. However, in the 60 mm probe

offset inspection, the 106% amplitude response in the first scan is significantly lower than the others. As a result, it is causing a significant reduction in the average response for that probe offset and consequently, the average response across all probe offsets. If the response was removed from the analysis, it improves the alignment of the custom TCG calibration approach with the experimental data to within 8%.

5.5.7 Defect 2 Half-skip Inspection Analysis

For the simulated and experimental scans inspecting the second LOF defect on the half-skip from the top surface, Figure 136 shows the custom TCG calibration approach of the 30 mm probe offset inspection and Figure 137 shows the equivalent experimental scan acquiring the highest amplitude response for the same probe offset:

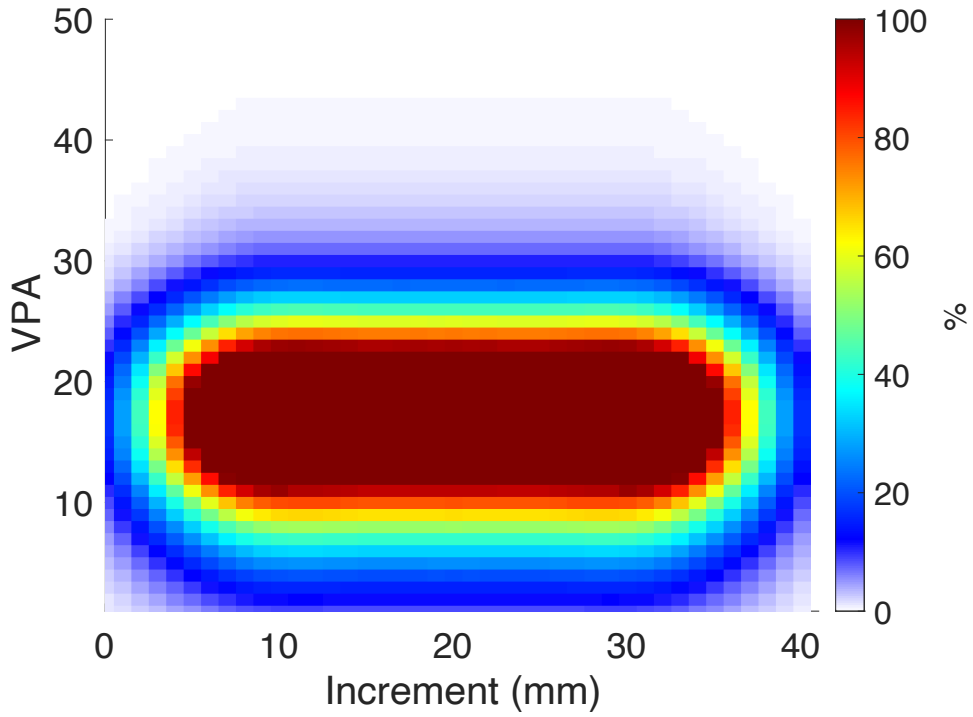

Figure 136: Custom TCG calibrated CIVA simulation data of top surface half-skip inspection of LOF defect 2 in butt weld at 30 mm probe offset

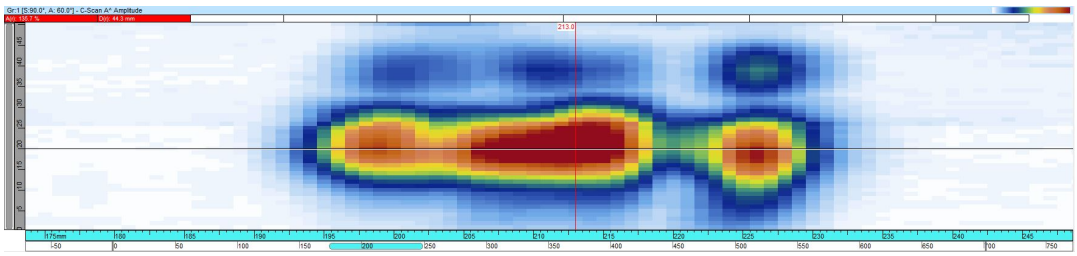

Figure 137: Experimental data of top surface half-skip inspection of LOF defect 2 in butt weld at 30 mm probe offset captured using an OLYMPUS Omniscan MX2 attached with a 5 MHz 60 element linear array PipeWizard probe and 55^0 Rexolite wedge

Of the comparisons made between experimental and calibrated simulation results thus far, the inspections for the half-skip scans in Figure 136 and Figure 137 show the greatest discrepancy. This is also the case for the experimental/simulation scan data of the other probe offset scans found in Appendices 7.9 and 7.10. Despite the low amplitude outlines showing some resemblance, the experimental half-skip scan image together with the experimental scan data of the direct inspection, in Section 5.5.6, highlight that some modifications to the simulated geometry would be required to fully replicate it.

Table 30 summarises all the highest amplitude responses from the experimental and simulated inspections, alongside their respective capturing apertures, while Figure 138 presents the averaged amplitude responses at each probe offset:

Table 30: Experimental, CIVA calibrated and custom TCG calibrated data of top surface half-skip inspection of LOF defect 2 in butt weld across three probe offsets

Probe Offset				CIVA Calibration		Custom Calibration	
	Scan No.	% Response	VPA	% Response	VPA	% Response	VPA
30 mm	1	136%	20	384%	18	171%	18
	2	87%	20				
	3	111%	20				
	AVG	111%	20				
40 mm	1	162%	26	358%	26	164%	26
	2	157%	26				
	3	143%	26				
	AVG	154%	26				
50 mm	1	140%	35	357%	34	159%	33
	2	164%	35				
	3	162%	36				
	AVG	155%	35				

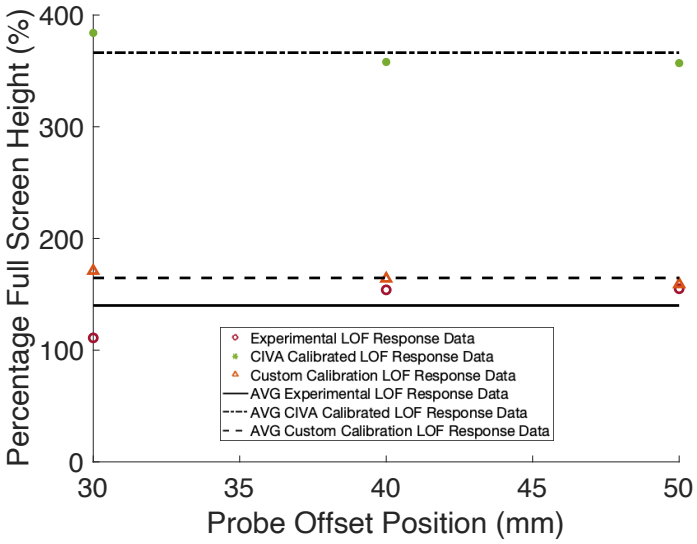

Figure 138: Comparison of experimental, CIVA calibrated and custom TCG calibrated data of top surface half-skip inspection of LOF defect 2 in butt weld across various three offsets

As with the previous three inspection setups, the basic CIVA calibration approach has considerably oversized the amplitude response of the flaw by a rounded factor of 2.6. The custom TCG calibration

approach, once again, exhibited a more accurate approximation with an average amplitude response within 18% of the experimental scan amplitudes. Moreover, between the experimental and calibrated simulation the VPAs capturing the peak responses scans mirror one another.

As with the previous set, the improved simulation approximations are higher in amplitude than the average experimental amplitudes. However, across the 30 mm probe offset experimental inspection, the average amplitude response of 111% is significantly lower than the average response of the other two probe offsets. The expectation for all scans across all probe offsets is that they produce similar amplitude responses, irrespective of the aperture capturing the highest amplitude response. This can be seen across nearly all the previous scans. For such a significant discrepancy to occur, incorrect scanning technique such as incorrect probe offset/orientation is the most probable cause. For the scans at the 30 mm probe offset, if the maximum response acquired (136%) was considered as the average response for that, the alignment of the custom TCG calibration approach with the experimental data improves to be within 11%. Taking this approach a step further, if the data for the 30 mm probe offset were to be removed from consideration or had produced similar responses to the other two averages, then the calibrated simulation response would be within an approximate 7% margin.

5.6 Defect Geometry Approximation

Across all the scan setups of the two LOF flaw geometries, the custom TCG calibrated simulations have been shown to better emulate the results acquired from their experimental scan counterparts. The amplitude responses of both flaws, relative to their experimental scans, were approximated to within a satisfactory margin. Moreover, the apertures simulated to have captured the highest responses for each scan were comparable to those within the experimental scans.

In validating the custom TCG calibration approach to approximate the amplitude response of LOF-type flaws/defects, there are several areas of interest that can be investigated further. These include the application of different probes/wedges, alternate aperture sizes, sectorial scanning, variations in material properties and alternate flaw geometries/approximation algorithms.

In addition to improving amplitude response prediction capabilities for planar flaw geometries within a structure; the investigation could continue into the optimisation of defining flaw geometries based on the physical scan images. Of the two LOF-type geometries investigated, implementing a simplistic planar geometry for the inspection simulations of the first LOF-type flaw generates comparable C-scan image with the experimental image, with regards to size and shape of the responses. However, comparison of the experimental and simulated C-scan images of the second flaw geometry highlights noticeable discrepancies. In particular, the amplitude responses closer to the edges of the flaw of the simulated scan image do not replicate the responses acquired experimentally.

5.6.1 Branched Flaw Approximation - General

The approach implemented within this Thesis can be applied to reverse engineer the geometry of flaws. For the second flaw, Figure 139 illustrates a possible branched flaw geometry generated based on the experimentally acquired scan images of the both the direct and half-skip inspections. The aim is to modify the modelled geometry to better replicate those images.

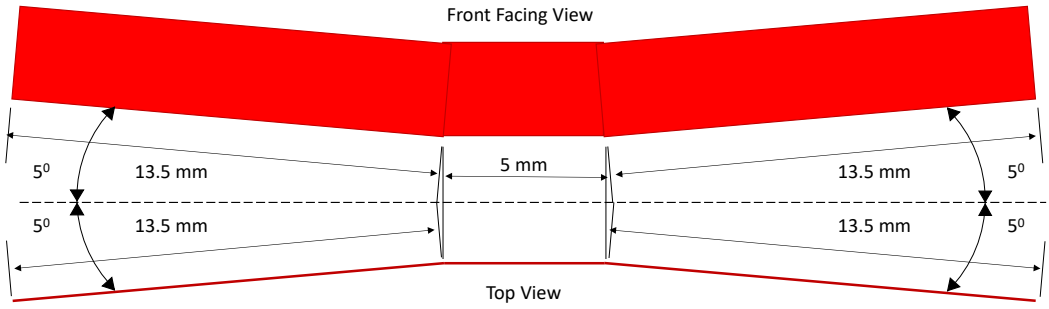

Figure 139: CIVA representation and dimensions of LOF flaw 2 in butt weld as a branched flaw

The basis of the flaw geometry shown in Figure 139 is that across all the experimental scans of the second LOF-type flaw, it appears to have a central body orientated normal to the beam angle with two lower amplitude 'wings' connected to it. The 5-degree angle deviation in the front facing view was chosen to try and replicate the amplitude responses for the winged sections of the flaw acquired on higher value apertures. For the top view, the 5-degree angle deviation from the neutral was to create a convex/concave reflector that maintained a normal reflector at its centre, with reductions in size towards the edges. The 5 mm width of the centre was chosen based on the acquired responses from the 3 mm FBHs captured as part of the custom TCG calibration process. Figure 140 and Figure 141 present the calibrated simulation C-scan images of the direct inspection at 40 mm probe offset and half-skip inspection setups at 30 mm probe offset:

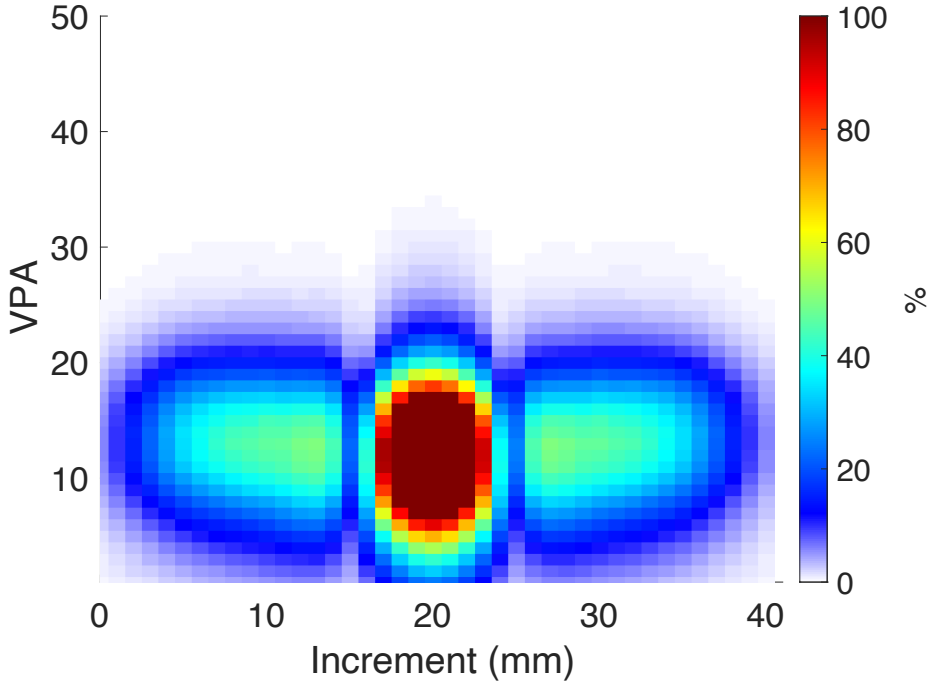

Figure 140: Custom TCG calibrated CIVA simulation data of top surface direct inspection of branched LOF defect 2 in butt weld at 40 mm probe offset

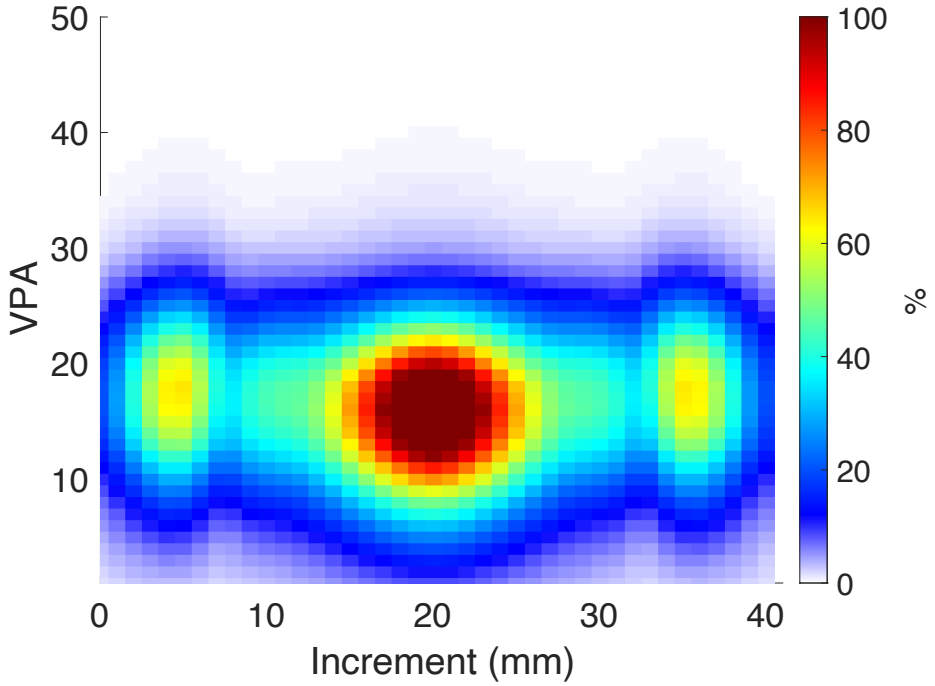

Figure 141: Custom TCG calibrated CIVA simulation data of top surface half-skip inspection of branched LOF defect 2 in butt weld at 30 mm probe offset

The simulated C-scan images of the inspection simulations at the other probe offsets, for both the direct and half-skip inspections, are in Appendices 7.11 and 7.12. Initial visual comparison of the two branched defect simulation scan images with the experimental scan counterparts, in Figure 134 and Figure 137, show potential for reverse engineering the geometry of the flaw. Both simulated scan images illustrate a central flaw body producing a high amplitude response with two lower amplitude extensions on either side. Despite these improvements in flaw geometry approximation, in relation to defect shape within the C-scan images, it is paramount that the amplitude responses also align. Table 31 presents the peak amplitude responses and capturing VPAs acquired from both the planar flaw and branched flaw inspection simulations of the direct inspection. Figure 142 presents a comparison of that data with the experimental scan data counterpart:

Table 31: Experimental, CIVA calibrated and custom TCG calibrated data of top surface direct inspection of LOF defect 2 in butt weld for planar and branched flaw geometry variants across three probe offsets

Probe Offset	Experimental		CIVA Defect	CIVA Calibration		Custom Calibration	
	% Response	VPA	Type	% Response	VPA	% Response	VPA
40 mm	150%	14	Planar	358%	13	174%	13
			Branched	364%	13	177%	13
50 mm	154%	21	Planar	332%	21	164%	21
			Branched	351%	20	168%	21
60 mm	136%	29	Planar	314%	29	154%	28
			Branched	337%	28	166%	27

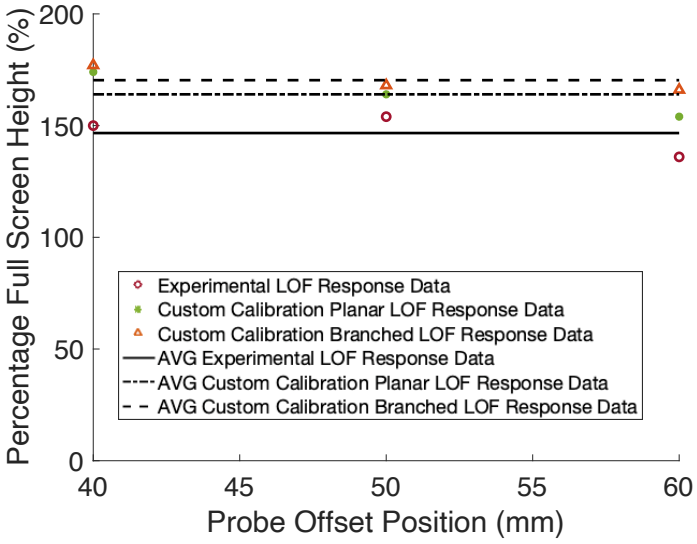

Figure 142: Comparison of experimental data with custom TCG calibrated data for both planar and branched flaw variants of top surface direct inspection of LOF defect 2 in butt weld across three probe offsets

Figure 142 highlights that the direct inspection simulation of the branched flaw has not improved on the approximation of the amplitude response relative to the planar flaw type. For the half-skip inspection, Table 32 presents the peak amplitude response data and capturing VPAs with Figure 143 displaying a comparison of the simulated data against experimental scan data:

Table 32: Experimental, CIVA calibrated and custom TCG calibrated data of top surface half-skip inspection of LOF defect 2 in butt weld for planar and branched flaw geometry variants across three probe offsets

Probe Offset	Experimental		CIVA Defect Type	CIVA Calibration		Custom Calibration	
	% Response	VPA		% Response	VPA	% Response	VPA
30 mm	111%	20	Planar	384%	18	171%	18
			Branched	278%	17	125%	16
40 mm	154%	26	Planar	358%	26	164%	26
			Branched	257%	25	116%	25
50 mm	155%	35	Planar	357%	34	159%	33
			Branched	248%	33	112%	33

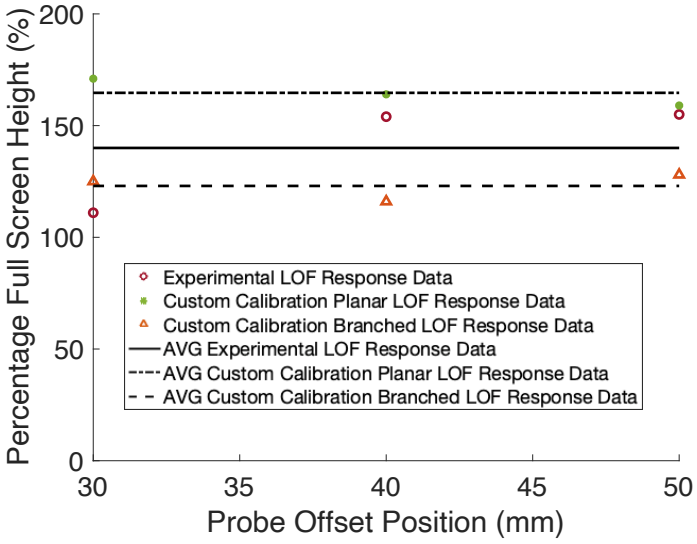

Figure 143: Comparison of experimental data with custom TCG calibrated data for both planar and branched flaw variants of top surface half-skip inspection of LOF defect 2 in butt weld across three probe offsets

Figure 143 shows that despite the half-skip inspection simulation approximating the response at 47% FSH less than the planar flaw, there has been an improved approximation using the branched flaw, relative to the experimental scan data. The reason for the large reduction is associated with the side of the flaw having a convex nature that reflects ultrasound away from the probe.

Between the improvements in the C-scan replication using a branched flaw geometry and notable similarity between the peak amplitude VPAs comparison in Table 31 and Table 32 (across all three probe offsets), these results warranted further study into improving the approximation of the geometry of the flaw.

5.6.2 Branched Flaw Approximation – Direct Inspection

The simulated direct inspection scan results of both the planar flaw and the branched flaw both oversized the flaw by approximately

16%. In both cases, the location of the flaw relative to the VPA capturing the peak amplitude response showed significant similarity, for all probe offsets. Additionally, the approximate scan step of the peak amplitude response of the branched flaw simulation aligned with the experimental scan data. These observations can used to make alterations to the geometry of the flaw to improve the simulation.

Where the branched flaw simulation had an improved C-scan image replication over the planar flaw simulation, it also oversized the peak amplitude response by a greater magnitude. This is due to the concave surface area of the flaw which causes more ultrasonic energy to be reflected toward the probe. Therefore, by increasing the width of the central section of the flaw it will reduce the concavity of the flaw geometry and reflect less ultrasonic energy back toward the probe. To replace the initial branched flaw simulation scan setup, Figure 144 illustrates the altered branched flaw geometry, with a larger central body and shorter branches that are angled in the same manner as the previous branched geometry (while maintaining the same total length):

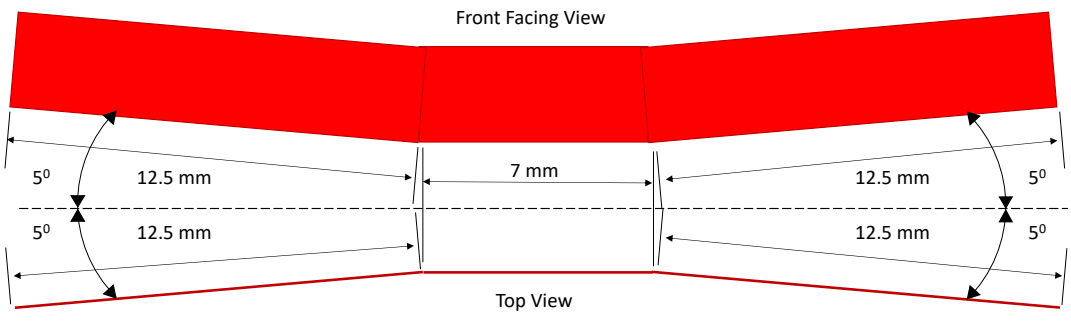

Figure 144: CIVA representation and dimensions of LOF flaw 2 in butt weld as a branched flaw – second iteration for direct inspection

The simulation results for each probe offset setup are presented in Figure 145 and in Appendix 7.13. The show the calibrated response approximations for the modified flaw geometry:

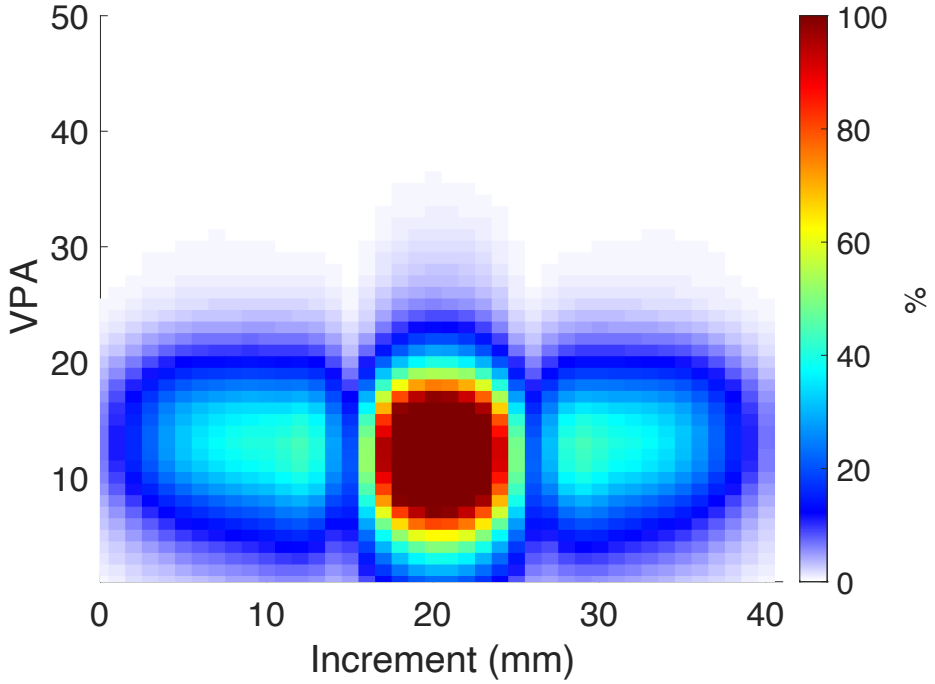

Figure 145: Custom TCG calibrated CIVA simulation data of top surface direct inspection of branched LOF defect 2 in butt weld at 40 mm probe offset (second iteration)

These simulated C-scan images for the adapted flaw geometry appear very similar to the simulated results from the initial branched flaw geometry. For these latest simulations, Table 33 presents the highest amplitude responses for both branched flaw geometries simulations, as well as the experimental response, while Figure 146 presents a comparison of the data:

Table 33: Experimental, CIVA calibrated and custom TCG calibrated data of top surface direct inspection of LOF defect 2 in butt weld for two branched flaw geometry variants across three probe offsets

Probe Offset	Experimental		CIVA Defect	CIVA Calibration		Custom Calibration	
	% Response	VPA	Type	% Response	VPA	% Response	VPA
40 mm	150%	14	Branched 1	364%	13	177%	13
			Branched 2	330%	13	160%	13
50 mm	154%	21	Branched 1	351%	20	168%	21
			Branched 2	308%	21	152%	21
60 mm	136%	29	Branched 1	337%	28	166%	27
			Branched 2	302%	28	149%	27

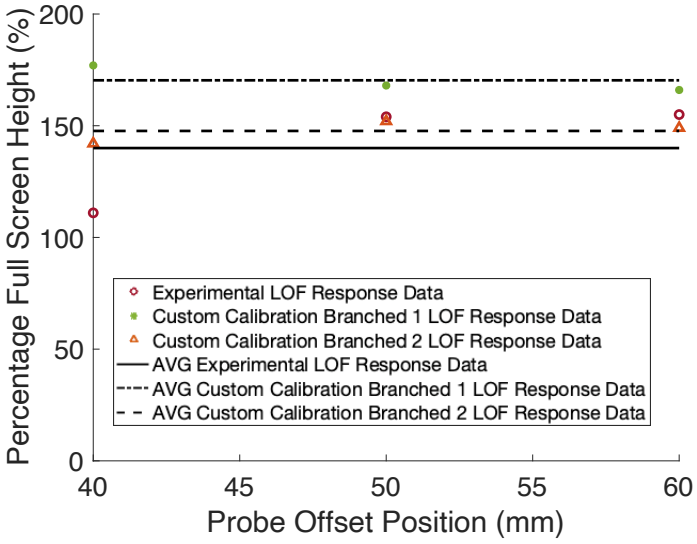

Figure 146: Comparison of experimental with custom TCG calibrated data for both branched flaw variants of top surface direct inspection of LOF defect 2 in butt weld across three probe offsets

The data presented in Table 33 shows that between the simulations of the first and second iterations of the flaw geometries, the apertures capturing the highest amplitude responses are near identical across all probe offsets. In doing so, the aperture approximations of both branched flaw geometry simulations closely resemble the experimental scan data. Furthermore, the average maximum amplitude responses for the second iteration branched flaw geometry show a significant improvement in agreement with the experimental data. To quantify the

improvement, the first iteration of the branched flaw geometry made an averaged approximation of 16% of the experimental scan data; while the second flaw geometry was able to acquire an averaged prediction that was within 5%. Based on these prediction capabilities, further analysis, including the implementation of parametric study tools, would continue to enhance the approximation definition of the flaw geometry.

5.6.3 Branched Flaw Approximation – Half-skip Inspection

The same process used in the previous section can be used to investigate the reverse side of the same defect using a half-skip inspection. By implementing the branched flaw, the simulated response better emulated the experimental C-scan image but the accuracy of the highest amplitude response was not significantly improved, despite it being on the same VPA.

Due to the flaw surface area being concave for the direct inspection, the half-skip inspection has the flaw surface inverted. The reverse side of the flaw is convex with respect to the ultrasonic beam. This was noticeable in the first iteration of the branch flaw geometry compared with the planar geometry, where a significant dip in amplitude response occurred. In a similar adaptation to the flaw for the direct inspection, the general shape of the flaw geometry remains the same, but the centre section of the flaw is lengthened and the two branches on either side are shortened. The flaw geometry used of the half-skip inspection is illustrated in Figure 148:

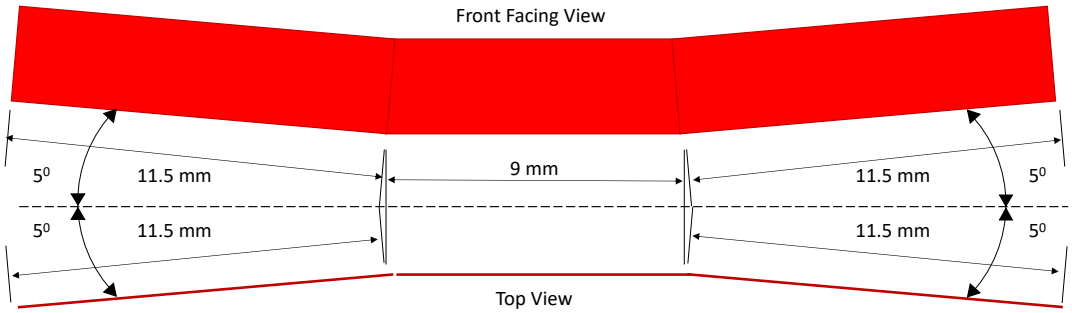

Figure 147: CIVA representation and dimensions of LOF flaw 2 in butt weld as a branched flaw – second iteration for half-skip inspection

Within CIVA, both planar and branched defects are considered infinitely thin with no volumetric thickness. So, despite both the direct and half-skip inspection setups scanning the same flaw from different skews, the inputted flaw geometry to replicate one surface face may be different to that needed on the reverse surface. Regarding the flaw geometry shown in Figure 148, the flaw has a 9 mm centre with two 11.5 mm wings on either side, whereas the flaw for the direct inspection (Figure 144) has a 7 mm centre with two 12.5 mm wings on either side. The driving factor for this difference is that the convex nature of the flaw for the half-skip inspection requires bigger incremental change to potentially improve both C-scan and peak amplitude response replication. The resulting C-scan images for the inspections for each probe offset setup using this altered flaw geometry are presented in Figure 148 and Appendix 7.14:

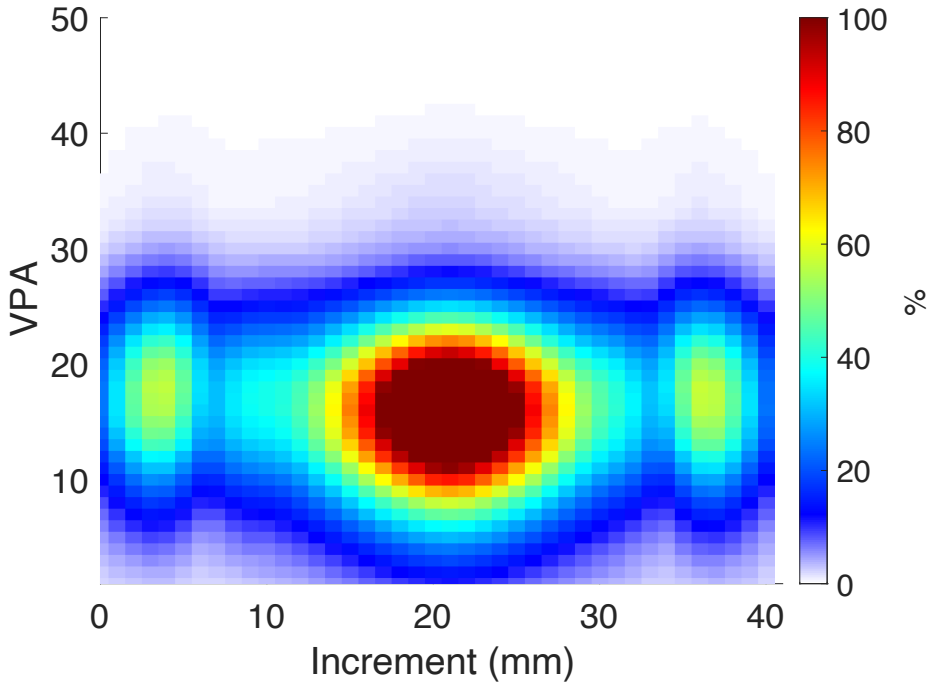

Figure 148: Custom TCG calibrated CIVA inspection simulation data of top surface half-skip inspection of branched LOF defect 2 in butt weld at 30 mm probe offset (Second Iteration)

These simulated C-scan images have excellent resemblance to the simulated results scanning the initial branched flaw geometry, shown in Figure 141, and the experimental scan data, shown in Figure 137. Table 34 highlights the highest amplitude responses acquired for the experimental scans and both branched flaw geometry simulations, while Figure 149 shows a comparison of the data:

Table 34: Experimental, CIVA calibrated and custom TCG calibrated data of top surface half-skip inspection of LOF defect 2 in butt weld for two branched flaw geometry variants across three probe offsets

Probe Offset	Experimental		CIVA Defect Type	CIVA Calibration		Custom Calibration	
	% Response	VPA		% Response	VPA	% Response	VPA
30 mm	111%	20	Branched 1	278%	17	125%	16
			Branched 2	319%	17	142%	16
40 mm	154%	26	Branched 1	257%	25	116%	25
			Branched 2	293%	25	132%	25
50 mm	155%	35	Branched 1	248%	33	112%	33
			Branched 2	285%	33	128%	33

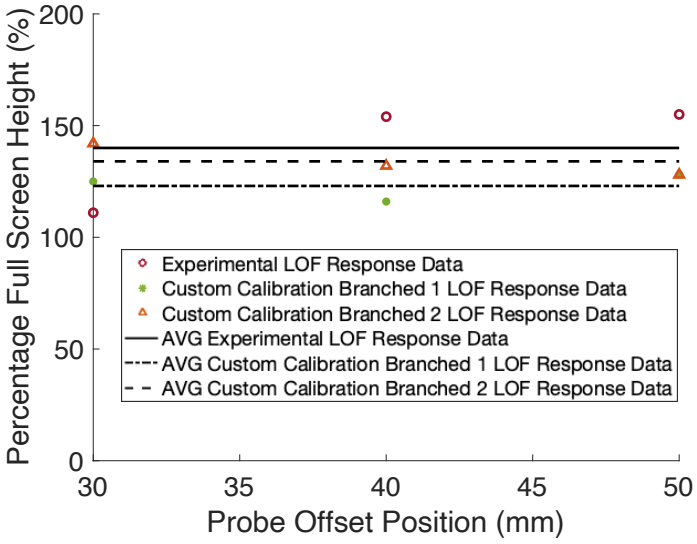

Figure 149: Comparison of experimental with custom TCG calibrated data for both branched flaw variants of top surface half-skip inspection of LOF defect 2 in butt weld across three probe offsets

Similar to enhancing the branched flaw in the direct inspection setup, Table 34 shows that near-identical apertures capture the highest amplitude responses for the second iteration of the flaw geometry when compared to the experimental scan data. Moreover, Figure 149 shows that the second flaw geometry was able to acquire an averaged prediction that was within 5% of the experimental data compared with the approximate 16% margin acquired for the first iteration of the branched flaw geometry. The outcomes from this analysis further reinforce the developments that have been made to amplitude response approximations and flaw geometry prediction capabilities.

6 Concluding Remarks

6.1 Key Findings

6.1.1 Capabilities and Limitations of CIVA Simulation

The initial stages in using CIVA were understanding and defining the capabilities and limitations of the simulation platform. The work in Section 4 established that CIVA calculates the responses of an inspection setup by making all FSH percentage responses of the scan relative to the highest approximated response. By analysing how attenuation is applied within CIVA and adapting attenuation coefficients accordingly, the responses of an individual defect type from multiple instances can be simulated accurately relative to experimentally acquired data.

In earlier versions of CIVA, the recommended calibration approach for PAUT setups was to calibrate the inspection simulation using the CRA acquired from an additional simulation that replaced the flaw with a SDH. This does not accurately replicate a physical TCG calibrated PAUT inspection setup and was deemed unsuitable for comparison with experimental data.

More recent improved versions of CIVA included a TCG calibration function that could be implemented either during the simulation setup or applied in post-processing. In terms of normalising the amplitude responses across all apertures and at all depths, this was an improvement on the previous calibration methodology. However, it still did not fully replicate the normalisation that would be obtained from a physical TCG calibration and was also deemed unsuitable.

6.1.2 Custom TCG for Linear Scanning PAUT Simulations

To overcome the limitations of CIVA's calibration approaches, Section 4 details the development of a custom MATLAB script to replicate the implementation of a TCG calibration. In accordance with the preferred PAUT approach required by the UK Defence Standard, the script effectively calibrates all inputted scan results of a linear scanning PAUT inspection setup.

The script implements a TCG by calibrating each amplitude response of an inspection simulation relative to the 80% FSH response of a SDH at the given depth and on the respective aperture acquired from the SDH calibration simulation. The calibrated data can then be displayed in a C-scan or S-scan view for analysis and appropriate comparison against experimental scan data.

Initial verification that the calibration had been implemented correctly was demonstrated by applying the TCG script to the SDH simulation used to acquire the calibration CRAs. This produced results in agreement with the expected results where an approximate 78% FSH response was acquired across all SDHs at all depths.

There are potential improvements that could be implemented to make the average FSH response of the SDHs closer to 80% FSH, such as reduced scan steps of the simulation for normal incidence. However, in a physical calibration setup, an exact 80% response for a defect may never be acquired. Depending on the standard used, it is typically accepted that responses acquired for each SDH on each aperture are within ±5% FSH of 80% This agreement confirms that the simulated

response data can be calibrated in the same way as any physical scan data would.

A key advantage of the developed script is that for each calibration simulation, the SDH CRAs from the simulation of the given probe setup can be stored in a digital archive. For future simulated inspections, a calibration simulation may not be required as the SDH CRA data can be pulled directly from the archive. This will save additional time and effort in the simulated weld inspection process in delivering the results for a given scan setup from a library of data.

A significant limiting factor to the first version of the script is that when applied to inspection simulations of alternate flaw types, it was not accurate. Section 5 highlights this and elaborates on how the two approximation algorithms, applied to the SDHs and FBHs respectively, did not replicate the amplitude responses of each defect respective to one another experimentally.

6.1.3 Experimental Data Mergence with Custom TCG

Once the discrepancy of the experimental and simulated relationships between the two known defect types was discovered, an improved calibration process that integrated physical response data to align the inspection and calibration simulations was investigated.

Section 5 presents the approach taken to use experimentally acquired amplitude response data from a known defect (FBH) relative to a SDH at 100% FSH and apply a factor to the inspection simulation data relative to the acquired percentage amplitudes before applying the

simulated TCG. Implementing this process and applying it back to simulation scans of FBH at various depths for verification of correct application, it was concluded that the amplitude approximations made were satisfactorily comparable to experimentally acquired scans.

The implementation of this process and development of the script is a significant step forward from CIVA's internal calibration processes, both basic and TCG. Where they inappropriately size defects due to the misalignment of approximation algorithms, the novel approach described in this Thesis overcomes the issues faced using relative experimental data. By calibrating effectively and acquiring more accurate approximations, it warrants further investigation into determining whether the amplitude responses of other simulated defect geometries can be predicted using the same FBHs as the known defect.

A noteworthy drawback to this approach is that the use of the FBH as the known defect to acquire the factor limits the flaw types that can be simulated in CIVA. Due to FBHs being simulated in CIVA using the Kirchhoff (& GTD) method, only flaw types that can be simulated using the same approximation algorithm can be investigated.

6.1.4 Defect Amplitude & Geometry Approximation

The complete calibration simulation procedure (i.e. including the FBH response relativity enhancement) produced comparable amplitudes to those achieved experimentally. Based on the flaw geometry information given by the master drawings and TOFD scan results, all the calibrated simulation scan results for the two defects considered showed

a significant improvement against the approximations made using the CIVA's internal calibration approach.

In addition, the simulated scan images also presented a significant likeness to their experimental counterparts based on the known dimensions, locations and orientations of the flaws. However, the planar flaw geometry option in CIVA is too basic for replicating defects with more complex branches and facets. Based on these findings, the procedure showed greater potential in its implementation to aid in the reverse engineering of an unknown flaw's geometry definition based on experimental scan data using the branched flaw CIVA option.

When running the calibration and inspection simulations, consideration must be taken of run-time that can range from minutes to days, depending on the size of the simulation setups. This provided motivation to simplify the complexity of an inspection setup as much as possible whether that be to reduce the inspection coverage volume, minimise the scanning length, and remove unneeded calculations.

6.2 Future Work

Significant progress has been made in the application of this TCG script for linear scanning PAUT setups and has presented significant potential for further investigation.

6.2.1 Calibrating Alternate Inspection Simulation Setups

The linear scanning PAUT setup presented in this thesis is one of an infinite number of inspection setups. Depending on the specimen under inspection, inspector preferences, standards used or available equipment, there are numerous factors that can affect the PAUT setup. As such, this presents the opportunity to investigate the application of the script with other probe/wedge setups, scanning at different propagation angles, and investigating different materials.

Similarly, this custom script is not limited to linear scanning PAUT setups; it has potential to be adjusted to accommodate sectorial scanning setups also. By adapting the import and looping mechanisms aimed at all apertures of a linear scanning setup, the method can be changed to accommodate a fan of angles propagating from a single aperture location on the probe.

In this thesis, all experimental data was collected using the Omniscan MX2 PAC manufactured by OLYMPUS. However, there are alternative PACs, such as the Zetec TOPAZ, Doppler Novascan, Eddyfi Gekko, etc. As different companies/inspectors carry out inspections using different PACs, an important feature to validate is checking the script's compatibility with other PAC platforms.

6.2.2 Validation for Simulation Inspections Standards

Greater knowledge and confidence will be built through the approach's on-going use and comparison against experimental data. By validating the approach over time, it has the potential of offering significant value and expansion to current inspection standards.

With continued development and validation, this approach could provide support in replacing the manufacturing of test specimens to understand the responses acquired from flaws and defects within specific specimens for given scan setups. A simulation approach, implementing the proposed script could provide inspection results of any given sample. Through parametric studies a variety of scan setups could be investigated including alternate probes, array settings, probe offsets, etc.

This can be extended to the inspection of complex geometry structures, which are significantly more expensive to manufacture and to inspect. Where surface access, probe positioning, and coverage limitations are significant factors, the presented work offers an approach that can demonstrate the success of a particular inspection setup with regards to coverage and by approximating in how a defect might respond within a scan. Alternatively, the approach can aid in the post-scan analysis in characterising a flaw's geometry.

6.2.3 Streamlining of Custom Block Design for Calibration

Several factors constrained the design of the custom carbon-steel block created for this thesis. These included material availability, accessible manufacturing processes, and budget limits.

The block was designed such that it had evenly spaced calibration reflectors and inspection flaws for analysis that replicated the sound path depths reached by inspection setups of thick materials. To ensure that the inspection of two reflectors/flaws did not interfere with one another and that half-skip setups replicated the depths required, the block is large and heavy. Consequently, this increased the costs of material and manufacture. Furthermore, manufacturing the FBHs at the designated depths and at the designated diameters was limited by manufacturing capabilities of the drilling depth of a drill bit being linked to its diameter. For the depth of drilling required, smaller diameter drill bits did not have the required drilling penetration based on the custom block design.

Other areas of interest that could be beneficial in improving approximation capabilities include variations in FBH diameters, FBHs at alternate angles, and potentially other defect types.

Therefore, the design of the block could be further streamlined. A logical next step is to investigate the optimal number/combination/size/types of reflectors and flaws needed that will produce the same comparable results to a physical scan as achieved in this thesis. This could be further developed into creating a procedure or methodology that will acquire that number/combination/size/types for the designated inspection.

6.3 Overall Conclusion

The objective of this thesis was to research and implement the use of advanced simulation packages to optimise weld inspection processes. Driving this research is the increasing need to incorporate modelling and simulation packages into current inspection standards and instructions to support defect detection, sizing, and geometry definition.

Where simulation alone has struggled to fully replicate the outputs of a physical scan, a calibration process has been implemented and tested that shows significant improvement to defect response approximations for linear scanning PAUT setups. Initial work into the development of a simulated calibration process replicating a physical TCG procedure led to the integration of experimental data of a known flaw to improve the defect amplitude approximation of an unknown defect. Comparison of experimental scan data and calibrated simulation data for a given unknown defect were found to show excellent agreement.

These findings demonstrate that an inspection setup can be replicated within simulation and acquire accurate defect response approximations. Stemming from this are numerous potential benefits that can be exploited to optimise the inspection process so that the probability of detecting defects can be improved and the size and shape of a defect can be effectively quantified. Some of those benefits include:

- **Verifying inspection setups** – simulating the inspection setup will certify that it conforms to the relevant inspection standard by ensuring that regulations such as an acceptable level of volume coverage is achieved and defects of a given size, shape and

orientation are detectable should they occur. Furthermore, in the instance that an inspector be required to justify why the chosen inspection setup was used, simulated parametric studies of inspection setup variations can be used to validate any decisions made. An example of this could be the inspection of a complex geometry struture.

- **Reduced expense and constraint in specimen manufacture** – with the improved defect response approximation capabilities, trialling inspection setups no longer needs to be solely reliant on performing them physically on manufacture test samples. Purchasing, manufacturing, storing and inspecting multiple, large, and/or complex geometry specimens can be expensive (in relation to both time and money) and the cost is directly proportional to each factor. By contrast, employing a simulated approach can minimise those costs with fewer test specimens needing to be built, less storage space required and less physical inspections to be performed. Furthermore, a digital test specimen allows for the internal make-up of it to be altered so that different defect types, sizes, geometries and orientations can be investigated through parametric study, whereas a physical test specimen is fixed once manufactured.

- **Expected results** – carrying out simulated inspections of a setup prior to a physical inspection will provide greater insight to an inspector as to what they should expect to see or not see when scanning. This could be of particular importance for complex

geometry strutures when distinguishing between responses from geometry interfaces and potential defects.

- **Data analysis of detected flaws** – as demonstrated within Section 5.6 the geometry, size and orientation of a flaw can be predicted through a parametric study. By better understanding the properties of a flaw allows for more accurate stress analysis to better predict if the flaw might grow, the direction of the growth, and the timeline of the growth.

In conclusion, integration of experimental scan data to calibrate simulation results has shown to effectively improve defect amplitude response approximations, providing a platform to predict how a given defect might present itself for a hypothetical scan setup. Furthermore, the proposed procedure and methodology has also shown potential for reverse engineering the geometry of a defect based on its experimental scans. The methodologies developed within this thesis have shown to be effective and have the potential to be developed further through future research.

7 Appendices

7.1 Appendix 1 – Custom MATLAB Script 1

```
% Custom MATLAB SCRIPT 1
% Extracts SDH CIVA Reference Amplitude Generator

% This script generates a table of CRAs that are associated with
the maximum response for each SDH depth on each aperture.

% These CRAs represent the reference values which would produce
a 100 response from the associated SDH for the given aperture.

%% Probe and Wedge Parameters

% Parameters for OLYMPUS PipeWizard probe (5L60-PWZ1)
element = 60; % No. of available elements
VPAaperture = 11; % No. of elements selected for all Virtual
Probe Apertures
pitch = 1e-3; % Element pitch

% Parameters for Carbon Steel sample
refractionangle = 60; % Refraction angle of Simulation Inspection
setup
structurevelocity = 3240; % (m/s) Transverse wave velocity
CalbBlockSDHs = [25, 37.5, 50, 62.5, 75, 87.5]*10^-3; % (m) Known
SDH depths

% Parameters of CIVA Simulation setup
Calalgorithm = 'SOV'; % Defect approximation algorithm used
within CIVA (SOV or K)
minDepth = 20*10^-3; % (m) Minimum depth for any response to be
considered

% Parameters for OLYMPUS PipeWizard wedge (SPWZ1-N55S-IHC-RevC)
wedgevelocity = 2330; % (m/s)
wedgeangle = 36.1; % (deg)
element1midheight = 8.08e-3; % (m)
```

```
element1midoffset = 3.64e-3; % (m)

% Angle of Incidence at Wedge/Sample Interface based on
Refraction Angle
propangle                                                    =
asind((wedgevelocity*sind(refractionangle)/structurevelocity));

% Co-ordinates of element centres
elementcentreloc = zeros(element,2);
elementcentreloc(1,1) = element1midheight;
elementcentreloc(1,2) = element1midoffset;

if element > 1
    h = pitch*sind(wedgeangle);
    l = pitch*cosd(wedgeangle);
    for i = 1:element
        elementcentreloc(i,1) = element1midheight + ((i-1)*h);
        elementcentreloc(i,2) = element1midoffset + ((i-1)*l);
    end
end



%% Calibration Simulation Data Import and Organisation

% Importing CIVA generated text file of SDH Calibration data
vpatext = '######'; % File Name
ScanData = dlmread(sprintf('%s.txt', vpatext), ';', 17, 0); %
Text File Import


VPAs = max(max(ScanData(:,1)))-1; % Number of VPAs used in
calibration simulation
VPAsplit = size(ScanData,1)/VPAs;
ScanStepsplit = (size(ScanData,2)-3)/2;
ScanStepValEnd = size(ScanData,2)-1;
```

```
% Separation of Scan Data CIVA Reference Amplitudes and dB values
CIVA_data_dB = zeros(VPAsplit,ScanStepsplit,VPAs);
CIVA_data_val = zeros(VPAsplit,ScanStepsplit,VPAs);
CIVA_data_percent = zeros(VPAsplit,ScanStepsplit,VPAs);

% Segragation and organisation of Scan Data CIVA Reference
Amplitudes, dB values, percentage amplitudes and time sequence
for counter = 1:VPAs
    CIVA_data_dB(:,:,counter)       =       ScanData(((counter-
1)*VPAsplit)+1:(VPAsplit*counter),3:ScanStepsplit+2);
    CIVA_data_val(:,:,counter)      =       ScanData(((counter-
1)*VPAsplit)+1:(VPAsplit*counter),(ScanStepsplit+3):ScanStepVal
End);
    CIVA_data_percent(:,:,              counter)              =
sqrt(10.^(CIVA_data_dB(:,:, counter)/10));

    % Remove inf values
    infremove1 = find(isinf(CIVA_data_percent(:,:, counter)) ==
1);
    infremoveVPA =  CIVA_data_percent(:, :, counter);
    infremoveVPA(infremove1) = 0;

    CIVA_data_percent(:, :, counter) = infremoveVPA(:,:) * 100;
    disp(counter)
end

time = ScanData(1:VPAsplit,2)*10^-6;

%% Disregarding of data within wedge and to minimum depth in
structure

% Co-ordinate locations of aperture centrelines at each bounndary
interface
VPA1boundaryloc = (VPAaperture+1)/2;
for counter = 1:VPAs
    boundaryrayloc(1,counter)                                   =
elementcentreloc(counter+(VPA1boundaryloc-1),2)                 +
```

```
elementcentreloc(counter+(VPA1boundaryloc-1),1)/tand(90-
propangle);
end


for i = 1:VPAs
    VPAstart(i,1)  =  elementcentreloc(round(VPAaperture/2)+(i-
1),1); % Aperture Centreline Starting Height
    VPAstart(i,2)  =  elementcentreloc(round(VPAaperture/2)+(i-
1),2); % Aperture Centreline Starting Offset
    VPAraylength(i,1)  =  VPAstart(i,1)/sind(90-propangle);  %
Total distance travelled in Wedge for aperture centreline
    VPAraylength(i,2)  =  2*VPAraylength(i,1)/wedgevelocity;  %
Time spent by ultrasound in Wedge for aperture centreline

    % Total timespan to be disregarded for aperture (including
time spent by ultrasound up to stated minmium depth
    VPAraylength(i,3) = VPAraylength(i,2) + (2*minDepth/sind(90-
refractionangle))/structurevelocity;

    timeboundary(i) = find(time >= VPAraylength(i,2),1);
    timeminmm(i) = find(time >= VPAraylength(i,3),1);

    % Negating unneeded data
    CIVA_data_val(1:timeminmm(i)-1,:,i) = 0;
    CIVA_data_percent(1:timeminmm(i)-1,:,i) = 0;
    CIVA_data_dB(1:timeminmm(i)-1,:,i) = 0;
end


%% Calculating Locations at each time step for each aperture

step = 1e-4; % (m) Minimum discretisation step
VPAtime = zeros(size(time,1)-timeminmm(end)+1,11,VPAs);

% General Values related to each VPA
for j = 1:VPAs
```

```
    % Applicable time values beyond structure boundary
    VPAtime(timeminmm(j):size(time,1),1,j)                    =
time(timeminmm(j):size(time,1));

    % Portion of time related to propagation within structure
    VPAtime(timeminmm(j):size(time,1),2,j)                    =
VPAtime(timeminmm(j):size(time,1),1,j)-VPAraylength(j,2);

    % Depth relating to specified time in structure
    VPAtime(timeminmm(j):size(time,1),3,j)                    =
structurevelocity*(VPAtime(timeminmm(j):size(time,1),2,j)/2)*si
nd(90-refractionangle);

    % Rounded depth within structure
    VPAtime(timeminmm(j):size(time,1),4,j)                    =
round(VPAtime(timeminmm(j):size(time,1),3,j),3);

    % Offset co-ordinate
    VPAtime(timeminmm(j):size(time,1),8,j)                    =
VPAtime(timeminmm(j):size(time,1),3,j)/tand(90-refractionangle)
+ boundaryrayloc(1,j);

    % Rounded offset co-ordinate
    VPAtime(timeminmm(j):size(time,1),9,j)                    =
round(VPAtime(timeminmm(j):size(time,1),8,j),3);

    % Indexed depth co-ordinate
    VPAtime(timeminmm(j):size(time,1),10,j)                   =
round(VPAtime(timeminmm(j):size(time,1),3,j)/step)+1;

    % Indexed offset co-ordinate
    VPAtime(timeminmm(j):size(time,1),11,j)                   =
round(VPAtime(timeminmm(j):size(time,1),8,j)/step)+1;

    % Generating C-scan representation using A-scan data to
extract SDH Maximum Percentage Amplitudes
```

```
    VPAmax(:,j,1)  =  max(CIVA_data_percent(:,:,j));     %  Max
Percent @ VPA
    VPAmax(:,j,2) = max(abs(CIVA_data_val(:,:,j)));  % Max CIVA
Val @ VPA

    for counter2 = 1:size(CIVA_data_percent,2)
        check    =    find(CIVA_data_percent(:,counter2,j)    ==
VPAmax(counter2,j,1));
        VPAmax(counter2,j,3) = check(1); % Time Index @ VPA Max
        VPAmax(counter2,j,4) = time(check(1)); % Time @ VPA Max
        VPAmax(counter2,j,5)                                    =
abs(CIVA_data_val(check(1),counter2, j)); % Confirming find at
VPAmax(:,counter,2)
    end

end

%% Extraction of SDH Maximum Percentage Amplitudes

minpercentage = 15; % Minimum amplitude response to be considered
percentdiff = 3; %
stepdiff = 10; %

% Extraction of SDH Maximum Percentage Amplitudes for imported
simulation data
for counter = 1:VPAs
    clear a
    clear b
    clear c

    % Locate all peak responses within C-scan representations
    [a(:,1),a(:,2)] = findpeaks(VPAmax(:,counter,1));

    % Acquire CRAs associated with peak amplitude responses
    a(:,3) = VPAmax(a(:,2),counter,2);
    a(:) = sortrows(a);
```

```
    % Qualiify peak responses greater than minimum requirement
    b = find(a(:,1)>minpercentage);
    c(:,1) = a(b(:,1),1);

    % Removal of potential duplicate peaks based on amplitude
response
    for counter2 = 2:size(b,1)
        if c(counter2,1) == 0
            break
        elseif   abs(c(counter2,1)   -   c(counter2-1,1))   <=
percentdiff
            minsearchloc   =   find(c(:,1)   ==   min(c(counter2-
1:counter2)));
            b(minsearchloc(1)) = 0;
        end
    end
    b = b(find(b)); %#ok<FNDSB>

    clear c
    c(:,1) = a(b(:),1);
    c(:,2) = a(b(:),2);
    c(:) = sortrows(c,2);

    % Removal of potential duplicate peaks based on co-ordinate
position
    for counter2 = 2:size(b,1)
        if abs(c(counter2,2) - c(counter2-1,2)) <= stepdiff
            minsearchloc   =   find(c(:,1)   ==   min(c(counter2-
1:counter2)));
            b(minsearchloc(1)) = 0;
        end
    end
    b = b(find(b)); %#ok<FNDSB>

    % Gather all relevent peaks
    clear c
    c(:,1) = a(b(:),1);
```

```
    c(:,2) = a(b(:),2);
    c(:,3) = a(b(:),3);

    % Determine the respective SDH depth for each of the measured
amplitude peaks
    for counter2 = 1:size(c,1)
        c(counter2,4)                                              =
find(CIVA_data_percent(:,c(counter2,2),counter)                 ==
c(counter2,1),1);
        c(counter2,5) = VPAtime(c(counter2,4),4,counter);
        c(counter2,6)   =   CalbBlockSDHs(find(CalbBlockSDHs   >=
c(counter2,5),1))*10^3;

        c_avg(counter2,counter) = c(counter2,5)*10^3;
    end

    % Removal of repeated SDH depth data
    c(:) = sortrows(c,6);
    freqcheck = tabulate(c(:,6));
    repeateddepths = find(freqcheck(:,2) > 1);
    noofrepeateddepths = size(repeateddepths,1);

    if isempty(noofrepeateddepths) == 0
        for counter2 = noofrepeateddepths:-1:1
            loc            =            find(c(:,6)            ==
freqcheck(repeateddepths(counter2)));
            for counter3 = loc(end-1):-1:loc(1)
                c(counter3,:) = [];
            end
        end
    end

    % Store found peaks and associated CRA data
    CIVAamp(:,1) = c(:,6);
    CIVAamp(:,counter+1) = c(:,3);

end
```

```
c_avg = flip(c_avg);

for counter = 1:size(c_avg,1)
    CIVAamp(counter,1) = (round(2*mean(c_avg(counter,:))))/2;
end


% Create New File to save data / Add data to existing fil
if isfile(file) % If a file exists

    % Read in matrix of CRAs from existing excel file
    TCG = readmatrix(file);
    TCG = transpose(TCG);

    % Read the known SDH depths for given data
    SDHdepths = CIVAamp(:,1);
    CIVAamp(:,1) = SDHdepths;

    TCGorig = size(TCG,1);
    counter2 = 1;

    % Add new CRA data to existing CRA matrix
    for counter = TCGorig+1:TCGorig+size(CIVAamp,1)
        TCG(counter,:) = CIVAamp(counter2,:);
        counter2 = counter2+1;
    end

    TCG = sortrows(TCG);

    % Perform frequency check on new data against existing data
    freqcheck = tabulate(TCG(:,1));
    repeateddepths = find(freqcheck(:,2) > 1);
    noofrepeateddepths = size(repeateddepths,1);

    if isempty(repeateddepths) == 0
        for counter = noofrepeateddepths:-1:1
```

```
            counter2 = counter - 1;
            TCG(repeateddepths(counter)+counter2,:) = [];
            counter2 = counter2 + 1;
        end
    end

    TCG = transpose(sortrows(TCG));

else % If a file does not exist

    % Create matrix to be saved to excel file
    SDHdepths = CIVAamp(:,1);
    CIVAamp(:,1) = SDHdepths;
    TCG = transpose(CIVAamp);
end

%% Save CRA data to CSV file

% File Name
file = sprintf('######');

% File Save
csvwrite(file,TCG);
```

7.2 Appendix 2 – Custom MATLAB Script 2

```
% Custom MATLAB SCRIPT 2
% Application of a TCG calibration on CIVA simulated inspection
setup

% This script performs a calibrated TCG on raw CIVA simulation
data of a
% phased array inspection setup.

% As inputs to the script, CMS-2 requires the necessary CRA
matrix generated using CMS-1
% and the raw CIVA simulation data of the inspection setup being
analysed

%#ok<*SAGROW>

%================================================================
===================================
%================================================================
===================================
%% Probe and Wedge Parameters

% Parameters for OLYMPUS PipeWizard probe (5L60-PWZ1)
element = 60; % No. of available elements
VPAaperture = 11; % No. of elements selected for all Virtual
Probe Apertures
pitch = 1e-3; % (m) Element pitch
VPAs = 50; % Number of Virtual Probe Apertures used in inspection
tw = element*pitch; % Transducer width

% Parameters for Carbon Steel sample
refractionangle = 60; % (deg) Refraction angle of Simulation
Inspection setup
structureTvelocity = 3240; % (m/s) Transverse wave velocity
bw = 0.1; % (m) Thickness of material for backwall reflection
(if required)
```

```
% Parameters of CIVA Simulation setup
Calalgorithm = 'SOV'; % Defect approximation algorithm used
within CIVA (SOV or K)
ScanSetup = 'HS'; % Sound path length to defect to be considered
(Direct or Half-Skip [HS])
defects = 'SDH'; % Individual or Mutiple defect(s) type being
investigated (SDH or LOF)
ScanDirection = 'Parallel'; % Scan Direction of probe relative
to the weld (Parallel or Perpendicular)

if strcmp(ScanDirection, 'Perpendicular')
    dir = 1;
elseif strcmp(ScanDirection, 'Parallel')
    dir = 2;
end

% Parameters for OLYMPUS PipeWizard wedge (SPWZ1-N55S-IHC-RevC)
wedgevelocity = 2330; % (m/s)
wedgeangle = 36.1; % (deg)
wedgelength = 0.086; % (m)
element1midheight = 8.08e-3; % (m)
element1midoffset = 3.64e-3; % (m)

% Co-ordinates of element centres
elementcentreloc = zeros(element,2);
elementcentreloc(1,1) = element1midheight;
elementcentreloc(1,2) = element1midoffset;

if element > 1
    h = pitch*sind(wedgeangle);
    l = pitch*cosd(wedgeangle);
    for i = 1:element
        elementcentreloc(i,1) = element1midheight + ((i-1)*h);
        elementcentreloc(i,2) = element1midoffset + ((i-1)*l);
    end
end
```

```
% Diameter of Calibration SDHs
SDHDiameter = 3*10^-3; % (mm)

% Angle of Incidence at Wedge/Sample Interface based on
Refraction Angle
propangle                                                    =
asind((wedgevelocity*sind(refractionangle)/structureTvelocity))
;

%=================================================================
==================================
%=================================================================
==================================
%% Data Import

% Import of SDH Calibration CRAs generated from CMS-1
cd ('######') % Directory CRAs excel file
file = sprintf('######'); % SDH Calibration CRAs file name to be
opened
CIVAamps = readmatrix(file); % Importing SDH Calibration CRAs
data

disp('Initiate CIVA Ref Amp Cal Values Definition')

TCGpts = size(CIVAamps,2);
SDHs = zeros(TCGpts,1);

for counter = 1:TCGpts
    SDHs(counter,1) = CIVAamps(1,counter);
end

%=================================================================
==================================

CalBlockSDHs = CIVAamps(1,:)*(1e-3);
```

```
% Inspection data prior to first SDH cannot be calibrated and
can be disregarded
minDepth = CalBlockSDHs(1) - 0.5*SDHDiameter;

if mod(round(SDHs(end)-SDHs(1))/scanstepsize,2) == 0
    CIVACalamps       =       zeros(VPAs,       round(SDHs(end)-
SDHs(1))/scanstepsize);
elseif  mod(round(SDHs(end)-SDHs(1)/scanstepsize)+1,2) == 1
    CIVACalamps       =       zeros(VPAs,       round(SDHs(end)-
SDHs(1)/scanstepsize)+1);
end

% Interpolation of Simulated SDH CRA data between SDH depths for
each active VPA
for b = 1:VPAs
    disp(b)
    for c = 1:size(CIVAamps,2)-1
        gradients(b,c)           =           (CIVAamps(1+b,c+1)-
CIVAamps(1+b,c))/(SDHs(c+1)-SDHs(c));
        intercept(b,c)    =    (-gradients(b,c)*SDHs(c+1))    +
CIVAamps(1+b,c+1);

        x = SDHs(c):SDHs(c+1)-SDHs(c):SDHs(c+1);
        xq = SDHs(c):scanstepsize:SDHs(c+1);

        v = (gradients(b,c)*x) + intercept(b,c);

        if c == 1
            CIVACalamps(b,1:((SDHs(c+1)-
SDHs(c))/scanstepsize)+1) = interp1(x,v,xq);
        else
            CIVACalamps(b,((SDHs(c)-
SDHs(1))/scanstepsize)+1:((SDHs(c+1)-SDHs(1))/scanstepsize)+1)
= interp1(x,v,xq);
        end
    end
end
```

```
CIVAampTCG          =          zeros(VPAs+1,          ((SDHs(end)-
SDHs(1))/scanstepsize)+2);
CIVAExpampTCG        =        zeros(VPAs+1,        ((SDHs(end)-
SDHs(1))/scanstepsize)+2);

CIVAampTCG(2:end,1) = 1:1:VPAs;
CIVAampTCG(1,2:end) = SDHs(1,1):scanstepsize:SDHs(end,1);
CIVAampTCG(2:end,2:end) = CIVACalamps(:,:);
CIVAExpampTCG(2:end,1) = 1:1:VPAs;
CIVAExpampTCG(1,2:end) = SDHs(1,1):scanstepsize:SDHs(end,1);
CIVAExpampTCG(2:end,2:end) = CIVAExpamps(:,:);

%============================================================
====================================

% Importing FBH response percentages where OmniScan gain settings
% are set for SDH at 100% FSH
cd ('######')
file = sprintf('######');
SDH_FBH_percent = readmatrix(file);
SDH_FBH_percent = round(SDH_FBH_percent,1);
SDH_FBH_percentamps = zeros(1,VPAs);

% Interpolation of FBH response percentages (SDH @ 100%) across
apertures
for b = 1:size(SDH_FBH_percent,1)-1
    disp(b)
    for c = 1:size(SDH_FBH_percent,2)-1
        gradients(b,c)       =       (SDH_FBH_percent(b+1,c+1)-
SDH_FBH_percent(b+1,c))/(SDH_FBH_VPAs(c+1)-SDH_FBH_VPAs(c));
        intercept(b,c) = (-gradients(b,c)*SDH_FBH_VPAs(c+1)) +
SDH_FBH_percent(b+1,c+1);

        x          =          SDH_FBH_VPAs(c):SDH_FBH_VPAs(c+1)-
SDH_FBH_VPAs(c):SDH_FBH_VPAs(c+1);
        xq = SDH_FBH_VPAs(c):1:SDH_FBH_VPAs(c+1);
```

```
        v = (gradients(b,c)*x) + intercept(b,c);

        if c == 1
            SDH_FBH_percentamps(b,1:((SDH_FBH_VPAs(c+1)-
SDH_FBH_VPAs(c)))+1) = interp1(x,v,xq);
        else
            SDH_FBH_percentamps(b,((SDH_FBH_VPAs(c)-
SDH_FBH_VPAs(1)))+1:((SDH_FBH_VPAs(c+1)-SDH_FBH_VPAs(1)))+1)   =
interp1(x,v,xq);
        end
    end
end

%============================================================
====================================

% Importing FBH CRA data
% for FBHs at depths of 25, 37.5, 42.5, 50, 62.5, 67.5, & 75 mm
cd ('######') % Directory change to FBH CRA data location
file = sprintf('######');

CIVAExpFBH = readmatrix(file);

% Depths of FBHs
FBH = [25, 37.5, 42.5, 50, 62.5, 67.5, 75];

CIVAFBHamps = zeros(VPAs, (FBH(end)-FBH(1)/scanstepsize)+1);
CIVAExpampFBH        =        zeros(VPAs+1,        ((FBH(end)-
FBH(1))/scanstepsize)+2);

gradients = zeros(VPAs,size(CIVAFBHamps,2)-1);
intercept = zeros(VPAs,size(CIVAFBHamps,2)-1);

% Interpolation of FBH CRAs across apertures
for b = 1:VPAs
    disp(b)
```

```
    for c = 1:size(CIVAExpFBH,2)-1
        gradients(b,c)          =          (CIVAExpFBH(1+b,c+1)-
CIVAExpFBH(1+b,c))/(FBH(c+1)-FBH(c));
        intercept(b,c)    =    (-gradients(b,c)*FBH(c+1))    +
CIVAExpFBH(1+b,c+1);

        x = FBH(c):FBH(c+1)-FBH(c):FBH(c+1);
        xq = FBH(c):scanstepsize:FBH(c+1);

        v = (gradients(b,c)*x) + intercept(b,c);

        if c == 1
            CIVAFBHamps(b,1:((FBH(c+1)-FBH(c))/scanstepsize)+1)
= interp1(x,v,xq);
        else
            CIVAFBHamps(b,((FBH(c)-
FBH(1))/scanstepsize)+1:((FBH(c+1)-FBH(1))/scanstepsize)+1)   =
interp1(x,v,xq);
        end
    end
end

CIVAExpampFBH(2:end,1) = 1:1:VPAs;
CIVAExpampFBH(1,2:end) = FBH(1):scanstepsize:FBH(end);
CIVAExpampFBH(2:end,2:end) = CIVAFBHamps(:,:);



%==========================================================
====================================
%==========================================================
====================================
%% Retriving Data from Scan Simulation

disp('Initiate Simulation Scan Data Acquisition')

if strcmp(defects, 'SDH') % If a simulated SDH defect is being
investigated
```

```
    cd ('######') % Directory change to SDH simulation data
location
    vpatext = sprintf('######'); % SDH data file name to be
opened
    ScanData = dlmread(sprintf('%s.txt', vpatext), ';', 17, 0);

elseif strcmp(defects, 'LOF') % If a simulated LOF/Crack-like
defect is being investigated
    cd ('######') % Directory change to LOF simulation data
location
    vpatext = sprintf('######'); % LOF data file name to be
opened
    ScanData = dlmread(sprintf('%s.txt', vpatext), ';', 17, 0);

end

% Different import methods are required for Inspection Probe
Scanning Directions
if dir == 1

    VPAs = max(max(ScanData(:,1)));
    VPAsplit = size(ScanData,1)/VPAs;
    ScanStepsplit = (size(ScanData,2)-3)/2;
    ScanStepValEnd = size(ScanData,2)-1;

    time = ScanData(1:VPAsplit,2)*10^-6;

    CIVA_data_dB = zeros(VPAsplit,ScanStepsplit,VPAs);
    CIVA_data_val = zeros(VPAsplit,ScanStepsplit,VPAs);
    CIVA_data_percent = zeros(VPAsplit,ScanStepsplit,VPAs);

    % Segragation and organisation of Scan Data CIVA Reference
Amplitudes,
    % dB values, percentage amplitudes and time sequence
    for counter = 1:VPAs
        CIVA_data_dB(:,:,counter)     =     ScanData(((counter-
1)*VPAsplit)+1:(VPAsplit*counter),3:ScanStepsplit+2);
```

```
        CIVA_data_val(:,:,counter)     =     ScanData(((counter-
1)*VPAsplit)+1:(VPAsplit*counter),(ScanStepsplit+3):ScanStepVal
End);
        CIVA_data_percent(:,:,            counter)            =
sqrt(10.^(CIVA_data_dB(:,:, counter)/10));

        % Remove inf values
        infremove1 = find(isinf(CIVA_data_percent(:,:, counter))
== 1);
        infremoveVPA =  CIVA_data_percent(:, :, counter);
        infremoveVPA(infremove1) = 0;

        CIVA_data_percent(:, :, counter) = infremoveVPA(:,:) *
100;
        disp(counter)
    end


elseif dir == 2

    ScanStepsplit = size(ScanData,1)/ScanData(end,1);
    No_of_Steps = ScanData(end,1);
    VPAs = max(max(ScanData(:,2)))-1;
    VPAsplit = ScanStepsplit/VPAs;
    ScanStepValEnd = size(ScanData,2)-1;

    time = ScanData(1:VPAsplit,3)*10^-6;

    CIVA_data_dB = zeros(VPAsplit,No_of_Steps,VPAs);
    CIVA_data_val = zeros(VPAsplit,No_of_Steps,VPAs);
    CIVA_data_percent = zeros(VPAsplit,No_of_Steps,VPAs);

    % Segragation and organisation of Inspection Scan Data CIVA
Reference Amplitudes,
    % dB values, percentage amplitudes and time sequence
    for counter = 1:VPAs
        for counter2 = 1:No_of_Steps
```

```
            CIVA_data_dB(:,counter2,counter)                    =
ScanData(((counter2-1)*ScanStepsplit)+((counter-
1)*VPAsplit)+1:(((counter2-
1)*ScanStepsplit)+VPAsplit*counter),4);
            CIVA_data_val(:,counter2,counter)                   =
ScanData(((counter2-1)*ScanStepsplit)+((counter-
1)*VPAsplit)+1:(((counter2-
1)*ScanStepsplit)+VPAsplit*counter),5);
            CIVA_data_percent(:,:,          counter)            =
sqrt(10.^(CIVA_data_dB(:,:, counter)/10));

            % Remove inf values
            infremove1    =    find(isinf(CIVA_data_percent(:,:,
counter)) == 1);
            infremoveVPA =  CIVA_data_percent(:, :, counter);
            infremoveVPA(infremove1) = 0;
            CIVA_data_percent(:, :, counter) = infremoveVPA(:,:)
* 100;

        end
        disp(counter)
    end
end


% Centre of first virtual aperture of inspection probe setup
if mod(VPAaperture,2) == 1
    VPA1boundaryloc = (VPAaperture+1)/2;
else
    VPA1boundaryloc = VPAaperture/2;
end

% Co-ordinate locations of aperture centrelines at each bounndary
interface
for counter = 1:VPAs
    boundaryrayloc(1,counter)                                   =
elementcentreloc(counter+(VPA1boundaryloc-1),2)                 +
```

```
elementcentreloc(counter+(VPA1boundaryloc-1),1)/tand(90-
propangle);
end


%% C-scan Data Generation

% Removal of unneeded inspection data prior to specified minimum
depth of first SDH
% Data removed based on time period prior to first SDH depth,
% calculated from sound path lengths and known material
velocities
for i = 1:VPAs
    VPAstart(i,1)  =  elementcentreloc(round(VPAaperture/2)+(i-
1),1);
    VPAstart(i,2)  =  elementcentreloc(round(VPAaperture/2)+(i-
1),2);
    VPAraylength(i,1) = VPAstart(i,1)/sind(90-propangle);
    VPAraylength(i,2) = 2*VPAraylength(i,1)/wedgevelocity;
    VPAraylength(i,3) = VPAraylength(i,2) + (2*minDepth/sind(90-
refractionangle))/structureTvelocity;
    timeboundary(i) = find(time >= VPAraylength(i,2),1);
    timeminmm(i) = find(time >= VPAraylength(i,3),1);
    CIVA_data_val(1:timeminmm(i)-1,:,i) = 0;
    CIVA_data_percent(1:timeminmm(i)-1,:,i) = 0;
    CIVAdatadB(1:timeminmm(i)-1,:,i) = 0;
end

VPA_time = zeros(size(time,1)-timeminmm(end)+1,15,VPAs);

step = 1e-4; % (m) Minimum discretisation step

% VPAmax relates to the maximum amplitudes of each VPA for the
scan simulation data
% VPAtime relates to the information extracted from the SDH
Calibration data
```

```
% General Values related to each VPA
for j = 1:VPAs
    % Applicable time values beyond structure boundary
    VPA_time(timeminmm(j):size(time,1),1,j)                    =
time(timeminmm(j):size(time,1));

    % Portion of time related to propagation within structure
    VPA_time(timeminmm(j):size(time,1),2,j)                    =
VPA_time(timeminmm(j):size(time,1),1,j)-VPAraylength(j,2);     %
portion of time related to propagation within structure

    % Depth relating to specified time in structure
    VPA_time(timeminmm(j):size(time,1),3,j)                    =
structureTvelocity*(VPA_time(timeminmm(j):size(time,1),2,j)/2)*
sind(90-refractionangle); % depth relating to specified time in
structure

    % Rounded depth within structure
    VPA_time(timeminmm(j):size(time,1),4,j)                    =
round(VPA_time(timeminmm(j):size(time,1),3,j),3);    %    rounded
depth

    % Offset co-ordinate
    VPA_time(timeminmm(j):size(time,1),8,j)                    =
VPA_time(timeminmm(j):size(time,1),3,j)/tand(90-
refractionangle) + boundaryrayloc(1,j); % x-position

    % Rounded offset co-ordinate
    VPA_time(timeminmm(j):size(time,1),9,j)                    =
round(VPA_time(timeminmm(j):size(time,1),8,j),3);  % rounded x-
position

    % Indexed depth co-ordinate
    VPA_time(timeminmm(j):size(time,1),10,j)                   =
round(VPA_time(timeminmm(j):size(time,1),3,j)/step)+1;         %
indexed depth position
```

```
    % Indexed offset co-ordinate
    VPA_time(timeminmm(j):size(time,1),11,j)                    =
round(VPA_time(timeminmm(j):size(time,1),8,j)/step)+1;          %
indexed x-position

    % Generating C-scan representation using A-scan data to
extract SDH Maximum Percentage Amplitudes
    VPAmax(:,j,1) = max(CIVA_data_percent(:,:,j)); % Max Percent
@ VPA
    VPAmax(:,j,2) = max(abs(CIVA_data_val(:,:,j))); % Max CIVA
Val @ VPA

    for k = 1:size(time,1)
        % Determine Experimental SDH CRA respective to aperture
and depth within structure
        if    VPA_time(k,4,j)    >=    ((SDHs(1)-2)*(10^-3))    &&
VPA_time(k,4,j) < (SDHs(end)*(10^-3))
            check        =        find(CIVAampTCG(1,:)        ==
round(VPA_time(k,4,j)/10^-3))-1;
            if  isempty(check)
                VPA_time(k,13,j) = CIVACalamps(j,1);
            else
                VPA_time(k,13,j) = CIVACalamps(j,check);
            end

        elseif VPA_time(k,4,j) >= (SDHs(end)*(10^-3))
            VPA_time(k,13,j) = CIVACalamps(j,end);
        end

        % Determine Experimental FBH CRA respective to aperture
and depth within structure
        if    VPA_time(k,4,j)    >=    ((FBH(1)-2)*(10^-3))    &&
VPA_time(k,4,j) < (FBH(end)*(10^-3))
            check       =       find(CIVAExpampFBH(1,:)       ==
round(VPA_time(k,4,j)/10^-3))-1;
            if  isempty(check)
                VPA_time(k,14,j) = CIVAFBHamps(j,1);
```

```
            else
                VPA_time(k,14,j) = CIVAFBHamps(j,check);
            end

        elseif VPA_time(k,4,j) >= (FBH(end)*(10^-3))
            VPA_time(k,14,j) = CIVAFBHamps(j,end);
        else
            VPA_time(k,14,j) = 0;
        end

    end

    % Locate the Time Indexes of Max Percentage response for C-
scan image
    for counter2 = 1:size(CIVA_data_percent,2)
        check    =    find(CIVA_data_percent(:,counter2,j)    ==
VPAmax(counter2,j,1));
        VPAmax(counter2,j,3) = check(1);
    end

    % C-scan layout of respective 80% & 100% SDH CRAs
    for l = 1:size(VPAmax,1)
        VPAmax(l,j,7)  =  VPA_time(VPAmax(l,j,3),13,j);  %  CIVA
Amps for SDHs at 100% FSH
        VPAmax(l,j,8) = VPAmax(l,j,7)/0.8; % CIVA Amps for SDHs
at 80% FSH

        % Raw CIVA inspection simulation made relative to FBH at
100% FSH
        VPAmax(l,j,17)                                          =
VPAmax(l,j,2)/(VPA_time(VPAmax(l,j,3),14,j));
    end
end

% Simulation data made relative to FBH percent data calibrated
against experimental SDHs at 100% FSH
for j = 1:VPAs
```

```
    VPAmax(:,j,18)                                                  =
(VPAmax(:,j,17).*SDH_FBH_percentamps(j))/100;
end

% Simulation data made relative to experimental SDH responses at
100% FSH
for j = 1:VPAs
    for l = 1:size(VPAmax,1)
        VPAmax(l,j,20) = VPAmax(l,j,18)*VPAmax(l,j,7);
    end
end

% Simulation data made relative to experimental SDH responses at
80% FSH
VPAmax(:,:,21) = (VPAmax(:,:,20)./VPAmax(:,:,8))*100;



%% C-scan Image Generation

cd /Users/Matthew/Documents/EngD/CIVA_Update

% C-scan axis dimensions
yCIVAVPA = 1:1:VPAs;
xCIVAinc = 0:1:size(CIVA_data_percent,2)-1;

% Rotation of C-scan images to correct orientation
Cscan_1 = rot90(VPAmax(:,:,1),3);
Cscan_2 = rot90(VPAmax(:,:,8),3);
Cscan_3 = rot90(VPAmax(:,:,21),3);

% Raw CIVA C-scan
figure()
hold on
imagesc(xCIVAinc, yCIVAVPA, fliplr(Cscan_1))
xlabel('Increment (mm)')
ylabel('VPA')
```

```
axis([0 size(VPAmax,1) 1 VPAs])
c = colorbar;
caxis([0 100]) % Colour to Percentage Limits
c.Label.String = '%';
cMap = jet_white;
colormap(cMap)
set(gca,'fontsize',20)


% EXTENDE Calibrated C-scan
figure()
hold on
imagesc(xCIVAinc, yCIVAVPA, fliplr(Cscan_2))
xlabel('Increment (mm)')
ylabel('VPA')
axis([0 size(VPAmax,1) 1 VPAs])
c = colorbar;
caxis([0 100]) % Colour to Percentage Limits
c.Label.String = '%';
cMap = jet_white;
colormap(cMap)
set(gca,'fontsize',20)


% TCG Calibrated C-scan
figure()
hold on
imagesc(xCIVAinc, yCIVAVPA, fliplr(Cscan_3))
xlabel('Increment (mm)')
ylabel('VPA')
axis([0 size(VPAmax,1) 1 VPAs])
c = colorbar;
caxis([0 100]) % Colour to Percentage Limits
c.Label.String = '%';
cMap = jet_white;
colormap(cMap)
set(gca,'fontsize',20)
```

7.3 Appendix 3 – Remote Surface Direct Inspection of LOF Flaw 1 in Butt Weld at 30 mm Probe Offset

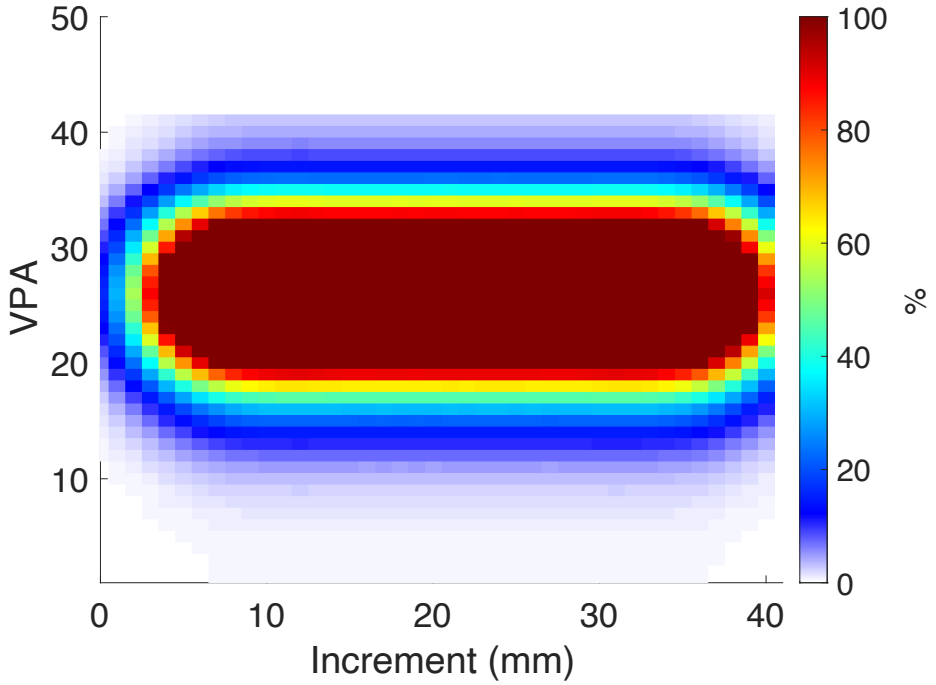

Figure 150: Custom TCG calibrated CIVA simulation data of remote surface direct inspection of LOF defect 1 in butt weld at 30 mm probe offset

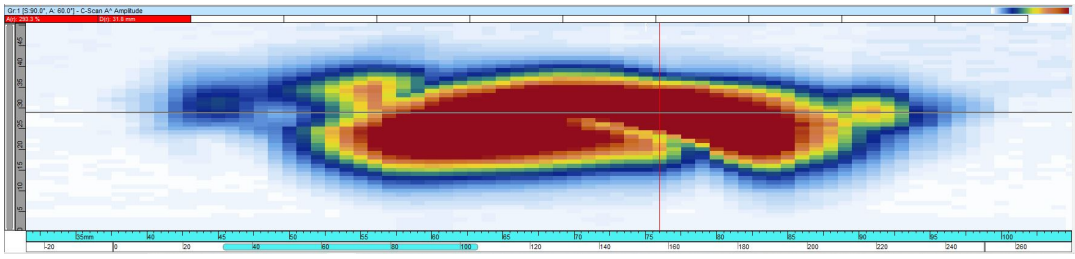

Figure 151: Experimental data of remote surface direct inspection of LOF defect 1 in butt weld at 30 mm probe offset captured using an OLYMPUS Omniscan MX2 attached with a 5 MHz 60 element linear array PipeWizard probe and 55^0 Rexolite wedge

7.4 Appendix 4 – Remote Surface Direct Inspection of LOF Flaw 1 in Butt Weld at 45 mm Probe Offset

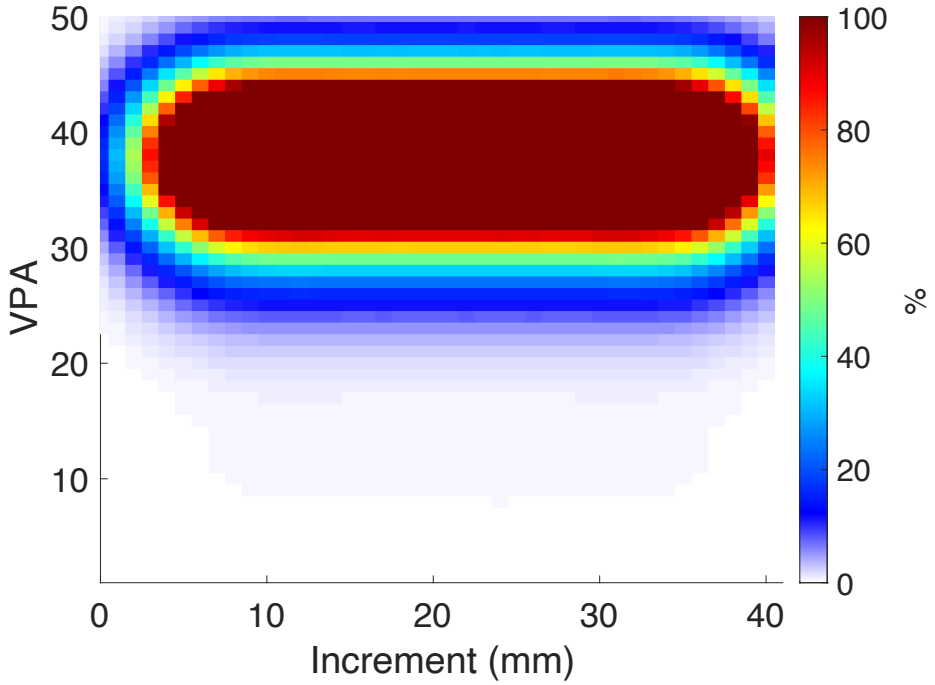

Figure 152: Custom TCG calibrated CIVA simulation data of remote surface direct inspection of LOF defect 1 in butt weld at 45 mm probe offset

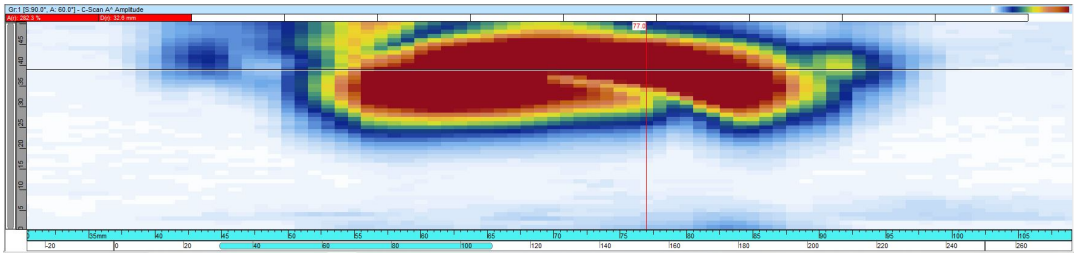

Figure 153: Experimental data of remote surface direct inspection of LOF defect 1 in butt weld at 45 mm probe offset captured using an OLYMPUS Omniscan MX2 attached with a 5 MHz 60 element linear array PipeWizard probe and 55^0 Rexolite wedge

7.5 Appendix 5 – Top Surface Half-Skip Inspection of LOF Flaw 1 in Butt Weld at 130 mm Probe Offset

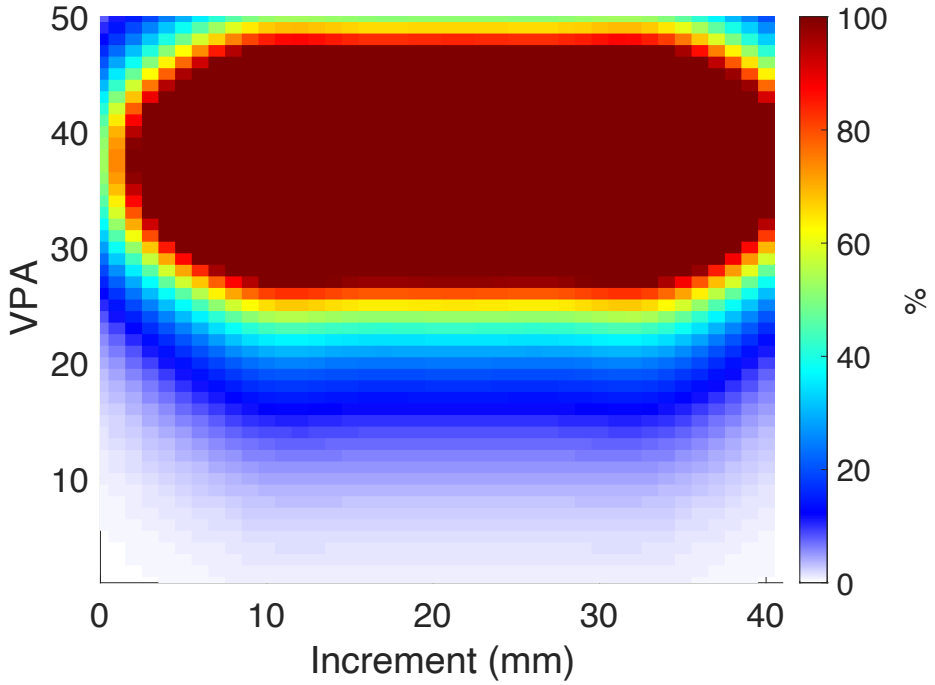

Figure 154: Custom TCG calibrated CIVA simulation data of top surface half-skip inspection of butt weld LOF defect 1 at 130 mm probe offset

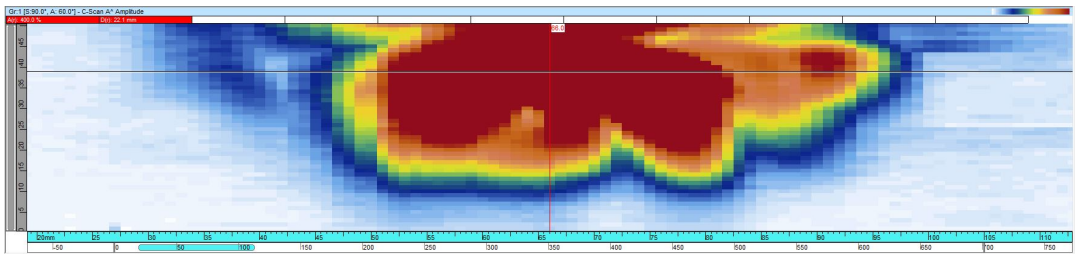

Figure 155: Experimental data of top surface half-skip inspection of LOF defect 1 in butt weld at 130 mm probe offset captured using an OLYMPUS Omniscan MX2 attached with a 5 MHz 60 element linear array PipeWizard probe and 55^0 Rexolite wedge

7.6 Appendix 6 – Top Surface Half-Skip Inspection of LOF Flaw 1 in Butt Weld at 145 mm Probe Offset

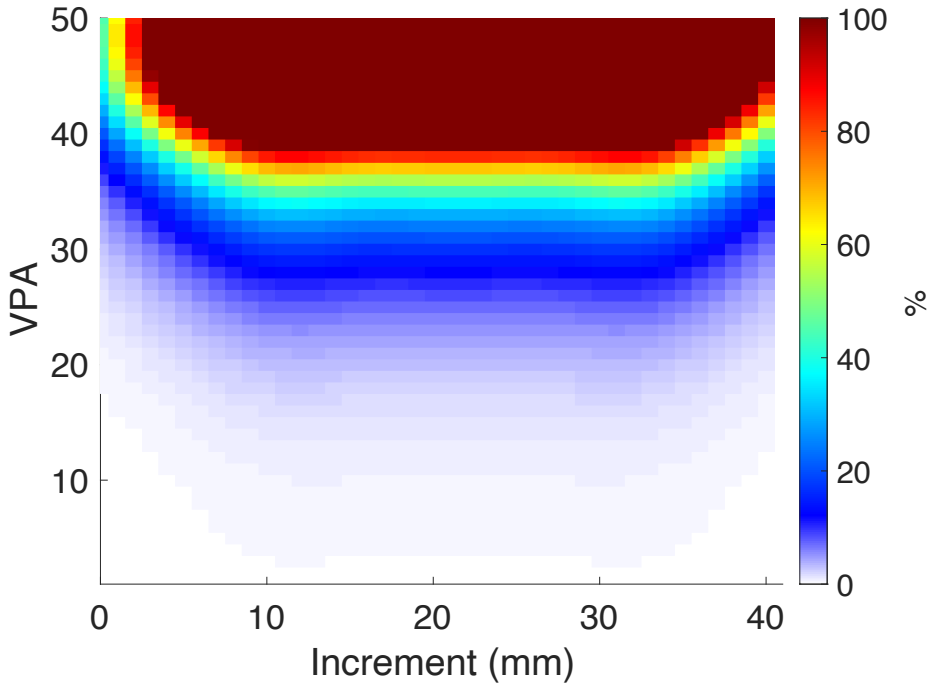

Figure 156: Custom TCG calibrated CIVA simulation data of top surface half-skip inspection of LOF defect 1 in butt weld at 145 mm probe offset

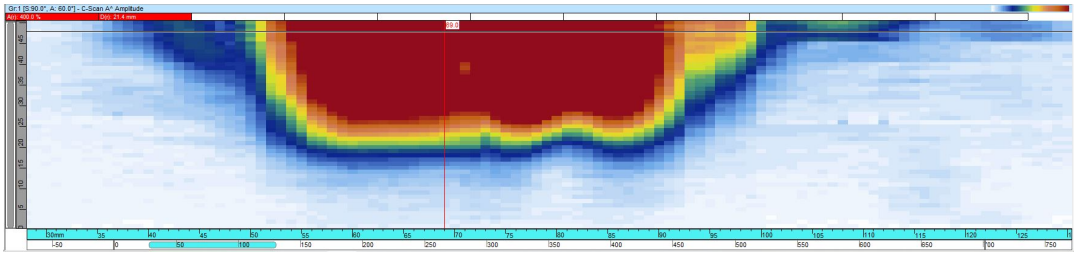

Figure 157: Experimental data of top surface half-skip inspection of LOF defect 1 in butt weld at 145 mm probe offset captured using an OLYMPUS Omniscan MX2 attached with a 5 MHz 60 element linear array PipeWizard probe and 55^0 Rexolite wedge

7.7 Appendix 7 – Top Surface Direct Inspection of LOF Flaw 2 in Butt Weld at 50 mm Probe Offset

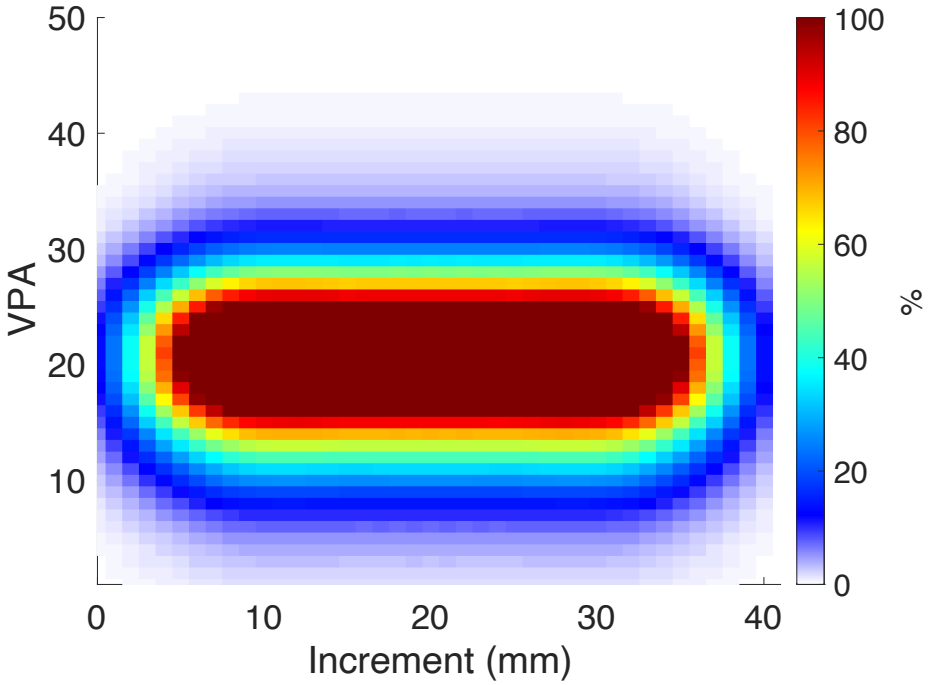

Figure 158: Custom TCG calibrated CIVA simulation data of top surface direct inspection of LOF defect 2 in butt weld at 50 mm probe offset

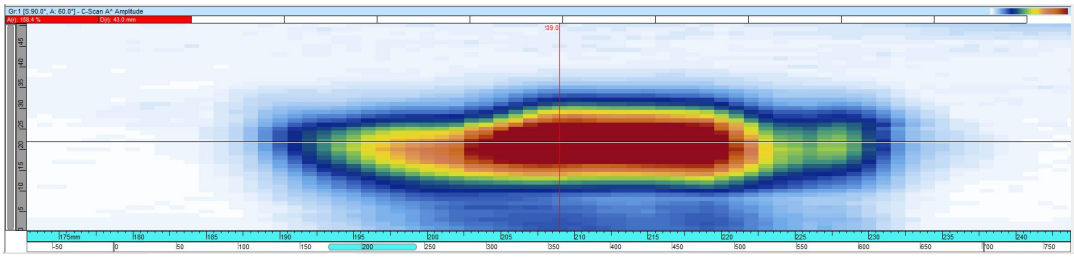

Figure 159: Experimental data of top surface direct inspection of LOF defect 2 in butt weld at 50 mm probe offset captured using an OLYMPUS Omniscan MX2 attached with a 5 MHz 60 element linear array PipeWizard probe and 55^0 Rexolite wedge

7.8 Appendix 8 – Top Surface Direct Inspection of LOF Flaw 2 in Butt Weld at 60 mm Probe Offset

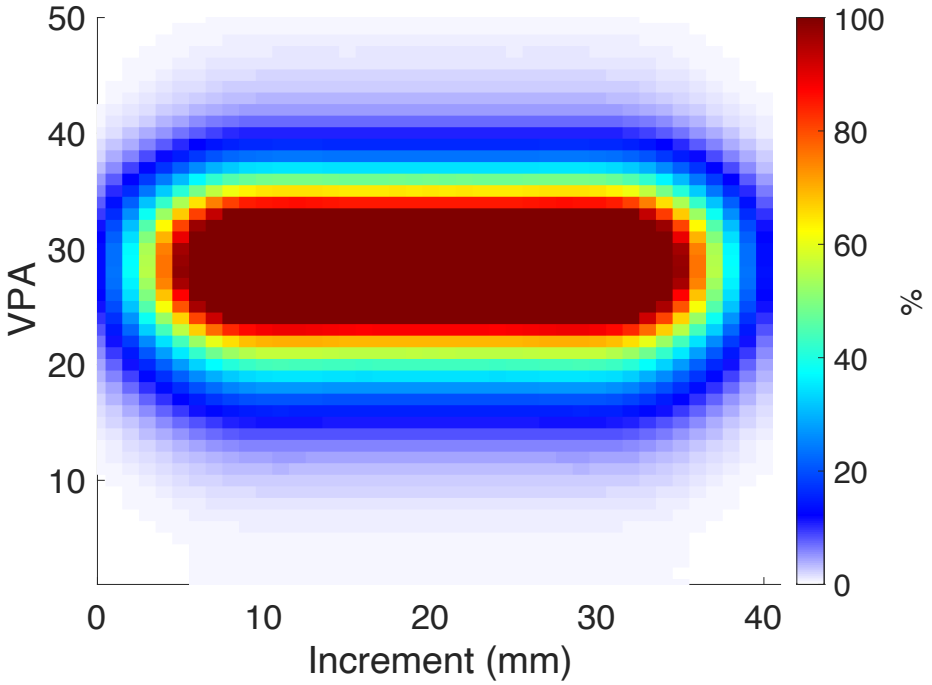

Figure 160: Custom TCG calibrated CIVA simulation data of top surface direct inspection of LOF defect 2 in butt weld at 60 mm probe offset

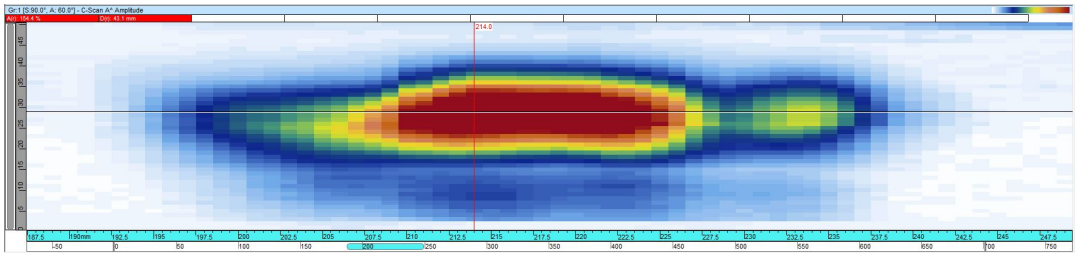

Figure 161: Experimental data of top surface direct inspection of LOF defect 2 in butt weld at 60 mm probe offset captured using an OLYMPUS Omniscan MX2 attached with a 5 MHz 60 element linear array PipeWizard probe and 55^0 Rexolite wedge

7.9 Appendix 9 – Top Surface Half-Skip Inspection of LOF Flaw 2 in Butt Weld at 40 mm Probe Offset

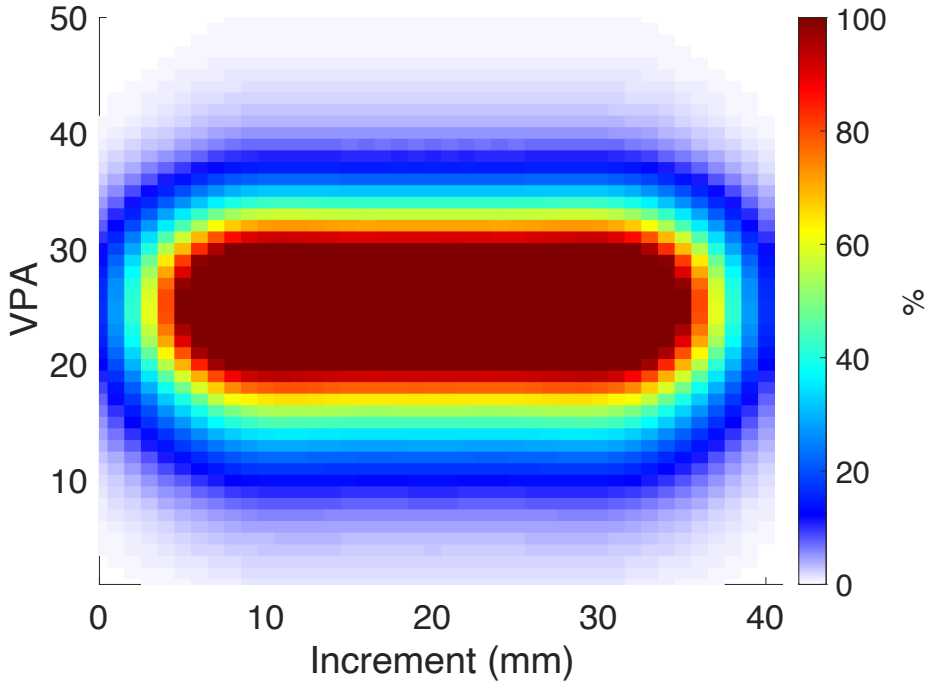

Figure 162: Custom TCG calibrated CIVA simulation data of top surface half-skip inspection of LOF defect 2 in butt weld at 40 mm probe offset

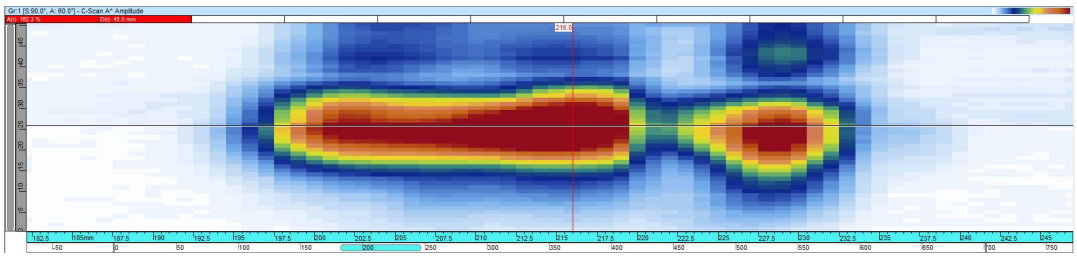

Figure 163: Experimental data of top surface half-skip inspection of LOF defect 2 in butt weld at 40 mm probe offset captured using an OLYMPUS Omniscan MX2 attached with a 5 MHz 60 element linear array PipeWizard probe and 55^0 Rexolite wedge

7.10 Appendix 10 – Top Surface Half-Skip Inspection of LOF Flaw 2 in Butt Weld at 50 mm Probe Offset

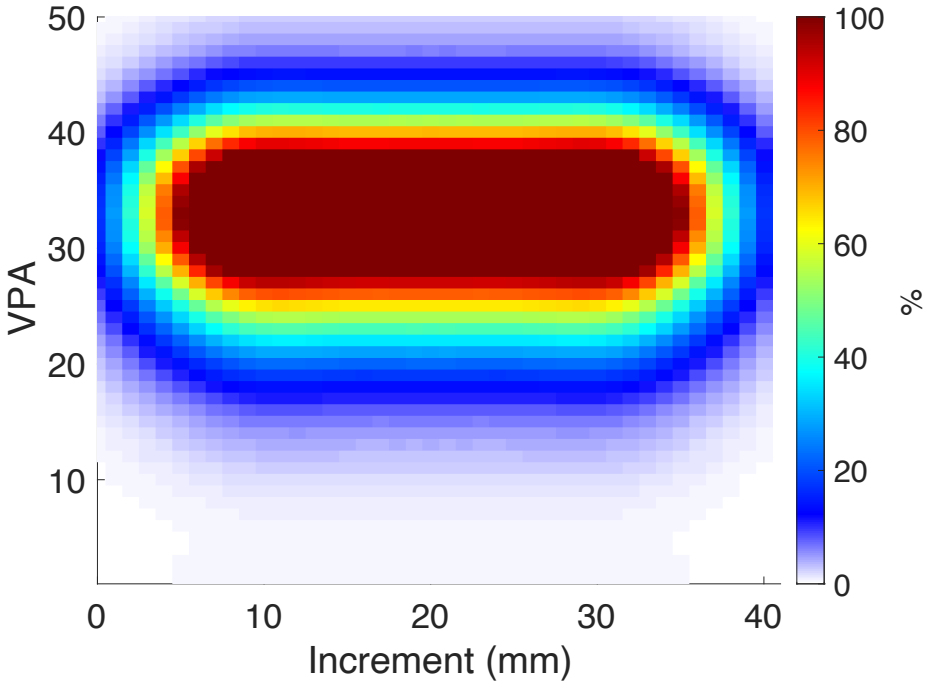

Figure 164: Custom TCG calibrated CIVA simulation data of top surface half-skip inspection of LOF defect 2 in butt weld at 50 mm probe offset

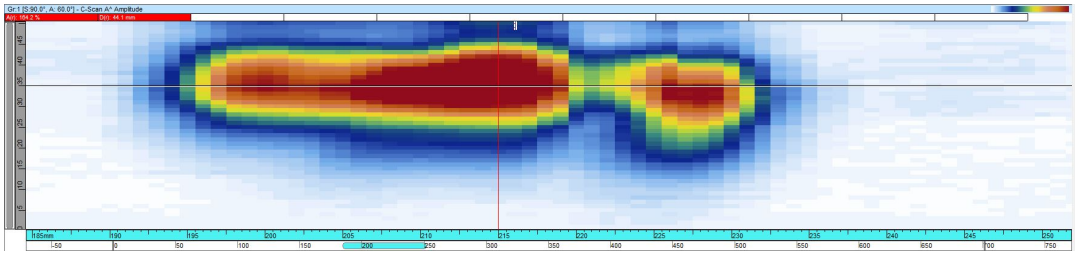

Figure 165: Experimental data of top surface half-skip inspection of LOF defect 2 in butt weld at 50 mm probe offset captured using an OLYMPUS Omniscan MX2 attached with a 5 MHz 60 element linear array PipeWizard probe and 55^0 Rexolite wedge

7.11 Appendix 11 – Top Surface Direct Inspections of Branched LOF Flaw 2 in Butt Weld (First Iteration)

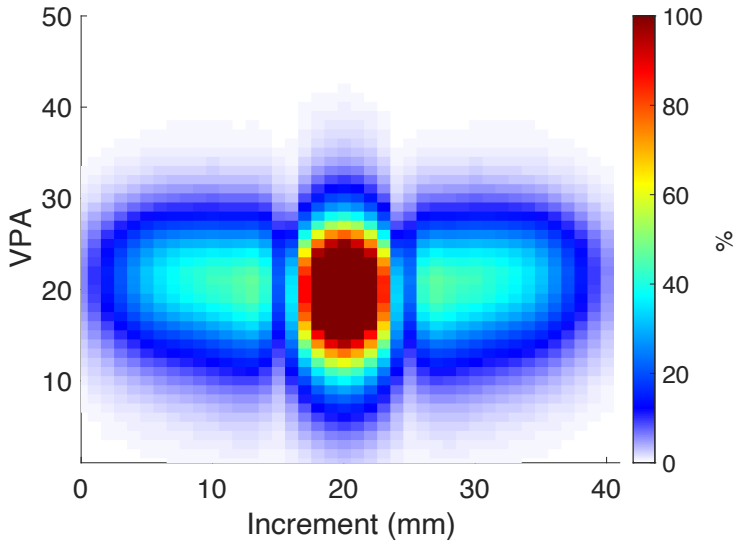

Figure 166: Custom TCG calibrated CIVA simulation data of top surface direct inspection of branched LOF defect 2 in butt weld at 50 mm probe offset (first iteration)

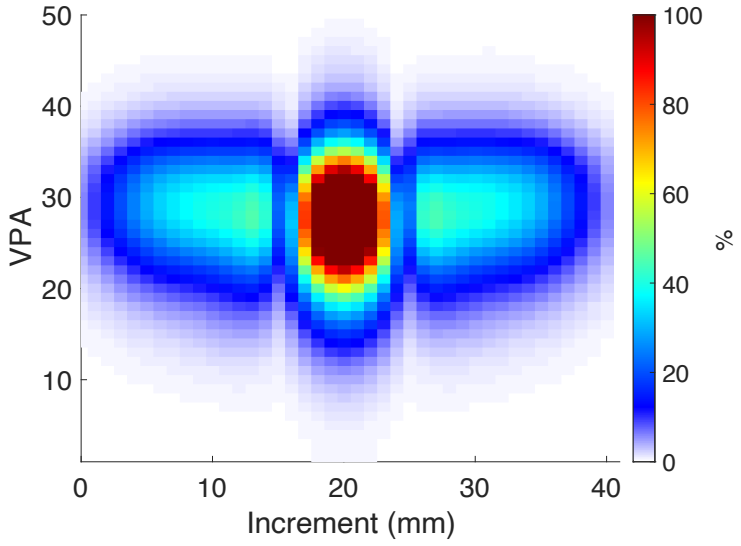

Figure 167: Custom TCG calibrated CIVA simulation data of top surface direct inspection of branched LOF defect 2 in butt weld at 60 mm probe offset (first iteration)

7.12 Appendix 12 – Top Surface Half-Skip Inspections of Branched LOF Flaw 2 in Butt Weld (First Iteration)

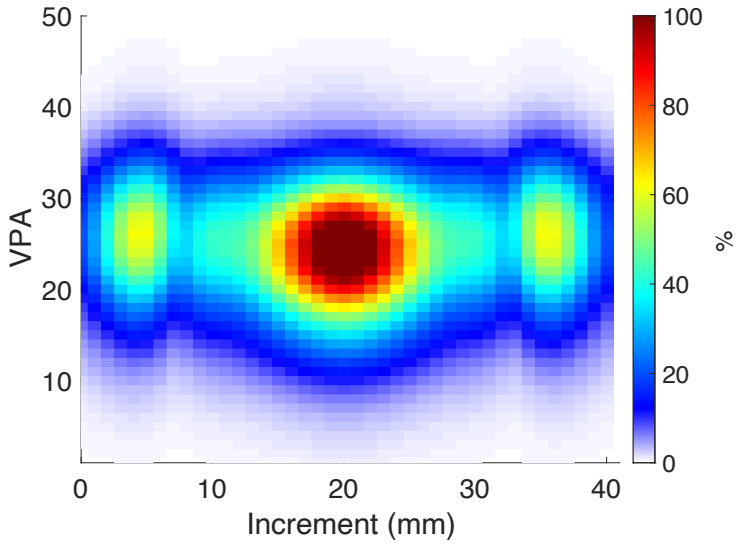

Figure 168: Custom TCG calibrated CIVA simulation data of top surface half-skip inspection of branched LOF defect 2 in butt weld at 40 mm probe offset (first iteration)

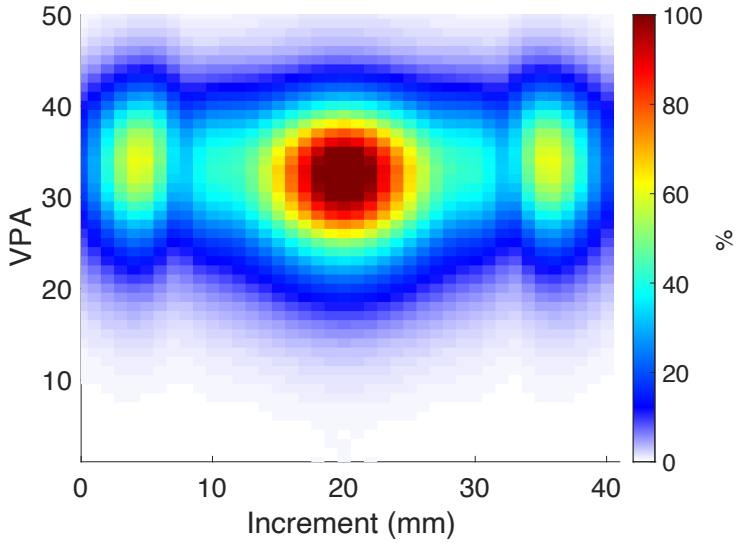

Figure 169: Custom TCG calibrated CIVA simulation data of top surface half-skip inspection of branched LOF defect 2 in butt weld at 50 mm probe offset (first iteration)

7.13 Appendix 13 – Top Surface Direct Inspections of Branched LOF Flaw 2 in Butt Weld (Second Iteration)

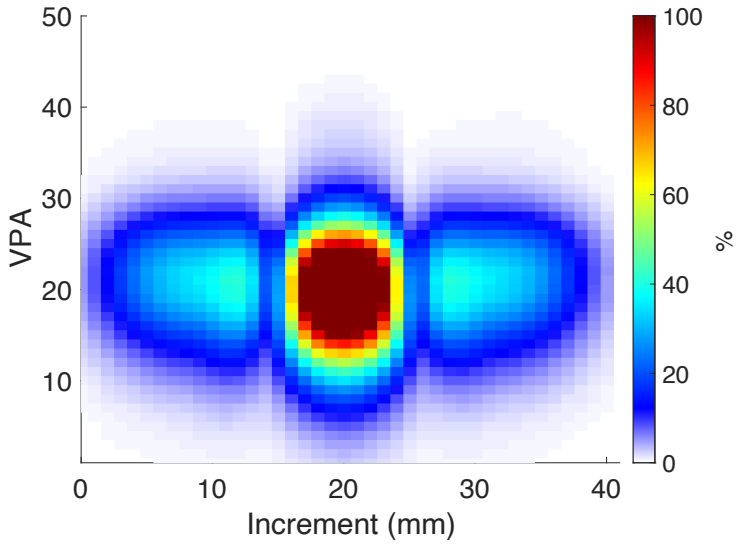

Figure 170: Custom TCG calibrated CIVA simulation data of top surface direct inspection of branched LOF defect 2 in butt weld at 50 mm probe offset (second iteration)

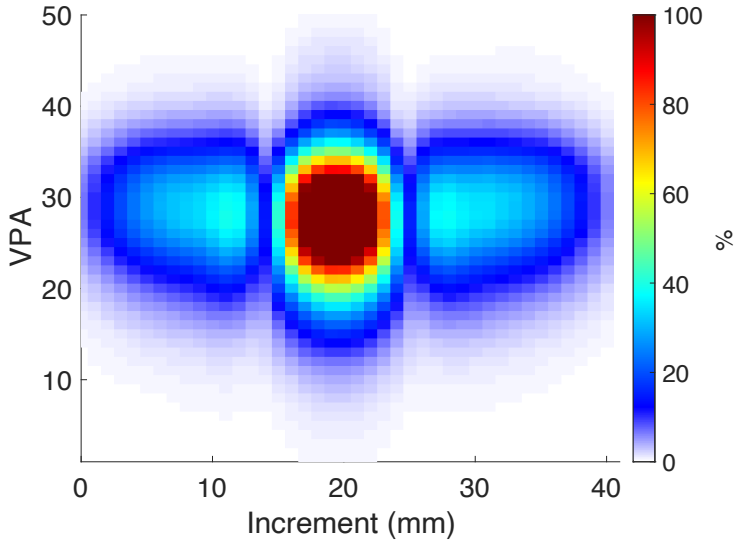

Figure 171: Custom TCG calibrated CIVA simulation data of top surface direct inspection of branched LOF defect 2 in butt weld at 60 mm probe offset (second iteration)

7.14 Appendix 14 – Top Surface Half-Skip Inspections of Branched LOF Flaw 2 in Butt Weld (Second Iteration)

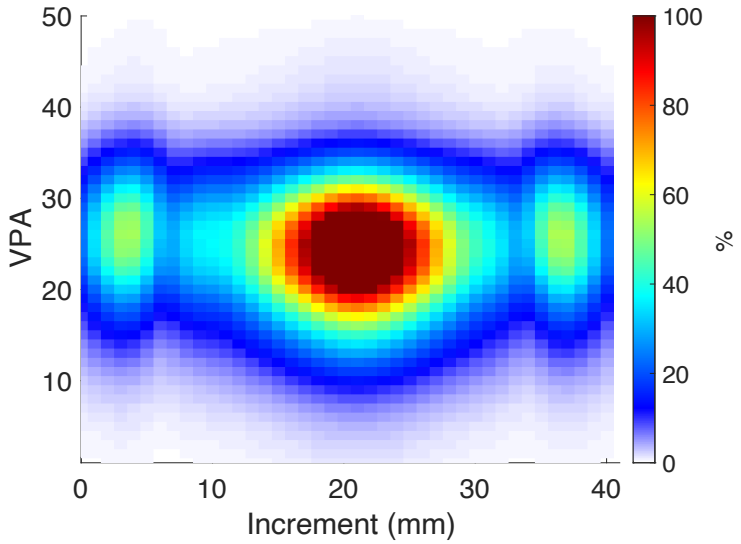

Figure 172: Custom TCG calibrated CIVA simulation data of top surface half-skip inspection of branched LOF defect 2 in butt weld at 40 mm probe offset (second iteration)

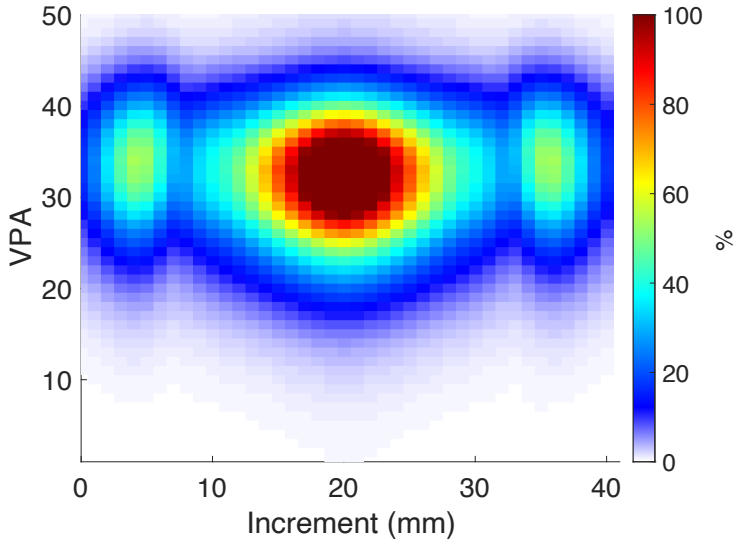

Figure 173: Custom TCG calibrated CIVA simulation data of top surface half-skip inspection of branched LOF defect 2 in butt weld at 50 mm probe offset (second iteration)

8 References

[1] H. K. Josef Krautkrämer, Ultrasonic Testing of Materials, 4th Edition ed., Berlin: Springer-Verlag, 1990.

[2] J. T. Boyle and R. Hamilton, Engineering Mechanics 1, Pearson, 2011.

[3] M. Williams, "Phys.org: What is Hooke's Law?," Science X, 16 February 2015. [Online]. Available: https://phys.org/news/2015-02-law.html. [Accessed 20 May 2020].

[4] T. Lardner, New Algorithms for Ultrasonic Non-Destructive Evaluation, PhD thesis: University of Strathclyde, 2016.

[5] E. A. López-Guerra and S. D. Solares, "Modeling viscoelasticity through spring–dashpot models in intermittent-contact atomic force microscopy," *Beilstein J Nanotechnol,* vol. 5, p. 2149–2163, 2014.

[6] M. Long, Architectural Acoustics, Oxford: Elsevier Inc., 2014, 2006.

[7] T. Atkins and M. Escudier, A Dictionary of Mechanical Engineering (1 ed.), Oxford: Oxford University Press, 2013.

[8] C. J. Hellier, Handbook of Non-Destructive Evaluation, New York, USA: The McGraw-Hill Companies, Inc., 2003.

[9] Engineering ToolBox, "Modulus of Rigidity," 2005. [Online]. Available: https://www.engineeringtoolbox.com/modulus-rigidity-d_946.html. [Accessed 3 June 2020].

[10] OLYMPUS NDT, "Ultrasonic Transducer Technical Notes," OLYMPUS CORPORATION, 2006. [Online]. Available:

https://mbi-ctac.sites.medinfo.ufl.edu/files/2017/02/ultrasound-basics.pdf. [Accessed 3rd June 2020].

[11] D. J. Cotter, T. E. Michaels, J. E. Michaels, D. Kass, M. E. Stanton, I. V. kosenko and F. H. C. Hotchkiss, "Squirter, Roller Probe, and Air-Coupled Ultrasonic Transducer Techniques for Low Frequency Inspection of Advanced Composites Materials," in *WCNDT*, Roma, 2000.

[12] G. M. Revel, G. Pandarese and A. Cavuto, "Advanced ultrasonic non-destructive testing for damage detection on thick and curved composite elements for constructions," *Journal of Sandwich Structures & Materials,* vol. 15, no. 1, pp. 5-24, 2013.

[13] P. Aryan, S. Sampath and H. Sohn, "An Overview of Non-Destructive Testing Methods for Integrated Circuit Packaging Inspection," *Sensors (Basel),* vol. 18, 1981.

[14] L. J. Bond and A. Ahmad, "Fundamentals of Ultrasonic Inspection," *ASM International: Nondestructive Evaluation of Materials,* vol. 17, 2018.

[15] D. E. Hardt and J. M. Katz, "Ultrasonic Measurement of Weld Penetration: The use of pulse-echo techniques to determine weld pool dimensions is investigated," in *Welding Research Supplement*, 1984.

[16] J. Turcotte, P. Rioux and J.-A. Lavoie, "Comparison Corrosion Mapping Solutions using Phased Array, Conventional UT and 3D scanners," in *World Conference on Non-Destructive Testing 2016*, Munich, 2016.

[17] NDT Resource Center, "Attenuation of Sound Waves," Iowa State University, 2012. [Online]. Available: https://www.nde-

ed.org/EducationResources/CommunityCollege/Ultrasonics/Physics/attenuation.htm#:~:text=Attenuation%20can%20be%20determined%20by,the%20time%20interval%20between%20them.. [Accessed 3rd June 2020].

[18] A. C. Woloszyn, S. Fisher and R. L. Jones, "The Application of Ultrasound to Refine Weld Metal Structures," in *JOM-9, 9th International Conference on Joining of Materials,*, Helsingør, 1999.

[19] A. J. Healey and S. Leeman, "Speckle reduction methods in ultrasound pulseecho imaging," in *International Conference on Acoustic Sensing and Imaging*, 1993.

[20] Y. Li, V. L. Newhouse and P. M. Shankar, "Speckle reduction in ultrasonic SAFT images in the coarse grained material through split spectrum processing," in *Review of Progress in Quantitative Nondestructive Evaluation*, 1989.

[21] B. Xiao, Methodologies for Enhancing Ultrasonic NDE of Coarse-Grained Materials, University of Strathclyde, 2016.

[22] E. P. Papadakis, "Ultrasonic Attenuation Caused by Scattering in Polycrystalline Metals," *The Journal of the Acoustical Society of America,* vol. 37, no. 4, 1965.

[23] J. v. Opstal, The Auditory System and Human Sound-Localization Behavior, Amsterdam: Elsevier Inc., 2016.

[24] A. Arnau, Piezoelectric Transducers and Applications, Berlin: Springer-Verlag Berlin Heidelberg, 2008.

[25] T. Rossing, Springer Handbook of Acoustics, New York: Springer Science+Business Media, 2007.

[26] International Atomic Energy Agency, Training Guidelines In Non-Destructive Testing Techniques, Vienna: International Atomic Energy Agency, 2018.

[27] J. David and N. Cheeke, Fundamentals and Applications of Ultrasonic Waves, Boca Raton: CRC Press, 2012.

[28] A. Butterfield and J. Szymanski, A Dictionary of Electronics and Electrical Engineering, Oxford: Oxford University Press, 2018.

[29] A. Safari and E. K. Akdogan, Piezoelectric and Acoustic Materials for Transducer Applications, Ney York: Springer Science+Business Media, LLC, 2008.

[30] NDT Resource Centre, "Characteristics of Piezoelectric Transducers," University of Iowa, 2012. [Online]. Available: https://www.nde-ed.org/EducationResources/CommunityCollege/Ultrasonics/EquipmentTrans/characteristicspt.htm. [Accessed 9th June 2020].

[31] OLYMPUS NDT, "A Review of Conventional Beam Characteristics," OLYMPUS CORPORATION, 7th November 2007. [Online]. Available: https://www.olympus-ims.com/en/ndt-tutorials/transducers/characteristics/. [Accessed 6th June 2020].

[32] NDT Resource Center, "Transducer Beam Spread," University of Iowa, 2012. [Online]. Available: https://www.nde-ed.org/EducationResources/CommunityCollege/Ultrasonics/Equipment Trans/beamspread.htm. [Accessed 9th June 2020].

[33] TWI Ltd., "Advantages and disadvantages of the through transmission method of ultrasonic inspection," TWI Ltd., 3rd November 2016. [Online]. Available: https://www.twi-global.com/technical-knowledge/faqs/faq-what-are-the-

advantages-and-disadvantages-of-the-through-transmission-method-of-ultrasonic-inspection. [Accessed 9th June 2020].

[34] TWI Ltd., "What are the advantages of using twin crystal ultrasonic probes?," TWI Ltd., 23rd March 2017. [Online]. Available: https://www.twi-global.com/technical-knowledge/faqs/faq-what-are-the-advantages-of-using-twin-crystal-ultrasonic-probes. [Accessed 9th June 2020].

[35] D. Kass, T. Nelligan and M. Moles, "Advances in Ultrasonic Weld Inspection," *Inspection Trends,* 2008.

[36] A. Fatemi, S.-E. Måsøy and A. Rodriguez-Molares, "Row-column based coherence imaging using a 2D-array transducer: a row based implementation," *IEEE Transactions on Ultrasonics, Ferroelectrics, and Frequency Control,* 2020.

[37] H. Wang, Z. Chen, H. Yang, H. Jiang and H. Xie, "A Ceramic PZT-Based PMUT Array for Endoscopic Photoacoustic Imaging," *Journal of Microelectromechanical Systems,* 2020.

[38] H. Zhang, B. Bai, J. Zheng and Y. Zhou, "Optimal Design of Sparse Array for Ultrasonic Total Focusing Method by Binary Particle Swarm Optimization," *IEEE Access,* vol. 8, pp. 111945-111953, 2020.

[39] A. Price and B. Long, "Fibonacci Spiral Arranged Ultrasound Phased Array for Mid-Air Haptics," in *IEEE INTERNATIONAL ULTRASONICS SYMPOSIUM*, Kobe, Japan, 2018.

[40] M. Acebes, D. Florez, N. Thorpe and T. Aguado, "Optimization of Phased-Array Transducers for Ultrasonic Inspection in Composite Materials Using Sliding Probes," in *6th International Symposium on NDT in Aerospace*, Madrid, 2014.

[41] Elcometer, “Transducers Characteristics Explained,” Elcometer Limited, [Online]. Available: https://www.elcometer.com/en/transducers-characteristics-explained.html. [Accessed 21 December 2020].

[42] J. Brizuela, J. Camacho, G. Cosarinsky, J. M. Iriarte and J. F. Cruza, “Improving elevation resolution in phased-array inspections for NDT,” *NDT & E International,* 2018.

[43] OLYMPUS NDT, “Introduction to Phased Array Probes,” OLYMPUS CORPORATION, 7th September 2017. [Online]. Available: https://www.olympus-ims.com/en/probes/pa/. [Accessed 9th June 2020].

[44] OLYMPUS NDT, “Beam Steering,” OLYMPUS CORPORATION, 2020. [Online]. Available: https://www.olympus-ims.com/en/ndt-tutorials/transducers/pa-beam/steering/. [Accessed 9th June 2020].

[45] OLYMPUS NDT, “Pulser and Receiver Operation,” OLYMPUS COORPORATION, 9th November 2007. [Online]. Available: https://www.olympus-ims.com/en/ndt-tutorials/flaw-detection/pulser-and-receiver/#:~:text=Pulse%20repetition%20frequency%20(PRF)%3A,with%20very%20long%20sound%20paths.. [Accessed 7th June 2020].

[46] BINDT, “S-Scan,” 2020. [Online]. Available: https://www.bindt.org/What-is-NDT/Index-of-acronyms/S/. [Accessed 8th June 2020].

[47] BINDT, “TOFD,” 2013. [Online]. Available: https://www.bindt.org/What-is-NDT/Index-of-acronyms/T/TOFD/. [Accessed 4 May 2020].

[48] J. Kitze, D. Brackrock, G. Brekow, J. Prager, M. Gaal and M. Kreutzbruck, “SAFT and TOFD – Compared in Ultrasonic Defect Detection,” in *8th International Conference on NDE in Relation to Structural Integrity for Nuclear and Pressurized Components*, Berlin, Germany, 2012.

[49] T. Armitt, “Phased Arrays Not The Answer To Every Application,” in *European conference on Non-Destructive Testing*, Sheffield.

[50] J. P. C. a. J. A. G. Temple, ENGINEERING APPLICATIONS OF ULTRASONIC TIME-OF-FLIGHT DIFFRACTION, 2nd Edition ed., D. M. J. Whittle, Ed., Baldock, Hertfordshire: RESEARCH STUDIES PRESS LTD., 2001.

[51] K. Manjula, K. Vijayarekha, B. Venkatraman and D. Karthik, “Ultrasonic Time of Flight Diffraction Technique for Weld Defects: A Review,” *Research Journal of Applied Sciences, Engineering and Technology,* 2012.

[52] Ministry of Defence, “Requirements for Non-Destructive Examination Methods - Part 5: Ultrasonic,” *Defence Standard 02-729,* 21 June 2013.

[53] U. Schlengermann, “Characterization of Reflectors by Ultrasonic Methods,” *NDTnet,* vol. 1, no. 12, December 1996.

[54] TWI Ltd., “What is Welding? - Definition, Processes and Types of Welds,” TWI Ltd., 18 February 2019. [Online]. Available: https://www.twi-global.com/technical-knowledge/faqs/what-is-welding. [Accessed 1 July 2020].

[55] R. Singh, Applied Welding Engineering: Processes, Codes and Standards, 1st Edition ed., Waltham, MA: Elsevier, 2012.

[56] The British Standards Institution, “BS EN ISO 9692-3:2016 - Welding and allied processes. Types of joint preparation. Metal inert gas welding and tungsten inert gas welding of aluminium and its alloys,” BSI Standards Limited, 2016.

[57] TWI Ltd., “Design - Part 3,” TWI Ltd., 20 October 2015. [Online]. Available: https://www.twi-global.com/technical-knowledge/job-knowledge/design-part-3-092. [Accessed 12 July 2020].

[58] B. Raj, “Nondestructive Testing and Evaluation: Overview,” in *Encyclopedia of Materials: Science and Technology*, Elsevier Ltd, 2001, pp. 6177-6184.

[59] Ministry of Defence, “Minimum Non-Destructive Examination Acceptance Standards for Welds in HM Submarines and Surface Ships not in Class,” *Defence Standard 02-773,* 21 June 2013.

[60] American Welding Society, “Weld Root,” 2020. [Online]. Available: https://awo.aws.org/glossary/weld-root/. [Accessed 7 July 2020].

[61] NDT Resource Center, “Loading,” Iowa State University, 2012. [Online]. Available: https://www.nde-ed.org/EducationResources/CommunityCollege/Materials/Mechanical/Loading.htm#:~:text=There%20are%20five%20fundamental%20loading,bending%2C%20shear%2C%20and%20torsion.. [Accessed 7 July 2020].

[62] TWI Ltd., “Distortion - Prevention by Design,” TWI Ltd., 19 October 2015. [Online]. Available: https://www.twi-global.com/technical-knowledge/job-knowledge/distortion-prevention-by-design-034. [Accessed 7th July 2020].

[63] TWI Ltd., “Distortion - Types and Causes,” TWI Ltd., 23 March 2017. [Online]. Available: https://www.twi-global.com/technical-knowledge/job-knowledge/distortion-types-and-causes-033. [Accessed 7th July 2020].

[64] P. J. Haagensen and S. J. Maddox, “IIW Recommendations on Post Weld Improvement of Steel and Aluminium Structures,” International Institute of Welding, 2001.

[65] ESAB, “MIG Handbook: Weld Defects - Undercutting,” ESAB, 2017. [Online]. Available: https://www.esabna.com/euweb/mig_handbook/592mig10_5.htm. [Accessed 17 March 2017].

[66] S. E. Hughes, A Quick Guide to Welding and Weld Inspection, C. Matthews, Ed., Woodhead Publishing Limited and Matthews Engineering Training Limited, 2009.

[67] ESAB, “MIG Handbook: Weld Defects - Incomplete Penetration,” ESAB, 2017. [Online]. Available: https://www.esabna.com/euweb/mig_handbook/592mig10_2.htm. [Accessed 17 March 2017].

[68] ESAB, “MIG Handbook: Weld Defects - Lack of Fusion,” ESAB, 2017. [Online]. Available: http://www.esabna.com/euweb/mig_handbook/592mig10_3.htm. [Accessed 5 March 2017].

[69] TWI Ltd., “Weld Defects - Lack of Sidewall and Inter-Run Fusion,” TWI Ltd., 19 October 2015. [Online]. Available: https://www.twi-global.com/technical-knowledge/job-knowledge/weld-defects-imperfections-in-welds-lack-of-sidewall-and-inter-run-fusion-041. [Accessed 07 August 2020].

[70] TWI Ltd., “What is magnetic arc blow?,” TWI Ltd., 3rd September 2015. [Online]. Available: https://www.twi-global.com/technical-knowledge/faqs/faq-what-is-magnetic-arc-blow. [Accessed 7th August 2020].

[71] Welding Engineers Ltd, “Porosity,” Welding Engineers Ltd, 2011. [Online]. Available: https://weldingengineers.co.nz/news/weld-defect/porosity. [Accessed 8th August 2020].

[72] O. W. Blodgett and James F. Lincoln Arc Welding Foundation, “Weld Cracking,” in *Fabricators' and Erectors' Guide to Welded Steel Construction*, James F. Lincoln Arc Welding Foundation, 1999.

[73] T. D. R. P. K. V. A. Laureys, “Characterization of hydrogen induced cracking in TRIP-assisted steels,” *International Journal of Hydrogen Energy 40,* 26 June 2015.

[74] TWI Ltd., “Chapter 3: Theory - PCS,” TWI: Virtual Academy, 2020. [Online]. Available: https://twi.phasexnde.com/home/tasters/tofd-taster/dashboard/section-2-tofd-theory/chapter-3-theory/pitch-catch/pcs/. [Accessed 27 July 2020].

[75] British Standards Institution, “Non-destructive testing — Ultrasonic testing — Sensitivity and range setting (ISO 16811:2012),” BSI Standards Limited 2014, 2014.

[76] BINDT, “DAC: Distance Amplitude Curve,” 2013. [Online]. Available: https://www.bindt.org/What-is-NDT/Index-of-acronyms/D/DAC/. [Accessed 4th May 2020].

[77] Dakota Ultrasonics, “DFX-7 Ultrasonic Flaw Detector Operation Manual,” 2017.

[78] The British Institute of Non-Destructive Testing, “TCG: Time-Corrected Gain,” The British Institute of Non-Destructive Testing, 2019. [Online]. Available: https://www.bindt.org/What-is-NDT/Index-of-acronyms/T/. [Accessed 6th June 2020].

[79] British Standards Institute, “BS EN 1330-4:2000: Non-destructive testing. Terminology. Terms used in ultrasonic testing,” BSI Standards Limited 2014, 2000.

[80] J. Drury, Ultrasonic Flaw Detection for Technicians (3rd Edition), UK: Silverwing Ltd., 2004.

[81] OLYMPUS NDT, “An Introduction to Ultrasonic Flaw Detection,” OLYMPUS CORPORATION, 1999. [Online]. Available: https://www.olympus-ims.com/en/applications-and-solutions/introductory-ultrasonics/introduction-flaw-detection/. [Accessed 07 August 2020].

[82] OLYMPUS NDT, “Basic Waveform Interpretation,” CORPORATION, 9th November 2007. [Online]. Available: https://www.olympus-ims.com/en/ndt-tutorials/flaw-detection/basic-waveform-interpretation/. [Accessed 14th August 2020].

[83] S. J. Klima and J. C. Freche , “Ultrasonic Detection and Measurement of Fatigue Cracks in Notched Specimens,” *Engineering Mechanics,* vol. 9, pp. 193-202, 1969.

[84] TWI Ltd., “Fatigue Testing,” TWI Ltd., 19 October 2015. [Online]. Available: https://www.twi-global.com/technical-knowledge/job-knowledge/fatigue-testing-078. [Accessed 15 December 2022].

[85] E. Ginzel, “NDT Modelling An Overview,” NDT.net, Ontario.

[86] NDT.net, “Eclipse Scientific Releases BeamTool 9.1,” *e-Journal of Nondestructive Testing,* 2019.

[87] M. I. Friswell and J. E. Mottershead, Finite Element Modelling Updating in Structural Dynamics, London: Kluwer Academic Publishers, 1995.

[88] J. Dobson, An Integrated Framework for Finite Element Modelling of Ultrasonic Inspections of Carbon Fibre Reinforced Polymer Components, Glasgow: University of Strathclyde, 2019.

[89] DOCAN Ltd., “Explicit vs implicit FEA: What’s the difference?,” 22 July 2022. [Online]. Available: https://docanco.com/explicit-vs-implicit-fea/. [Accessed May 2023].

[90] Cadence CFD, “Methods for Grid Generation in CFD Simulations,” Cadence CFD, 13 October 2022. [Online]. Available: https://resources.system-analysis.cadence.com/blog/msa2021-methods-for-grid-generation-in-cfd-simulations. [Accessed February 2023].

[91] EXTENDE, “UT Modelling - Theory,” in *CIVA 2020 Manual*, 2020.

[92] EXTENDE, “SOV,” in *CIVA 2020 Manual*, 2020.

[93] N. Gengembre and A. Lhémery, “Pencil method in elastodynamics: application to ultrasonic field computation,” *Ultrasonics,* vol. 38, pp. 495-499, 2000.

[94] N. Gengembre, “PENCIL METHOD FOR ULTRASONIC BEAM COMPUTATION,” in *World Congress of Ultrasonics*, Paris, 2003.

[95] S. Mahaut, S. Lonne and L. de Roumilly, “Validation of CIVA Simulation Tools for Ultrasonic Inspection in Realistic Configuration,” in *ECNDT*, 2006.

[96] J. Lambert, G. Rougeron, S. Chatillon and L. Lacassagne, “Interactive Ultrasonic Field Simulation For Non Destructive Testing,” in *Twelfth International Conference on Quality Control by Artificial Vision*, Le Creusot, France, 2015.

[97] L. S, d. R. L, L. B. L, M. S and C. G, “EXPERIMENTAL VALIDATION OF CIVA ULTRASONIC SIMULATIONS,” in *International Conference on NDE in relation to structural Integrity for Nuclear and Pressurized Components*, 2006.

[98] P. Calmon, “Simulation of Complex Configurations,” in *ECNDT*, Berlin, 2006.

[99] M. Darmon, V. Dorval and F. Baqué, “Acoustic Scattering Models from Rough Surfaces: A Brief Review and Recent Advances,” *Applied Sciences,* vol. 10, no. 22, 2020.

[100] M. Darmon, N. Leymarie, S. Chatillon and S. Mahaut, “Modelling of scattering of ultrasounds by flaws for NDT,” in *Ultrasonic Wave Propagation in Non Homogeneous Media*, Berlin, Springer-Verlag Berlin Heidelberg, 2009.

[101] J. R. Pettit, A. E. Walker and M. J. S. Lowe, “Improved Detection of Rough Defects for Ultrasonic Nondestructive Evaluation Inspections Based on Finite Element Modeling of Elastic Wave Scattering,” *IEEE Transactions on Ultrasonics, Ferroelectrics, and Frequency Control,* vol. 62, no. 10, 2015.

[102] F. Shi, W. Choi, M. J. Lowe and E. A. Skelton, “The validity of Kirchhoff theory for scattering of elastic waves from rough surfaces,” in *Royal Society*, 2015.

[103] N. J. Pignier, C. J. O'Reilly and S. Boij, “A Kirchhoff approximation-based numerical method to compute multiple

acoustic scattering of a moving source," *Applied Acoustics,* vol. 96, pp. 108-117, 2015.

[104] L. W. Schmerr Jr., Fundamentals of Ultrasonic Phased Arrays, Springer International Publishing Switzerland, 2015.

[105] E. I. Thorsos, "The validity of the Kirchhoff approximation for rough surface scattering using a Gaussian roughness spectrum," *The Journal of the Acoustical Society of America,* vol. 83, no. 78, 1988.

[106] M.-j. Jung, B.-c. Park, J.-h. Bae and S.-c. Shin, "PAUT-based defect detection method for submarine pressure hulls," *International Journal of Naval Architecture and Ocean Engineering,* vol. 10, pp. 153-169, 2018.

[107] Dakota Ultrasonics, "References: Appendix A Velocity Table," Dakota Ultrasonics, 2017. [Online]. Available: https://dakotaultrasonics.com/reference/. [Accessed 15th June 2017].

[108] M. McInnes, R. O'Leary, A. Gachagan and A. Glover, "Defect amplitude response approximation using TCG calibrated CIVA simulation of PAUT inspection," in *BINDT NDT 2021 Webinar Week*, Webinar, 2021.

[109] D. J. Roth, R. P. Tokars, R. E. Martin, R. W. Rauser, J. C. Aldrin and E. J. Schumacher, "Ultrasonic Phased Array Inspection Simulations of Welded Components at NASA," *Materials Evaluation,* vol. 67, no. 1, 2009.